

University of Nottingham
UK | CHINA | MALAYSIA

# New multi-material formulations for vat-photopolymerisation and their application in manufacturing ocular implants

Andrea Alice Konta, MPharm.

Supervised by Laura Ruiz Cantu, Derek J. Irvine, Cameron Alexander, Ricky Wildman

Thesis submitted to the University of Nottingham

for the degree of Doctor of Philosophy

March 2022

This work is dedicated to Irma Lobontz (*in memoriam*) and Angela Konta. The strength, resilience, perseverance, braveness, and kindness both of you showed in your lives greatly inspired me and shaped me into who I am today.

# Declaration

This dissertation is the result of my own work and includes nothing, which is the outcome of work done in collaboration except where specifically indicated in the text. It has not been previously submitted, in part or whole, to any university or institution for any degree, diploma, or other qualification.

Signed:



Date: 29/03/2022

Andrea Alice Konta, MPharm.

# Abstract

Additive Manufacturing (AM), often referred to as 3D printing, encompasses a series of processes that build structures in an additive fashion, layer by layer. This is usually possible by translating a 3D computer-aided design (CAD) into a standard tessellation language (STL) file that is then directly manufactured into a physical structure. The process that manufactures structures illuminating liquid photosensitive resins with a light source is called vat-photopolymerisation. From the different vat-photopolymerisation techniques, two-photon polymerisation is the technique that allows micro- and nano-printing at the highest resolution. Besides high resolution, it also offers the possibility of manufacturing complex structures without need for support. And it also allows to select degrees of porosity, defined shapes, or intricate topologies. These features had made the technique attractive for several applications like microfluidics, metamaterials, cell culture, or drug delivery.

However, there are several challenges that need to be resolved for the technique to reach its full potential and be embraced on a commercial basis outside the research community. This thesis aims to tackle two of the disadvantages of this technique. First, the lack of suitable materials available for it. Currently, there are few materials that are 2PP processable that are also of interest for biological applications. Second, the research developed on the technique has mainly focused on mono-material formulations. Therefore, the work presented in this thesis addresses both drawbacks by developing new materials that could be potentially used for biological applications and optimises them for 2PP processing in multi-material formulations.

This was achieved by initially synthesizing a new mono–functional poly(trimethylene carbonate) acrylate (PTMCA) polymer and optimizing it for 2PP printing in several multi-

material formulations. The optimisation was done by mixing the biodegradable PTMCA with a hydrophilic (poly(ethylene glycol) diacrylate (PEGDA)) and hydrophobic (tricyclo [5.2.1.$0^{2,6}$] decanedimethanol diacrylate (TCDMDA)) cross-linker monomer at different concentrations. The multi-material formulations containing the mono–functional PTMCA were successfully processed in the 2PP system, and the structures manufactured with them showed a sharp increase in reacted vinyl groups (RVG) compared to structures manufactured with only commercial monomer (between 20% and 50% increase depending on the formulation used). The addition of PTMCA to the monomers also significantly expanded the polymerisation threshold of the formulations when compared to thresholds of only cross-linkers. The presence and disposition of both materials in structures manufactured with multi-material formulations were confirmed via Time-of-Flight Secondary Ion Mass Spectrometry (TOF – SIMS). PTMCA + PEGDA samples showed a continuous single phase. PTMCA + TCDMDA samples showed phase separation at certain concentrations. This phase separation could be controlled by the formulation concentration or the processing parameters of the 2PP system.

The library of 2PP materials was also expanded by synthesizing two new hyperbranched polymers: Hyperbranched poly(PEGDA) (HBpPEGDA) and Hyperbranched poly(TCDMDA) (HBpTCDMDA). This would allow to manufacture with highly functionalised materials with a high molecular weight, compared to the mono-functional low molecular weight PTMCA. The hyperbranched materials were optimized for 2PP manufacturing in mono-material (HBpTCDMDA based) or multi-material (HBpPEGDA based) formulations. Structures manufactured with HBpTCDMDA also showed a sharp increase in RVG (>50 %) when compared to structures manufactured with TCDMDA monomer. The hyperbranched formulations also significantly broadened the polymerization threshold when compared to thresholds of formulations prepared with commercial PEGDA and TCDMDA monomers. The presence of both materials in multi-

material formulations was confirmed via ToF-SIMS, with a single continuous phase. Scaffolds printed with HBpTCDMDA also showed high viability on LIVE/DEAD assay with mouse fibroblasts, indicating the potential biocompatibility of this material.

Last, to show the potential of one of the formulations developed in this thesis for a biological application, one of the PTMCA + PEGDA mixtures was selected and further optimised to fabricate a proof-of-concept intravitreal implant for sustained release of fluocinolone acetonide (FA). Different implant designs based on a diamond lattice were created to study the influence of implant geometry on drug release. Printing optimisation was initiated in the 2PP system to determine the initial feasibility of lattice design printing at small scale while using small amounts of formulation, but micro projection stereolithography (PμSLA) was chosen as the technique for scale-up and final implant manufacturing due to faster printing times compared to 2PP while still maintaining adequate resolution. N – vinyl pyrrolidone (NVP) was added to the formulation to facilitate drug release from the implant matrix. The percent of NVP needed was optimised by studying the release of model drug Rhodamine B from Ultraviolet (UV) cast samples. The concentration that allowed for a sustained release of ~80 % of model drug over 39 days was 25 wt% NVP, which was the formulation selected to manufacture the FA intravitreal implants. Cylindrical lattice implants (1.85 ± 0.05 mm in length, 0.5 mm in diameter) loaded with 6.25 wt% of FA were manufactured via PμSLA using the optimised formulation containing 25 wt% NVP. They showed high cell viability and no cytotoxicity in *in vitro* assays with human corneal epithelial cells. All lattice implants showed ~60 % of cumulative drug release over 35 days. The profile of release varied depending on the geometry of the implant, indicating an influence of the pore size and surface area over release. The microstructure analysis of samples indicated some phase separation and a possible preference of the drug for Poly - vinyl pyrrolidone (PVP), which

further facilitated the drug release from the polymer matrix when it dissolved into aqueous media.

# Publications

## Included in this thesis:

(Drafted) Konta, A.A, Trindade, F. G., Hege, C., Ruiz-Cantu, L., Turyanska, L., Alexander, C., Wildman, R., Irvine, D, J. Two photon multi – material printing with controlled microstructure and high reacted vinyl groups.

(Drafted) Konta, A.A, Stimpson, A., Goodwin, S., Touré, A., Trindade, F. G., Ruiz-Cantu, L., Alexander, C., Wildman, R., Irvine, D, J. Two photon multi – material printing of hyperbranched polymers with high reacted vinyl groups and threshold expansion.

# Conferences

The research described in this thesis has been presented at the following conferences in poster format:

- Biomaterials Discovery Workshop, Nottingham, UK (2017, 2018 and 2019)
- APS PharmSci Conference, London, UK (2019). Winner of *2nd prize best poster*.
- 3D Medical Conference & Expo, Maastricht, Netherlands (2020)

# Acknowledgements

The PhD journey is a challenging one in many ways. Not only because of the research itself but because throughout its duration, the world keeps spinning and changing at light speed while you try to expand the walls of knowledge. To be able to reach the end of my PhD journey in the circumstances that surrounded it, I had the support and help of many people that I would like to thank in this acknowledgement section.

First, I would like to thank my supervisors Dr Laura Ruiz Cantu, Professor Derek J. Irvine, Professor Cameron Alexander, and Professor Ricky Wildman, for the guidance, help, and understanding they provided me throughout the years of my PhD studies.

Second, I would like to thank all the people that collaborated with me, providing data and discussions that further enriched this thesis: Adja Touré, Gustavo Ferraz Trindade, Sophie Goodwin, Cordula Hege, Yinfeng He, Lyudmila Turyanska, Lydia Beeken, Stefanie Kern. I would also like to thank Dr Graham Rance and Paul Cooling, for the training and the help they provided me with my experiments.

To the colleagues I met throughout the years in B19 (and CfAM) that then turned into friends, thanks for being the most fun, sociable, and supportive bunch that one could have asked for. Doing a PhD alongside all of you brought me immense joy. Special shout-outs to Yaz and Sam, for welcoming me into the office when I was a newbie and into their lives. To Leo, Ling, Marica, and Chris Strong, for making lab, conferences, thesis writing, and everything in between much more entertaining. To Kristian Plender, for your friendship, for your help, for all the laughing, and, of course, for all the dancing.

To Laura and Richard H., thank you for allowing me to enter your lives, your home, and for becoming like a second family to me. I was lucky to stumble upon you, Gracie and Kai.

To the “gals”: Arielle, Salome, Negar and Shreeja. Thank you for all the great memories we created together. The sport clubs, the parties, the games, the travels, the food, the chatting, the laughing, and for lending me your ears and hugs when I needed them the most.

To Claudio, thank you for getting me addicted to the chai lattes of the Malt Cross and the pizzas of Oscar & Rosie’s. Thank you for all the discussions about our beloved philosophy, science, life, and everything in between. Thank you for all the jokes and all the memes.

To my *farmaceuticos*, thank you for being just as great as when we were studying pharmacy together, as if I had never left thousands of miles away. And to Almudena, whom pharmacy also put into my life, for turning into a big sister and a great support throughout the years.

To Carol, Cesar, and Victor, thanks for more than a decade of friendship and support, no matter the distance, the years, and life changes.

To Richard, thank you for all the love and support you always give me. Going through the PhD journey with you by my side enriched this experience tenfold. Not only that, but meeting you also enriched every other aspect of my life. Thank you for becoming my partner, my best friend, and for having the greatest times together. Thank you for also being there during my most heart-breaking moments, when no one else knew what to say or do. And thank you for always making me laugh, no matter the circumstances.

To the family members that proudly watched me start this journey but could not be here to see me finish it: my uncle, Öcsi; my paternal grandma, Ana; my maternal grandma, Irma; and my father, Adrian. You all loved me unconditionally and were proud of me no matter what, but I know it would have made you very happy to watch me reach the end of this journey. Especially you, Dad. Sadly, life had other plans and because of that, all

achievements now feel bittersweet. Thomas Campbell once said: “To live in hearts we leave behind is not to die.” And you will always be very much alive in mine.

To the family that is still with me, thank you for also loving me unconditionally and always being there for me. I am very grateful for having a family that it’s as close as ours. That is fun, supportive, understanding and that is always around you when needed, no matter the physical distance between us all. You all contributed to the person that I am today, and I appreciate every moment that we spend together.

And finally, to my mother, Angela. Words will never be enough to express all my gratitude and love towards you. Thank you for being the bravest woman I know as well as the kindest. Thank you for being so inspiring. Thank you for raising me with great love and for pushing me in the right direction when needed. Thank you for supporting me unconditionally all my life. Thank you for also being a friend. If there’s one thing I’m truly grateful for, is to have coincided in this lifetime with you.

# Contents

**Abstract** ..... **iii**

**Publications** ..... **vii**

**Conferences** ..... **viii**

**Acknowledgements** ..... **ix**

**Contents** ..... **xii**

**List of Tables** ..... **xvi**

**Abbreviations** ..... **xxi**

**Nomenclature** ..... **xxvi**

**1 Introduction** ..... **28**

1.1 Aim and objectives of the Thesis ..... 28

1.2 Structure of the thesis ..... 29

**2 Literature Review** ..... **31**

2.1 Introduction to Additive Manufacturing ..... 31

2.1.1 Introduction to stereolithography techniques ..... 32

2.2 Vat-photopolymerisation techniques ..... 33

2.2.1 Two-photon polymerisation ..... 33

2.2.2 Projection micro stereolithography ..... 38

2.2.3 Volumetric Additive Manufacturing ..... 39

2.3 Free Radical Polymerisation ..... 41

2.4 Resins for two-photon polymerisation ..... 43

2.4.1 SU – 8 and ORMOCER ..... 44

2.4.2 (Meth)acrylate Biocompatible Resins ..... 44

2.5 Characteristics of (meth)acrylate 2PP photosensitive resins ..... 50
2.6 Hyperbranched polymers ..... 51
2.7 Implants for corticosteroid ocular drug delivery ..... 55
2.7.1 Human eye anatomy and pathology ..... 55
2.7.2 Ocular implants available on the market for corticosteroid delivery ..... 57
2.7.3 Synthetic polymers explored for ophthalmic drug delivery ..... 59
2.8 Key findings of the literature ..... 60
2.9 Summary of gaps in the literature ..... 61
**3 Materials and Methods ..... 63**
3.1 Introduction ..... 63
3.2 Materials ..... 63
3.2.1 Material acquisition ..... 63
3.3 Methodology ..... 64
**4 2PP multi material printing with controlled microstructure and high reacted vinyl groups ..... 91**
4.1 Introduction ..... 91
4.2 Results and Discussion ..... 96
4.2.1 Material characterization ..... 96
4.2.2 The effect of varying printing parameters on Reacted Vinyl Group Reactivity 110
4.2.3 Evaluation of effective 2PP processing window for multi-material printing with monoacrylate PTCMA macromers ..... 113
4.2.4 Multi-material microstructure control and characterization ..... 119
4.3 Conclusions ..... 127
4.4 Chapter Appendix: Supplementary Information ..... 129

**5 2PP multi-material printing of hyperbranched resins ..... 131**

5.1 Introduction ..... 131

5.2 Results and Discussion ..... 134

5.2.1 Material characterization ..... 134

5.2.2 Degree of conversion (quantity of reacted vinyl groups) ..... 136

5.2.3 Polymerisation threshold ..... 141

5.2.4 Microstructure characterization ..... 147

5.2.5 Biocompatibility of hyperbranched resin ..... 149

5.3 Conclusions ..... 153

**6 Optimisation of photo-sensitive multi-material formulation for drug release application ..... 155**

6.1 Introduction ..... 155

6.2 Results and Discussion ..... 159

6.2.1 Designs of diamond lattice-based implants for sustained drug release for ocular therapy ..... 159

6.2.2 Initial implant printing optimisation of PTMCA + PEGDA 1:20 molar ratio mixture *via* 2PP and PμSLA systems ..... 162

6.2.3 Selection of optimal NVP concentration in PTMCA + PEGDA formulation and sustained Rhodamine B drug release from PTMCA + PEGDA+NVP UV cast structures ..... 171

6.2.4 Determination of maximum drug loading of FA to PTMCA + PEGDA + NVP formulation ..... 176

6.2.5 Manufacturing optimisation of final implant prototypes loaded with FAc drug *via* PμSLA ..... 177

6.2.6 Biocompatibility of drug loaded diamond lattice implants ..... 181

6.2.7 Microstructure characterization of PμSLA structure manufactured with implant formulation....183
6.2.8 Drug release of Fluocinolone Acetonide from lattice implants manufactured *via* PμSLA....186
6.3 Conclusions....189
**7 Conclusions and Future Work....191**
7.1 Conclusions....191
7.1.1 Mono-acrylate oligomers for 2PP....191
7.1.2 Hyperbranched materials for 2PP....192
7.1.3 Diamond lattice implants manufactured with photo-sensitive formulation for sustained release of FA....194
7.2 Future Work....195
7.2.1 Further characterization and optimisation for 2PP....195
7.2.2 Exploring controlled phase-separated microstructure in multi-material printing....196
7.2.3 Cell viability of 2PP manufactured scaffolds with hyperbranched polymers 198
7.2.4 Improving printing resolution with multi-material formulations....199
7.2.5 Biocompatibility of diamond lattice implants....199
7.2.6 Drug release and microstructure....200
**8 Bibliography....202**

# List of Tables

Table 2.1. Comparison between structure and properties of hyperbranched polymers, dendrimers, and linear polymers [62]. 53

Table 3.1. Numerical values of polynomial 4$^{th}$ order constants used in Equation 3.5 and Equation 3.6 for $P_{xy}$ and $P_z$ calculations. 79

Table 4.1. 2PP formulations, comprising of a combination of monomer/oligomer (M1) and a reactive solvent (M2). Each experiment utilised 2 wt% of the photoinitiator (Irgacure 369). Long > 1000 g/mol and short < 1000 g/mol. 99

Table 4.2. LogP values for the different materials used in the 2PP formulations. 100

Table 4.3. Flory-Huggins interaction parameter, $\chi$, calculated using Equation 3.5 for the formulations tested in the 2PP system. 101

Table 4.4. RVG values ($n$ = 3) ± Standard Deviation (SD) of printed structures using 2PP formulations prepared with PEGDA, PTMCA+PEGDA, eDEGA+PEGDA and LA+PEGDA at different concentrations. 104

Table 4.5. Mean RVG values ($n$ = 3) ± SD of printed structures using 2PP Formulations prepared with TCDMDA, PTMCA + TCDMDA, TCDMDA + BAEDA and PTMCA + BPAEDA at different concentrations. 109

Table 5.1. Summary of conversion, number average molecular weight ($M_n$), weight average molecular weight ($M_w$), dispersity (D) and yield. 135

Table 5.2. 2PP formulations prepared with one or two materials at different concentrations, using 2% wt photoinitiator (Irgacure 369) in all of them. 136

Table 6.1. Formulations prepared for UV-cast implants by maintaining a constant 50%wt of PTMCA while varying the wt% of PEGDA and NVP. All formulations had 2wt% (of total weight of all materials) of PI added and loaded with 0.1%wt (of total weight of all materials) of Rhodamine B. 172

# List of Figures

Figure 2.1. Jablonski Diagram showing excitation of photoinitiator molecule by absorbing either one photon (UV light, blue colour) or two photons (NIR light, green colour). Then it can relax to the lower $S_1$ state via vibrational relaxation and reach back the ground state via fluorescence or it can undergo intersystem crossing (orange) to the triplet state. There it will form radicals via α – cleavage. These radicals will initiate the polymerisation reaction. .....34

Figure 2.2. a) One–photon excitation of fluorescein using focused 488 nm light (0.16 NA). b) Two-photon excitation using femtosecond pulse 960 nm focused light (0.16 NA) [13].....35

Figure 2.3. Exposure doses are shown as light intensity profiles generated by a laser beam in one photon (dark blue) and two-photon polymerisation (purple) thresholds using the same experimental conditions [11]. .....36

Figure 2.4. a) Common 2PP setup showing the main and necessary components: ultrafast laser, beam/sample motion system, beam focusing optics, beam control, and software system. (N.D. filter = Neutral density filter, acts as laser beam attenuator) [9]. b) Principle of manufacturing structures via two-photon polymerisation process [14]. .....37

Figure 2.5 Commercial PμSLA system schematic with its parts indicated. [18]. .....39

Figure 2.6. Example of tomographic volume AM set up [21].....40

Figure 2.7. Steps of free radical polymerisation. .....41

Figure 2.8. Mechanism of the chain transfer reaction that can take place during free radical polymerisation. .....42

Figure 2.9. (a) Prototype of benzophenone radical. (b) Schematic showing the mechanism of Norrish Type I photinitators. (c) Schematic showing the mechanism of Type II photoinitiators [7].....44

Figure 2.10. Anatomy of the human eye [82]. .....56

Figure 3.1. UV absorption spectrum of photoinitiator Irgacure 369.....68

Figure 3.2 Representation of model assumptions: a) 3D model showing the laser beam manufacturing a voxel (red colour) while highlighting the possible 3 voxels affected by the incident laser power (yellow voxels). b) View of several voxels in the *xy*-plane showing the distance from one centre of the voxel to another (hatching distance, *h*) and the voxel radius (A). c) 3D model representing the assumption A<*h*<2A in which 3 voxels overlap and the effective laser power takes into account $P_{xy}$ for total power calculations. d) 3D model representing the assumption *h*>2A in which voxels do not overlap and $P_{xy}$ does not contribute to total power calculations. .....78

Figure 4.1. $^1$H NMR spectrum of PTMCA showing the region between 4.0 and 6.7 ppm with characteristic peaks of the oligomer assigned to the material's structure. Peaks a,b, and c are representative of the acrylate functional group and peak d is representative of the polymer backbone. .....97

Figure 4.2. Chemical structures of: a) poly(trimethylene carbonate) acrylate (PTMCA) b) poly(ethylene glycol) diacrylate (PEGDA) c) tricyclo[5.2.1.02,6] decanedimethanol diacrylate (TCDMDA) d) di(ethylene glycol) ethyl ether acrylate (eDEGA) e) lauryl

acrylate (LA) f) bisphenol A ethoxylate diacrylate (BPADA) g) 2-Benzyl-2-(dimethylamino)-4'-morpholinobutyrophenone (Irgacure 369, photo-initiator).....98

Figure 4.3. Raman spectrum of PTMCA+PEGDA 1:2 molar ratio formulation before printing (dark blue) and spectrum of the 2PP printed structure with that formulation (orange) showing the sharp decrease in C=C band after polymerisation while the C=O band does not change as it does not participate in the reaction. See RVG % calculated from this spectra in Table 4.4. .....102

Figure 4.4. a) RVG values for rectangles manufactured with the same formulation but at different applied laser powers (*n*=3, ± SD) b) RVG results from the same structures related to their effective laser power.....112

Figure 4.5. a) to d) CAD models of cube, buckyball, spicky hemisphere, and woodpile. e) to h) associated SEM images from the manufactured structures by 2PP. .....115

Figure 4.6. Polymerisation thresholds of the following formulations: 100 % PEGDA (0), PTMCA+PEGDA 1:20 molar ratio (0.05) and PTMCA+PEGDA 1:2 molar ratio (0.5).....116

Figure 4.7. Polymerisation thresholds of the following formulations: TCDMDA (0), PTMCA + TCDMDA 1:2 molar ratio (0.5), PTMCA + TCDMDA 1:8 molar ratio (0.125), PTMCA + TCDMDA 1:20 molar ratio (0.05), and PTMCA + TCDMDA 1:46 molar ratio (0.02),). The colours represent the same processing window zone as in Figure 4.6.....118

Figure 4.8. SEM images of rectangles printed with PTMCA + TCDMDA 1:46 molar ratio formulation: a) structure printed in the first 20 min of the printing session with 25 mW laser power and 4 mm/s writing speed. b, c) rectangles printed after 20 min in the printing session with 15 mW laser power at 6 mm/s writing speed and 20 mW laser power at 10 mm/s writing speed respectively. .....119

Figure 4.9. Normalised intensities of PTMCA (103 u) and TCDMDA (67 u) ions throughout the manufactured structure a) Surface view of PTMCA intensity (displayed on Y axis, from low (black) to high (yellow) b) Surface view of TCDMDA intensity c) Depth view of TCDMDA intensity d) Depth view of PTMCA intensity e) Ion intensity of both materials through the *xy*-plane f) Ion intensity of both materials through the *xz*-plane. MC = Maximal counts in one pixel. TC = Total counts in the image. MVA = Multivariate analysis. .....122

Figure 4.10. ToF-SIMS analysis of 3D printed cubes printed with 100% PEGDA, PTMCA + PEGDA 1:20 molar ratio, PTMCA + PEGDA 1:2 molar ratio formulations. The 5$^{th}$ sample was a droplet of PTMCA dissolved in acetone and UV cured on a coverslip. Graph a) displays the normalised intensities of the samples. Graph b) shows the normalised intensity of the PTMCA peak in relation to the PEGDA peak on each sample. R represents the normalised intensity of each sample while $R_{PTMCA}$ (assigned as 1) and $R_{PEGDA}$ (assigned as 0) represent the normalised intensities of each material.....125

Figure 5.1. Monomers and 3-MPA CTA were used for CTP synthesis to produce Hyperbranched materials. Blue spheres represent the monomer that will form part of the backbone of the polymer and the green spheres represent the CTA molecules that will be at the end of the polymer chain as functional groups. .....134

Figure 5.2. Raman spectra of 2PP manufactured samples and the comparative un-polymerised formulations they were fabricated with. a) Blue (printed sample) and red (formulation) spectra were obtained from the HBpPEGDA 50 wt% + TCDMDA

50 wt% mixture. Green (printed sample) and yellow (formulation) spectra were obtained from the PEGDA 50 wt% + TCDMDA 50 wt% mixture. b) Blue (formulation) and green (printed structure) were obtained from TCDMDA monomer mixtures. Red (formulation) and black (printed sample) were obtained from the HBpTCDMDA mixture. ..... 138

Figure 5.3. RVG data for 50 µm cubes manufactures from the 2PP formulations prepared containing either one material or two materials formulations with 50:50 wt% concentrations of each material. 2 wt% photoinitiator (Irgacure 369) was utilised in every case, and the corresponding. Data points show the Mean ± Standard Deviation (SD). Statistical significance was determined with ONE-WAY Anova followed by Tukey test. ..... 139

Figure 5.4. Map of the Polymerisation thresholds for the following formulations (top to bottom): 100 wt% HBpTCDMDA, TCDMDA 70 wt% + HBpPEGDA 30 wt%, and TCDMDA 100 wt%. ..... 141

Figure 5.5. Map of the polymerisation thresholds of the following formulations (top to bottom): HBpPEGDA 50 wt% + TCDMDA 50 wt%, PEGDA 50 wt% + TCDMDA 50 wt%, and PEGDA 100 wt%. ..... 144

Figure 5.6. SEM images of 2PP manufactured buckyball structure produced from the following mixed material inks a) HBpPEGDA 50 wt% + TCDMDA 50 wt% at 30 mW (laser power) and 6 mm/s (writing speed) b) PEGDA 50 wt% + TCDMDA 50 wt% at 30 mW and 6 mm/s c) HBpPEGDA 50 wt% + TCDMDA 50 wt% at 20 mW and 4 mm/s d) PEGDA 50 wt% + TCDMDA 50 wt% at 30 mW and 4 mm/s e) HBpPEGDA 50 wt% + TCDMDA 50 wt% at 25 mW and 30 mW at 8 mm/s. f) PEGDA 50 wt% + TCDMDA 50 wt% at 25 mW and 30 mW at 8 mm/s. ..... 145

Figure 5.7. ToF-SIMS spectra of 50 µm a HBpPEGDA+TCDMDA cube at a) the beginning of analysis characterising the top surface, b) the end of depth profile analysis, and c) detailing the normalised intensity of HBpPEGDA (43u) and TCDMDA (67u) ions obtained from depth profile analysis. MC = Maximal counts in one pixel. TC = Total counts in the image. ..... 148

Figure 5.8. Fluorescence microscope images from a LIVE/DEAD assay using mouse fibroblast cells: a) LIVE cells shown in green on HBpTCDMDA scaffold, b) Greyscale image of LIVE cells on HBpTCDMDA scaffold, c) Grayscale image of DEAD cells on HBpTCDMDA scaffold, d) LIVE cells shown in green on TCDMDA scaffold, e) Grayscale image of LIVE cells on TCDMDA scaffold, f) Grayscale image of DEAD cells shown on TCDMDA scaffold. The contour of the scaffolds was highlighted with the dashed orange line. ..... 151

Figure 6.1. Depiction of the implant's designs (2 mm × 0.5 mm) proposed for sustained drug delivery, showing from left to right a control design (cylinder) and 3 diamond matrix lattice designs that vary in cell number. The lattice implants were named based on their surface area: low surface area (LSA), medium surface area (MSA), and high surface area (HSA). ..... 161

Figure 6.2. Implant designs (0.1 mm length × 0.03 mm diameter and 0.2 volume fraction) printed with the 2PP system using PTMCA + PEGDA 1:20 molar ratio formulation. Parameters used for manufacturing: 45 mW laser power and 40 mm/s writing speed. Hatching and slicing distances were 0.2 µm and 0.4 µm, respectively. ..... 164

Figure 6.3. Implant designs (0.9 mm length x 0.3 mm diameter and 0.3 volume fraction) printed with the 2PP system with PTMCA + PEGDA 1:20 molar ratio formulation using the stitching method: a) LSA implant b) MSA implant c) HSA implant.

Parameters used for manufacturing all implants: 50 mW laser power and 33 mm/s writing speed. Hatching and slicing distances were both set to 0.4 µm. ..... 166

Figure 6.4. Structures manufactured via DLP by Dr Yinfeng He using PTMCA + PEGDA 1:20 molar ratio formulation containing 2 wt% PI and 0.75 wt% curcumin ..... 169

Figure 6.5. Lattice implants (0.9 mm × 0.3 mm) manufactured *via* PµSLA using PTMCA + PEGDA 1:20 molar ratio mixture with 0.75 wt% curcumin as photoabsorber. Parameters used for manufacturing were 100 % intensity and 8 s exposure time. The layer thickness was set to 10 µm. ..... 170

Figure 6.6. a) Optical microscope image from the surface of a 15 wt% NVP UV-cast implant after 39 days in PBS. b) SEM image of the same sample shown in image a). c) Optical microscope image from the surface of a 20 wt% NVP UV-cast implant after 39 days in PBS. d) SEM image of the same sample shown in image c). ..... 173

Figure 6.7. a) Sample manufactured with formulation containing 25 wt% NVP on day 0 before being submerged in PBS. b) 25 wt% NVP sample on day 39. c) Mass loss of the UV-cast samples at different time points. d) Cumulative drug release of Rhodamine B from samples prepared with formulations containing 25 wt%, 35 wt%, and 40 wt% NVP. Data points from c) and d) show Mean values (n=3) ± SD. ..... 175

Figure 6.8. Left vial: DLP formulation prepared with PTMCA/PEGDA/NVP and 0.75 wt% curcumin loaded with 6.25 wt% FA after 24h stirring at 60C. The clear formulation indicates adequate mixing and drug incorporation into the mixture. Right vial: DLP formulation prepared with PTMCA/PEGDA/NVP and 0.75 wt% curcumin loaded with 8 wt% FA after 24 h stirring at 60 ºC. The solution is visibly saturated. ..... 177

Figure 6.9. HSA implant manufactured with PµSLA system at 195 % intensity and 7.5 seconds exposure time. SEM image shows sample after post-processing steps (24 h washing in IPA and 15 min UV oven at 40 ºC). ..... 178

Figure 6.10. PµSLA manufactured 1.85 ± 0.05 mm implants with PTMCA + PEGDA + NVP + FAc + curcumin + PI formulation: a) Cylinder implant b) LSA implant c) MSA implant d) HSA implant. SEM image shows samples after post-processing steps (24 h washing in IPA and 15min UV oven at 40ºC). ..... 180

Figure 6.11. Results from assays performed on all printed implants (cylinder (Control) plus lattice designs) with HCE2 cells: a) PrestoBlue assay results showing the fold change of the cells on the Y axis vs the positive control (media only), negative control (lysed) and the implant designs. b) LDH assay results showing the calculated percent of cytotoxicity for all implants plus the lysed cells. N=3 (3 x cell samples at different passages), n=3 (3 x implant technical repeats / sample). Data points show the Mean ± SD. Statistical significance was determined via ONE WAY Anova followed by Tukey test. ..... 182

Figure 6.12. a) ToF-SIMS spectras highlighting the peaks of secondary ions identified from each individual implant formulation component. b) ToF-SIMS 3D reconstruction of PµSLA manufactured rectangle with data obtained from depth profile analysis. All samples were analysed in triplicates. ..... 185

Figure 6.13. Cumulative drug release values obtained from LSA, MSA, and HSA implants over 35 days. Data points show Mean values ($n$ = 3) ± SD. ..... 186

# Abbreviations

| | |
|---|---|
| $^{1}$H NMR | Hydrogen Nuclear Magnetic Resonance |
| 2PP | Two-photon polymerisation |
| 3-MPA | 3-Mercaptopropionic acid |
| AbAm | Antibiotic and antimycotic |
| Ad12-SV40 | Adenovirus 12 - SV40 virus hybrid |
| AIBN | 2,2′-Azobis(2-methylpropionitrile) |
| AM | Additive Manufacturing |
| AMD | Age – related macular degeneration |
| ANOVA | Analysis of Variance |
| BMF | Boston Micro Fabrication |
| BPAEDA | Bisphenol A Ethoxylate diacrylate |
| BSA | Bovine Serum Albumine |
| CAD | Computer Aided Design |
| CCD | Charged-coupled device |
| $CDCl_3$ | Deuterated chloroform |
| CDR | Cumulative drug release |
| CMOS | Complementeray metal-oxide semiconductor |
| CNT | Carbon nanotubes |
| CNV | Choroid neovascularization |
| CTA | Chain transfer agentt |
| DB | Degree of Branching |
| DCM | Dicloromethane |

| | |
|---|---|
| DLP-AM | Digital light projection additive manufacturing |
| DLW | Direct laser writing |
| DM | Diabetes Miellitus |
| DMD | Digital Micromirror Device |
| DME | diabetic macular edema |
| DNA | Deoxyribonucleic acid |
| DR | diabetic retinopathy |
| DRI | Differential refractometer |
| eDEGA | Di(ethylene glycol) ethyl ether acrylate |
| EthD-1 | Ethidium homodimer-1 |
| FA | Fluocinolone acetonide |
| FBS | Foetal bovine serum |
| FDA | Food Drug Administration |
| GCIB | Gas cluster ion beam |
| GPC | Gel Permeation Chromatography |
| HBP | Hyperbranched Polymers |
| HBpPEGDA | Hyperbranched poly(ethylene glycol) diacrylate |
| HBpTCDM | Hyperbranched tricyclo [5.2.1.$0^{2,6}$] decanedimethanol diacrylate |
| HEA | 2-Hydroxyethyl acrylate |
| HEPA | High efficiency particulate air |
| HPLC | High Performance Liquid Chromatography |
| HSP | Hansen solubility parameter |
| INT | Tetrazolium salt |
| IPA | Isopropanol. |
| iPSC | induced pluripotent stem cell |

| | |
|---|---|
| Irgacure 369 | benzoic acid, 2-Benzyl-2-(dimethylamino)-1-[4-(morpholinyl) |
| ITV | Intravitreal |
| KSFM | Keratinocyte serum free media |
| LA | Lauryl acrylate |
| LDH | Lactate dehydrogenase |
| LMIS | Liquid metal ion source |
| MEM | Minimum Essential Medium (MEM) |
| MSC | Mesenchymal stem cells |
| MVA | Multivariate analysis |
| NA | Numerical aperture |
| $NAD^+$ | Nicotinamide adenine dinucleotide |
| NADH | Nicotinamide adenine dinucleotide + hydrogen |
| NIR | Near Infrared |
| NMF | Non-negative matrix factorisation (NMF) |
| NPDR | Non – proliferative diabetic retinopathy |
| NVP | N – vinyl pyrrolidone |
| PμSLA | Micro projection stereolithography |
| PBS | Phosphate buffered saline |
| PCA | Principal component analysis |
| PCL | Poly ($\varepsilon$ – caprolactone) |
| PDI | Polydispersity Index |
| PDLA | poly (d – lactic acid) |
| PDLLA | poly (DL – lactic acid) |
| PDR | Proliferative diabetic retinopathy |
| PEG | Poly (ethylene glycol) |

| | |
|---|---|
| PEGDA | Poly(ethylene glycol) diacrylate |
| PEGMA | PEG – methacrylate |
| PFA | Perfluoroalkoxy |
| PGMEA | Propylene glycol methyl ether acetate |
| PI | Photoinitiator |
| PLA | Poly (lactic acid) |
| PLGA | Polylactide-co-glycolide |
| PLLA | poly (l – lactic acid) |
| png | portable network graphics |
| ppm | Parts per million |
| PTFE | Polytetrafluoroethylene |
| PTMCA | Poly(trimethylene carbonate) acrylate |
| PVA | Poly(vinyl alcohol) |
| PVP | Poly (N-vinyl pyrrolidone) |
| RNA | Ribonucleic acid |
| RPE | Retinal pigment epithelial |
| RPM | Revolutions per minute |
| RVG | Reacted vinyl groups |
| SD | Standard Deviation |
| SEM | Scanning electron microscope |
| SLA | stereolithography |
| STL | Standard tessellation language |
| TBD | Triazabicyclodecene |
| TCDMDA | Tricyclo [5.2.1.$0^{2,6}$] decanedimethanol diacrylate |
| THF | Tetrahydrofuran |

| | |
|---|---|
| TMC | Trimethylene carbonate |
| ToF-SIMS | Time-of-Flight Secondary Ion Mass Spectrometry |
| TPA | Two photon absorption. |
| TPM | 3-(Trimethoxysilyl) propyl methacrylate |
| TPMS | Triply periodic minimal surfaces |
| UV | Ultraviolet |
| VEGF | vascular endothelial growth factor |

# Nomenclature

| | |
|---|---|
| $T_g$ | Glass transition temperature |
| $M_w$ | Weight average molecular weight |
| $M_n$ | Number average molecular weight |
| $dn/dc$ | differential index of refraction value |
| $wt\%$ | Weight percent |
| $P_0$ | Original applied laser power |
| $P_{xy}$ | Laser power from overlapping voxels in x,y plane |
| $P_z$ | Laser power from overlapping voxels in x,y plane |
| $P$ | Effective laser power |
| $h$ | Hatching distance |
| $s$ | Slicing distance |
| $A$ | Voxel radius in x,y plane |
| $C$ | Voxel radius in z plane |
| $\chi$ | Flory Hugins para;eter |
| $\delta_d$ | Hansen solubility parameter for dispersion |
| $\delta_p$ | Hansen solubility parameter for polarity |
| $\delta_h$ | Hansen solubility parameter for hydrogen bonding |
| $\delta_{TOT}$ | Total Hansen solubility parameter |
| $V_r$ | Reference volume |
| $R$ | Universal gas constant |
| $T$ | Absolute tenperature |
| $\delta_1$ | Hansen solubility parameter of solvent |
| $\delta_2$ | Hansen solubility parameter of solute |

| | |
|---|---|
| $logP$ | Logarithmic partition coefficient |
| $CDR_n$ | Cumulative drug release at time point $n$ |
| $CDR_{n-1}$ | Cumulative drug release at time points previous to $n$ |
| $CDR_{\%}$ | Percent of cumulative drug release |
| $R_{PTMCA}$ | Normalised intensity of PTMCA ion |
| $R_{PEGDA}$ | Normalised intensity of PEGDA ion |
| $u$ | unified atomic mass unit |

# 1 Introduction

The scope of this chapter is to outline the aims and objectives of this thesis as well as its structure.

## 1.1 Aim and objectives of the Thesis

The main aim of this thesis was to expand the library of materials available for two-photon polymerisation (2PP) and expand the research with the multi-material formulations for this manufacturing technique. The second aim of this thesis was to use one of the formulations developed in this work to manufacture a proof-of-concept implant for an ocular bio-application. The overall aims were achieved by targeting the following objectives:

- To synthesize a biocompatible monofunctional polymer via ring-opening polymerisation and optimize it for 2PP multi-material printing.
- To optimise in–house synthesised hyperbranched polymers for 2PP manufacturing in mono- and multi-material printing.
- To characterise the structures manufactured with the developed formulations to understand their effect over several parameters, like the degree of conversion (reacted vinyl groups in case of multi-material formulations), the polymerisation threshold, the microstructure, or their biocompatibility.
- To select one of the multi-material formulations for further optimisation to manufacture intravitreal ocular implants *via* the most suitable vat-photopolymerisation technique available for this research.
- To test the *in vitro* biocompatibility and the *in vitro* drug release capabilities of the developed implants.

## 1.2 Structure of the thesis

This thesis is divided into eight chapters and a description of each chapter is listed below:

**Chapter 1**: A description of the aims and objectives of this thesis. Also, a breakdown of the chapters of the thesis with a brief description of each one of them.

**Chapter 2**: A literature review of several topics related to the research presented in this thesis. First, an introduction of additive manufacturing followed by a more in-depth exploration of two vat photopolymerization techniques: two-photon polymerisation and projection micro – stereolithography (PμSLA). The research presented in chapters 4, 5, and part of chapter 6 is focused on and carried out using 2PP, while a certain part of the research carried out in chapter 6 is performed using PμSLA. Therefore, a more in-depth review of the 2PP process is provided than that of PμSLA. This is then followed by a description of the reaction steps of free radical polymerisation. After, a review is provided on the photosensitive resins used for 2PP alongside their characteristics with a special focus on (meth)acrylate resins. This is followed by a section on hyperbranched polymers and then continued with a section on implants for corticosteroid ocular drug delivery. The chapter concludes with a summary of the key findings followed by a summary of gaps found in the literature that this thesis will tackle.

**Chapter 3**: A comprehensive description of the materials and methods used in this thesis is provided in this chapter.

**Chapter 4**: This chapter presents the work related to the synthesis of a mono-functional polymer and its printing optimisation in multi-material formulations. It details the characterisation of the new polymer and the formulations used throughout the chapter. It then follows with the characterisation of the manufactured structures via different analytical techniques that provide information on their reacted vinyl groups (degree of conversion), their microstructure, or the processing window of the formulations. This

chapter as well as chapter 5 and chapter 6, are divided into the following sections: Introduction, Results, and Discussion, followed by Conclusions.

**Chapter 5**: The work presented in this chapter focuses on the development of new mono- and multi-material formulations with hyperbranched polymers and their optimisation for 2PP manufacturing. As in Chapter 4, the hyperbranched materials are characterised and the manufactured structures with the different formulations analysed. The influence of the new materials is compared to commercial monomers regarding their reacted vinyl groups, the polymerisation threshold, and biocompatibility. The results of microstructure analysis of a manufactured sample with a multi-material hyperbranched formulation are also presented and discussed in this chapter.

**Chapter 6**: This chapter focuses on the manufacturing of an intravitreal ocular implant for sustained drug delivery of a corticosteroid (fluocinolone acetonide). This goal was achieved in several steps detailed in this chapter. First, one of the formulations of chapter 4 was selected for implant manufacturing. Second, the selected design implants were tested in 2PP and PμSLA with the selected formulation, and PμSLA was chosen as the printing technique to up-scale the manufacturing process. The formulation was further optimised to obtain the desired drug release rate as well as printing resolution. The biocompatibility of the final implants manufactured via PμSLA was assessed *in vitro* as well as their drug release of fluocinolone acetonide and their microstructure.

**Chapter 7**: This chapter highlights the conclusions of the research presented in this thesis. It also explores the research alleys that could not be explored in this thesis and outlines recommendations for future work.

**Chapter 8**: This chapter reports the bibliography used for this thesis.

# 2 Literature Review

## 2.1 Introduction to Additive Manufacturing

Additive Manufacturing (AM), also known as 3D printing, is a manufacturing process in which an object is created in an additive fashion, layer by layer. The object is created as a 3D model using computer-aided design (CAD) and sliced into individual layers. This sliced model is usually exported into a stereolithography file (STL) and loaded into the AM machine.[1]

The ISO/ASTM52900-15 standard of AM process categorisation, classifies the different AM techniques into seven main processes:

- Binder jetting: in which structures are manufactured on a powder bed using a liquid bonding agent to bind them. It can be used for several materials like sand, glass, metal, etc.
- Direct energy deposition: where metal in powder or wire feedstock form is put in front of an energy source (like a laser beam) held by a multi-axis robot arm and is then melted on a substrate layer by layer. This technique is usually used with metals like titanium.
- Material extrusion: here material is melted by a heating mechanism and extruded onto the substrate through a hot end. Typically, the material is a thermoplastic filament.
- Material jetting: in which a piezoelectric printhead sprays a liquid photosensitive resin onto the substrate that is then hardened by UV light exposure.
- Powder bed fusion: this technique uses an energy source (laser or electron beam) to melt together particles of powder beads to manufacture samples. The powders are usually metals, like titanium.

- Sheet lamination: that manufactures structures by fusing sheets of materials, forming layers. The final object is extracted from the block of bound sheets by using other processes like laser cutting.
- Vat photopolymerisation: in which a vat of resin (made of photopolymer) is exposed to an energy source, like UV light, and it solidifies into the desired structure layer by layer. The unreacted resin is washed by solvents in post-processing steps [1].

### 2.1.1 Introduction to stereolithography techniques

One of the first AM techniques to be developed was stereolithography (SLA), a type of vat photopolymerisation. It was born in the mid-1980s thanks to Charles (Chuck) Hull, who was experimenting with UV curable materials by exposing them to a scanning laser and realizing that he could solidify the materials into a 3D structure layer by layer. Shortly after he created the company 3D Systems to market SLA machines [2].

Micro – SLA is a technique based on SLA that underwent different modifications and improvements throughout the years to achieve a better resolution that would allow for micro size fabrication. The first micro-SLA developments were published in 1993 and all the different modifications that have taken place since then fall into the following three categories:

- Scanning micro–SLA in which an object is created layer by layer by focusing a light beam into the surface of a photosensitive resin and scanning vector by vector.
- Projection micro–SLA (also known as digital light projection) in which images of the layers are projected onto the surface of the photopolymer resin at high resolution. This technique does not use a vector-by-vector approach but projects the whole layer in one step, making it faster than scanning micro-SLA.

- Sub micrometer micro-SLA in which the material is built inside the photoreactive resin voxel by voxel (the voxel being a small 3D volume analogue of the pixel in 2D printing) instead of polymerizing layer by layer on the surface [3].
- Volumetric AM, a recently developed technique that manufactures an entire 3D object by irradiating the full volume of photosensitive resin from multiple angles. Compared to the previously mentioned vat – photopolymerization systems, volumetric AM offers faster printing times and a layer-less approach [4].

Two-photon polymerisation (2PP), also known as direct laser writing (DLW), is a type of sub micrometer micro-SLA technique [3].

## 2.2 Vat-photopolymerisation techniques

### 2.2.1 Two-photon polymerisation

The two-photon fabrication field can be first traced back to Maru *et al*. [4] published in 1997, where they manufactured a spiral structure with a 7 μm diameter. In 2001 another milestone was achieved when Kawata *et al.* [5] fabricated a 120 nm microbull beyond the diffraction limit (which would be 390 nm using $\lambda$ = 780 nm and numerical aperture (NA) = 1 in Abbe's diffraction limit formula $d = \lambda/(2NA)$ ). Since then, the field has grown exponentially, reaching almost 5000 published papers by 2015 and 1500 citations annually [6, 7].

Two photon-fabrication is based on two-photon absorption (TPA). TPA was predicted for the first time in 1931 by Maria Göppert-Mayer in her doctoral thesis. However, the experimental verification would only be performed 30 years later by Werner Kaiser, after the invention of the laser as incoherent light source does not allow to drive nonlinear optical processes efficiently [7, 8].

Two-photon absorption (TPA) refers to the simultaneous absorption of two photons to excite a molecule from a low energy state (ground state) to a higher energy state (excited state). The energy difference between these two states can be equivalent to the energy sum of two photons of Near Infrared (NIR) light or equivalent to one photon of Ultraviolet (UV) light [9]. After reaching the excited state, the photoinitiator (PI) molecule relaxes and reaches a triplet state *via* an intersystem crossing. In that triplet state, the PI molecule can α-cleave and generate radicals (**Figure 2.1**), which are highly reactive species that will interact with olefinic bonds and other radical species following the free radical polymerisation mechanism. These interactions will lead to polymer chain growth until two radicals encounter each other and terminate the reaction [10].

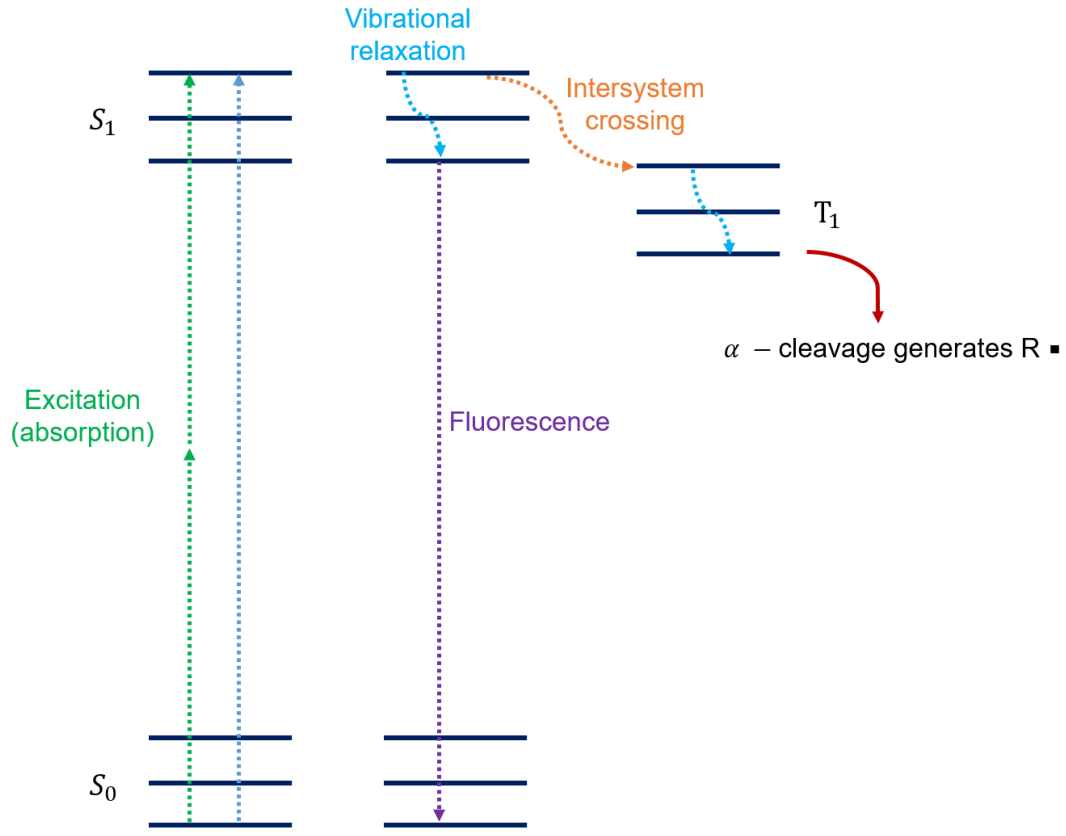



**Figure 2.1. Jablonski Diagram showing excitation of photoinitiator molecule by absorbing either one photon (UV light, blue colour) or two photons (NIR light, green colour). Then it can relax to the lower $S_1$ state via vibrational relaxation and reach back the ground state via fluorescence or it can undergo intersystem crossing (orange) to the triplet state. There it will form radicals via α – cleavage. These radicals will initiate the polymerisation reaction.**

In photolithography, the polymerisation takes place in the resin volume irradiated by the energy source[11]. In one-photon absorption, the excitation follows the Beer-Lambert law, and the absorption is linearly dependent on the light intensity and starts from the surface of the resist even if that is not the focal plane of the laser [12]. In two-photon absorption, two photons produce an equivalent excitation as that of a single photon absorbed possessing twice the energy. For both photons to be absorbed, they have to interact with the molecule almost simultaneously, in a matter of femtoseconds ($\sim 10^{-16}$ s), resulting in a quadratic dependence between light intensity and absorption instead of the linear dependence of the one-photon absorption mechanism. Therefore TPA processes are called nonlinear and their nonlinearity is the basis of the localised polymerisation happening at the focal point of the laser: doubling the intensity produces four times the fluorescence [13].

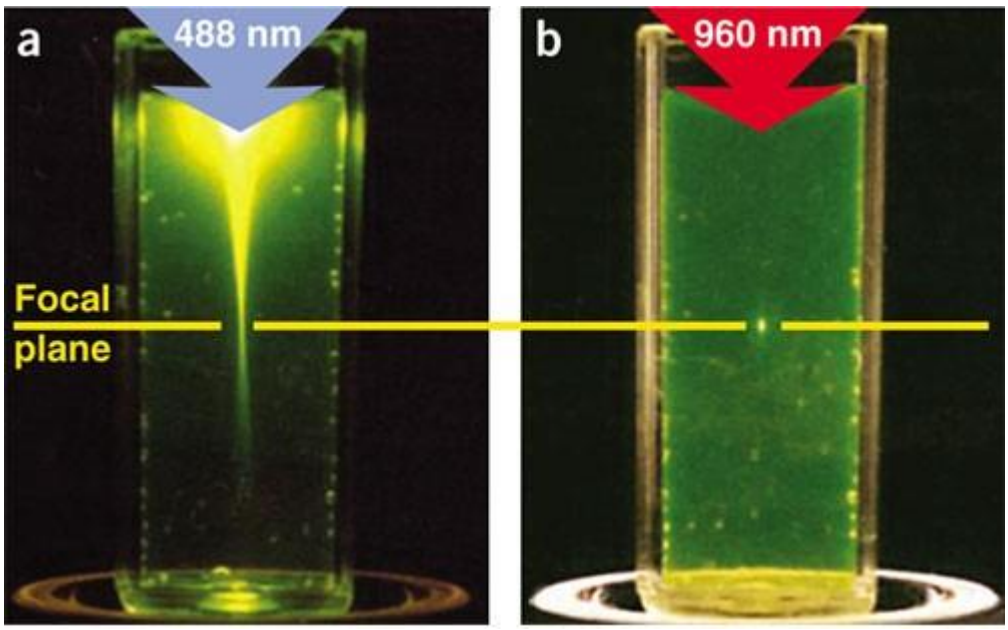



**Figure 2.2. a) One–photon excitation of fluorescein using focused 488 nm light (0.16 NA). b) Two-photon excitation using femtosecond pulse 960 nm focused light (0.16 NA) [13].**

In two-photon polymerisation, the profile of the exposure dose is not the same as the shape of the focal volume because the absorption of the photons depends on the square of the light intensity. The exposure dose refers to the concentration profile of active species generated in the resin after light absorption. When a NIR laser source is tightly focused into a resin containing the materials and photoinitiator, with an objective of high numerical aperture (NA), only in the centre of the focal volume will there be enough photogenerated active species to drive the chemical reactions that turn the liquid resin into solid. This is denominated as a threshold response and it does not happen in the periphery of the focal volume. In the periphery, the active species are below the threshold concentration needed for polymerisation and they are eliminated during the developing step (washing manufactured samples with solvent to remove unreacted resin) [11].

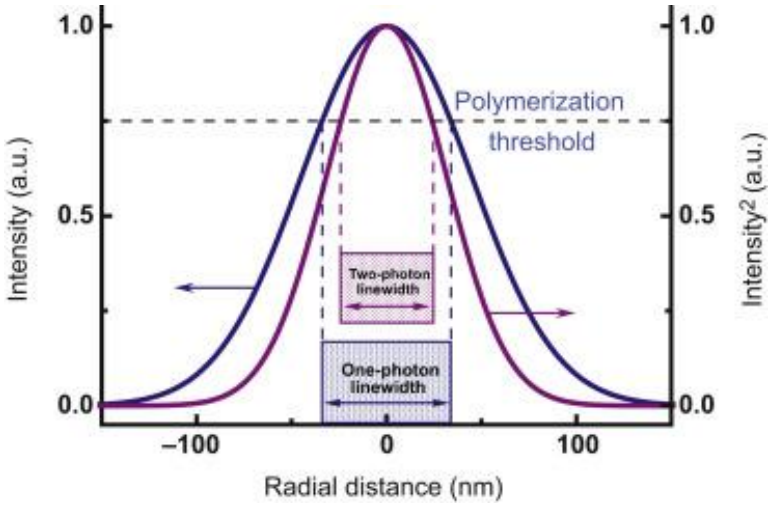



**Figure 2.3. Exposure doses are shown as light intensity profiles generated by a laser beam in one photon (dark blue) and two-photon polymerisation (purple) thresholds using the same experimental conditions [11].**

The threshold for polymerisation is fixed for every resin and photoinitiator. Therefore, if the laser source is optimised to have its maximum intensity slightly above the polymerisation threshold, we will be able to obtain the smallest features possible. That is

how two-photon polymerisation allows fabricating structures below the diffraction limit [11].

#### 2.2.1.1 Common 2PP set up

The most common basic components of a two-photon system are the following: a femtosecond NIR laser as the energy source with a typical 80 MHz frequency, a high NA objective to tightly focus the laser in the resin, and a beam expander to reduce its divergence angle. A shutter controls the exposure time and a digital camera with charged-coupled device (CCD)/complementeray metal-oxide semiconductor (CMOS) sensors that allow online process monitoring. The scanning of the laser in the sample can be done via a piezoelectric moving stage. However, the high-resolution piezoelectric stage comes at a price of slow writing speed. To improve this, galvanometric mirrors can be used to scan at a faster speed in the x-y directions while using the piezo stage for scanning in the z direction [6].

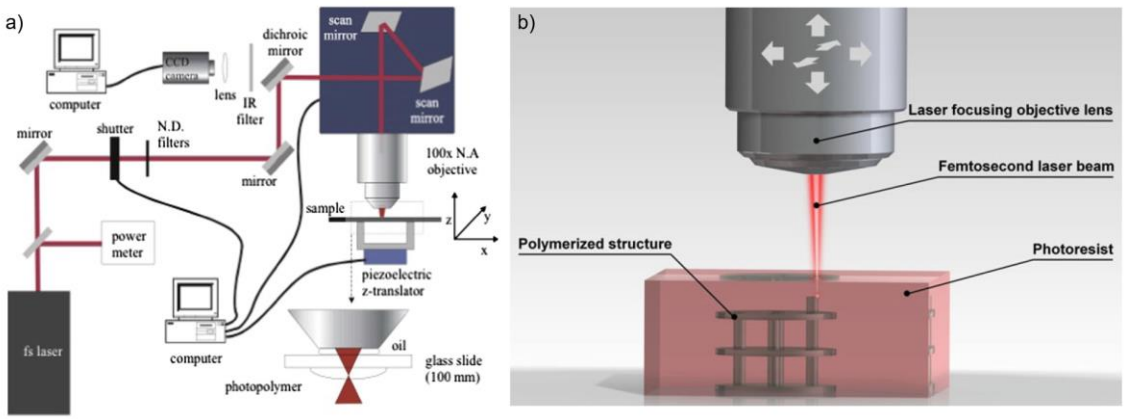



**Figure 2.4. a) Common 2PP setup showing the main and necessary components: ultrafast laser, beam/sample motion system, beam focusing optics, beam control, and software system. (N.D. filter = Neutral density filter, acts as laser beam attenuator) [9]. b) Principle of manufacturing structures via two-photon polymerisation process [14].**

### 2.2.2 Projection micro stereolithography

Projection micro stereolithography (PμSLA) is a vat – photopolymerization 3D printing technique based on one-photon absorption of UV light instead of two-photon absorption of NIR light [15]. In this printing technique, UV light is projected through a digital mask onto the surface of a liquid photosensitive resin, which polymerizes a complete layer with a single exposure [16]. Manufacturing layer by layer allows for faster printing times than manufacturing voxel by voxel. However, the resolution achieved with PμSLA is lower than the resolution achieved with 2PP systems [15]. The first developed PμSLA system by Sun *et al*. allowed to manufacture structures with a feature size of 0.6 μm [17]. As in 2PP, the polymerisation in PμSLA also takes place via free radical polymerisation (see section 2.3 for more details).

The printing process *via* PμSLA starts with a CAD model that is sliced into a sequence of cross-sectional images of the 3D model. These images are then transferred to a digital mask to optically pattern UV light, which is projected onto the surface of a photo-sensitive resin through a reduction lens to start the polymerisation reaction [16]. Once a layer is printed, the stage platform where the sample is manufactured drops, and the next layer is polymerised on top of the preceding one in the same manner [16]. This process is repeated until the whole 3D object is manufactured. The digital dynamic mask is usually a Digital Micromirror Device (DMD), that consists of millions of micromirrors. Each mirror stands for 1 pixel of the projected image and can be controlled individually. The size and number of mirrors will determine the resolution of the images [15]. The schematics of a commercial PμSLA (Boston Micro Fabrication (BMF) Materials Technology, Ltd.) setup can be seen in **Figure 2.5** [18]:

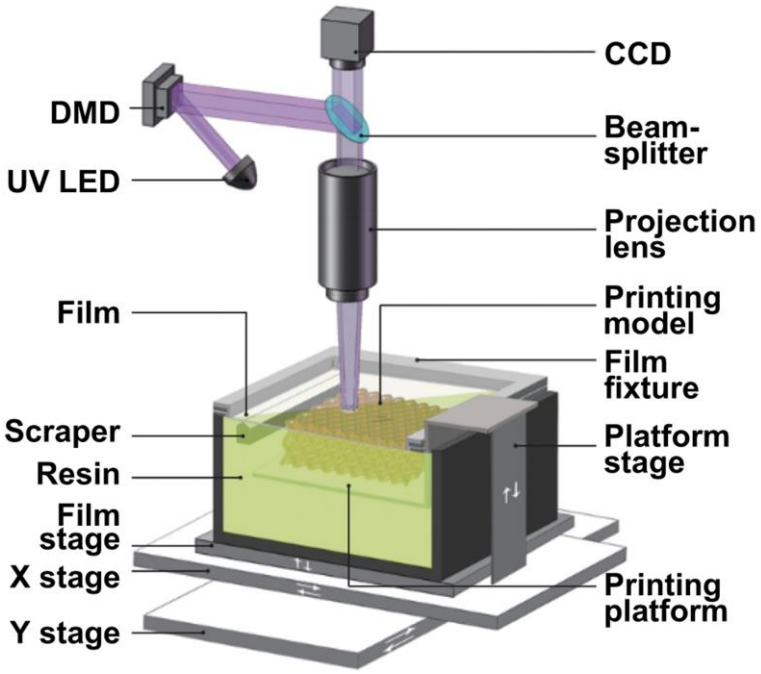



**Figure 2.5 Commercial PμSLA system schematic with its parts indicated. [18].**

Besides the elements previously described above, **Figure 2.5** shows the presence of a pre-stretched transparent and anti-sticky perfluoroalkoxy (PFA) membrane. This membrane helps to accurately control layer thickness. Before manufacturing, the stage coordinated with a CCD camera automatically moves the membrane to a position in which the focal plane of the projection lens coincides with the wet surface of the membrane [18].

### 2.2.3 Volumetric Additive Manufacturing

Volumetric AM, also known as multi-beam AM or Computed Axial Lithography, is a novel AM technique recently developed at the University of Berkeley and Lawrence Livermore National Laboratory [20]. In volumetric AM the object is not manufactured in a layer by layer fashion, but rather created in one step by irradiating a resin bath from multiple angles [4]. The local accumulation of sufficient light dose in specific areas, as defined by the 3D geometry, leads to photopolymerization and, hence, the simultaneous solidification of specific object voxels [21]. The photopolymerization threshold is only

surpassed in the voxels with cumulative light while the other areas remain under the polymerization threshold [4].

Currently, there are two approaches to this technique: a) tomographic reconstruction, in which a series of 2D light patterns are projected synchronously into a photosensitive resin bath [20], and b) employing a system that divides a single light beam into three orthogonal beams using mirrors [22], which will project a holographic figure into the photosensitive resin bath to manufactured the desired sample [4]. An example of a volumetric AM system can be seen in the following figure:

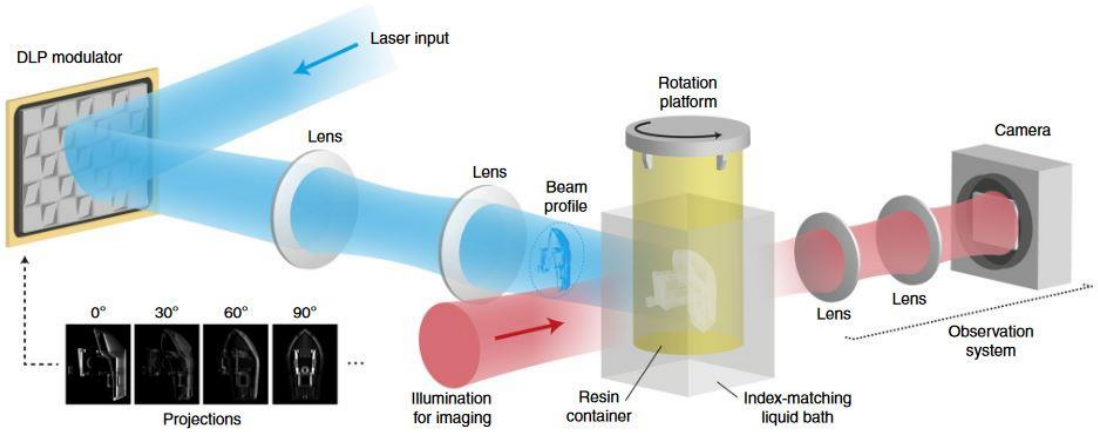



**Figure 2.6. Example of tomographic volume AM set up [21]**

By allowing to fabricate objects in a single step, volumetric AM greatly reduces printing times. This technique can manufacture full objects between 30s and 120s and it currently offers a resolution between 80µm and 300µm [21, 23]. It also allows processing more viscous resins compared to SLA or DLP systems [21].

Although this AM system is not used in the research work presented in this thesis, it is described in this section due to its importance in the field and the possibility of adapting current vat-photopolymerization resins for this system in the future, like the ones developed in this work

## 2.3 Free Radical Polymerisation

The reactions that take place during two-photon polymerisation of resins are those of the free radical polymerisation: initiation, propagation, chain transfer, and termination (see **Figure 2.7**).

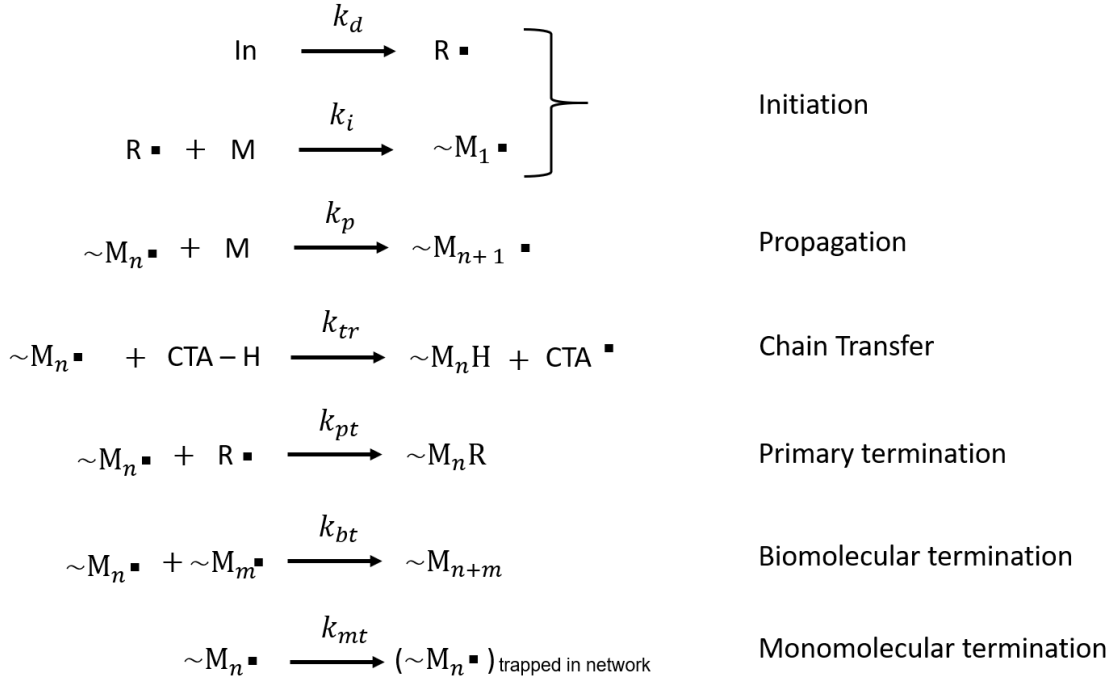



**Figure 2.7. Steps of free radical polymerisation.**

During initiation, the PI molecule absorbs photons and yields primary radicals following a $K_d$ constant rate [19]. The expression giving the rate of initiation is as follows:

$$R_i = 2\, K_d\, f\, [I] \qquad \textbf{Equation 2.1}$$

Where *f* is the efficiency factor and measures the fraction of initiator radicals that can react with the material. The "2" corresponds to the formation of two radicals for each initiator molecule that decomposes and *[I]* is the initiator concentration [20]. These radicals add to monomer molecules subsequently with a rate coefficient $K_i$. The

propagation step takes place by addition of the monomer molecules to the radical centre with a rate coefficient $k_p$. The propagation reaction rate is expressed by:

$$R_p = k_p\,[M]\,[R] \qquad \textbf{Equation 2.2}$$

Where *[M]* represents the monomer concentration and *[R]* the concentration of primary radicals [19, 20].

This step can be accompanied by a side reaction, *chain transfer*, in which the radical centre interacts with a small molecule (chain transfer agent (CTA), initiator, monomer) or a polymer molecule. The CTA abstracts a hydrogen atom from the growing chain, resulting in a dead polymer chain and a CTA free radical. The CTA fragment can then go on to initiate other monomers, resulting in new growing chains (as illustrated in **Figure 2.8**). This can lead to a molecular weight decrease or branching if the polymer molecule is involved in the chain transfer [19].

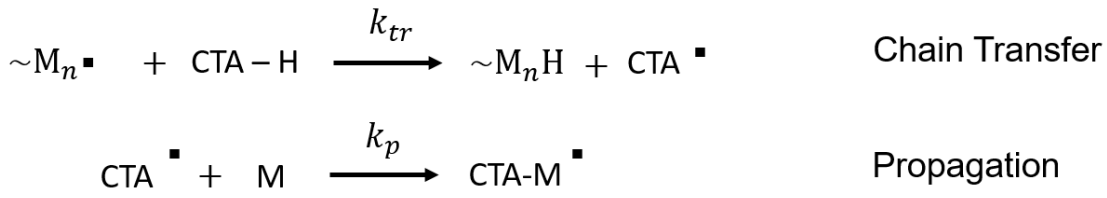



**Figure 2.8. Mechanism of the chain transfer reaction that can take place during free radical polymerisation.**

The termination step happens when radical centres react with each other and thus annihilate their activity. The other reactive centre could be a primary radical or another growing polymer chain. The latter is the dominant termination step in the absence of transfer agents or inhibitors. This termination step, known as biomolecular termination, is irreversible and its reaction rate $R_{bt}$ is shown in the following second-order equation [19, 20]:

$$R_{bt} = 2\,K_{bt}\,[R]^2 \qquad \textbf{Equation 2.3}$$

But terminations can also take place if the radical centre is trapped in the polymer network. This step, known as monomolecular termination, is reversible as these radicals could be reactivated if the network mobility increases (i.e., rise in temperature). This process involves only one polymer radical, and its reaction rate $R_{mt}$ is expressed by the **Equation 2.4** [19, 20]:

$$R_{mt} = K_{mt}\,[R] \qquad \textbf{Equation 2.4}$$

## 2.4 Resins for two-photon polymerisation

Two-photon resins consist of a monomer/oligomer mixture with a photoinitiator molecule. The material has to be transparent to the two-photon absorption wavelength [9]. This will allow the laser to penetrate the resin without being absorbed at the surface and trigger the photopolymerisation reaction in a small volume around the focus. This small volume is called voxel and is the 3D analogue of a pixel [21]. The photoinitiators used in these resins can be divided into two groups: Norrish Type I (free radicals are generated through α-cleavage of the photoinitiator molecule from the triplet state) and Norrish Type II (they need to react with a co-initiator to create radicals through hydrogen abstraction) [9, 22]. A schematic of their mechanism is shown in **Figure 2.9**.

Different materials have been used throughout the years for direct laser writing, for example: epoxy based resins like SU – 8, hybrid inorganic-organic polymers like Ormocer, (meth)acrylate photoresists, or hydrogels [9].

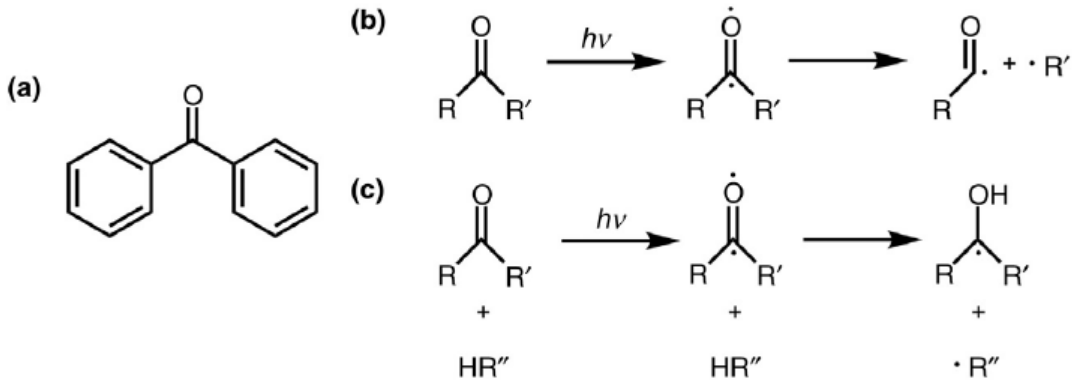



**Figure 2.9. (a) Prototype of benzophenone radical. (b) Schematic showing the mechanism of Norrish Type I photinitators. (c) Schematic showing the mechanism of Type II photoinitiators [7].**

### 2.4.1 SU – 8 and ORMOCER

SU – 8 is an epoxy Bisphenol A-based resin that was first used in the microelectronic industry and was one of the most used materials in 2PP until recently [9]. It has been used for many different applications ranging from optical devices like photonic crystals, micro-lenses arrays, micro-robots with magnetic control, to microfluidics [23]. ORMOCER (Organically Modified Ceramics) is a hybrid inorganic-organic polymer resin with properties similar to glass, ceramic, silicone, and organic polymers [24]. It has been mainly applied in the photonics field, although there are also some examples of its use in bioapplications like scaffolds for cellular growth [9] or microneedles for drug delivery [25]. Although these materials are not the focus of this thesis, they have been briefly mentioned in it due to their importance in the field [9]. The first materials used for 2PP and currently the most used resins for 2PP, which are the focus of this thesis, are (meth)acrylate photopolymers [9, 19].

### 2.4.2 (Meth)acrylate Biocompatible Resins

Biomaterials are materials that interact with biological systems to evaluate, treat/heal, or replace tissue or a body function [26]. (Meth)acrylate photoreactive biomaterials can be

produced synthetically or by modifying natural materials with (meth)acrylate groups [27]. Photoreactive biomaterials are of high interest in fields like tissue engineering, implants, or drug delivery [28]. They allow for short reaction times, spatial control, and gentle reaction conditions [27].

#### 2.4.2.1 Natural materials and proteins

Photoreactive biomaterials can be divided into two broad categories: a) natural materials and proteins, and b) synthetic materials (polymers and hydrogels). Natural materials and proteins will be briefly discussed in this paragraph; however, they will not be extensively reviewed as they are not the focus of this thesis. The 2PP printing of proteins has been extensively investigated by Campagnola and his co-workers , who processed several different proteins like Bovine Serum Albumine (BSA), fibrogen, or collagen [9]. Wei *et al*. have also used BSA and Rose Bengal as photoinitiator to manufacture pH-responsive microstructures [29]. Another natural material that can be functionalised for 2PP is hyaluronic acid, a major component of connective tissue [21, 30]. Seidilitis *et al*. immobilized BSA inside hyaluronic acid scaffolds and used those for neural cell guidance [31]. Gelatin, a biomaterial extracted from collagen, has also been used for two-photon printing [32, 33]. Van Hoorick *et al*. have worked on modifying gelation to create novel gelatin derivatives that are biocompatible and have increased processing capabilities [34, 35]. Their work has focused on methacrylol and thiol norborene gelatin (gel-MOD and gel-NB, respectively) hydrogels. In the work presented in Van Hoorick *et al*. [41], they demonstrated the benefits of gel-NB, synthesised via thiol-ene click chemistry, over gel-MOD in 2PP manufacturing. The gelatin-NB hydrogel allowed faster printing due to higher reactivity of the thiol-ene functionalities, better CAD-CAM mimicry and a comparable biocompatibility to gel-MOD.

The natural materials and proteins previously mentioned do not always allow for the best mechanical properties and topography of the microstructures manufactured with them. Because of this, synthetic materials have been also investigated and applied in 2PPto allow for customable mechanical properties, versatility and degradation profiles [36].

#### 2.4.2.2 Synthetic polymers and hydrogels

Synthetic polymers like Poly ($\varepsilon$ – caprolactone) (PCL), Poly (lactic acid) (PLA), Poly (trimethylene carbonate) (PTMC) or synthetic hydrogels like Poly (ethylene glycol) (PEG) are heavily used for different bioapplications due to their good biocompatibility and tuneable degradation profiles [37]. These types of biomaterials have been adapted for photopolymerisation and 2PP by modification with (meth)acrylates groups. They have been used on their own as a resin or in different copolymer combinations between themselves [27].

PCL is a hydrophobic, semi-crystalline polymer with a low glass transition temperature ($T_g$ approximately -60 ℃) and a melting point range of 59 to 64 ℃. It degrades through non-enzymatic hydrolysis of its ester bonds [38].

PLA is an aliphatic chiral polyester that has the following stereoisomers: poly (l – lactic acid) (PLLA), poly (d – lactic acid) (PDLA), and poly (DL – lactic acid) (PDLLA) [39]. The melting point of PLA is 160℃ and it has a $T_g$ of 60 ℃. Like PCL, it also degrades via hydrolysis of its ester groups [37, 39].

PEG is one of the main synthetic hydrogels used for bioapplications. This is related to its biocompatibility, water solubility, and non-toxicity, making it a suitable candidate for drug delivery or tissue engineering. The hydroxyl end groups of PEG oligomers or polymers can be modified and reacted with (meth)acrylates to transform the material into a photoreactive resin. (Meth)acrylate PEG hydrogels have a low $T_g$ (-55 ℃) and high

water uptake (900 – 1700 % wt). Cross-linked networks from (meth)acrylate PEG do not degrade *in vivo*, but below a molecular weight of approximately 30 kg.mol$^{-1}$ they can be eliminated from the body via the renal pathway [28].

PTMC is a hydrophobic non-crystalline polymer with a low $T_g$ (-20 ℃). Its degradation behavior is marked by resistance to non-enzymatic hydrolysis and its affinity for enzymatic degradation via surface erosion mechanism. This allows for a slow degradation that prolongs its lifetime compared to polyesters and the mechanical properties of the polymer are maintained with surface erosion. PTMC degrades by hydrolysis in the presence of enzymes into 1,3 – propanediol and carbon dioxide. As opposed to PLA, its degradation byproducts are non-acidic, which reduces the risk of adverse reactions in *in vivo* applications. Because of all this, PTMC has been extensively studied for different bioapplications [40].

#### 2.4.2.3 Synthetic biomaterials use in the 2PP field

The synthetic materials previously described can be used as two-photon resins by themselves or in different combinations as copolymers. For example, Claeyssen *et al*. developed a triblock dimethacrylate copolymer made of $\varepsilon$ – caprolactone, PEG chains and trimethylene carbonate. Their resin and the structures manufactured with them were shown to be biocompatible, being used for cell proliferation, and biodegradable, degrading in 1 month. However, it showed resolution and shrinkage issues [41].

Another combination can be observed in the work of Weiß *et al*., which synthesised and 2PP processed trimethacrylate oligolactones based on L – lactide and $\varepsilon$ – caprolactone. The mixture allowed for well-defined structures to be printed with good resolution. These structures showed to be biocompatible after being tested with 3T3 bovine chondrocytes. Similar results were obtained from processing urethane dimethacrylate and PEGDA [27, 42].

Felfel *et al*. also used a lactic acid and $\varepsilon$ – caprolactone monomer units to prepare methacrylated poly(D,L-lactide-co-$\varepsilon$-caprolactone) copolymers with different compositions and chain lengths. Scaffold structures of $2 \times 4 \times 2$ mm were 2PP manufactured and their degradation was studied *in vitro* at different temperatures (37 ℃, 50 ℃, and 65 ℃). Scaffold degradation was influenced by the chemical composition of the structures, with those with higher content of caprolactone degrading at a slower rate. By superposing results from the different temperatures, a time-accelerated method was generated that allowed prediction of degradation times at body temperature [43]. PCL has also been used alone as reported by Thompson *et al*.. Their triacrylate and diacrylate PCL polymers were used to manufacture 3D models for retinal cell replacement. Triacrylate materials were shown to have the best fidelity between the produced scaffold and the 3D model. These scaffolds successfully supported human induced pluripotent stem cell (iPSC) retinal cells *in vitro* and did not cause inflammation or toxicity in *in vivo* model after one month [44].

Polymers like PLA have also been 2PP processed without being part of a copolymer. Scaffolds manufactured with 4-arm methacrylate PLA were produced by Koroleva *et. al.* Their biocompatibility was tested with Schwann neural cells to assess their possible use for nerve repair applications. The scaffolds enabled proliferation for 7 days and showed to be a suitable substrate for Schwann cell adhesion [45]. Methacrylated 4 – arm PLA stars were also developed by Timashev *et al*. In this case, scaffolds were studied for bone regeneration applications. Preseeding with murine mesenchymal stem cells (MSC) showed a beneficial microenvironment for osteogenesis and bone regeneration both *in vitro* and *in vivo* [46].

PEGDA has been another material used to prepare microstructures of different sizes and geometries using 2PP. Gou *et al*. studied the relationship between Young's modulus of PEGDA structures and achieving high fidelity structures. They explored the fabrication

of red blood cell structures at arbitrary angles, indicating potential applications in tissue engineering or drug delivery [47]. A drug delivery system example can be seen in Gittard *et al.*'s work, where they used PEGDA in combination with Gentamicin sulfate to prepare microneedle arrays resistant to bacterial infections [48]. Another drug delivery system study based on PEG was the one from Do *et al.*, which created dimethacrylate PEG structures loaded with Rhodamine B and studied the effect of different hatching and slicing distances on drug release. Bigger hatch/slice distances provided a higher release than smaller spacings and all devices showed good biocompatibility [49]. The PEGDA hydrogel has also been applied to scaffold manufacturing, as shown by Accardo *et al.* that used this material to produce free-standing structures that allowed neuronal interconnections to be formed [50].

Besides the previously copolymer mixtures mentioned before, PTMC has also been used as a polymer by itself, though fewer 2PP examples are available of this than in the case of PLA or PCL. Several examples of photo-cross-linkable PTMC can be seen in the SLA field, where they have been used in tissue engineering to produce scaffolds for meniscus implants [51], to fabricate biocompatible microvascular networks [52], or to manufacture orbital floor implants with PTMC mixed with nano-hydroxyapatite [28, 53, 54]. Although the most common ways of using PTMC for 2PP has been as part of a copolymer with other synthetic materials, one recent example of PTMC being used as a polymer instead of a copolymer is the three-arm methacrylated PTMC used by Weisgrab *et al.* Their group prepared large and porous scaffolds (18 × 18 × 0.9 mm) that allowed proliferation and differentiation of human adipose-derived MSC towards osteogenic and chondrogenic lineages [55].

The materials reviewed in this section are (meth)acrylate biomaterials with several functional groups per molecule, as this is preferred in the 2PP field because these molecules lead to higher reaction rates and higher cross-linking densities [56]. This aspect

and others that have to be taken into account for 2PP resins are explained in the following section.

## 2.5 Characteristics of (meth)acrylate 2PP photosensitive resins

The main functionalities used for 2PP are acrylate and methacrylate groups. Acrylates are more reactive than methacrylates. This is related to the stabilizing effect of the $\alpha$-methyl on the propagating radical of the methacrylate, which is responsible for a lower propagation rate of methacrylate radicals than those of acrylates [19].

Besides the type of end group, is also important to highlight the importance of their functionality which is the number of functional groups per molecule. A high functionality will allow for higher reaction rates and faster gelation due to denser networks forming. However, a higher cross-link density will reduce the amount of double conversion, translating into a higher quantity of uncured residual vinyl groups (up to 50% for monomers with rigid spacers)[19]. Another factor influencing the cross-linking density and the conversion is the length of the spacer group. In the case of di(meth)acrylate monomers, higher spacer length between the two insaturations leads to higher conversions. This is related to the decrease in cross-linking density, which allows for more mobility in the system [19, 57]. A similar effect has also been observed when increasing the flexibility of the spacer group [19, 58]. Flexible spacers between vinyl groups allow for their individual reactivities to remain independent from each other. In the case of rigid spacers, the motion of the divinyl groups could be coupled and the reaction of one unit could strongly influence the mobility and reactivity of the second one. This could lead to potential reactive groups being trapped in a non-reactive matrix incapable of reaction because of the network's topology [59].

Besides the factors mentioned above related to di(meth)acrylates, another important one to consider for two-photon materials is viscosity. High viscosities are important as they allow the early parts of the manufacturing to remain where they are created, thus higher precision, while low viscosities help with the removal of unsolidified resin during post-processing steps [19].

During the free radical polymerisation steps the distance between carbon atoms changes from the van der waals distance that double bonds exhibit to the shorter distance present between carbon atoms in covalent bonds. This leads to shrinkage because of volume contraction and this shrinkage is the main drawback of free radical polymerisation. Polymerisation shrinkage is related to the initial functionality concentration and the degree of conversion achieved. Monomers with higher molecular weight and lower degrees of functionality will show lower shrinkage levels [19]. The type of functional group also influences on shrinkage: methacrylates show lower levels of shrinkage than acrylates due to their lower conversion related to their lower reactivity and higher rigidity [19].

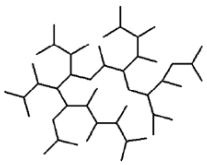
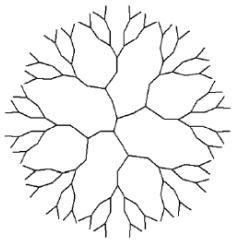
One way of reducing shrinkage is ethoxylation, as the introduction of ethoxy groups in multifunctional monomers will reduce significantly the double bond concentration while increasing molar mass [19]. Another approach to reduce shrinkage is by using thiol-ene chemistry [10]. Jiang *et al*. show in their work that by adding 10 % of thiol to a multifunctional acrylate resin, the shrinkage percent reduces by more than half [60].

## 2.6 Hyperbranched polymers

Dendritic polymers are a class of polymers that appeared in the 1980s formed by highly-branched three-dimensional macromolecules. Depending on their Degree of Branching (DB), they are classified into different subclasses; dendrimers have the perfect and ideal

branched structure with a DB of 1.0 while hyperbranched polymers are molecules that show random and irregular branching with a DB between 0.4 – 0.6 [61]. The DB is related to the type of structural units that form the dendritic polymer. Dendrimers are made of two structural units: uniform terminal units on their globular surface and dendritic units inside the polymer backbone. This allows to have well-defined molecular weights ($M_w$) and a unique symmetric structure. However, their synthesis is a complicated multi-step process and requires time-consuming purification at each step. Therefore, simpler ways of producing branched polymers were created. Hyperbranched polymers (HBP) are made of randomly distributed linear and dendritic units inside with terminal multifunctional units on their periphery. This is responsible for their more irregular structures with a higher polydispersity of molecular weight than dendrimers. However, compared to dendrimers, they are synthesised in a single-step operation and they still have many of the advantages that dendrimers show [62]. A comparison of the different properties of dendrimers, HBP, and linear polymers can be found in **Table 2.1**.

**Table 2.1. Comparison between structure and properties of hyperbranched polymers, dendrimers, and linear polymers [62].**

| | Linear | Hyperbranched | Dendrimer |
|---|---|---|---|
| Structure |  |  |  |
| Topology | 1D, linear | 3D, irregular | 3D, regular |
| Synthesis | One-step, facile | One-step, relatively facile | Multi-step, laborious |
| Purification | Precipitation | Precipitation or classification | Chromatography |
| Scaling-up | Already, easy | Already, easy | Difficult |
| MW [1] | Discrepant | Discrepant | Identical |
| PDI [2] | >1.1 | >1.1 | 1.0 (<1.05) |
| DB [3] | 0 | 0.4–0.6 | 1.0 |
| Entanglement | Strong | Weak | Very weak or none |
| Viscosity | High | Low | Very low |
| Solubility | Low | High | High |
| Functional group | At two ends | At linear and terminal units | On periphery (terminal units) |
| Reactivity | Low | High | High |
| Strength | High | Low | Very low |

[1] Molecular weight; [2] Polydispersity index; [3] Degree of branching.

One of the main attractive properties of HBP is their low viscosity and good solubility. The intrinsic viscosity of polymers is dependent on their molecular architecture. Generally, the intrinsic viscosity of linear polymers increases steadily with the increase of $M_w$ due to chain entanglement. Dendrimers do not follow this rule as they show no entanglement owing to their spherical shape. Although the architecture of HBP is more irregular than that of dendrimers, they still show little entanglement compared to linear polymers and this allows them to keep a low viscosity even when their $M_w$ increases. Their branched architecture also influences other polymer characteristics like solubility or $T_g$, with HBP having better solubility and lower $T_g$ than linear polymers [63, 64]. The lower entanglement of HBP also influences their mechanical properties, showing poor mechanical integrity, sometimes resulting in brittleness. However, they can be used as additives for other materials to enhance their processability [62].

The characteristics of HBP have been explored and used for different fields and applications like supramolecular chemistry, nanotechnology, hybrid materials and composites, coatings and adhesives, or bioapplications [65]. Regarding bioapplications, these have ranged from tissue engineering to drug delivery and antimicrobial properties [62]. Massoumi *et al*. prepared scaffolds from hyperbranched polyester-poly (D,L-lactide)-polyaniline via electrospinning that allowed cell proliferation, indicating their possible use in tissue engineering [66]. HBP have also been used to deliver drugs like cytotoxic molecules for cancer therapy or to deliver Ribonucleic acid (RNA)/ Deoxyribonucleid acid (DNA) as gene vectors [67]. Zhuang *et al*. prepared hyperbranched PEG – methacrylate (PEGMA) functionalised with thiol-bearing drugs that could release the drug by reductive degradation and presented acceptable cytotoxicity [68]. HBP have also been used to impart antimicrobial activity to mixtures and devices. Zhao *et al*. prepared hyperbranched polyamides that contained carbonyl biscaprolactam that had anti-microbial activity against gram-positive and gram-negative bacteria as well as fungi [69]. Another way of giving anti-microbial properties to HBP is how Prabu *et al*. did, by capping the polymer with salicylic acid [70]. Another use of HBP is to modify the properties of biodegradable polyesters [71]. PLA is a material with several advantages for bioapplications already mentioned in this chapter. However, its high crystallinity is a disadvantage as it can lead to brittleness and poor compatibility with soft tissue. Several experiments have shown that an increase in branching of polyesters (like PLA or PCL) was associated with a decrease in crystallinity. A lower crystallinity is expected to lead to an increase in biodegradability as well as higher biocompatibility with soft tissues [63, 72, 73]

In the past years HBP have started to be used in AM, more specifically, in Inkjet Printing. Chang *et al*. have synthesised polyurethane – methacrylates HBP and formulated them to manufacture colour patterns on glass via inkjet printing [74]. Wheeler *et al*. demonstrated

that poly (methyl methacrylate) HBP with different branching density were all allowing for a significantly greater maximum printable concentration and faster print speed than their linear counterparts [75]. Jafarifard *et al*. also studied HBP for inkjet printing by observing the effects of the surface chemistry of a polyester-amid base HBP on UV-curable inkjet inks. By studying the rheological behaviour of the ink during the curing process, they observed that the HBP did not significantly affect the rheological properties of the inks but that they did improve the curing process at the final curing steps [76]. These examples and others [77, 78], indicate that HBP can be good candidates for photosensitive resins and can help enhance the processability of the formulations.

## 2.7 Implants for corticosteroid ocular drug delivery

### 2.7.1 Human eye anatomy and pathology

The human eye is a globular structure of around 8 g of weight and a diameter of 24 mm that plays a central role in vision and is formed by several tissues with each showing different features [79]. It is well protected from toxic materials by structural and physiological barriers. At the same time, these barriers increase the difficulty to deliver active ingredients to it by topical or systemic routes [79, 80]. The eye anatomy can be divided into anterior and posterior segments. The anterior segment is comprised of tear, cornea, conjunctiva, anterior and posterior chamber, iris, ciliary body, lens, and aqueous humour. On the other hand, the posterior segment is formed by the sclera, choroid, retina, Bruch’s membrane, vitreous humor, optic nerve, and retinal blood vessels [81].

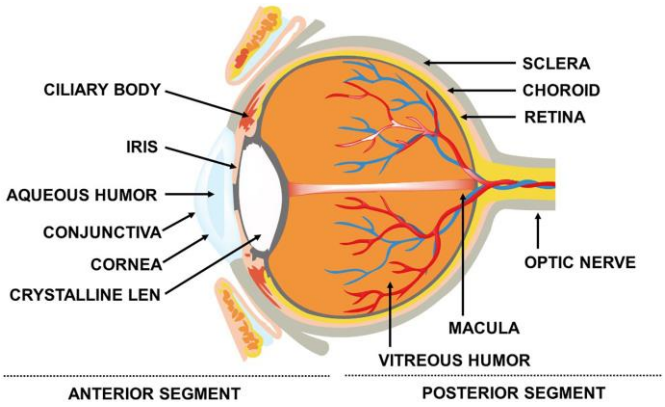



**Figure 2.10. Anatomy of the human eye [82].**

Many diseases affect the eye, but the major ones impacting the posterior segment of the eye are age-related macular degeneration (AMD), diabetic retinopathy(DR), and diabetic macular edema (DME) [79]. The following paragraphs describe the pathology of these illnesses:

- AMD is a neurodegenerative disease in which there is progressive degeneration of photoreceptors/retinal pigment epithelial (RPE) complex in the macular region of the retina with age, resulting in irreversible central vision loss. Non-exudative AMD is characterised by the presence of acellular debris called drunsen between the RPE and Bruch's membrane and atrophy of the area. Exudative AMD is characterised by choroid neovascularization (CNV), that can lead to capillaries breaking, leaking, and scarring, which damages the macula and induces vision loss [83, 84].
- DR is a major complication of diabetes miellitus (DM) that also manifests with vascular abnormalities in the retina. It can be classified into non-proliferative diabetic retinopathy (NPDR) and proliferative diabetic retinopathy (PDR). NPDR manifests with microaneurysms, hemorrhages, and hard exudates, although the patient may be asymptomatic at this stage. PDR manifests with neovascularization and the patient can experience severe vision loss when the abnormal blood vessels

bleed into the vitreous. The main leading cause of blindness of DR patients is diabetic macular edema (DME). DME can occur at any moment in DR and manifests with thickening of the macula due to sub- and intra-retinal accumulation of fluid in the macula caused by the breakdown of the blood-retina barrier [85].

If left untreated, these illnesses can lead to blindness. In the older population of developed countries, they are the leading cause of blindness [84, 85]. In AMD, DR, and DME high vascular endothelial growth factor (VEGF) levels, inflammation, and diminished antioxidants are found to be present. Therefore, corticosteroids and anti-VEGF are the main lines of treatment used against these diseases [81]. Corticosteroids exert anti-inflammatory properties as well as anti-neovascular effects with the inhibition of the formation of new blood vessels. Because of this, they can be used for treating both AMD and DR, for example [86]. Corticosteroids are also the therapy of choice in patients who are resistant to anti-VEGF therapy [85]. Currently, the main routes of administration for active ingredients for posterior segment diseases are intravitreal (ITV) injections or implants. However, intravitreal injections increase the burden on healthcare professionals as they have to be performed by specialists. They also only provide moderate relief and often result in side effects like cataract formation or retinal detachment, resulting in low adherence to the therapy of patients [80]. Delivering drugs with a long-acting and slow-release implant can reduce the burden on healthcare professionals as well as reduce the associated risks that come with repeated intraocular injections for patients [86].

### 2.7.2 Ocular implants available on the market for corticosteroid delivery

Several implants loaded with corticosteroids as the active ingredient are available on the market. The first corticosteroid-loaded implant, Retisert, was approved by the Food Drug Administration (FDA) in 2005 for the treatment of uveitis (ocular inflammatory disorder

affecting the uvea and its adjacent tissues). It is loaded with 0.59 mg fluocinolone acetonide (FA) and releases 0.6 $\mu$g/day of drug up to 30 months. Retisert is a 1.5 mm tablet encased in a silicone elastomer cup with a release orifice and a Poly(vinyl alcohol) (PVA) membrane situated between the tablet and the orifice [81, 87]. Retisert is attached to the pars plana and needs suturing during implantation to be kept hanging in the vitreous humor [81]. Iluvien is another non-degradable implant that contains 0.19 mg of fluocinolone acetonide and is inserted via intravitreal injection with a 25 gauge needle, a simpler procedure than the one for Retisert [80]. Iluvien was approved in 2014 by the FDA for the treatment of DME and uveitis. It has a cylindrical tube shape of 3.5 mm in length and 0.37 mm in diameter and it has the drug dispersed in a PVA matrix inside a polyimide tube. It releases between 0.23 – 0.45 $\mu$g/day of drug for 18 to 36 months after injection [80, 81, 87].

Ozurdex is the first biodegradable implant approved by the FDA in 2009 for treating DME [79]. It is a rode shape implant (6 mm in length) that contains 0.7 mg of dexamethasone dispersed in a Polylactide-co-glycolide (PLGA) matrix. It allows for a slow release of 0.1-1 $\mu$g/day of drug over a period of 6 months [80, 88]. The PLGA matrix degrades by hydrolysis and it has been shown that its degradation products can create an acidic environment that can cause inflammation of the ocular tissue [80]. Retisert and Iluvien are non-biodegradable devices that need to be removed from the eye after releasing the drug. This includes another surgical step that is not convenient for patients, as it increases the risk of side effects on the eye. Biodegradable implants like Ozurdex, which are easily injected via needle and do not need an extra procedure to be extracted due to their degradation, are advantageous to patients despite the inflammation that PLGA degradation byproducts can cause [81]. Because of this, in recent years there has been a change of focus in research toward biodegradable implants [89].

### 2.7.3 Synthetic polymers explored for ophthalmic drug delivery

Several biodegradable polymers have been explored for ocular therapy in the past years. PLA, PLGA, PCL, PEG, Poly (N-vinyl pyrrolidone) (PVP), and PTMC are synthetic polymers that have been used for ophthalmic drug delivery [90, 91]. PLGA is the most commonly used biodegradable polymer for ophthalmic drug delivery. Its good biocompatibility and versatility have made it popular for a plethora of bioapplications. Both PLA and PLGA have been used for ocular systems such as microspheres, nanoparticles, or implants like Ozurdex [91]. PCL is another polyester that has been applied in the ocular field. It is an attractive choice for sustained drug delivery due to its excellent permeability to drug molecules and its slow degradation times [91]. Yin *et al*. investigated a PCL triblock copolymer (PEG-PCL-PEG) for ophthalmic applications and showed good biocompatibility with ocular tissue as well as controlled drug release [92]. PCL was also prepared as a triblock copolymer with PEG and TMC and used in polymersome and polymeric micelles for the posterior segment of the eye. They showed to be a promising technology for drug delivery to the back of the eye [93]. PVP is also a synthetic biocompatible material that has been used in ophthalmic applications. Different researchers have used PVP cross-linked polymers as artificial vitreous substances, for lens scaffolds [94], or intraocular drug delivery systems like microneedles [91, 95]. As mentioned before, PTMC has been used as part of copolymers for ocular applications. Jansen *et al*. studied the *in vivo* ocular degradation of linear and cross-linked PTMC polymers compared to PLA linear and cross-linked networks. The rod shape specimens were inserted into rabbit eyes and their degradation behaviour was studied for 13 weeks. All materials were well tolerated in the vitreous, but PTMC specimens degraded very slowly with no significant mass loss visible during the 13 weeks [96]. Therefore, most works have focused on PTMC copolymers that allow better control and tuneable degradation than the material cross-linked by itself [28].

## 2.8 Key findings of the literature

- Most commonly used 2PP resins are (methacrylate)materials. These types of materials were initially developed for applications like photonics or microelectronics, which is why there is not a wide range of biomaterials available for this printing technique.
- The current range of biocompatible 2PP resins goes from natural materials (i.e chitosan, BSA, hyaluronic acid) to synthetic ones like PLA, PCL, PEGDA, or PTMC. They are often copolymerised and functionalised with multiple (meth)acrylate groups. They are applied in applications like tissue engineering or drug delivery.
- The main characteristics to consider when selecting or preparing a 2PP resin are type and number of functional groups, viscosity, and shrinkage.
- The multifunctionality of 2PP resins helps them be more reactive but this usually comes with the price of low degrees of conversion (<50%). More distance and flexibility between the cross-linking groups can allow for more mobility in the system that can translate into a higher degree of conversion.
- HBP show several of the advantages of dendrimers with a simpler synthesis and scale-up process. They have been applied in several bioapplications, in aiding the curing process of UV resins and coatings, and recently have also started to be used in Inkjet printing.
- AMD and DR are the leading causes of blindness in developed countries in the older population. Corticosteroids are one of the therapeutical lines used for treatment, either via intravitreal injections or intravitreal implants. IVT implants produce fewer side effects than injections, but the non-degradable implants have to be surgically extracted, being inconvenient for healthcare workload and patients. Ozurdex is the only biodegradable implant available that delivers

corticosteroids (dexamethasone). It releases drug over 6 months and it does not need extra surgical procedures to be extracted.

- Different biomaterials have been researched for ocular applications like PLA, PLGA, PCL, PEG, PVP, or PTMC. PLGA is the most widely applied polymer in ocular systems due to its excellent biocompatibility and tuneable degradability. However, its degradation products are acidic which can cause irritation at the degradation site. The other materials mentioned have been mainly used in different copolymer combinations in ocular therapy.

## 2.9 Summary of gaps in the literature

The development of bioapplications in the 2PP field has been slower than in other areas (i.e optics) due to the toxicity of the initial resins used in photolithography [22]. Although some commercial materials like OrmoComp or SU – 8 have shown biocompatibility, commercial resins do not meet all the properties needed for different bioapplications in the field. New materials have to be developed to meet different mechanical properties, degradability profiles, or biocompatibility [21]. Many of the multifunctional materials used in 2PP display low degrees of conversion. Their use presents risks as toxic uncross-linked material can leach from structures manufactured from such resins [19]. Developing new materials with high degrees of conversion is needed to avoid this risk and expand the 2PP material library with biocompatible polymers.

Hyperbranched polymers are highly branched materials with low viscosity due to their low entanglement, good solubility, and high number of functional groups. They have been for several applications like aiding UV curing of coatings and resins, in bioapplications, and inkjet printing [65]. This indicates that they are highly reactive materials that could be adequate to use in other AM techniques that use light to manufacture, like for example, two-photon polymerisation as they present characteristics desired in 2PP resins. Despite

these indications, HBP have not been explored in the 2PP field yet. Further studies to determine the suitability of these materials for the 2PP technique are needed as well as more research into the biocompatibility of such potential resins, to determine for what application they would be more suitable.

The main focus in 2PP printing until now has been on homogeneous resins. Besides developing new materials for the technique, another aspect that would highly benefit the field would be multi-material printing. Tailoring composition and structure simultaneously at the nanoscale and creating multi-material systems that allow integrating stiffer with softer material, for example, would open new possibilities for 2PP [97].

Regarding the sustained intraocular delivery of corticosteroids for DR or AMD, the main therapeutical route of administration has been performed via IVT injections. Due to their side effects, financial burden, and poor patient compliance, the research focus changed towards long-term release implants [85]. The biodegradable implant Ozurdex, made of PLGA matrix, shows benefits over IVT as they need fewer injections, they do not need extra surgical removal steps like non-degradable implants, and show better patient compliance. However, PLGA can produce acidic byproducts upon degradation that can cause inflammation in ocular tissue [80]. Further research is needed regarding biomaterials that can be used for ocular therapy without producing byproducts upon degradation that cause inflammation in the application area. Although current ocular implants on the market allow delivering drug over long periods of time, they do not allow for a tuneable release of drugs. Drug release platforms that encompass both characteristics would be of interest in this field [80].

# 3 Materials and Methods

## 3.1 Introduction

The following section describes the materials and the methodology used in the chapters of this thesis.

## 3.2 Materials

### 3.2.1 Material acquisition

Poly(trimethylene carbonate) acrylate (PTMCA), Hyperbranched Poly (ethylene glycol) diacrylate (HBpPEGDA), and Hyperbranched Tricyclo [5.2.1.$0^{2,6}$] decanedimethanol diacrylate (HBpTCDMDA) were synthesized in house. Tri(methylene carbonate) (TMC) was purchased from Polysciences Europe GmbH (Germany). Poly(ethylene glycol) diacrylate (PEGDA) (250 g/mol), 2-Hydroxyethyl acrylate (HEA), Triazabicyclodecene (TBD), Dicloromethane (DCM), deuterated chloroform ($CDCl_3$), benzoic acid, 2-Benzyl-2-(dimethylamino)-1-[4-(morpholinyl) phenyl)]-1-butanone (Irgacure 369, photoinitiator), Tricyclo [5.2.1.$0^{2,6}$] decanedimethanol diacrylate (TCDMDA), Bisphenol A Ethoxylate diacrylate (BPAEDA), Di(ethylene glycol) ethyl ether acrylate (eDEGA), Lauryl acrylate (LA), N – Vinylpyrrolidone (NVP), 3-Mercaptopropionic acid (3-MPA), 3-(Trimethoxysilyl) propyl methacrylate (TPM), Rhodamine B, Curcumin, Phosphate buffered saline (PBS) and propylene glycol methyl ether acetate (PGMEA), Trypan blue, foetal bovine serum, penicillin, streptomycin, amphotericin B, L-Glutamine, insulin from bovine pancreas, M199 medium, foetal bovine serum (FBS) and L L-glutamine were all obtained from Sigma Aldrich, Inc (UK). Alpha Minimum Essential Medium (MEM) was obtained from BioWhittaker Reagents, Lonza Walkerville Inc, (United States). 2,2′-Azobis(2-methylpropionitrile) (AIBN) was acquired from Fluorochem, Ltd (UK).

Fluocinolone Acetonide was obtained from Carbosynth Ltd (UK). Isopropanol (IPA), Toluene, Hexane, Tetrahydrofuran (THF), Methanol, Trypsin-EDTA solution were acquired from Fisher Scientific, Ltd (UK). Keratinocyte serum-free media (KSFM), TrypLE Express Dissociation Reagent, PrestoBlue Cell Viability Reagent, and the Pierce lactate dehydrogenase (LDH) Cytotoxicity Assay Kit were obtained from ThermoFisher Scientific, Ltd (UK).

## 3.3 Methodology

#### 3.3.1.1 Synthesis of PTMCA

PTMCA synthesis was performed following the methodology previously reported in the literature [98], which details the preparation of methacrylated and/or acrylated polymers *via* ring-opening polymerisation. The synthesis was performed as it follows: 1000 mg (9.79 mmol) of trimethylene carbonate monomer and the required quantity of HEA (23.22 mg, 0.2 mmol) to achieve the correct *[M]:[I]* ratios to produce a polymer with a final molar mass of 5000 Dalton (Da) were introduced into a vial, which had been dried at 50 °C overnight and capped with a rubber septum. DCM (3 ml) was then added, and the reagents were allowed to dissolve at 30 °C for 5-10 minutes. The catalyst TBD 1% mol/mol was also dissolved in DCM (1 mL) and then added to trigger the ring-opening process which was completed within 1 hour at ambient conditions. The reaction was terminated by catalyst deactivation *via* the addition of 5 mg of benzoic acid and the product polymer was then isolated and purified using multiple precipitation steps into cold methanol (40 mL), followed by being dried in a vacuum oven for 24 h.

#### 3.3.1.2 Characterization of PTMCA

The monofunctional acrylate macromers were characterized by Hydrogen Nuclear Magnetic Resonance ($^{1}$H NMR) using a Bruker AV3400 400.1 MHz spectrometer.

Deuterated chloroform ($CDCl_3$) was selected as the reference solvent (7.26 ppm). Chemical shifts, measured in dH (parts per million (ppm)), were referenced to residual CHCl3 at 7.26 ppm. Analysis of spectra was carried out using Mestrelab Mnova 10.0 software.

The number average molecular weight ($M_n$) was calculated with the following equation:

$$M_n = \frac{Polymer\ integration\ n°\ x\ Monomer\ M_w}{Protons\ associated\ with\ signal} \qquad \textbf{Equation 3.1}$$

where $\frac{Polymer\ integration\ n^o}{Protons\ associated\ with\ signal}$ determines the number of repeats units in the polymer, which is then multiplied by the molecular weight of the monomer unit to obtain the $M_n$ of the polymer.

The gravimetric yield percent of the polymer was determined by the following formula:

$$Yield\ \% = \frac{Grams\ of\ end\ product}{Grams\ of\ monomer}\ x\ 100 \qquad \textbf{Equation 3.2}$$

The monofunctional acrylate macromers were also analysed *via* Gel Permeation Chromatography (GPC). The GPC was performed on an Agilent 1260 Infinity system (Agilent Technologies, USA) equipped with a PL-gel 5 mm guard column and two PL-gel mixed-C (7.5 mm × 300 mm) columns in series. Tetrahydrofuran (THF, High Performance Liquid Chromatography (HPLC) grade, Fisher Scientific) was used as the mobile phase at a flow rate of 1 mL/min. A Wyatt Optilab light scattering detector and a differential refractometer (DRI), were used for sample detection and analysis. The differential index of refraction value (dn /dc), 0.0816, was used to calculate the polymer molecular weight and dispersity. GPC samples were made up of 3 mg/mL solutions in HPLC grade THF which were filtered into a sample vial through a syringe filter (Whatman, 25 mm, 0.2 mm). Analysis of the spectra obtained was carried out using Astra software.

**Acknowledgment:** The GPC analysis of PTMCA was carried out by Dr Cordula Hege (University of Nottingham).

### 3.3.1.3 Synthesis of Hyperbranched Polymers.

The hyperbranched materials were synthesised with the following protocol: The di-functional TCDMDA or PEGDA monomer (1 mL), toluene solvent (2 mL), 3-Mercaptopropionic acid (3-MPA) control transfer agent (CTA) (65 mol%) and 2,2'-Azobis(isobutyronitrile) (AIBN) initiator (0.1 wt%) were all added to a reaction vessel. The mixture was degassed with argon for 30 min, then immersed in a pre-heated oil bath at 65 °C and reacted for 25 min. The polymerisation was quenched via oxygen ingress and immersion in an ice bath to prevent cross-linking. The polymer (HBpPEGDA or HBpTCDMDA) was isolated via dropwise precipitation into cold (0 °C) hexane antisolvent. The supernatant was poured off and the viscous product was allowed to dry to constant mass in a fume hood in the case of HBpTCDMDA. For HBpPEGDA, the supernatant was poured off and the viscous product was dried to constant mass *via* bubbling with argon (Ar) for 30 min.

**Acknowledgment:** The experimental work for HBpTCDMDA synthesis was performed by Dr Sophie Goodwin (University of Nottingham). The experimental work for HBpPEGDA synthesis was performed by Dr Amy Stimpson (University of Nottingham).

### 3.3.1.4 Characterization of HBpTCDMDA

HBpTCDMDA and HBpPEGDA polymers were characterized using $^{1}$H NMR, GPC, and gravimetric analysis.

$^{1}$H NMR was performed on a Bruker AV400 spectrometer (400 MHz) at 25 ºC. Samples were prepared as 10 mg/mL solutions in deuterated chloroform (CDCl3) to which

chemical shifts, measured in dH (ppm), were referenced to residual CHCl3 at 7.26 ppm. Analysis of spectra was carried out using Mestrelab Mnova 10.0 software.

The GPC analysis was performed using the same methodology explained in section **3.3.1.2**. The only difference was that GPC samples for hyperbranched polymers were made up of 2 mg/ml solutions.

**Acknowledgment:** The experimental and analytical work of this section was performed by Dr Sophie Goodwin for thecharacterisation of HBpTCDMDA and by Dr Amy Stimpson for the characterisation of HBpPEGDA.

#### 3.3.1.5 Preparation of formulations for AM

##### 3.3.1.5.1 2PP formulations used in Chapter 4

Formulations for use in the 2PP printer were prepared by mixing pre-calculated target concentrations of the reagents required in a 5 ml amber glass vial in a UV-free environment using the following procedure, where Irgacure 369 (2 wt% of the total solution) was adopted as the photoinitiator in all formulations. The absorption spectra of the photoinitiator can be observed in the following figure:

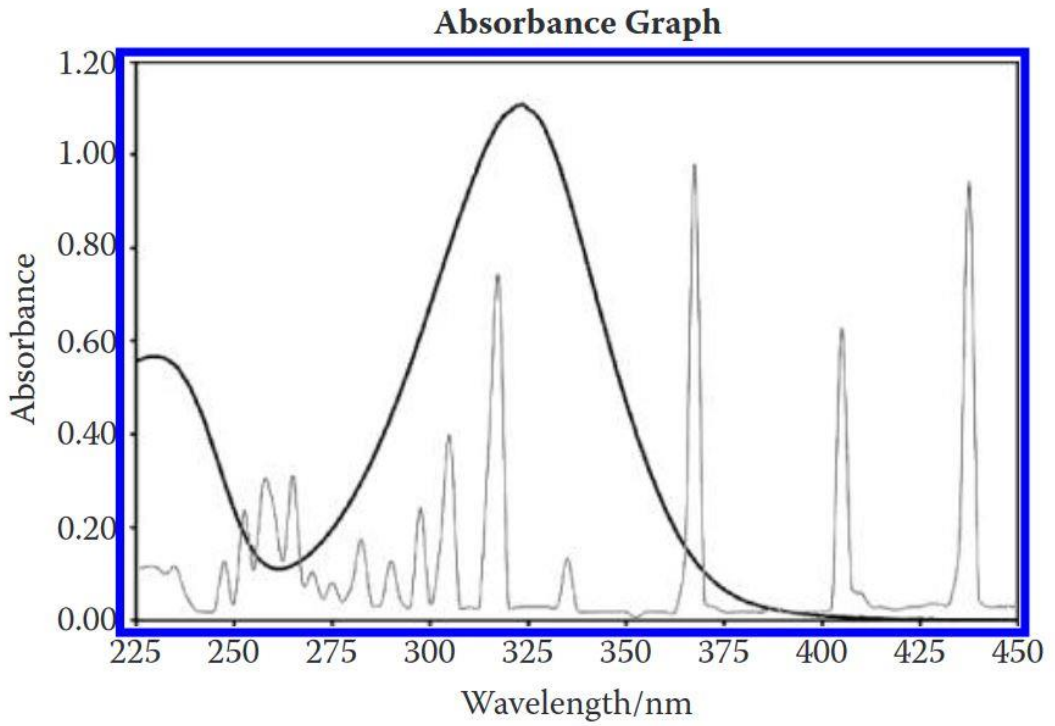



**Figure 3.1. UV absorption spectrum of photoinitiator Irgacure 369**

The PI was selected due to its adequate solubility in both hydrophobic and hydrophilic molecules used in this thesis. The 2 wt% concentration was selected based on previous optimization work performed in our group (unpublished), which indicated that this concentration allowed manufacturing at a wide range of processing parameters and could produce samples with good biocompatibility.

By maintaining the 2 wt% constant in the multi-material mixtures of monoacrylate oligomer and diacrylate monomer, the mol% concentration of the photoinitiator increased when the amount of double bonds per formulation decreased due to higher amount of PTMCA being added in the formulations. Example: PTMCA+PEGDA 1:20 molar ratio formulation (2 wt% and 2,5 mol% I369), PTMCA+PEGDA 1:2 molar ratio formulation (2 wt% and 9,4 mol% I369). In this example, the 1:20 molar ratio mixture has 4,17 times more acrylate end groups than the 1:2 molar ratio mixture.

For mixtures involving the low molecular weight monomers, the materials were mixed on a hotplate at 60 °C for 30 min prior to the addition of the photoinitiator. Once the

Irgacure was introduced to the formulations, they were left stirring for a further 2 h prior to use. For mixtures involving the PTMCA macromer and PEGDA, the Irgacure 369 was added to the PEGDA which had been stirred for 20 min at 60 °C in a 5 ml amber glass vial. The PTMCA was then introduced to the vial and the mixture was left stirring for a further 6 h stir at 60 °C. For the PTMCA and TCDMDA formulations, the same procedure as with the PEGDA formulation was adopted. However, following the 6 hours, 100 µl of PGMEA was added to all PTMCA + TCDMDA formulations to further reduce viscosity and these final mixtures were left stirring for another hour at 60 °C.

#### 3.3.1.5.2 2PP formulations used in Chapter 5.

Formulations used in Chapter 5 for the 2PP system were also prepared by mixing pre-calculated target concentrations of the materials needed in 5 ml amber glass vials in UV-free environment with 2 wt% Irgacure 369. Formulations containing only PEGDA or TCDMDA monomer were prepared by adding the monomer to the vial, followed by the previously weighted amount of photoinitiator. The vial was left stirring on a hotplate at 60 °C for 1 h. Formulations containing only hyperbranched materials were prepared by adding the polymers to the vial, followed by the photoinitiator amount, and leaving the vial stirring for 30 min at room temperature (25 °C). Formulations containing both hyperbranched polymer and linear monomer were prepared by adding the materials to the amber vial and mixing them at low stirring on a hotplate for 20 min. Once well mixed, photoinitiator was added to the vial and the formulation was left stirring for another 30 min at room temperature.

#### 3.3.1.5.3 PµSLA formulations used in Chapter 6

One of the PTMCA+PEGDA formulations of section **3.3.1.5.1** was selected and modified to allow its use for projection micro-stereolithography (PµSLA). The formulation was

prepared by mixing pre-calculated target concentrations of the reagents required in a 20 ml silanization glass vial in a UV-free environment using the following procedure, where Irgacure 369 (2 wt% of the total solution) was also adopted as the photoinitiator. The Irgacure 369 was added to the PEGDA, which had been previously stirred at 60 °C for 20 min. Once dissolved, PTMCA was added next to the vial and the mixture was left stirring for one hour. After that, NVP was added, and the materials continued mixing for another half hour. This was then followed by the addition of curcumin (0.75 wt% of material's weight) and stirring overnight. This was followed by the addition of FA (6.25 wt% of material's weight) and mixing of the formulation for 4h until fully dissolved.

Mixtures of individual components of the PμSLA formulation (PTMCA + PEGDA + NVP + FA) were prepared as follows: pre-calculated target concentrations of the reagents required were added in a 20 ml silanization glass vial in a UV-free environment. For PEGDA and NVP mixtures, the addition of the required material was followed by the addition of Irgacure 369 (2 wt% of the total solution), and the mixture was left stirring at 60 °C for 1h. For the PTMCA mixture, acetone solvent was added (targeting 17% w/v concentration) alongside the polymer to the vial to reduce viscosity and facilitate mixing. The polymer was dissolved in acetone solvent at 45 °C for 30 min. Then, the photoinitiator was added to the formulation, which was kept stirring for another hour. A drop of each formulation (70 µl) was pipetted on glass microscope slides (76 mm × 26mm) and cross-linked under UV light (395 nm, 5 cm distance from the sample) for 7 min. The cross-linked drops were used as controls for microstructure analysis experiments (see section **6.2.7**).

#### 3.3.1.6 Manufacturing structures via AM

##### 3.3.1.6.1 Manufacturing structures with 2PP system

Structures were printed using a commercial two-photon system (Nanoscribe Photonic Professional GT) equipped with a 780 nm wavelength fibre laser, a pulse frequency of 80 MHz, and a pulse duration of 120 fs. The laser beam was focused with an oil immersion objective (63X, Numerical Aperture (NA) = 1.4). The full power of the system was 50 mW. The structures were manufactured by moving the laser beam in X-Y directions with mirrors and by moving the piezo stage in the Z direction (printing in galvo-mode).

A glass coverslip was used as the substrate for printing. The coverslips were mounted on the sample holder with tape. Thus, a drop (50 µl) of the test formulation was loaded onto the coverslip, which was then mounted into the 2PP system's sample holder. This was then loaded into the Nanoscribe system to allow printing to commence. The structures were designed on AutoCAD software. They were sliced with the DeScribe software.

To eliminate unpolymerized material being retained in the final structures, the specimens were washed after printing by immersionin propylene glycol monomethyl ether acetate (PGMEA) for 2 h to 48 h. After this, the structures were then thoroughly washed in isopropanol for 10 min, to remove any residual solvent and then air-dried.

##### 3.3.1.6.2 Manufacturing structures with PµSLA

Structures were manufactured using a commercial projection micro – stereolithography system: Boston Micro Fabrication (BMF) microArch S130 (BMF Material Technology Inc., Shenzhen, China). The system is equipped with a 405 nm wavelength UV light source and a Digital Mirror Device (DMD) as digital dynamic mask. The light was focused on the vat with a projection lens. The system has a motorized stage that moves in X, Y, and Z directions. It also has a pre-stretched transparent and anti-sticky

perfluoroalkoxy (PFA) membrane to help with layer thickness control. It also helped level the resin and avoid bubbles on its surface during the manufacturing process.

To manufacture, 4 mL of resin were deposited in the small vat of the printer with a 5 mL syringe. The membrane was put on top of the vat containing the resin and printing platform, assuring that no bubbles were present in this process. After manufacturing, structures still attached to the platform were briefly washed of excess resin for 30 sin isopropanol (IPA). They were then detached from the platform using a razor and left in IPA for 24 h. After IPA washing, samples were air-dried and post-processed inside a UV-oven (Formlabs Form Cure, 405 nm wavelength) for 15 min at 40 ºC.

#### 3.3.1.7 Methacrylate functionalization of glass coverslips

Glass slides (22 mm × 22 mm) were activated using $O_2$ plasma ($p_i$ = 0.3 mbar, 100 W, 5 min) and immediately transferred into dry (4 Å MS) toluene (50 mL) under argon. 3-(Trimethoxysilyl) propyl methacrylate (1 mL) was added, and the reaction mixture was heated to 50 °C for 24 h. The slides were then cooled to room temperature and washed three times by sonication with 3 × 10 mL of fresh toluene. The slides were then dried under vacuum in a silicone-free vacuum oven at 50 °C for 24 h.

#### 3.3.1.8 Polymerisation threshold

Adequate manufacturability and resin cross-linking were determined by testing the 2PP resins at different laser powers and scan speeds. This step was used to determine the polymerisation thresholds and burning thresholds of the different resins. The combination of parameters that allowed for successful manufacturing was confirmed by imaging the sample using a scanning electron microscope (SEM).

#### 3.3.1.9 Sample characterization by optical microscope

Samples were imaged and analysed with a Nikon Eclipse LV100ND Optical Microscope.

#### 3.3.1.10 Sample characterization by SEM

Sample observation was performed using Hitachi TM3030 table-top SEM. The images were obtained using a 15 keV acceleration voltage with the composition (COMPO) imaging mode. The samples were previously coated with gold before SEM imaging.

#### 3.3.1.11 Sample characterisation by Raman Spectroscopy

##### 3.3.1.11.1 Raman theory and system specifications

Raman spectroscopy studies the interaction of a monochromatic laser beam with molecules of samples that originates from a scattered light source. This interaction excites molecules from the ground state (E0) to a virtual energy state. The molecule can relax back to the ground state releasing the same amount of energy as the incoming photon (Rayleigh scattering), which does not yield information about the molecule under investigation. However, the molecule can relax in an inelastic manner by releasing a different amount of energy to that of the incident photon, known as Raman scattering [99]. There are two types of Raman scattering: Stokes scattering, if the frequency of incident radiation is higher than that of scattering radiation, and Anti-Stokes scattering, if the frequency of incident radiation is lower than that of the scattering radiation. Stoke bands are more intense than Anti-Stokes bands and so they are the ones used in conventional Raman spectroscopy [100]. To show this energy transitions in a Raman spectrum, the frequency is converted into wavenumbers. As specific molecular bonds vibrate at particular wavenumbers and the intensity of this wavenumber is related to the concentration of the molecules, Raman analysis gives valuable information about the composition and concentration of molecules in samples [99].

2PP samples manufactured for this thesis were analysed with Raman spectroscopy using a Horiba Jobin Yvon LabRAM HR equipped with an automated *xyz* stage (Märzhäuser). Excitation was provided by a laser line at λ = 785 nm (*P* = 24 mW). A 100x objective lens and a confocal pinhole of 50 µm were used. To simultaneously scan a range of Raman shifts, a 600 lines·mm$^{-1}$ rotatable diffraction grating along a path length of 800 mm were employed. Spectra were acquired using a Synapse CCD detector (1024 pixels) thermoelectrically cooled to −60 °C. Before spectra collection, the instrument was calibrated using the zero-order line at 0 nm and a standard Si(100) reference band at 520.7 cm$^{-1}$. For single point measurements, spectra were acquired over the range 600-1850 cm$^{-1}$ with an acquisition time of 60 to 120 seconds and 4 accumulations. The spectral resolution is 0.6 cm$^{-1}$ for the 785 nm laser. The spatial resolution is ~1 µm and ~3 µm in the lateral (*xy*) and axial (*z*) directions respectively. Spectra were baseline-corrected using a fourth-order polynomial fitting model.

#### 3.3.1.11.2 Reacted Vinyl Group calculation

During polymerisation, the carbon double bonds (C=C, Raman peaks at 1635 cm$^{-1}$) are converted to carbon-carbon single bonds (C-C), meanwhile, the carbon-oxygen double bond (C=O, Raman peak at 1723 cm$^{-1}$) remains unchanged as it does not participate in the reaction [10]. The amount of RVG was calculated using the following equation:

$$RVG = 1 - \frac{A_{C=C}/A_{C=O}}{A'_{C=C}/A'_{C=O}} \qquad \textbf{Equation 3.3}$$

where $A_{C=C}/A_{C=O}$ is the area under the peaks in polymerized structures and $A'_{C=C}/A'_{C=O}$ is the peak area of unpolymerised formulation [10]. The percent of RVG is obtained by multiplying the result of **Equation 3.3** by 100.

#### 3.3.1.12 Sample characterization by Time-of-Flight Secondary Ion Mass Spectrometry (ToF-SIMS)

##### 3.3.1.12.1 Technique Introduction

ToF – SIMS is an analysis technique that allows for specific identification of molecules on the surface of samples. It does this by focusing a high-energy primary ion beam, typically in the order of keV, onto the sample. The primary ion source can be a gas cluster ion beam (GCIB) or a liquid metal ion source (LMIS), which are typically argon, bismuth, or caesium [101, 102]. The primary ion directed towards the sample results in secondary ions (SI) being emitted from its outmost molecular layers. The secondary ions are mass-analysed by measuring the time they require to fly from the sample to the detector. In dual beam systems, the primary ion generates SI from a monomolecular surface of the sample using a low ion dose, while a second sputter ion gun is used for depth profiling (removing several nanometers from the surface) at a higher ion dose. During measurements, individual mass spectra of each raster point are created. The obtained data can be used to produce: a) images showing the intensity of the SI across the analysis area and b) mass spectra for selected regions of interest [102, 103].

##### 3.3.1.12.2 ToF-SIMS methodology used in Chapter 4 and Chapter 5:

2PP samples were post processed before ToF-SIMS analysis by submerging them in PGMEA solvent for 24 h and then rinsing them in IPA for 10 min. They were then dried with an air-pump.

ToF-SIMS analysis of positively charged secondary ions was carried out using a TOF-SIMS IV system from IONTOF GmbH (Münster, Germany) using 25 keV $Bi^{3+}$ ion beam operated in the high current bunched mode delivering 0.3 pA with 100 µs cycle time, resulting in a mass range between 0 and 694 unified atomic mass unit (u) and a low-energy (20 eV) electron flood gun employed to neutralise charge build-up. Secondary ion maps were acquired by raster scanning the primary ion beam over areas up to

500 × 500 μm$^2$. 3D depth profiling of the chapter 4 samples was carried out in dual-beam mode with the 25 KeV $Bi^{3+}$ primary ion beam in burst alignment mode (high spatial resolution) and a 200 × 200 μm$^2$ sputter crater formed using a 10 keV argon GCIB delivering 5 nA. For chapter 5 samples, a sputter crater was formed using a 20 keV argon GCIB delivering 5 nA. The analysis was performed in the "non-interlaced" mode with one sputter frame and single analysis scan per cycle and a pause time in between cycles of 0.5 s. The ToF analyser was set with 200 μs cycle time, resulting in a mass range between 0 and 3400 mass units

#### 3.3.1.12.3 Multivariate Analysis performed on ToF-SIMS data in Chapters 4 and 5

Multivariate analysis was carried out using the mass as the variable and each individual sample spectrum or 3D image voxel was used as observations. Surface Lab 7.1 (IONTOF GmbH) was used to perform an automated peak search on the total spectra. Peak areas were exported for each observation. Principal component analysis(PCA) and non-negative matrix factorisation (NMF) were performed using the simsMVA software [104], which yields components loadings with groups of peaks that shared the same intensity (scores). Prior to MVA, data was Poisson scaled to account for heteroscedasticity [105].

**Acknowledgment:** The experimental ToF-SIMS work from chapters 4 and 5 and multivariate analysis was performed by Dr Gustavo Ferraz Trindade (University of Nottingham).

#### 3.3.1.12.4 ToF-SIMS methodology used in Chapter 6:

ToF-SIMS analysis of negatively charged secondary ions was carried out using a Hybrid SIMS instrument (ION-TOF GmbH., Münster, Germany) using a 30 keV $Bi^{3+}$ ion beam operated in the high current bunched mode delivering ~1 pA with 180 μs cycle time, resulting in a mass range between 0 and 450 u. Secondary ion maps were acquired with the following settings. For surface analysis: 256 × 256 Pixels, 10 scans, afield of view:

500 × 500 μm$^2$, 3 shots/pixel. For depth profile analysis: 256 × 256 Pixels, a field of view: 100 × 100 μm$^2$, 3 shots/pixel. 3D depth profiling was carried out in dual-beam mode with the 30 KeV $Bi^{3+}$ primary ion beam in burst alignment mode (high spatial resolution) and a 300 × 300 μm$^2$ sputter crater formed using a 10 keV argon GCIB delivering 5 nA. Data analysis was performed using SurfaceLab 7.3 software (IONTOF GmbH.).

**Acknowledgment:** The experimental work and data processing of this section was performed by Dr Stefani Kern (University of Nottingham)

#### 3.3.1.13 Effective laser power calculation

A model was developed to calculate the effective laser power per voxel. It considers that each point of laser exposure could affect that voxel plus 3 other voxels surrounding it, if the hatching/slicing distances are smaller than the radius of the voxels. Furthermore, part of that power would contribute to voxels resident on both the *xy*-planeand the build direction (**Figure 3.2-a**). The assumptions taken for this model and its calculations are explained as follows.

It was assumed an ellipsoid voxel shape in which the voxel radius A=B in *xy*-plane (perpendicular to laser power) and voxel radius in z plane is C = 2A (parallel to laser power) (see **Figure 3.2-b**). It was assumed *h* is the distance between centres of neighbouring voxels (hatching distance) and *s* is distance between centres of neighbouring voxels in z-direction (slicing distance). The laser power was assumed to have a Lorentzian distribution.

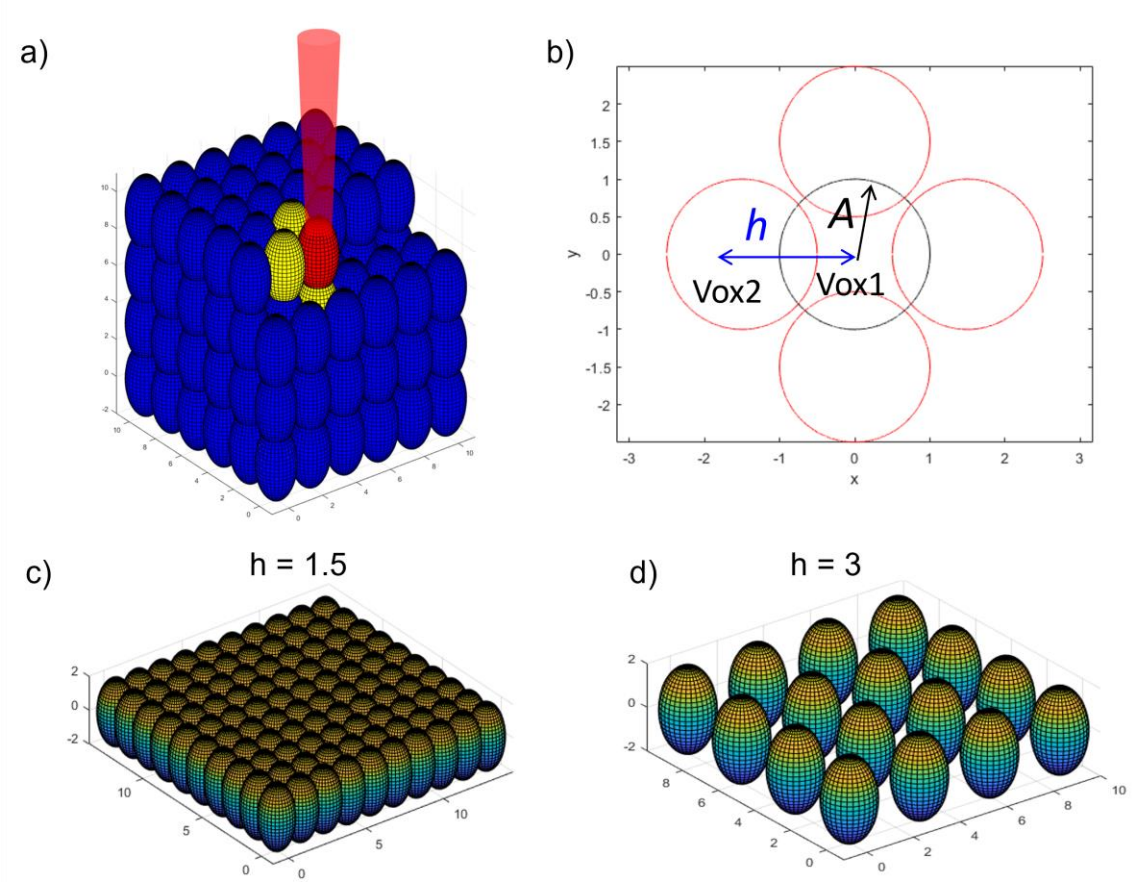



**Figure 3.2 Representation of model assumptions: a) 3D model showing the laser beam manufacturing a voxel (red colour) while highlighting the possible 3 voxels affected by the incident laser power (yellow voxels). b) View of several voxels in the *xy*-plane showing the distance from one centre of the voxel to another (hatching distance, *h*) and the voxel radius (A). c) 3D model representing the assumption A<*h*<2A in which 3 voxels overlap and the effective laser power takes into account $P_{xy}$ for total power calculations. d) 3D model representing the assumption *h*>2A in which voxels do not overlap and $P_{xy}$ does not contribute to total power calculations.**

When A<*h*<2A (see **Figure 3.2– c**). and C<*s*<2C, 3 neighbouring voxels are overlapping with each other: 2 in the *xy*-plane and 1 in the build direction. Therefore, in this case, every voxel is exposed to the original laser power ($P_0$),the powers of the neighbouring edges in the x,y plane ($2P_{xy}$),and the neighbouring edge power in the z plane ($P_z$). This means the effective laser power per voxel is represented by the following equation:

$$P = P_o + 2P_{xy} + P_z \qquad \textbf{Equation 3.4}$$

In the case of *h*>2A (see **Figure 3.2- d**) and *s*>2C, then $P_{xy} = 0$ and $P_z = 0$ and the effective laser power equals the original processing power $P_0$.

To numerically describe the Lorentzian power distribution inside the voxel, a 4$^{th}$ order polynomial equation was used. This allow calculating $P_{xy}$ (if *x*,*y* is described in units of *h*/A) and $P_z$ (if *z* is described in units of *s*/C) with the following equations:

$$P_{xy} = P_o[(ax^4) + (bx^3) + (cx^2) + (dx) + 0.9967 \quad \textbf{Equation 3.5}$$

$$P_z = P_o[(az^4) + (bz^3) + (cz^2) + (dz) + 0.9967 \quad \text{Equation 3.6}$$

The values of *a, b, c, d* from the above equations are reported in Table 3.1.

**Table 3.1. Numerical values of polynomial 4$^{th}$ order constants used in Equation 3.5 and Equation 3.6 for $P_{xy}$ and $P_z$ calculations.**

| Numerical constant | Numerical value |
|---|---|
| a | -0.03995 |
| b | 0.28379 |
| c | -0.3939 |
| d | -0.52505 |

The $P_{xy}$ and $P_z$ values obtained from Equation 3.5 and Equation 3.6 were substituted in Equation 3.4 to obtain the total effective laser power per voxel.

**Acknowledgment:** The effective laser power model and equations development, as well as the effective laser power calculations were carried out by Dr Lyudmila Turyanska (University of Nottingham).

### 3.3.1.14 Flory-Huggins interaction parameter

The Flory-Huggins parameter determines the excessive free energy of mixing and considers the cohesive energy density between the two materials. A strong difference in the cohesive energy density corresponds to higher $\chi$ parameter and, therefore, a blend more prone to phase separating [106, 107]**.** To calculate the $\chi$ value we first obtained the Hansen solubility parameter (HSP) of the individual components of the formulation. The HSP values for each individual component was calculated using the HSPiP program, which allows for the dispersion, polarity, and hydrogen bonding solubility parameters ($\delta_d, \delta_p, \delta_h$, respectively) and total HSP value ($\delta_{TOT}$) to be obtained *via* use of the software's DIY (Do It Yourself) tool. Consequently, the HSP values were used to ascertain their miscibility behaviour by applying them to the Flory-Huggins parameters equation. Flory-Huggins parameters ($\chi$) were determined with the following formula[107]:

$$\chi = \frac{V_r}{RT}(\delta_1 - \delta_2)^2 \qquad \textbf{Equation 3.7}$$

where $V_r$ is reference volume (the molar volume of a single unit of the material), $R$ is the universal gas constant, $T$ is the absolute temperature, $\delta_1$ is total HSP value of solvent material and $\delta_2$ is the total HSP values of solute material.

### 3.3.1.15 LogP parameter

The logarithmic partition coefficient (logP) of several materials was calculated to determine their polarity. The values were obtained using the ADC labs ChemSketch software, which allowed the molecular structures of the materials to be drawn and/or their SMILE formula imported. The software then calculated the logP value from this input data.

#### 3.3.1.16 LIVE/DEAD cell viability test

##### 3.3.1.16.1 3T3 cell cultures

3T3 fibroblasts were harvested and cultured (p.20) from mice. After thawing, the 3T3 cells were grown in Alpha MEM Medium. Cell culture media was complemented with 10% foetal bovine serum, 1 % antibiotic and antimycotic (AbAm) (100 mg/ml penicillin, 100 mg/ml streptomycin, and 0.25 mg/ml amphotericin B) and 1% of L-Glutamine. Cell cultures were maintained in T75 $cm^2$ flasks in standard culture conditions of 37 °C and 5% $CO_2$, cells were passaged every 3 days after harvesting them by trypsinization using 0.05% Trypsin-EDTA solution at 70% culture confluence and further subcultivated into culture flasks.

##### 3.3.1.16.2 Preparation of the samples for direct viability assessment

The scaffolds were sterilised using UV for 20 min then rinsed 3 times using PBS. Following this step, the scaffolds were covered with 2.5 mL of media and placed in an incubator under standard culture conditions of 37 °C and 5% $CO_2$.

##### 3.3.1.16.3 Cell seeding

3T3 cells were counted using the Trypan blue and a hemocytometer. 10000 cells were seeded on top of the scaffolds placed in a 6 well-plate. Well plates were incubated under standard conditions of 37 °C and 5% $CO_2$ for 24 h.

##### 3.3.1.16.4 LIVE/DEAD Staining protocol

A solution of 2 µM calcein AM and 4 µM Ethidium homodimer-1 (EthD-1) in PBS was prepared. Media was removed from the scaffold and the scaffolds were delicately washed once with PBS. Staining solution was then added, and the well plate was incubated for 1 h. Fluorescence microscope images were taken using a Leica fluorescence microscope and a Lumen dynamic Mercury Source at an exposition of 500 ms. Image analysis was performed using ImageJ

**Acknowledgment:** This experimental cell viability work was performed by Dr Adja Touré (University of Nottingham).

#### 3.3.1.17 Fluorescence Intensity Measurement of Rhodamine B

Rhodamine B fluorescence intensity was measured with a TECAN Spark Multimode Microplate Reader using an excitation wavelength of 485 nm and emission wavelength of 535 nm. The standard calibration curve gain was set as optimal, giving a gain of 126 that would be further used (with manual mode) for release samples in later measurements. The counts were selected to 50. The data was analysed using Microsoft Excel.

100 µl of each sample (with 3 repeats per sample) were loaded on a 96-well black micro-plate reader and the fluorescence intensity measurements were obtained. The average value was calculated from the triplicates of each sample, which was then inserted into the standard calibration curve equation to obtain the concentration of Rhodamine B released at each timepoint in 1 mL of media. This concentration value was multiplied by 5 to obtain the total concentration released in the 5 mL of PBS in each vial.

#### 3.3.1.18 High Performance Liquid Chromatography (HPLC)

HPLC analysis was performed using an Agilent (Santa Clara, USA) HPLC Series 1260 system, equipped with an autosampler, degasser, UV lamp, and multi-diode array detection. A wavelength of 238 nm was used to quantify fluocinolone acetonide. Method mobile phase compositions were 60 % methanol and 40 % deionized water (HPLC gradient grade). An Agilent Poroshell 120 EC-C18 column (2.7 µm, 4.6 × 100 mm diameter) was used to separate the samples at 40 °C. A flowrate of 0.7 mL/min was selected and a 50 µL injection volume was implemented with a runtime of 7 min. Three injections were performed per sample. Signal to noise ratio was 10. Preparation of FA

stock solution and solutions for the FA standard calibration curve will be explained in detail in section **3.3.1.19.2**.

### 3.3.1.19 Standard calibrations

#### 3.3.1.19.1 Standard calibration for Rhodamine B

A stock solution (50 µg/mL) of a determined concentration was prepared by dissolving a specific weighted amount of Rhodamine B in PBS. Serial dilutions with PBS from this stock solution were performed with a range of concentrations (0.001 µg/mL, 0.025 µg/mL, 0.05 µg/mL, 0.1 µg/mL, 0.5 µg/mL, and 1 µg/mL) that allowed to obtain a standard calibration curve (linear fit applied, $R^2$ = 0.98) used to determine the concentration of Rhodamine B released at different time points. This was done by fluorescence measurements with the methodology detailed in section **3.3.1.17**.

#### 3.3.1.19.2 Standard calibration for FAc

A FAc stock solution (50 µg/mL) was prepared by dissolving a previously weighted amount of drug in Methanol. A range of concentrations (0.5 µg/mL, 1 µg/mL, 5 µg/mL, 10 µg/mL and 25 µg/mL) were prepared by further dilutions with Methanol. From each diluted solution prepared, 1 mL was taken with a syringe and filtered (0.22 µm Polytetrafluoroethylene (PTFE) filter) into a transparent HPLC vial. The filtered samples were analysed *via* HPLC, and the calibration curve was obtained by plotting the values of the area under the curve of the drug peak against the concentrations of the solutions previously prepared. A linear fit ($R^2$ = 0.999) was applied.

### 3.3.1.20 UV – cast samples for Rhodamine B release

Formulations for Rhodamine B release studies were prepared similarly to 2PP formulations. Irgacure 369 (2 wt% of the weight of all materials) was adopted as photoinitiator for all formulations. The materials and concentrations used were as follow: PTMCA (50 wt% in all vials), PEGDA (35 wt%, 30 wt%, 25 wt%, 15 wt%, and 10 wt%),

and NVP (15 wt%, 20 wt%, 25 wt%, 35 wt% and 40 wt%) The photoinitiator was added to a glass vial with PEGDA that had been stirring for 20 min at 45 °C. PTMCA was also added and mixed in the vial with PEGDA and I369 for 2 h. NVP was introduced next into the mixture and the formulation was left stirring at 45 °C for another 2 h. After that, Rhodamine B, which acted as a model drug, was added to all vials (0.1 wt% of weight of all materials) that were left stirring for 1 h.

Once formulations were ready, 200 µl of them were extracted with a pipette and introduced between 4 taped glass slides that acted as rectangle mould for UV-A irradiation. The samples were UV cross-linked using a UV-LED lamp (FireFly, Phoseon Technology, US) at 395 nm with an irradiance of 4 W/cm$^2$ for 5 min with 4.5 cm distance between the lamp and the sample. The casted samples were cut into three pieces (for repeats). They were measured and weighted.

The samples were then placed into 20 mL glass silanisation vials filled with 5 mL PBS and kept inside an incubator at 37 °C. The PBS solution was previously prepared by dissolving 1 tablet of PBS in 200 mL of deionized water, producing a media with pH 7.4. At different time points, samples were removed from the vials and their wet weight was recorded. They were then dried for 1 h at 50 ºC in a vacuum oven and weighted again to record their dry weight. At each time point, 1 mL of PBS was extracted from the vials to analyse Rhodamine B release via Fluorescence microscopy (TECAN Spark Multimode Microplate Reader). The millilitre extracted was replenished afterward with fresh PBS. Fluorescence measurements were performed in triplicates (N=3, n=3).

#### 3.3.1.21 FAc drug release study

The lattice implants manufactured via PµSLA were placed into 2 mL glass vials filled with 1.5 mL of PBS. They were kept inside an incubator at 37 °C at 40 revolutions per minute (rpm). At specific time points, 1 mL of PBS was extracted from the vial and

filtered into a 2 mL HPLC glass vial with a 0.22 µm filter. The extracted PBS was refreshed at each time point. The 1 mL extracted and filtered PBS was analysed via HPLC following the methodology described in section **3.3.1.18**.

**Acknowledgment:** This experimental work was carried out with the help of Kristian Plender (PhD Student, University of Nottingham), who extracted 1 mL of media at each time point and refreshed the extracted PBS.

#### 3.3.1.22 Theoretical drug loading and cumulative drug release calculations

##### 3.3.1.22.1 Theoretical drug loading calculations

The amount of drug loaded into each UV-cast sample or 3D printed implant was theoretically calculated. The known volume ($mm^3$) of the casted samples (obtained using the sample measurements in the rectangle volume formula) or implants (provided by FlattPack software) was translated into volume in mL. By knowing the corresponding wt% and volume % of the drug from the total weight or volume of the formulation, the amount of drug loaded into the volume of the sample could be estimated.

##### 3.3.1.22.2 Cumulative drug release calculations

The cumulative drug release (CDR) was calculated by considering the drug concentration present at each time point in the total media volume ($CDR_n$) plus the drug concentration present in the media volume discarded at all previous time points ($CDR_{n-1}$). The CDR percent was obtained by multiplying the CDR by 100. The formulas used were the following:

$$CDR = CDR_n + (\sum CDR_{n-1}) \qquad \textbf{Equation 3.8}$$

$$CDR_{\%} = \frac{CDR\ x\ 100}{Total\ theoretical\ drug\ loaded\ per\ sample} \qquad \textbf{Equation 3.9}$$

#### 3.3.1.23 Mass loss calculations for UV cast samples

UV-cast rectangle samples manufactured with PTMCA + PEGDA + NVP formulations were submerged in 5mL PBS media at 37 ºC. At each time point, they were removed from the media and dried in a vacuum oven at 50 ºC for 1 h to reach constant weight. The dry weight was recorded, and the mass loss percentage was calculated using the following formula:

$$Mass\ loss_{\ \%} = \frac{initial\ dry\ weight - dry\ weight}{initial\ dry\ weight}\ x\ 100 \qquad \textbf{Equation 3.10}$$

#### 3.3.1.24 Biocompatibility assays performed on lattice implants manufactured in Chapter 6

**Acknowledgment:** All the experimental work described in this section was performed by Lydia Beeken (PhD Student, QMC, University of Nottingham).

##### 3.3.1.24.1 Cell line

Human corneal epithelial HCE2 cells are a cell line generated through the immortalisation of normal human cornea with Adenovirus 12 - SV40 virus hybrid (Ad12-SV40). Cells demonstrate a cobblestone-like appearance, similar to normal corneal epithelial cells, with maintenance of corneal, epithelial features

##### 3.3.1.24.2 HCE 2 cell culture

All cell culture was carried out using aseptic techniques in a class II microbiological safety cabinet, fitted with high efficiency particulate air (HEPA) filters. Cell cultures were stored in an incubator at 37 ºC in a humidified atmosphere containing 5% $CO_2$. During culture, full media change occurred every 3 – 4 days, and cells were passaged at 90% confluence.

HCE2s were cultured in Keratinocyte serum-free media, supplemented with human recombinant epidermal growth factor and bovine pituitary extract, supplied with the

media. Additional supplementation of 500 ng/mL hydrocortisone, 0.05% (v/v) insulin from bovine pancreas and 1 % antibiotic-antimycotic (AbAm).

Following 1 PBS wash, HCE2s were dissociated at each cell passage by incubation with TrypLE Express Dissociation Reagent for 10 minutes at 37 ºC. This reagent is a recombinant fungal, serine protease, which works through the cleavage of arginine and lysine. Although TrypLE Express follows a similar dissociation mechanism to the traditional porcine trypsin, it is preferable due to its improved capacity to maintain cell surface antigen expression.

The single cell suspension was neutralised using serum-containing M199 medium (M4530) supplemented with 20% (v/v) foetal bovine serum (FBS), 2 mmol/L L-glutamine, and 1% (v/v) AbAm and centrifuged at 250 RPM for 5 min for pellet formation. The supernatant was discarded and cells were resuspended in 1 ml SCM. Cell number was measured and calculated using the Countess II FL via Trypan blue uptake, and cells were consistently reseeded at $2^5$ cells/cm$^2$.

#### 3.3.1.24.3 Implant experiment

Implants were prepared by incubating in 1% AbAm in PBS (v/v) for 24 h, followed by incubation in supplemented KSFM (previously defined) for 24 h at 37 ºC. HCE2s were seeded in a 96 well plate at a cell density of $2^5$ cells/cm$^2$ and left overnight to attach. One implant was then added to each well (N=3, n=3), with additional wells for untreated (media only) and lysed cell controls, and left for 24 h in normal cell culture conditions. Cytotoxicity and cell viability were then assessed using the lactate dehydrogenase cytotoxicity assay and PrestoBlue viability assay respectively.

#### 3.3.1.24.4 PrestoBlue cell viability assay

PrestoBlue Cell Viability Reagent quantitatively measures cell proliferation through the determination of the cell reducing ability. Viable cells reduce PrestoBlue resazurin, which

is blue in colour and non-fluorescent, to the red and highly fluorescent compound, resorufin. This change can be detected by a plate reader using fluorescence and absorbance measurements.

PrestoBlue solution was diluted 10 fold in the respective cell culture medium. Cells were washed with PBS and incubated with 100 µl PrestoBlue solution at 37$^{o}$C for 20 min. 100µl of PrestoBlue solution from each well was then transferred to a clear bottom, black plate, and fluorescence was measured at excitation 535 nm (25 nm bandwidth) and emission 615 nm (10 nm bandwidth). CLARIOstar (BMG LABTECH) plate reader was used to obtain measurement data.

#### 3.3.1.24.5 Lactate dehydrogenase (LDH) cytotoxicity assay

The Pierce lactate dehydrogenase (LDH) cytotoxicity assay kit was used to quantify cell cytotoxicity induced by the implants. LDH is a ubiquitously expressed, cytosolic enzyme, which is rapidly released into the culture medium following plasma membrane damage. The assay is based on an enzymatic: coupling reaction, where LDH catalyses the conversion of lactate to pyruvate, through the reduction of Nicotinamide adenine dinucleotide ($NAD^{+}$) to Nicotinamide adenine dinucleotide + hydrogen (NADH). Sequentially, NADH reduces tetrazolium salt (INT) to a red formazan, which can be quantified using absorbance.

10 µl of lysis buffer (included in the kit) was added to triplicate wells of each sample and incubated for 45 min at 37 $^{o}$C. The lysed controls represent the maximum LDH release. 50 µl of cell media from each sample and control well was then transferred to a flat-bottomed, clear, 96 well plate. The reaction mix was prepared by reconstituting the substrate mix in 11.4 ml deionized water (di$H_2O$), and 600 µl assay buffer. 50 µl of the reaction mixture was then added to each well of sample media, mixed by gently tapping, and incubated at room temp for 30 min, protected from the light. 50 µl stop solution

(included in the kit) was then aliquoted into each well. Absorbance was measured at 490 nm and 680 nm using a CLARIOstar (BMG LABTECH) plate reader, and the values obtained from 680 nm subtracted from the 490 nm. Percentage cytotoxicity was then calculated using the equation below.

$$\left[\frac{Sample\ LDH\ Release - Spontaneous\ LDH\ Release}{Maximum\ LDH\ Release - Spontaneous\ LDH\ Release}\right] \times 100 \quad \textbf{Equation 3.11}$$

In the above formula, sample LDH release is the value obtained from the treated cells; spontaneous LDH release is the value obtained from untreated cells, and maximum LDH release is the value obtained from the lysed cells.

**Acknowledgment:** All the experimental work described in this section was performed by Lydia Beeken (PhD Student, QMC, University of Nottingham).

#### 3.3.1.25 Pore size and length measurement of lattice implants with Fiji ImageJ software

To measure the implant pore size using imageJ software, a known measurement in an image was set as scale using the Set Measurement option. This allowed translating pixels of the image into measuring units. The images used were portable network graphics (png) files containing the 3D design of the lattice implants. Pore measurements were obtained by manually measuring with the previously set scale the smallest pore feature of each design.

The length of 3D printed lattice implants was obtained using SEM images of the structures instead of design images. The calculated lengths were obtained by averaging the results of 3 measurements ± standard deviation.

#### 3.3.1.26 Statistical analysis

Mean values ($n$ = 3) ± standard deviation (SD) were calculated using Microsoft Excel 2016. One-way ANOVA, Tukey tests, and t-tests were performed using Microsoft Excel 2016 software and GraphPad Prism software.

# 4 2PP multi material printing with controlled microstructure and high reacted vinyl groups

## Acknowledgement

Part of this chapter has been adapted into a manuscript for publication: Konta, A.A, Trindade, F. G., Hege, C., Ruiz-Cantu, L., Turyanska, L., Alexander, C., Wildman, R., Irvine, D, J. Two photon multi-material printing with controlled microstructure and high reacted vinyl groups. 2021 (Drafted).

## 4.1 Introduction

The main focus until now in the 2PP field has been on homogeneous resins and so two aspects that would highly benefit the field are: (a) developing new materials for it to expand the library of available resins and (b) multi-material printing. Both of these, but especially the latter, could allow researchers to tailor composition and structure at the micro and nanoscale. This, in turn, will deliver new and tuneable mechanical properties to the 2PP manufactured structures. Whilst there has been some work conducted on nanocomposites for 2PP by adding particles, fibres, or carbon nanotubes (CNT) into the formulations, the monomer component of the mixture that transforms into polymer matrix is generally a single specie [21]. Such nanocomposites with carbon nanotubes were reported to provide the benefit of adding conductivity to polymer structures. The Lu group, for example, used CNT in their acrylate-thiol resin for this purpose [108]. Meanwhile, Xiong *et al.* prepared nanocomposite hydrogels by mixing PEGDA with

magnetic nanoparticles and obtaining structures that acted as magnetic actuators [109]. Other recent approaches to processing mixtures of different phases of materials have involved adding ceramic or metallic moieties to the monomer formulation prior to printing. In these cases, once the 2PP sample is manufactured, it undergoes high-temperature pyrolysis/sintering during which the organic material is eliminated leaving the ceramic or metal structure behind [97] as the final product structure.

There have also been recent reports exploring multi-material printing with other micro-stereolithography techniques outside 2PP [97]. Wang *et al.* developed lattice structures with copper nanoparticles reinforced PEGDA beam frames and internal tilted beams with pure PEGDA. These lattice structures allowed for tuneable negative thermal expansion. The multi-material printing in the same structure was done by alternatively switching the two formulations [110]. Another approach was taken by Schwartz *et al.* that produced multi-material acrylate and epoxide-based structures using a multi-wavelength digital light projection AM (DLP-AM) method. The use of long-wavelength irradiation during manufacturing stimulated the curing of mainly acrylate components of the resin, while the use of short-wavelength irradiation allowed for both acrylate and epoxide components to react and be incorporated into the structures [111]. A different route for multi-material printing with DLP-AM was taken by Ge *et al.*, they used an automated material exchange process incorporated in the apparatus, i.e., the system was designed to be able to "swap" resins during a manufacturing task. This methodology allowed the manufacturing of shape memory structures that responded to external stimuli, i.e., temperature change. Their multi-material resins consisted of monofunctional benzyl-methacrylate mixed with difunctional cross-linkers like poly(ethylene glycol) dimethacrylate, bisphenol A ethoxy dimethacrylate or diethylene glycol dimethacrylate. By tuning the materials that constituted the formulations, different copolymer cross-linked network formed which allowed for a range of thermomechanical properties to be obtained delivering the shape

memory behaviour [112]. Despite providing a step toward multi-material printing direction, these DLP examples by Schwarts *et al.* and Ge *et al.* [111, 112] required direct changes to the printing system during fabrication, e.g., switching of the formulation or modifying the wavelengths used to achieve their multi-material goal. Thus, while these multi-material examples are relevant to the 2PP field, they are made of non-miscible substances that do not achieve complete mixing. Consequently, there is still a lack of different monomer/oligomer mixtures with tuneable properties like the ones studied by Ge *et al.* in the DLP field.

Therefore, the work of this chapter tackles two main aspects that need further development for 2PP: expanding the library of materials and multi-material printing. Firstly, a biocompatible material was identified and synthesised which possessed the required characteristics for suitable 2PP processing. This material, poly(trimethylene carbonate) (PTMC), was selected as the key material for this study because of its low $T_g$ (-17 ºC) that allows it to maintain a viscous liquid state at room temperature. This is related to PTMC being an amorphous, non-crystalline polymer [46, 119], meaning that it presents a broad softening range and, above its $T_g$, molecular mobility increases, thus showing an adequate viscosity range for 2PP processing. Semi-crystalline polymers, like PCL or PLA polyesters, show densely packed and ordered crystalline regions compared to amorphous counterparts. This crystallization process provides these thermoplastics with a typical lamellar morphology consisting of polymer chains packed parallel to each other with disordered or amorphous regions in between these lamellae. To induce sufficient molecular mobility to allow 2PP processing, semi-crystalline polymers have to be warmed up above their melting temperature. Also, a result of this crystalline morphology, semi-crystalline polymers are generally opaque [120]. Therefore, PTMC was selected as it could be easily optimised for 2PP processing at room temperature and showed transparency, a feature needed for ocular applications. It is also transparent to the

2PP laser source, avoiding interferences during manufacturing. On the other hand, amorphous raw PTMC shows less mechanical strength than semi-crystalline PCL or PLA. One way to address this issue is by crosslinking or co-polymerising it with another material [46, 119]. As such, it was hypothesised that using PTMC for multi-material 2PP processing would allow to manufacture structures with adequate mechanical resistance.

Additionally, the biocompatibility and biodegradability of this polymer have been extensively studied. The latter of which has shown that it does not produce strongly acidic byproducts, as in the case of PLA/PLGA, so avoiding irritation at the degradation site [40].

In this study, PTMC was initially synthesized as a mono-acrylate oligomer (referred to as PTMCA) to be able to obtain the physical characteristics of the polymer, i.e., the product will be a thermoplastic and so amenable to solvent-based analysis techniques. This will provide the information that will allow for it to be easily introduced/formulated into the 2PP resin system. Mono-acrylate PTMC was selected as material in this work instead of multifunctional polymer due to: 1) its easier and shorter synthesis process, 2) less functionality would lead to less crosslinking density, which could potentially allow to obtain higher degrees of conversion compared to the low conversion (often < 50 %) shown by multifunctional meth(acrylates) [62]. Then, PTMCA mono-acrylate oligomer was used in the development and optimisation of new 2PP multi-material resin formulations, which contained the oligomer along with difunctional cross-linker monomers, such as poly(ethylene glycol) diacrylate (PEGDA) or tricyclo [5.2.1.$0^{2,6}$] decanedimethanol diacrylate (TCDMDA). These cross-linker monomers were selected because they have been previously used in bioapplications. This should increase their potential for rapid adoption in the biomedical industrycompared to new unregistered material [113-116]. More so, TCDMDA has also shown antimicrobial properties, which could be beneficial when used for certain bioapplications, like implants [124]. PEGDA

and TCDMDA were also chosen as di-functional/cross-linker monomers because they exhibit different polarity/hydrophilicity characteristics, to determine how this would affect the interaction with the macromere and so the success for the multi-material printing. To further study the printability of mono-acrylates and their interaction with the selected cross-linker, di(ethylene glycol) ethyl ether acrylate (eDEGA) and lauryl acrylate (LA) were also formulated with di-functional monomers. They were chosen based on their molecular weight as well as their hydrophilicity/hydrophobicity to determine the influence of these characteristics on their printability and the properties of printed structures, as a comparison to the much larger PTMCA. Based on combining these materials, a library of formulations was proposed and their tendency to mix homogeneously or phase separate during printing was predicted by calculating the Flory–Huggins interaction parameter. The experimentally prepared formulations were used to conduct 2PP processing and the products were subjected to Raman spectroscopy to determine the amount of vinyl groups reacted during printing polymerisation. In addition to the material types and their concentrations in the formulations, the influence of the laser power and the voxel size on the level Reacted Vinyl Groups (RVG) achieved was also studied using an in-house developed process model on PTMCA+PEGDA printed structures. The influence of the multi-material formulations, based on PTMCA+PEGDA/TCDMDA mixtures, on the onset of polymerisation processing thresholds exhibited by the inks was also studied and compared to the thresholds of mono-material formulations of the di-functional PEGDA and TCDMDA monomers. To confirm if multi-material printing was taking place and to better understand the microstructure of the manufactured samples, printed specimens were also analysed *via* ToF-SIMS.

## 4.2 Results and Discussion

### 4.2.1 Material characterization

**Acknowledgment:** The GPC analysis of PTMCA was carried out by Dr Cordula Hege

The PTMCA macromer was synthesized *via* ring-opening polymerisation following the methodology described in section **3.3.1.1**. The targeted molecular weight for the oligomer was 5000 g/mol. In practice, number average molecular weight ($M_n$.) of the final material, calculated as described in section **3.3.1.2**. from the $^1$H NMR data, was 3000 g/mol. A 55 % gravimetric yield was achieved (500-600 mg experimentally obtained from the initial 1 g of monomer weighted). Its weight average molecular weight ($M_w$) was calculated via GPC to be 2440 g/mol with a dispersity (*D*) of 1.3. A typical $^1$H NMR spectrum of a sample of PTMCA is reported in **Figure 4.1**.

The characteristic peaks of the acrylate functional group (a, b, c) can be observed on the spectrum between the 5.9 ppm and 6.5 ppm region, while two of the carbons of the polymer backbone are represented by the peak at 4.2 ppm (d). The presence of these peaks confirmed that the polymerisation reaction had occurred and allowed the calculation of the $^1$H NMR $M_n$ molecular weight of the synthesised material by rationing the integrals of the peaks at 5.9 ppm (corresponding to the acrylate end group moiety) with those at 4.2 ppm (polymer backbone moiety) and correcting for the hydrogen number of each group.

The resultant PTMCA product was found to be a highly viscous, transparent liquid. Thus, to make it suitable for processing by 2PP, the viscosity of PTMCA was decreased by using the reactive solvents PEGDA (250 g/mol) and TCDMDA (304.38 g/mol). The previous use of these reactive solvents in bioapplications [116, 117], their transparency, and their lower viscosity compared to PTMCA made them suitable candidates for 2PP photo-reactive resins. Additionally, as they are di-functional, they would facilitate the

cross-linking process of the formulation. The solvents were also chosen to be comparators in their physical properties, i.e. one is hydrophilic (PEGDA) and one hydrophobic (TCDMDA), to observe the influence of the solvent's polarity on material printing and manufacturing.

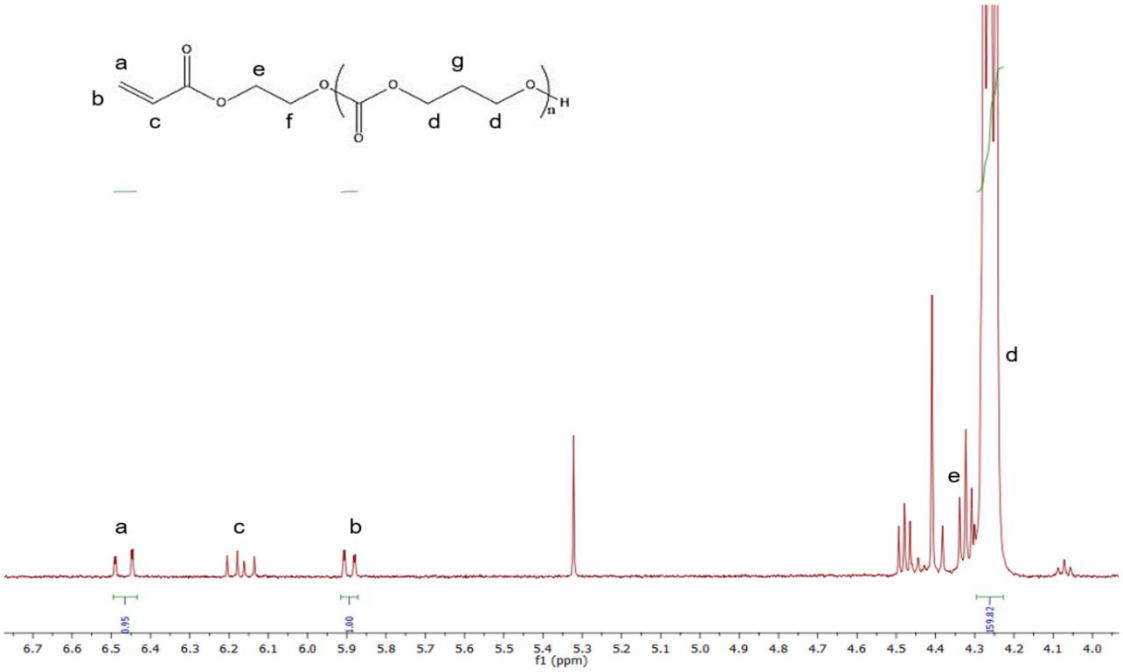



**Figure 4.1. $^{1}$H NMR spectrum of PTMCA showing the region between 4.0 and 6.7 ppm with characteristic peaks of the oligomer assigned to the material's structure. Peaks a,b, and c are representative of the acrylate functional group and peak d is representative of the polymer backbone.**

#### 4.2.1.1 Materials library miscibility

To further understand the printability of monoacrylate materials formulated into "inks" with the selected cross-linkers, several additional materials were selected as counterpoints to PTMCA based on either their molecular weight, polarity, hydrophilicity/phobicity and/or predicted mixing interaction. These materials are shown in **Figure 4.2**:

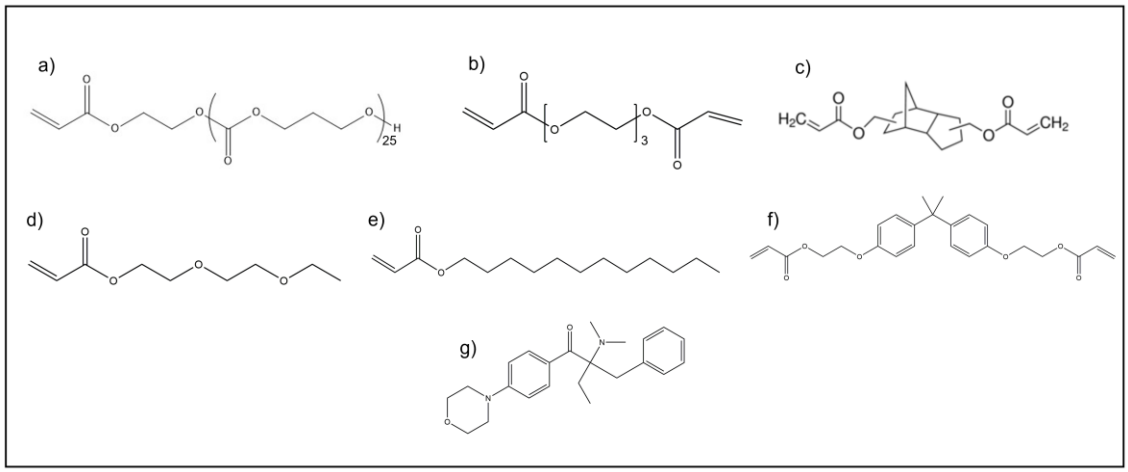



**Figure 4.2. Chemical structures of: a) poly(trimethylene carbonate) acrylate (PTMCA) b) poly(ethylene glycol) diacrylate (PEGDA) c) tricyclo[5.2.1.02,6] decanedimethanol diacrylate (TCDMDA) d) di(ethylene glycol) ethyl ether acrylate (eDEGA) e) lauryl acrylate (LA) f) bisphenol A ethoxylate diacrylate (BPADA) g) 2-Benzyl-2-(dimethylamino)-4'-morpholinobutyrophenone (Irgacure 369, photo-initiator).**

Hence, to investigate; the processability improvements that the additions of PEGDA/ TCDMDA delivered to all the mono-functional monomers used in the study, they were added to the formulations at different concentrations. The ink mixtures prepared are defined in **Table 4.1**.

**Table 4.1. 2PP formulations, comprising of a combination of monomer/oligomer (M1) and a reactive solvent (M2). Each experiment utilised 2 wt% of the photoinitiator (Irgacure 369). Long > 1000 g/mol and short < 1000 g/mol.**

| Entry | M1 Material | M1 Length | M2 Material | M2 Length | M1:M2 molar ratio |
|---|---|---|---|---|---|
| 1 | PTMCA | Long | PEGDA | Short | 1:02 |
| 2 | PTMCA | Long | PEGDA | Short | 1:08 |
| 3 | PTMCA | Long | PEGDA | Short | 1:20 |
| 4 | eDEGA | Short | PEGDA | Short | 1:02 |
| 5 | eDEGA | Short | PEGDA | Short | 1:08 |
| 6 | eDEGA | Short | PEGDA | Short | 1:20 |
| 7 | eDEGA | Short | PEGDA | Short | 1:46 |
| 8 | LA | Short | PEGDA | Short | 1:02 |
| 9 | LA | Short | PEGDA | Short | 1:08 |
| 10 | LA | Short | PEGDA | Short | 1:20 |
| 11 | LA | Short | PEGDA | Short | 1:46 |
| 12 | PTMCA | Long | TCDMDA | Short | 1:02 |
| 13 | PTMCA | Long | TCDMDA | Short | 1:08 |
| 14 | PTMCA | Long | TCDMDA | Short | 1:20 |
| 15 | PTMCA | Long | TCDMDA | Short | 1:46 |
| 16 | PTMCA | Short | BPAEDA | Short | 1:02 |
| 17 | PTMCA | Short | BPAEDA | Short | 1:20 |
| 18 | BPAEDA | Short | TCDMDA | Short | 1:02 |
| 19 | BPAEDA | Short | TCDMDA | Short | 1:20 |

The polarity of the materials used in formulations from **Table 4.1** was determined by calculating the logP parameter as described in section **3.3.1.15** (see Table 4.2)

**Table 4.2. LogP values for the different materials used in the 2PP formulations.**

| **2PP Materials** | **LogP** [a)] |
|---|---|
| eDEGA | 0.66 ± 0.33 |
| PEGDA | 1.06 ± 0.28 |
| IRGACURE 369 | 4.02 ± 0.53 |
| PTMCA | 4.27 ± 0.86 |
| BPAEDA | 4.35 ± 0.57 |
| TCDMDA | 4.39 ± 0.27 |
| LA | 6.64 ± 0.22 |

[a)] Calculated with ACDS Chemsketch software

Negative values (i.e., Leucine with a logP value of -1.55 [118] or 2-methacryloyloxyethyl phosphorylcholine with logP value of -2.95 [119]) and those close to 0 (i.e, Theophylline with a logP value of 0.00 [118]) indicate greater hydrophilicity, while higher positive values indicate increasing hydrophobic character. Hence, based on this data formulations of hydrophilic/hydrophilic, hydrophobic/hydrophilic, and hydrophobic/ hydrophobic materials were prepared to understand the effect of polarity on the processability of these formulations.

Furthermore, to better predict/understand the mixing/phase separation behaviour of these multi-material formulations during processing, the Flory – Huggins interaction parameter

was calculated using **Equation 3.7** for the following mixtures as described in section **3.3.1.14** (see **Table 4.3**).

**Table 4.3. Flory-Huggins interaction parameter, χ, calculated using Equation 3.5 for the formulations tested in the 2PP system.**

| Formulation No | 2PP formulations | Calculated χ |
|---|---|---|
| 1 | eDEGA+PEGDA | 0.012 |
| 2 | PTMCA+PEGDA | 0.08 |
| 3 | BPAEDA+TCDMDA | 0.207 |
| 4 | PTMCA+TCDMDA | 0.211 |
| 5 | LA+PEGDA | 0.446 |

The Flory-Huggins parameter determines the excessive free energy of mixing and considers the cohesive energy density between the two materials. A strong difference in the cohesive energy density corresponds to a higher χ parameter and, therefore, a blend more prone to phase separating [106, 107]. Thus, formulations like PTMCA+TCDMDA and LA+PEGDA would be more prone to phase separation than eDEGA+PEGDA or PTMCA+PEGDA. The tendency of the formulation to phase separate or not could influence the way the materials disperse throughout the printed structures and the type of microstructure created within them.

#### 4.2.1.2 Reacted vinyl groups (degree of conversion)

Raman spectroscopy analysis of these structures was used to determine the level of reacted vinyl groups (RVG) following 2PP processing, as per methodology stated in section **3.3.1.11**. The RVG % was calculated using **Equation 3.3**, detailed in section **3.3.1.11.2**. Briefly, for each RVG measurement, the amount of vinyl groups in the

formulation before printing was measured *via* Raman spectroscopy. Once structures were successfully manufactured with said formulation, the amount of vinyl groups was measured again. By comparing the initial amount of vinyl groups with the final amount in the printed structure, a percent of RVG can be obtained (see spectra example for PTMCA + PEGDA 1:2 molar ratio in **Figure 4.3** and **Figure S4.1** and **Figure S4.2** for further spectra examples).

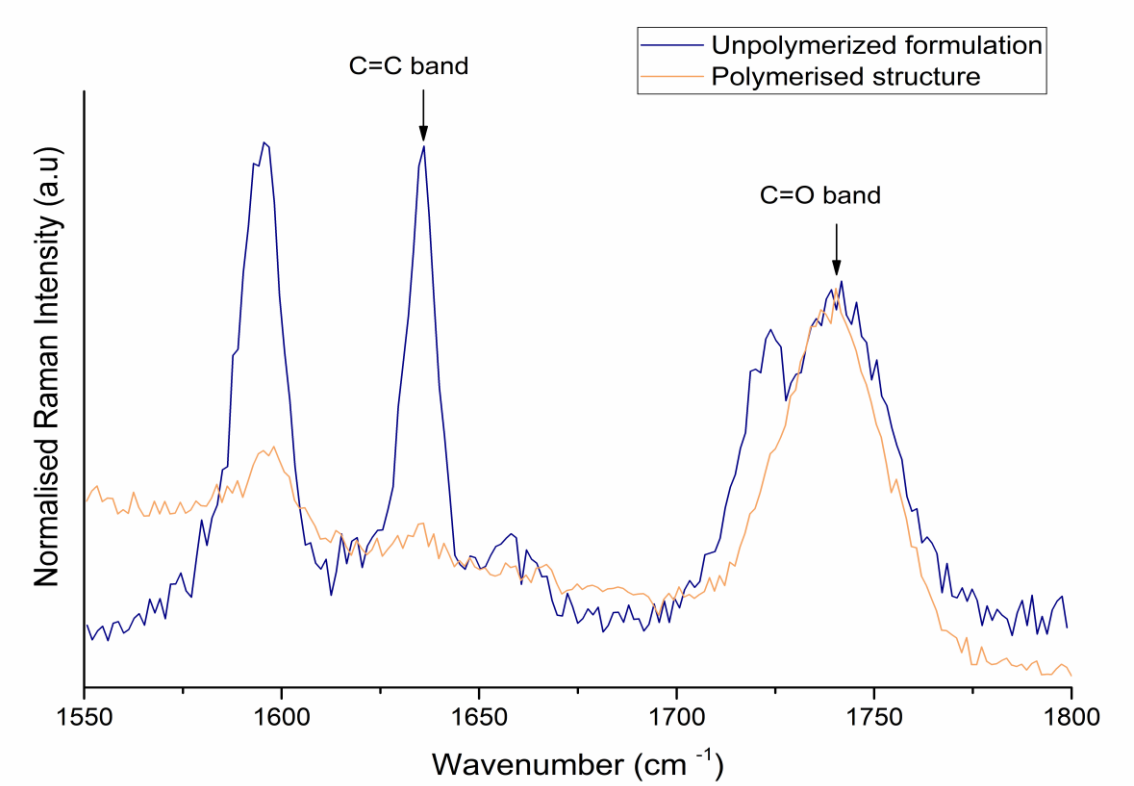



**Figure 4.3. Raman spectrum of PTMCA+PEGDA 1:2 molar ratio formulation before printing (dark blue) and spectrum of the 2PP printed structure with that formulation (orange) showing the sharp decrease in C=C band after polymerisation while the C=O band does not change as it does not participate in the reaction. See RVG % calculated from this spectra in Table 4.4.**

To study and compare the RVG of structures produced with various mono-acrylate materials + PEGDA, rectangular block structures were produced *via* 2PP using formulations defined in **Table 4.1**. From these mixtures, eDEGA + PEGDA 1:2 molar ratio and LA + PEGDA 1:2 and 1:8 molar ratio did not allow successful printing.

However, formulations 5, 6, 7, 10, and 11 that had higher molar ratios of PEGDA added to eDEGA or LA, did allow successful manufacturing. All the samples were printed using a common set of printing parameters (25 mW laser power, 10 mm/s writing speed), following the methodology described in section **3.3.1.6.1**. The parameters selected for manufacturing were the same for all structures to take into account the effect that introducing mono-functional materials and higher molecular weight oligomers (i.e. PTMCA) would have on the RVG % and reduce the influence of other possible variables. For comparison, similar blocks were also manufactured from 100 % PEGDA, i.e. a reactive monomer only formulation. However, at a processing power of 25 mW the 100 % PEGDA formulation did not polymerise and manufacture structures, hence a higher laser power of 40 mW was used in this case.

Formulations 12 to 19 were also used to manufacture structures but will be discussed later in this section when addressing the RVG of formulations of mono-acrylate materials combined with TCDMDA or BPAEDA (see **Table 4.5** and the discussion that follows).

Raman results from the PTMCA + PEGDA manufactured structures showed that increasing the concentration of PTMCA in the formulation led to higher RVG levels being achieved. For example, structures printed with only PEGDA have a RVG of around 70 %, while structures printed with Formulation 1, **Table 4.1** (i.e. 1:2 molar ratio) have RVG values of up to 89 %. Meanwhile, the RVG results from structures manufactured with certain eDEGA+PEGDA (1:8, 1:20, 1:46 molar ratios) and LA+PEGDA (1:20, 1:46 molar ratios) formulations that had high concentrations of PEGDA, were found to be similar to RVG from samples printed with only PEGDA. Although they showed small increases or decreases in RVG compared to only PEGDA, those were not as significant as the ones obtained with the PTMCA oligomer. The mean RVG values for these formulations are reported in **Table 4.4.**

**Table 4.4. RVG values (*n* = 3) ± Standard Deviation (SD) of printed structures using 2PP formulations prepared with PEGDA, PTMCA+PEGDA, eDEGA+PEGDA and LA+PEGDA at different concentrations.**

| Formulation number | Formulation | Molar Ratio | RVG % | SD |
|---|---|---|---|---|
| 1 | PEGDA | - | 70.3 | 1.41 |
| 2 | PTMCA + PEGDA | 1:02 | 89.5 | 1.29 |
| 3 | PTMCA + PEGDA | 1:08 | 82.5 | 0.26 |
| 4 | PTMCA + PEGDA | 1:20 | 74.3 | 2.68 |
| 5 | eDEGA+PEGDA | 1:08 | 77.2 | 5.68 |
| 6 | eDEGA+PEGDA | 1:20 | 72.6 | 4.15 |
| 7 | eDEGA+PEGDA | 1:46 | 71.7 | 3.5 |
| 8 | LA+PEGDA | 1:20 | 65.1 | 4.49 |
| 9 | LA+PEGDA | 1:46 | 70.5 | 2.65 |

These results demonstrated that adding low molecular weight monoacrylate monomers to PEGDA, did produce changes in the RVG % observed. The hydrophobic LA defined a slight reduction in RVG, whilst the hydrophilic eDEGA produced a minor increase. It was also defined that none of these trends were statistically significant. The difference in behaviour of apparent trends was attributed to the potential phase separation of the LA limiting its ability to copolymerise. In contrast, addition of the PTCMA macromonoer did produce a significant and statistically meaningful increase in the level of RVG % observed.

Thus, comparing the addition to PEGDA of the oligomeric PTCMA and monomeric eDEGA and LA reagents indicated that the former should be able to produce viable multi-material structures over a wide range of PEGDA concentrations, where a reduction in potential post-reactive groups may also result from this addition. Meanwhile, the monomeric reagents may only be co-processable in multi-material formulations containing high concentrations of PEGDA.

Thus, it was hypothesised that these results were related to the molecular weight of the macromer. Previous reports for diacrylate monomers defined that higher numbers of repeat units between the unsaturated reactive groups led to higher degrees of conversion, due to a decrease in cross-link density. Furthermore, it was proposed that this allowed for more mobility within the system, allowing for more opportunities for vinyl groups to come into close proximity [56]. Thus, it was proposed that this effect was also present in the formulations with macromeric monoacrylate materials, resulting in the longer chain of the macromer being responsible for its effect on RVG data of its multi-material formulations. This conclusion was supported by the experimental data, where Formulation 1 (PTMCA+PEGDA), **Table 4.1**, which has the highest quantity of monoacrylate macromer (M1:M2 = 1:2) and thus would have the lowest cross-link density, led to the highest RVG when compared to Formulations 2, 3 and 100 % PEGDA.

These results are of significant importance to the development of 2PP processing. It has been previously reported in the literature that multi(meth)acrylates resins are the preferred choice in 2PP, because they typically exhibit higher reaction rates than mono functional acrylates and produce stronger resultant cross-linked networks [56]. However, having the possibility to process monoacrylates with high RVG would significantly expand the library of reagent materials and multi-material combinations available for this technique. Being able to use monoacrylates would also reduce the number of steps needed to synthesise 2PP materials, as it is more complex to synthesis a multi-functional monomer.

The high RVG levels could also make the resultant materials more suitable for bio-applications, as they would have less risk of leaching uncured materials or secondary interactions with post-reactive C=C functionalities than other multi(meth)acrylates, such as those that typically result in <50 % RVG [10]. Finally, the ability to vary the cross-link density by controlling the macromeric monofunctional monomer concentration within the resin will also allow tuning the mechanical properties of the printed samples [120].

The substantial levels of reactivity of PTMCA with PEGDA could also be related to the molecule's polarity. The results from the eDEGA and LA suggested that the polarity potentially did matter with low molecular weight monomers, with respect to the level of reactivity. However, the data did not show a statistically meaningful trend and so this data could only be used as indicative. When the potential influence of these polarities with respect to phase separation within the final structure were reviewed, it was highlighted that there was a potential credible link to the $\chi$ parameter for these low molecular weight monoacrylates. The $\chi$ parameter of the eDEGA+PEGDA combination was 0.012 whilst that of LA+PEGDA was 0.446 indicating that the latter has a much greater potential to phase separate and so isolate the initiator into one of the domains, reducing the polymerisation of one of the monomers.

Comparing $\chi$ parameter of the eDEGA case with that of PTMCA highlighted that the $\chi$ of PTMCA+PEGDA was 0.08, very similar to the of the eDEGA case and suggesting limited phase separation. However, a significantly higher RVG percentage was observed for the macromer, an observation that required further investigation.

Thus, to investigate if this higher molecular weight characteristic contributed in general to a mechanism that enabled improved reaction of a mono-functional species with di-functional monomers in 2PP, further experiments were conducted by preparing new multi-material formulations. In these, TCDMDA was formulated with both PTMCA and

BPAEDA in the molar ratios stated in **Table 4.1**. The TCDMDA (304 g/mol) and BPAEDA (362 g/mol) monomers are both hydrophobic diacrylates that are of a similar molecular weight to the PEGDA (250 g/mol) used in this study. All formulations were tested in 2PP system using the previously optimised parameters (i.e 25 mW laser power, 10 mm/s writing speed). Also, the $\chi$ parameters of the BPAEDA+TCDMDA and PTMCA+TCDMDA mixture were similar, 0.207 and 0.211 respectively, thus we should expect similar phase separation behaviour from both these formulations. Thus, any change in RVG values was likely to be related to the molecular weight. Again, the formulation that was successfully printed were subjected to Raman spectroscopy and their RVG data are represented in **Table 4.5.**

The RVG data from samples produced with BPAEDA+TCDMDA and 100 % TCDMDA formulations represent the use of low molecular weight hydrophobic diacrylate monomers. The use of BPAEDA combined with TCDMDA does not show a significant increase either when compared to RVG results of the structures manufactured with TCDMDA alone. All three formulations show around very low levels of RVG (~30 %) compared to the PEGDA equivalents. This indicates that the polarity/hydrophobicity of the diacrylate monomers also does not influence significantly the mechanism that enables the reactivity within multi-material formulations as they both have similar LogP values in the 4.2 – 4.4 range (see **Table 4.2**). Rather, the rigidity of these diacrylate structures, compared to that of PEGDA, was thought to dominate these results, making it harder for the vinyl groups to come into close enough proximity to react as the 3D structure becomes more developed. Meanwhile, comparing this data to the RVG levels exhibited by samples manufactured by adding PTMCA to TCDMDA in molar ratios up to 1:46, results in RVG increases of 10 % to 50 %, depending on the molar ratio applied. Furthermore, the RVG value from PTMCA+TCDMDA 1:2 molar ratio structures (~83 %) is similar to that of the PTMC+PEGDA 1:2 (~90 %) molar ratio manufactured structures. The RVG value of

PTMCA+BPAEDA 1:2 molar ratio structures (~68 %) is also significantly high when compared to RVG results of structures manufactured with very low levels of PTMCA (e.g. PTMCA+BPAEDA 1:20 molar ratio formulation) or BPAEDA + TCDMDA mixtures. The slightly lower RVG achieved by the mixtures of PTMCA with TCDMDA or BPAEDA compared to PTMCA+PEGDA mixtures was again attributed to their more rigid molecular structure compared to PEGDA [58, 59]. This was supported by the fact that samples manufactured with only TCDMDA (30 % RVG) also exhibited levels of reactivity significantly lower than PEGDA alone (70 % RVG). This rigidity would influence the mobility in the system and affect the cross-link density. Therefore, in all types of multi-material formulations with PTMCA the trend is similar, with a higher RVG % the more PTMCA is added to the monomers. This supported the conclusion that the main influence over their reactivity is related to the molecular weight and molecular flexibility of the monoacrylates, not their polarity/hydrophobicity as PTMCA also has LogP values in the 4.2 – 4.4 range.

**Table 4.5. Mean RVG values (*n* = 3) ± SD of printed structures using 2PP Formulations prepared with TCDMDA, PTMCA + TCDMDA, TCDMDA + BAEDA and PTMCA + BPAEDA at different concentrations.**

| Formulation number | Formulation | Molar Ratio | RVG % | SD |
|---|---|---|---|---|
| 1 | TCDMDA | - | 29.5 | 4.50 |
| 2 | TCDMDA + UV | - | 36.7 | 3.00 |
| 3 | PTMCA + TCDMDA | 1:02 | 84.6 | 1.52 |
| 4 | PTMCA + TCDMDA | 1:20 | 69.2 | 5.77 |
| 5 | PTMCA + TCDMDA | 1:46 | 39.9 | 4.64 |
| 6 | PTMCA + BPAEDA | 1:02 | 68.4 | 3.83 |
| 7 | PTMCA + BPAEDA | 1:20 | 22.4 | 2.75 |
| 8 | BPAEDA + TCDMDA | 1:02 | 25.0 | 6.11 |
| 9 | BPAEDA + TCDMDA | 1:20 | 34.5 | 8.37 |

To further investigate the importance of monomer mobility in achieving high levels of 2PP reactivity, the influence of post-polymerisation processing was also investigated. Several TCDMDA structures were selected and subjected to ultra-violet (UV) post-treatment after printing. This was conducted to observe if any vinyl groups that were not reacted during 2PP would further react under UV irradiation. Raman spectroscopy was performed on those samples post the UV treatment. The Raman results did not show a statistically significant increase in RVG following post-treatment. This data suggested

that the lack of mobility within these structures prevented further reaction and highlighted the importance of this characteristic to obtain high RVG values. Thus, the successful methodology that allowed to manufacture structures containing TCDMDA with RVG >50% was with the PTMCA multi-material formulations. Besides higher RVG, printing TCDMDA or BPAEDA with PTMCA could allow to tune mechanical properties of the final structures, as PTMCA is both more flexible than the monomers and its presence reduced the cross-link density within the final material [40, 121].

### 4.2.2 The effect of varying printing parameters on Reacted Vinyl Group Reactivity

**Acknowledgment:** The effective laser power model development and effective laser power calculations were carried out by Dr Lyudmila Turyanska (University of Nottingham).

Besides the materials and their concentration used in 2PP formulations as previously described, the printing parameters could also influence the RVG of the manufactured structures. The main parameters that can be varied during 2PP printing are laser power and writing speed. It has been described in the literature that the applied laser power during printing can influence the amount of cross-linking (degree of conversion) within the voxel, with increasing laser powers producing structures with higher RVG (degrees of conversion) values [10]. It has also been reported that the laser power also influences the voxel size, with their size growing as the laser power increases. As a result of this, voxels will overlap at certain laser powers. Therefore, both laser power and voxel overlap could influence the RVG [10].

To study the influence of the laser power and voxel overlap on the RVG, the following experiment was performed. Cuboids were manufactured with the same formulation (Formulation 3, **Table 4.1**) using specific hatching and slicing distances (0.2 µm, 0.4 µm

respectively), a fixed writing speed (10 mm/s), and a laser power varying from 20 mW to 35 mW in 5 mW increments. The RVG values for the structures produced at different laser powers are shown in **Figure 4.4**.

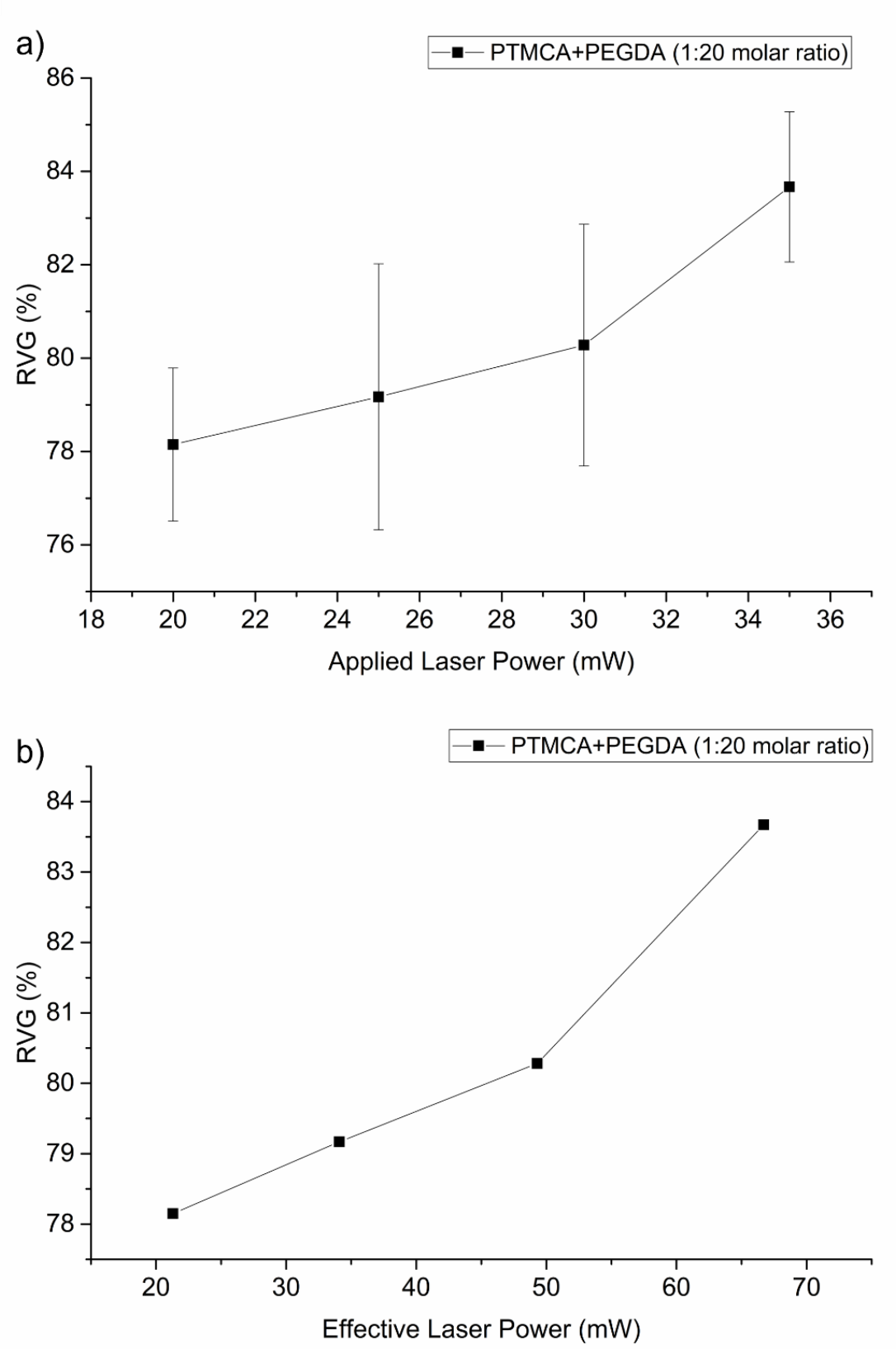



**Figure 4.4. a) RVG values for rectangles manufactured with the same formulation but at different applied laser powers (*n*=3, ± SD) b) RVG results from the same structures related to their effective laser power.**

In Figure 4.4 the applied laser power (Figure 4.4-a) is shown alongside the effective laser power (Figure 4.4-b). The latter is calculated using Equation 3.4 described in section 3.3.1.13 and defines the mW of power applied per voxel taking into consideration the level that they overlap in the cases where the hatching distance is smaller than the voxel radius. This is a similar process to that adopted by Thijs *et al* [122] to define the overlapping assumptions within the system.

The results show that the difference between effective and applied powers was larger for higher laser power. Therefore, at higher laser powers, the voxel sizes are bigger, and more overlapping takes place at the fixed hatch/slice parameters used. Additionally, the Raman data collected from these samples showed a slight increase in RVG value with each 5 mW increase in laser power. In total there was a 5 % increase between the cubes printed with 21 mW effective power and those printed with 66 mW. However, this increase was not statistically significant, despite the difference in energy applied.From these results it was concluded that the ratio between the two materials within the formulation had a bigger influence on RVG than the different effective laser powers used.

### 4.2.3 Evaluation of effective 2PP processing window for multi-material printing with monoacrylate PTCMA macromers

The processing window defines the range of parameters at which two-photon structures can be manufactured successfully. It determines to be the processing zone that lies between the threshold for the onset of polymerisation at low powers and the occurrence of “burning” at high powers for a specific 2PP resin. Typically, printing just above the polymerisation threshold enables manufacturing with the smallest feature size for that formulation, allowing high-resolution printing [11]. However, this is usually at the cost of long production times and reduced cure levels in the final object. Manufacturing samples with higher laser powers can help achieve higher RVG levels up to a certain

limit [10] and reduced processing times. However, above certain laser powers, the formulation will boil, and/or defects will appear within the structures which is often referred to as the burning threshold.

In this study, multi-material resin processability was investigated in two stages. First by printing a simple cube geometry (50 μm) using multi-material formulations and second by printing more complex structures with PTMCA + PEGDA in a 1:20 molar ratio formulation. This formulation was selected because it showed in section **4.2.1.2** that it can print simple structures with high RVG %, which could be useful if it is used in the future for bioapplications. Also, its high molar ratio of PEGDA lead to stronger cross-linking and potentially better mechanical properties compared to formulations that have a low concentration of PEGDA (i.e. PTMCA + PEGDA 1:2 molar ratio). **Figure 4.5** contains the SEM images of the structures that were produced in these experiments and indicated that this formulation resulted in the printing of structures with high mimic to the CAD models. It also showed that the formulation provides enough mechanical strength to manufacture complex structures like the buckyball without collapse.

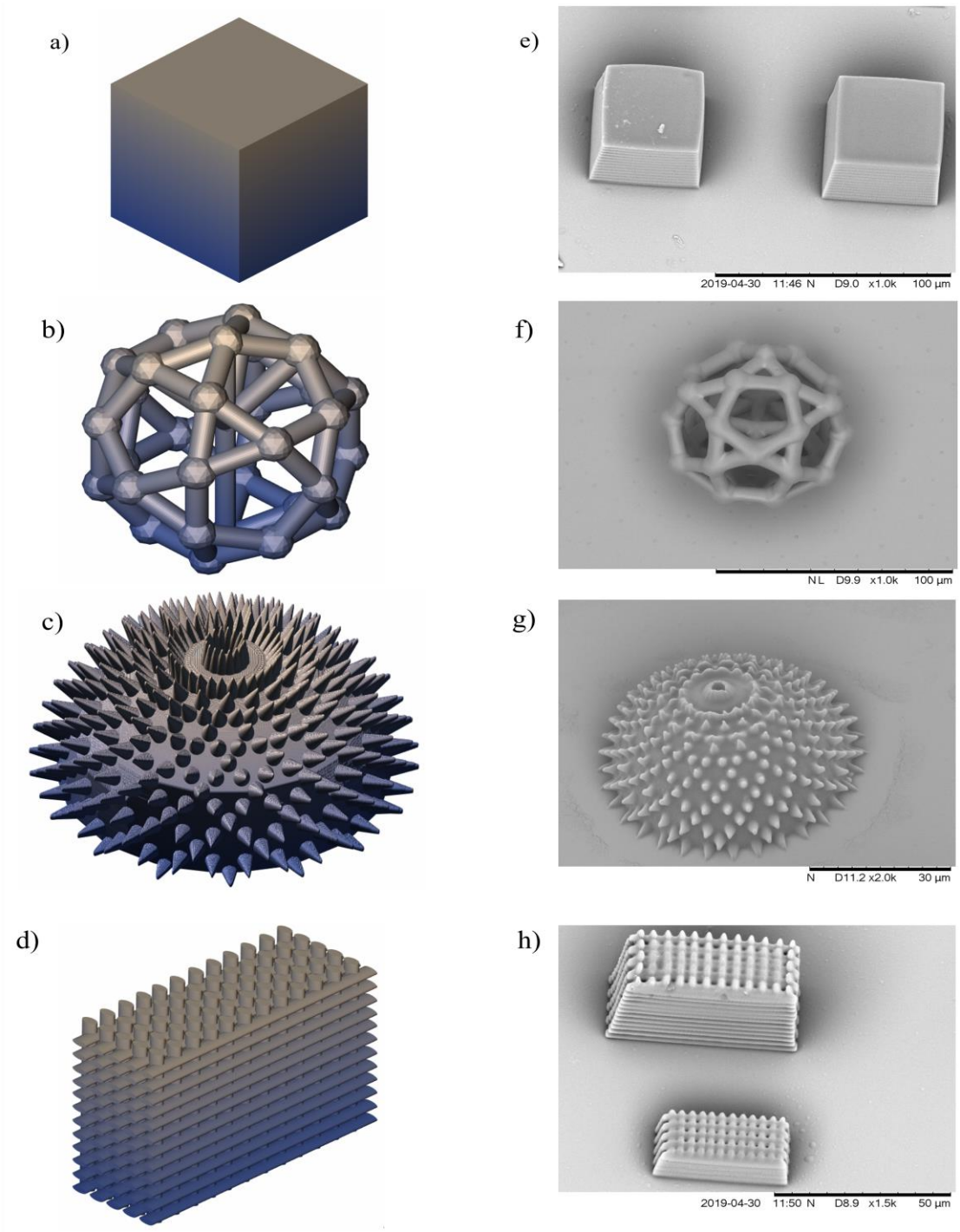



**Figure 4.5. a) to d) CAD models of cube, buckyball, spicky hemisphere, and woodpile. e) to h) associated SEM images from the manufactured structures by 2PP.**

The RVG % of the structures shown in **Figure 4.5 b-d** was of 70 % ± 3.3 while the RVG % for the cube (**Figure 4.5-a**) was 74 % ± 2.7, indicating that the different designs did not statistically significantly influence the material conversion and a high RVG level had been maintained in the multi-material manufacture of complex structures.

Multi-material formulations were also scanned at different laser powers and speeds to compare the polymerisation thresholds of PTMCA/PEGDA mixtures to that of pure PEGDA. The thresholds of the different formulations can be seen in **Figure 4.6**.

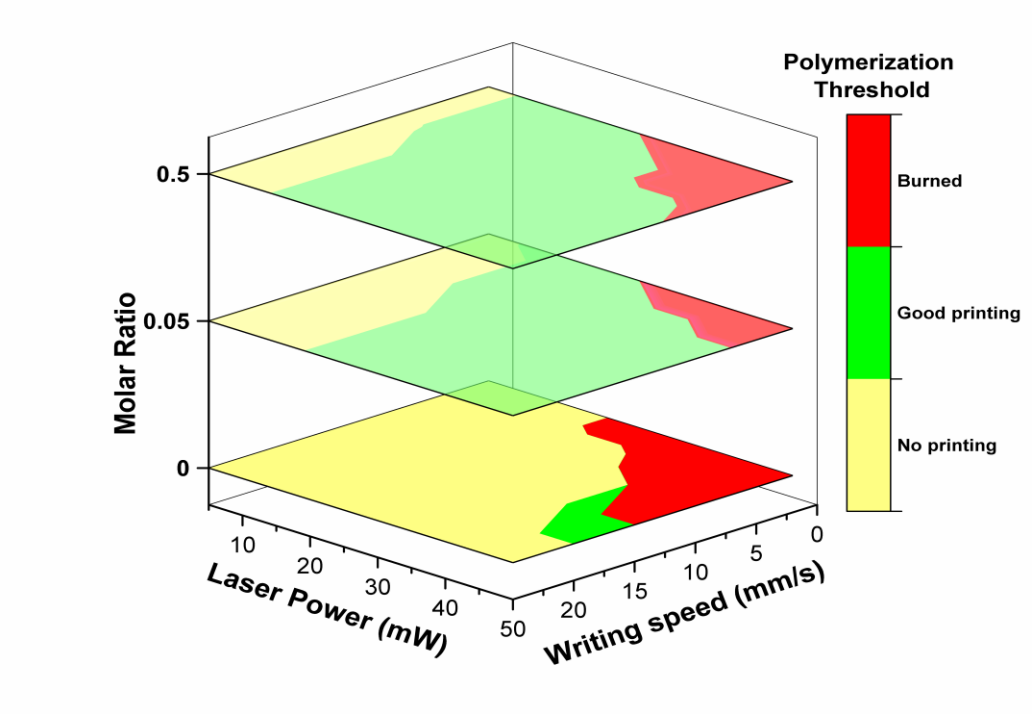



**Figure 4.6. Polymerisation thresholds of the following formulations: 100 % PEGDA (0), PTMCA+PEGDA 1:20 molar ratio (0.05) and PTMCA+PEGDA 1:2 molar ratio (0.5).**

The data presented above showed that PTMCA+PEGDA formulations had a significantly larger processing window than the mono-material (PEGDA) formulation. Both the 1:2 and 1:20 molar ratios expanded the process window by similar levels, allowing specimens to be manufactured with both lower and higher energy that PEGDA alone. This provides the potential to increase the definition that can be achieved by allowing lower energy

processing or increasing processing speed with both higher processing energy and writing speed. There may also be the possibility of retaining the fidelity of the structure at higher processing speeds due to the increased level of cure that is achieved with the macromer resins. It was hypothesised that the expansion of the processing window could also be related to the length and flexibility of the macromer chain, allowing for higher mobility in the system and increased chances of an encounter between functional groups in a similar fashion to how it would influence the RVG %, whilst at the same time reducing the amount of more volatile difunctional monomer that is in the resin.

The process window was also determined for the PTMCA + TCDMDA formulations. In this case (**Figure 4.7**), adding PTMCA to the diacrylate monomer also significantly expanded the range of successful processing parameters compared to the threshold of 100 % TCDMDA at all the molar ratios investigated. As in the PEGDA case, this broadening involved both a considerable reduction in the polymerisation onset and an increase in the burning threshold, with the exception of PTMCA + TCDMDA 1:2 molar ratio that significantly increased the burning threshold but also significantly increased the power needed for the polymerisation onset compared to the monomer. This indicates that there is a limit in the concentration of PTMCA that can be added to TCDMDA to obtain benefits at lower laser powers. This could be related to the rigidity and possibly different reactivity of the TCDMDA monomer in relation to the PTMCA, making the interaction between both materials more difficult than with PEGDA. It could also be related to the high viscosity of the PTMCA + TCDMDA 1:2 molar ratio system, which could restrict the mobility in the system making it harder for molecules to interact with each other. The mixtures with increased TCDMDA concentration (i.e., 1:8, 1:20, 1:46 molar ratios) are less viscous and the materials would have more mobility in the system, which could help PTMCA and TCDMDA molecules to interact with each other more easily even at low laser powers. Therefore, more energy density (higher laser powers in 1:2 molar ratio

formulation) or higher TCDMDA concentration (i.e with the polymerisation onset needing significantly lower energy density to start at 1:8 molar ratio) was needed to trigger cross-linking of both materials. This indicated that the physical properties and reactivities of both the macromer and the monomer have to be taken into account when developing 2PP formulations that target expanding the processing window of the resin.

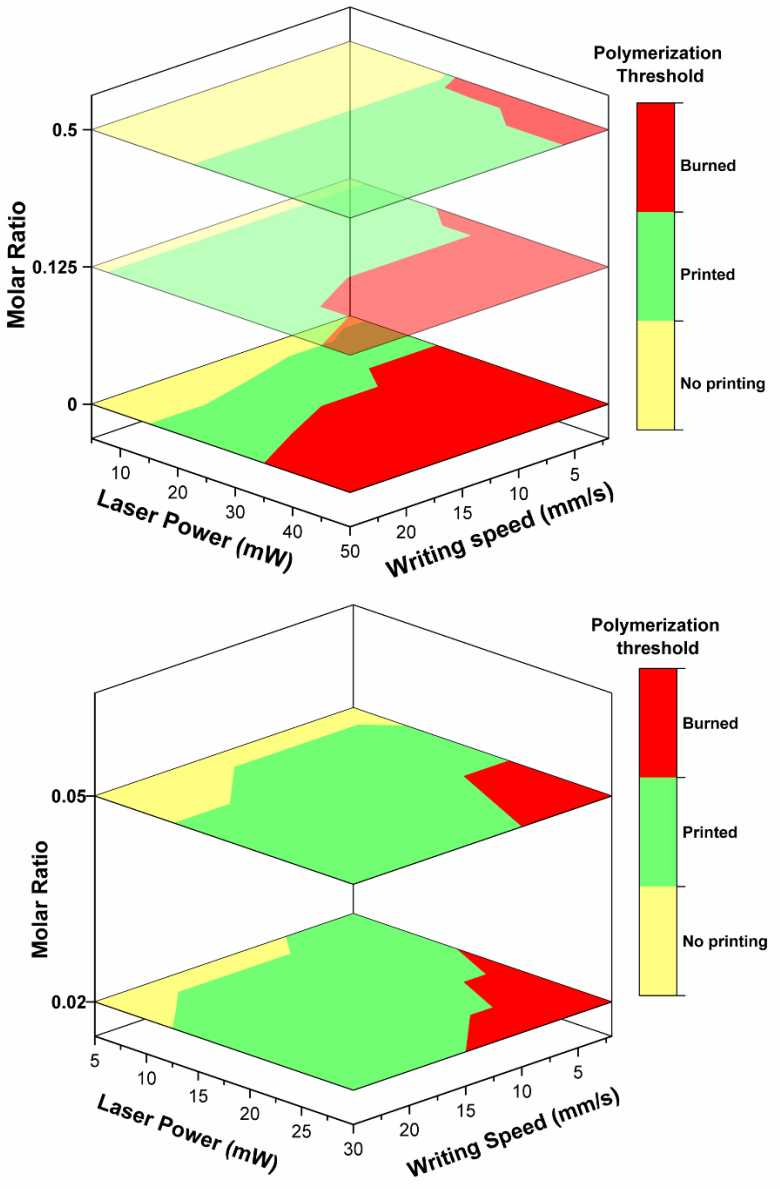



**Figure 4.7. Polymerisation thresholds of the following formulations: TCDMDA (0), PTMCA + TCDMDA 1:2 molar ratio (0.5), PTMCA + TCDMDA 1:8 molar ratio (0.125), PTMCA + TCDMDA 1:20 molar ratio (0.05), and PTMCA + TCDMDA 1:46 molar ratio (0.02),). The colours represent the same processing window zone as in Figure 4.6.**

### 4.2.4 Multi-material microstructure control and characterization

**Acknowledgment:** The ToF-SIMS and multivariate analysis of this section was carried out by Dr Gustavo Ferraz Trindade (University of Nottingham).

Rectangular cuboid structures printed with different concentrations of PTMCA and both PEGDA and TCDMDA were also analysed *via* optical or scanning electron microscopy (SEM). This analysis showed that the structures printed from homo-monomers or mixtures with low molecular weight monoacrylate reagent and PEGDA all exhibited a continuous single phase. However, certain cuboids printed with PTMCA + TCDMDA showed phase separation in their microstructure (**Figure 4.8**).

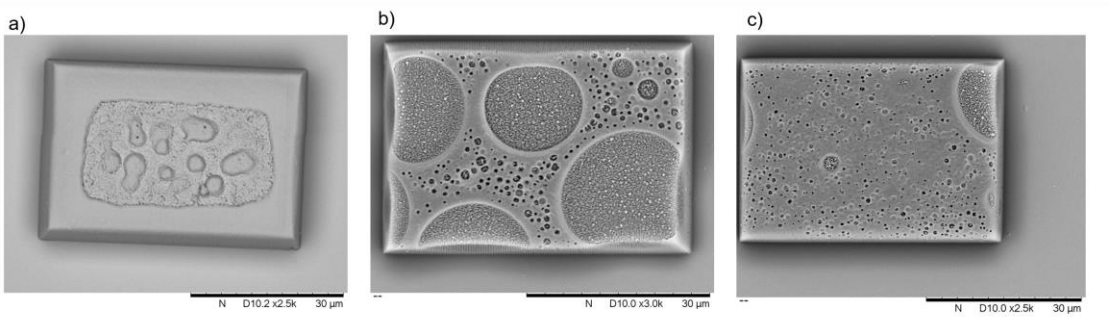



**Figure 4.8. SEM images of rectangles printed with PTMCA + TCDMDA 1:46 molar ratio formulation: a) structure printed in the first 20 min of the printing session with 25 mW laser power and 4 mm/s writing speed. b, c) rectangles printed after 20 min in the printing session with 15 mW laser power at 6 mm/s writing speed and 20 mW laser power at 10 mm/s writing speed respectively.**

Structures manufactured with PMTCA + TCDMDA in 1:2 and 1:8 molar ratio formulations showed a continuous single phase. However, samples printed with 1:20 and 1:46 molar ratio formulations exhibited phase separation. The observation of phase separation was noted to be consistent with the Flory – Huggins interaction parameters from **Table 4.3**. The calculations highlight that PTMCA + TCDMDA blend has a significantly higher $\chi$ parameter than PTMCA + PEGDA blend. As noted in previous reports by the authors [117], the development of phase-separated structures in AM is a

balance between reaction and phase separation kinetics. It was observed that the 1:2 and 1:8 molar ratio mixtures of PTMCA + TCDMDA were much more viscous than the 1:20 and 1:46, due to higher quantity of macromer present. Thus, it was proposed that this restricted the mobility of the molecules in the formulation, and the polymerisation kinetics dominated, leading to the reagents polymerisation, whilst they were still in a single phase. Meanwhile, the 1:20 and 1:46 molar ratios were less viscous due to their higher diacrylate monomer content, which allowed molecules to have more mobility and allowed phase separation kinetics to dominate. Thus, they phase-separated before the reaction could occur.

Consequently, two different printing experiments were performed with the same formulation, PTMCA + TCDMDA 1:46 molar ratio, to determine if the phase separation was altered when the processing parameters where modified. In these experiments, the PTMCA + TCDMDA 1:46 molar ratio was printed using a series of laser powers in the range from 5 mW to 30 mW directly as it was on deposited upon a coverslip, and a second series using the same conditions was left 20 min after deposition on coverslip prior to commencing polymerisation. This delay was to allow phase separation to occur. Polymerising directly after depositing the formulation onto the coverslip produced all the types of phase separation shown in **Figure 4.8.** In the first 20 min of printing, some cuboids had one material primarily concentrated in the middle of the rectangle, with the other material wrapped around it (**Figure 4.8-a**). Meanwhile, those that were manufactured after 20 min of printing exhibited structures with droplets of both materials mixed throughout the cuboid (**Figure 4.8 b-c**). The later in the print (>20 min) that the cuboid was processed, the smaller the droplets and the more “homogeneous” the mixture became. In the second set of experiments, the same conditions were used with the exception of leaving the formulation for 20 min after deposition on the coverslip instead of starting the print right away. However, printing under the same conditions 20 min after

deposition on the coverslip only produced rectangles with the type of phase separation shown in **Figure 4.8.b-c**, with none of them showing the pattern present in the structure shown in **Figure 4.8.-a**. This indicated that time, which allowed phase separate kinetics to act, also influences the microstructure that can be obtained besides the concentration of the formulation and the printing parameters. No burning was observed while printing all three types of phase-separated structures, therefore the features observed on their surface were droplets of both materials from the formulation and were not products of burnt or damaged material by the laser.

Thus, it was demonstrated that by controlling either the reagent concentration or the processing parameters with formulations containing macromeric components, the microstructure of the multi-material composite can be controlled and guided to deliver differently assembled structures. By doing this, rectangular cuboids can be created where the PTMCA macromer concentrates in a domain in the centre of the structure going throughout the structure from top to bottom, while the TCDMDA monomer "wraps" around it (**Figure 4.8.-a**). Samples that have several circular domains of one material concentrated and scattered throughout the second material in the structure (**Figure 4.8-b**) can be obtained, alongside rectangular cuboids with less visible phase-separated domains (**Figure 4.8-c**).

This disposition and relative positioning of both materials into the printed rectangle from **Figure 4.8-a** was then confirmed by ToF-SIMS analysis (**Figure 4.9**), performed following the methodology detailed in section **3.3.1.12**.

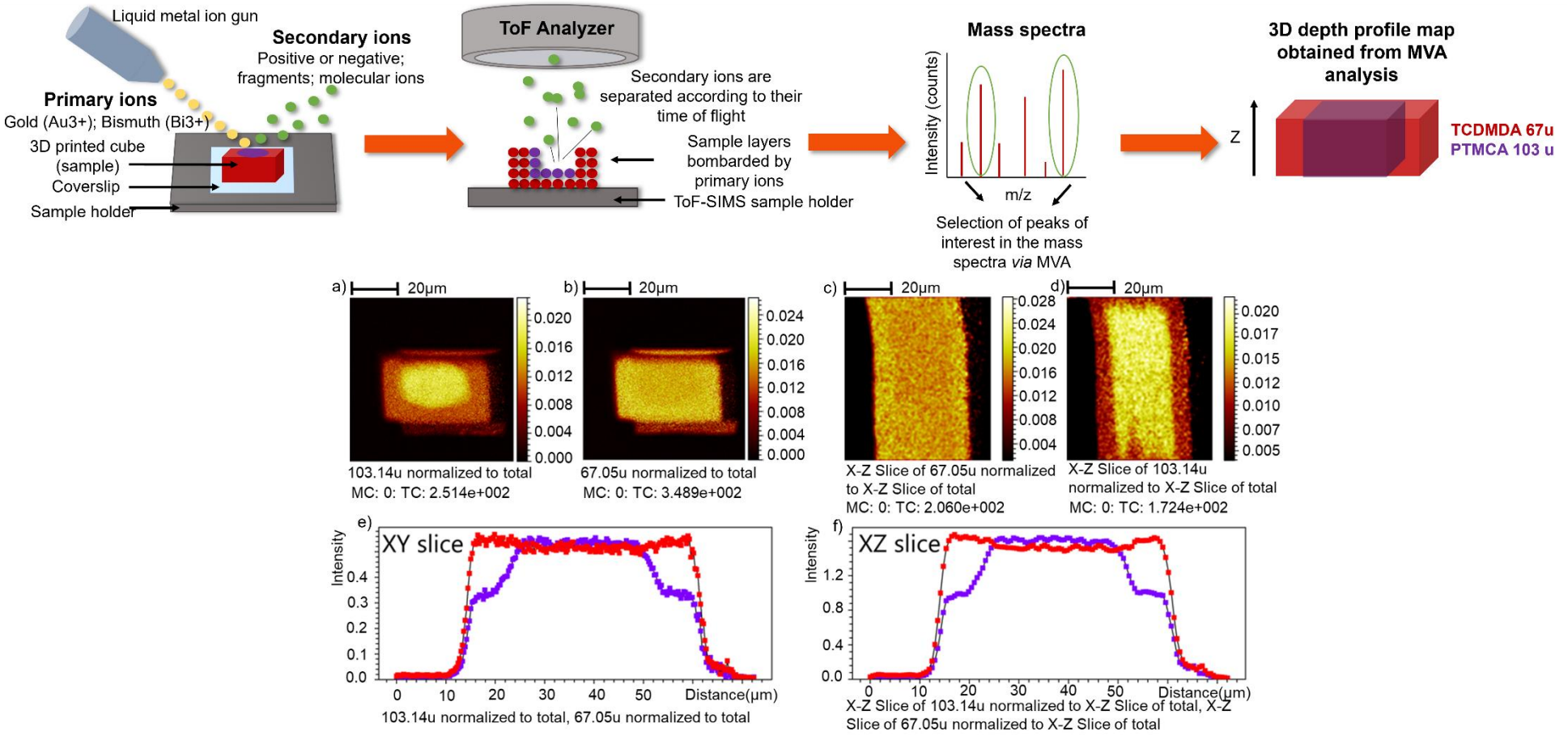



**Figure 4.9. Normalised intensities of PTMCA (103 u) and TCDMDA (67 u) ions throughout the manufactured structure a) Surface view of PTMCA intensity (displayed on Y axis, from low (black) to high (yellow) b) Surface view of TCDMDA intensity c) Depth view of TCDMDA intensity d) Depth view of PTMCA intensity e) Ion intensity of both materials through the *xy*-plane f) Ion intensity of both materials through the *xz*-plane. MC = Maximal counts in one pixel. TC = Total counts in the image. MVA = Multivariate analysis.**

The positive secondary ions characteristic of the two materials were selected by performing multivariate analysis (MVA) on the mass spectra obtained from sample analysis (see section **3.3.1.12.3** for methodology). The peaks selected through MVA were also present in the pure PTMCA and pure TCDMDA samples, indicating that the MVA had correctly selected representative peaks of each material. The secondary ion of the macromer ($[C_4H_7O_3^+]$, 103 u) was detected mainly in the centre of the rectangle going from the surface of the structure to the bottom, as can be seen in the *xy*- and *xz*- plane images from ToF – SIMS analysis in **Figure 4.9.** Meanwhile, the secondary ion of the diacrylate monomer ($[C_5H_7^+]$, 67 u) was mainly present in the corona around the PTMCA domain. While both materials could be detected throughout the whole rectangle, they were each strongly concentrated in these highlighted defined areas. These results supported the visual phase separation previously detected in **Figure 4.8-a** and helped to better understand the disposition of the materials and their phase separation kinetics during manufacturing.

To obtain further information with higher resolution regarding the phase separation, TOF-SIMS analysis could be combined with Atomic Force Microscopy (AFM). ToF-SIMS has a lateral and depth resolution of 100 nm and 1 nm, respectively, while AFM shows a lateral resolution ~30 nm and a vertical resolution of ~0.1 nm. AFM can also add information about the topography and the roughness of the sample and complement it with the ion information provided by TOF-SIMS [131]. Ruiz-Cantu *et al.*[125], for example, used both techniques to analyse the microstructure of drug eluting implants obtained via inkjet printing, showing both continuous and phase separated microstructure depending on the formulation used. By combining in future work both techniques, a deeper understanding of the phase separation presented in this chapter could be obtained. And other microstructures like the ones presented in Fig 4.8 b) and c) or samples that showed continuous phase in SEM analysis, could also be analysed via TOF-SIMS and

AFM. This would allow a better and broader understanding of the microstructure profiles obtained with the multi-material mixtures.

The phase-separated microstructures discussed on PTMCA + TCDMDA structures were not visible on cuboids manufactured with the different PTMCA + PEGDA formulations. To assess that both materials of the PTMCA + PEGDA multi-material formulations were incorporated into the manufactured structures during printing and their disposition throughout the structures, ToF-SIMS analysis was performed on the following samples (see data in **Figure 4.10**):

a) 50 µm cube printed with PEGDA.
b) 50 µm cube printed with PTMCA + PEGDA 1:20 molar ratio.
c) 50 µm and 20 µm cubes printed with PTMCA + PEGDA 1:2 molar ratio.
d) A drop of 100 % PTMCA dissolved in acetone polymerized using UV light, this sample format was adopted because the macromer cannot be printed on the 2PP system on its own due to its very high viscosity.

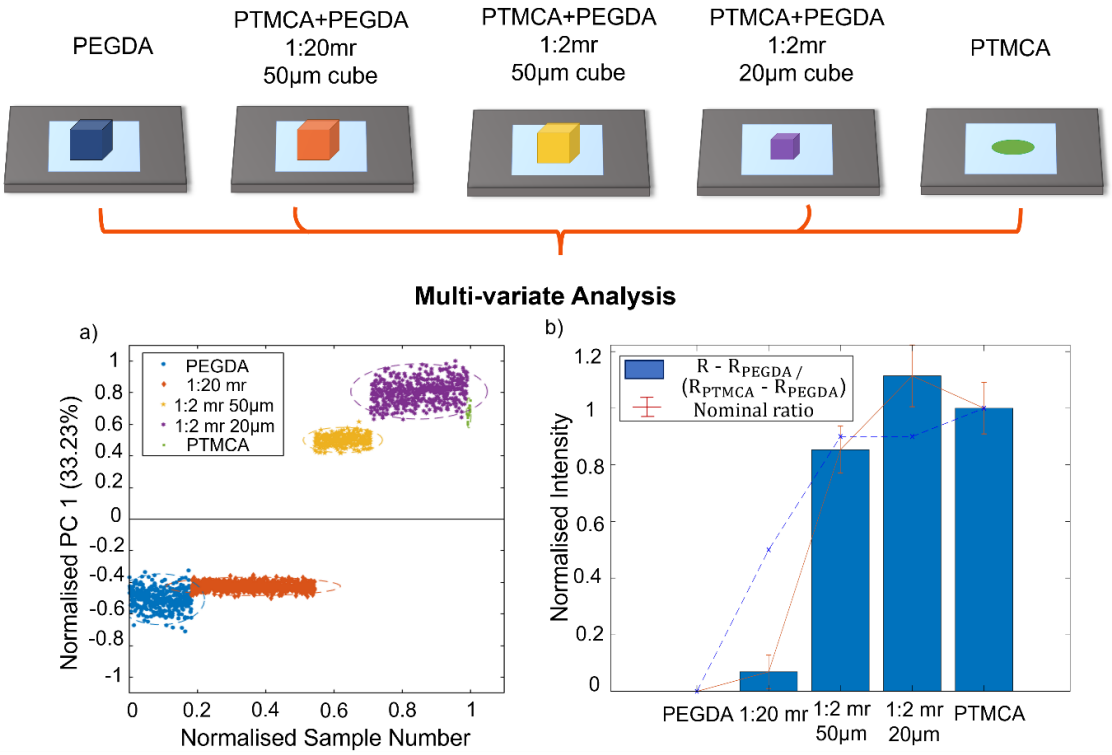



**Figure 4.10. ToF-SIMS analysis of 3D printed cubes printed with 100% PEGDA, PTMCA + PEGDA 1:20 molar ratio, PTMCA + PEGDA 1:2 molar ratio formulations. The 5th sample was a droplet of PTMCA dissolved in acetone and UV cured on a coverslip. Graph a) displays the normalised intensities of the samples. Graph b) shows the normalised intensity of the PTMCA peak in relation to the PEGDA peak on each sample. R represents the normalised intensity of each sample while $R_{PTMCA}$ (assigned as 1) and $R_{PEGDA}$ (assigned as 0) represent the normalised intensities of each material.**

The positive secondary ions of PTMCA and PEGDA samples were detected again via MVA analysis. The selected peaks were confirmed to be representative of the materials by detecting their presence in analysed samples of 100% PEGDA and 100% PTMCA. The characteristic positive secondary ion for PTMCA was [$C_4H_7O_3^+$], 103.05 u and for PEGDA it was [$C_2H_5O^+$], 45.03 u. Cubes of the same size (50 µm) but manufactured with different molar ratio of PTMCA and PEGDA were analysed to observe the influence of the concentration on the distribution of both materials throughout the structure.

Cubes printed with the same molar ratio (i.e 1:2 molar ratio) but of different sizes were also included in the experiment to study if the volume of the structure would influence

the material disposition through it. When the multi-material manufactured samples were analysed, the presence of both secondary ions were well dispersed throughout the samples. The intensity of the ions differed depending on the sample's formulations. In **Figure 4.10-a** the normalised intensity of the pure PEGDA ions are shown in blue colour on the bottom left of the graph while the normalised intensity of the pure PTMCA ions is shown in green at the top right of the graph. The normalised intensities of ions from the multi-material samples (i.e, red for 50 µm 1:20 molar ratio sample, yellow for 50 µm 1:2 molar ratio sample, purple for 20 µm 1:2 molar ratio sample) are situated between the signals of the normalized intensities of both pure materials. The normalised intensity obtained from cubes fabricated with PTMCA + PEGDA 1:20 molar ratio was closer to that of PEGDA samples, as it has a higher concentration of PEGDA, while the normalised intensities obtained from PTMCA + PEGDA 1:2 molar ratio cubes were closer to those of pure PTMCA, as they have a higher concentration of PTMCA in them. A similar trend could be observed in **Figure 4.10-b** when comparing the normalised intensity of the PTMCA ion ($R_{PTMCA}$ assigned as 1 when only PTMCA ions are detected) in relation to the PEGDA ion ($R_{PEGDA}$ assigned as 0 when only PEGDA ions are detected). The normalised intensity of 1:20 molar ratio 50 µm cube was < 0.2, indicating a high PEGDA concentration in the sample, while the normalised intensities of 1:2 molar ratio samples were > 0.6, indicating a high PTMCA concentration in the structures. The >1 value of the 20 µm 1:2 molar ratio cube was assumed to be caused by residual PTMCA material on top of the sample that might have not been properly cleaned with the GCIB ion gun..

The ToF-SIMS results indicated that both materials cross-linked during printing with an even distribution throughout the sample as would be predicted by the Flory-Huggins calculation in **Table 4.3**. This also indicated that the materials co-reacted during the printing in these formulations. The results also indicated that ToF-SIMS analysis might differentiate the molar ratios of the samples analysed when comparing them to the

normalised intensities obtained from structures manufactured with pure PEGDA or pure PTMCA.

## 4.3 Conclusions

The work presented in this chapter focused on multi-material printing for 2PP based on PTMCA macromer formulations. A new monoacrylate polymer was developed and it was 3D printed in multi-material formulations by mixing it with PEGDA or TCDMDA monomers. The presence of both macromer and monomer in the manufactured samples was confirmed by ToF-SIMS and the difference in molar ratios of the concentrations could also be detected with this technique. Formulations of different concentrations of PTMCA + PEGDA produced structures with homogeneous microstructure. Formulations of different concentrations of PTMCA + TCDMDA showed different behaviours during printing depending on the concentration and the processing parameters. Two formulations (1:2 and 1:8 molar ratios) printed homogeneous structures while the other two formulations (1:20 and 1:46 molar ratios) showed phase separation on the 3D printed rectangles. This was related to the domination of polymerisation or phase separation kinetics, depending on the molar ratio of the formulations. Even more, this phase separation and the microstructure created in the multi-material sample can be changed by modifying the processing parameters of the printing process. This allows to produce rectangles where TCDMDA concentrates on the edges while PTMCA concentrates in the middle creating a circle feature. The disposition of the materials in the microstructure was confirmed by ToF-SIMS. The phase separation behaviour between the different formulations could be related to the cohesive energy density of these blends, as their calculated Flory-Huggins interaction parameters showed that PTMCA + PEGDA formulations have a smaller $\chi$ value than PTMCA + TCDMDA formulations. This makes the latter more prone to immiscibility and phase separation.

The structures manufactured with these multi-material formulations show high RVG, with some of them reaching almost 90 %. When compared to RVG values of samples printed with just PEGDA or TCDMDA, which show around 70 % and 30 % RVG respectively, it can be seen that adding macromer to the monomers rises the RVG values by 20 % and 50 % respectively. The effect of applied and effective laser power on the RVG % was also studied in PTMCA + PEGDA cubes. However, the results indicate that their effect on RVG % is negligible and that the molar ratio between the two materials in the formulation has a much stronger influence on the increase of RVG %.

Another difference in printing multi-material formulations compared to just the diacrylate monomers was the broadening of the polymerisation and burning thresholds. These blends allowed for a significantly broader processing window parameter to be used for successful printing compared to the mono-material printing of just the monomers. This is beneficial as lower laser powers allow for higher resolution printing while higher laser powers and speed can allow for faster printing with more cross-linking.

## 4.4 Chapter Appendix: Supplementary Information

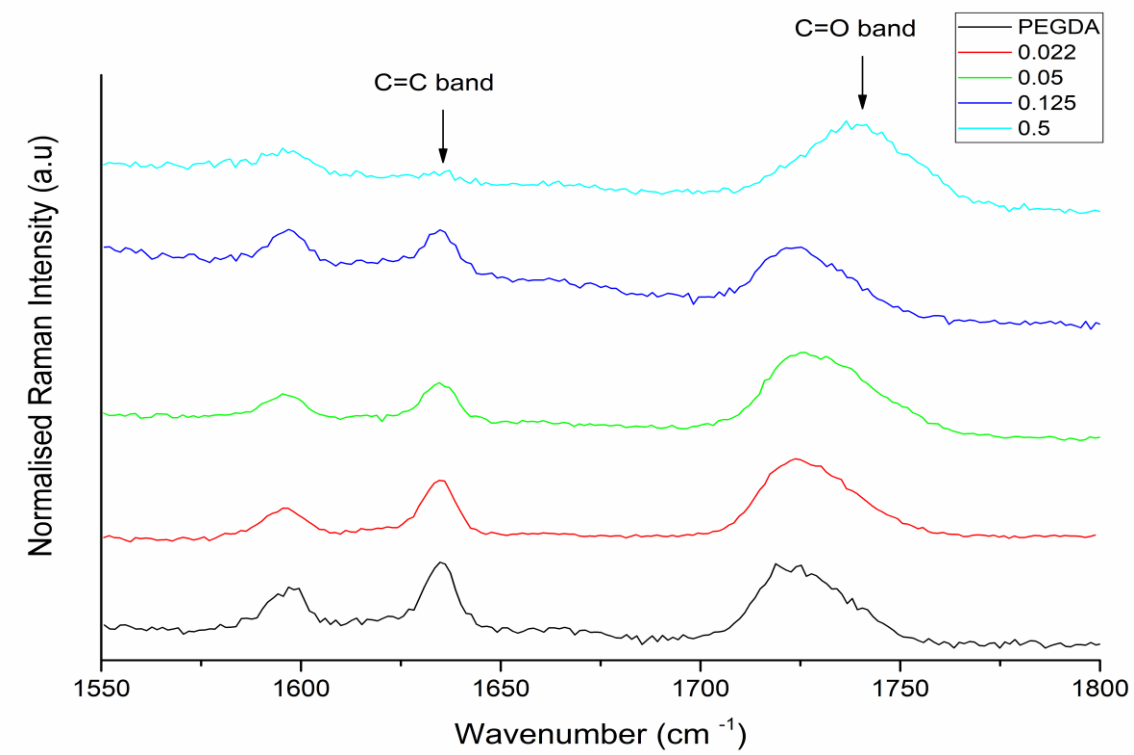



**Figure S4.1. Raman spectrum of 2PP manufactured samples with PEGDA and PTMCA + PEGDA formulations mixed at different ratios (black spectra for PEGDA, red for PTMCA + PEGDA 1:46mr, green for PTMCA + PEGDA 1:20mr, dark blue for PTMCA + PEGDA 1:8mr, and cyan for PTMCA + PEGDA 1:2mr) with C=C and C=O bands highlighted. The results show how the C=C band decreases the higher the PTMCA amount is in the formulation printed, with the highest conversion reached at 0.5 ratio.**

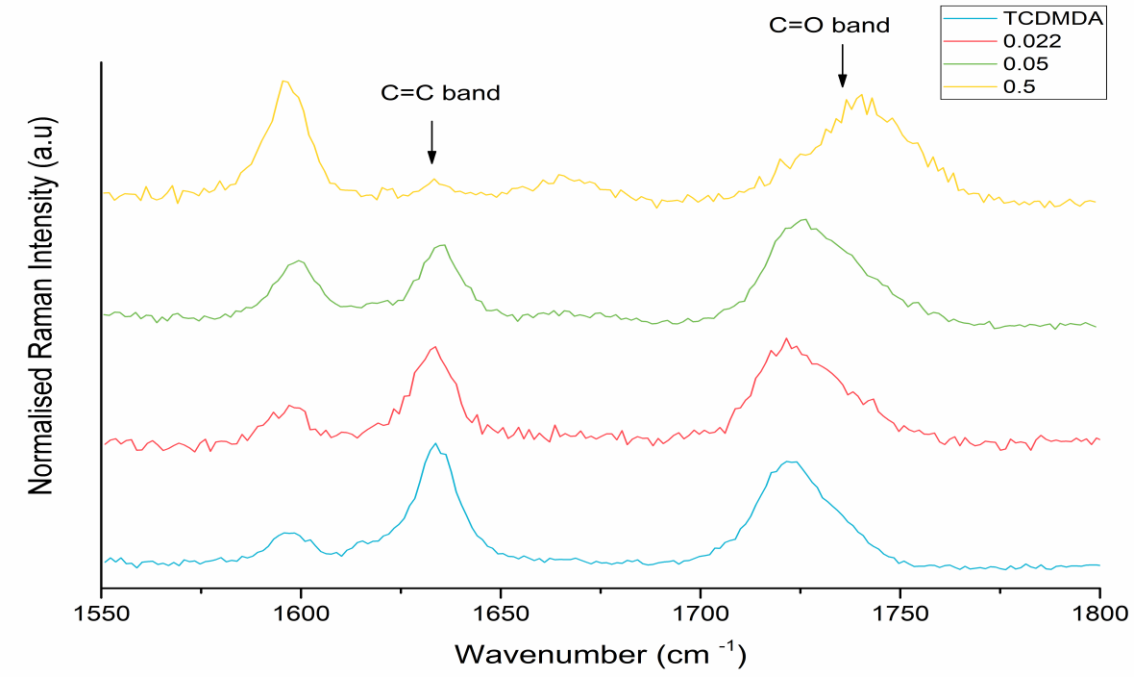


**Figure S4.2. Raman spectrums of 2PP printed specimens with TCDMDA, and PTMCA + TCDMDA formulations mixed at different ratios (X:TCDMDA in legend) with C=C and C=O bands highlighted. As in the previous figure, here the results also highlight the increase in RVG% as the PTMCA content in the formulation used for manufacturing increases.**

# 5 2PP multi-material printing of hyperbranched resins

## Acknowledgments

Part of this chapter has been adapted into a manuscript for publication: Konta, A.A, Stimpson, A., Goodwin, S., Touré, A., Trindade, F. G., Ruiz-Cantu, L., Alexander, C., Wildman, R., Irvine, D, J. Two photon multi-material printing of hyperbranched polymers with high reacted vinyl groups and threshold expansion. (Drafted).

## 5.1 Introduction

One of the most important characteristics that determine a resin's suitability for vat-photopolymerisation techniques such as 2PP is that it exhibits mobility in the system, allowing molecules to move and participate in the photopolymerization process. When processing with resins that contain polymeric materials, rather than just monomer, species with low glass transition temperature ($T_g$) are more suitable for this type of printing. The viscosity oligomer/polymer exhibits is also influenced by molecular weight and chain entanglement, with those exhibiting higher molecular weights and/or involving more chain entanglement tending to possess higher viscosities [123]. Lower viscosities are preferred in vat-photopolymerisation techniques as they allow functional groups to interact with each other via chain mobility, so increasing cure rates. They also allow for easier cleaning of uncured resin from the printed samples in the post-processing step. Materials with low viscosities can be produced as oligomers or branched polymers like

multi-arm stars and hyperbranched polymers [123]. The former properties are typically related to their low molecular weight, whilst the latter cannot chain pack so efficiently.

Hyperbranched polymers are highly branched molecules with multiple functional groups in their architecture [74]. As previously mentioned, their low chain entanglement, due to the "globular" nature of their molecular structures is responsible for the unexpectedly low viscosities that they exhibit. This allows materials with high molecular weights to be produced that still show significantly lower viscosities when in the hyperbranched form than materials containing similar monomer pendant group functionality but in the comparative linear form. This is important for 2PP because such high molecular weights would be too viscous to be processable in stereolithography techniques. Additionally, the hyperbranched polymers' high amount of photoreactive functional groups within the molecule (i.e., functional group density) has the potential to also help increase curing times [123]. Thus, the properties of hyperbranched materials make them an interesting option for UV curing applications and they have been applied in different fields like additives [77], coatings [78], or inkjet printing inks [74, 76, 124]. In these inkjet printing applications, different hyperbranched polymers have been used to study their influence on the curing process, which was observed to be faster than their linear counterpart. Their influence on polymer degradation during printing was also studied and it was shown that increasing chain branching above a critical value avoided degradation during printing as the polymer architecture would help it maintain its conformation and not be affected by the constrictional flow of the print head [75, 76].

Although several examples can be found of hyperbranched polymers used in additive manufacturing inkjet printing systems [76, 124], there are not many instances of these materials being used for vat-photopolymerisation techniques. One recent example can be found in the work of Ning *et al*. [125], in which hyperbranched polysiloxane is used to modify epoxy resins for stereolithography 3D printing. This study showed that the

addition of the hyperbranched polysiloxane to the epoxy resin at different concentrations improved the heat resistance of the resin. It also had an effect on the mechanical properties of the structures, with resins containing a 5 wt% loading of hyperbranched material shown to exhibit significant increases in the toughness of printed structures [125].

This example, along with the inkjet printing case, indicates that hyperbranched polymers could bring different advantages to AM. Such advantages range from faster printing through better curing to modifying mechanical properties. However, these materials have not yet been explored in the 2PP field. Therefore, the focus of this chapter was to develop new hyperbranched materials that could be optimised for 2PP use, expanding the library of the materials available for the technique in a new strategy and compared the use of these additives to those explored in chapter 4. Using hyperbranched polymers for 2PP could also help to process high molecular weight materials that in their linear counterpart would not meet the low viscosity characteristics that are ideal for this printing system. Thus, in this work, two hyperbranched materials were synthesised: Hyperbranched poly(ethylene glycol) diacrylate (HBpPEGDA) and Hyperbranched poly(Tricyclo [5.2.1.$0^{2,6}$] decanedimethanol diacrylate) (HBpTCDMDA). These materials were optimised for printing in 2PP in mono- and multi-material formulations and then structures were manufactured with them with the AM technique. To understand the influence of the hyperbranched materials on the degree of cure, the samples were analysed under Raman Spectroscopy to determine their reacted vinyl group (RVG) percentage. To study their effect on the formulation reactivity and the printing speed, the polymerisation threshold of the formulations was assessed and compared to those of their linear counterparts. The materials disposition throughout printed structures manufactured with multi-material formulation was investigated utilising ToF-SIMS analysis. This was performed to detect if ions characteristics of both materials were present in the sample. Finally, LIVE/DEAD cell viability tests were performed on scaffolds manufactured with

HBpTCDMDA and TCDMDA to observe if there was cytotoxicity difference between samples printed with the hyperbranched or linear version of the same material that showed significant differences in their RVG %.

## 5.2 Results and Discussion

### 5.2.1 Material characterization

**Acknowledgement**: The material synthesis and polymer characterization discussed in this section were performed by Dr Sophie Goodwin (HBpTCDMDA) and Dr Amy Stimpson (HBpPEGDA).

The hyperbranched polymers used in this chapter were synthesised via thermally initiated chain transfer polymerisation (CTP) using a 3-Mercaptopropionic acid thiol control transfer agent (3-MPA CTA) following the methodology described in section **3.3.1.3.** The mechanism of this reaction is explained in section **2.3** and is depicted in **Figure 2.8.**

The materials obtained with this type of synthesis and the schematic of the reaction can be observed in **Figure 5.1**:

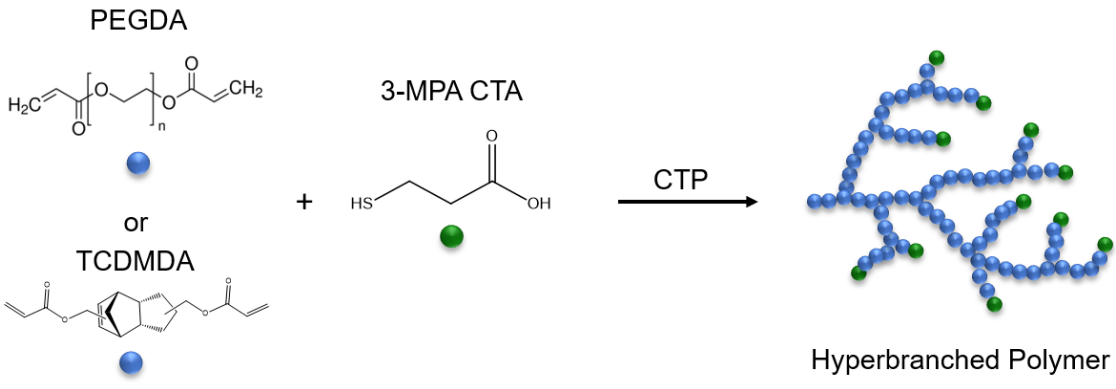



**Figure 5.1. Monomers and 3-MPA CTA were used for CTP synthesis to produce Hyperbranched materials. Blue spheres represent the monomer that will form part of the backbone of the polymer and the green spheres represent the CTA molecules that will be at the end of the polymer chain as functional groups.**

Depending on the monomer used for the synthesis, HBpPEGDA or HBpTCDMDA were obtained and were characterised as described in section **3.3.1.4**. The characterisation results regarding the hyperbranched materials can be seen in **Table 5.1**:

**Table 5.1. Summary of conversion, number average molecular weight ($M_n$), weight average molecular weight ($M_w$), dispersity (D) and yield.**

| Material | Conversion (%)[a] | Yield (%)[b] | $M_n$ (kDa)[c] | $M_w$ (kDa)[c] | Đ[c] |
|---|---|---|---|---|---|
| HBpTCDMDA | 60.0 | 121.9 | 3.31 | 12.92 | 3.90 |
| HBpPEGDA | 86 | 81 | 29 | 190 | 6.6 |

[a] Determined via H NMR [b] Determined gravimetrically [c] Determined via GPC

From the GPC results, we can observe a wide polydispersity of molecular weights, with a Đ of 3.9 for HBpTCDMDA and 6.0 for HBpPEGDA. This indicated that the branching of the monomers was successful as hyperbranched polymers show Đ > 3.0. The HBpTCDMDA polymer was precipitated as a very viscous liquid and due to the high volatility of the monomer, the samples could not be efficiently vacuum dried as any application of heat would lead to gelation. When preparing this material at small scale (aiming for 2 g instead of the 10 g prepared and analyzed in **Table 5.1**), overnight room temperature drying was sufficient to eliminate solvent whilst presenting a low gelation risk. This allowed yields of 84 % ± 10.1 to be obtained at small scale. However, when the process was scaled up and 10 g of HBpTCDMDA were produced, the overnight solvent evaporation process proved to be insufficient for all solvent to evaporate. This was the reason attributed to a polymer yield >100 % being recorded in **Table 5.1**. The material was not left to dry for longer due to the risk of gelation increasing with the greater length of time the material spends at room temperature.

In the case of the HBpPEGDA, the obtained material seemed to show visually less viscosity than HBpTCDMDA. This could have helped with the drying step, as although both materials were dried with the same process, the yield of HBpPEGDA polymer was <100 %. It was hypothesized that the potential lower viscosity of this material compared to HBpTCDMDA might have facilitated faster solvent evaporation. The results could also suggest a higher reactivity of the PEGDA monomer than the TCDMDA monomer, as the HBpPEGDA shows higher conversion, Đ (indicating more branching), and molecular weights than the HBpTCDMDA. This could indicate that more PEGDA reacted and converted into polymer and more branching was also obtained with this monomer than with TCDMDA.

### 5.2.2 Degree of conversion (quantity of reacted vinyl groups)

2PP formulations were prepared following the methodology detailed in section **3.3.1.5.2** with the following components: (a) hyperbranched polymers (HBP) alone, (b) a mix of HBP and a commercial monomer, and (c) just commercial monomers (see details of all formulations used in **Table 5.2.**).

**Table 5.2. 2PP formulations prepared with one or two materials at different concentrations, using 2% wt photoinitiator (Irgacure 369) in all of them.**

| **2PP Formulations** | **M1 wt% : M2 wt%** |
|---|---|
| TCDMDA | 100:0 |
| PEGDA | 100:0 |
| PEGDA + TCDMDA | 50:50 |
| HBpPEGDA + TCDMDA | 50:50 |
| HBpTCDMDA | 100:0 |

These formulations were tested on the 2PP printing system to observe if HBP were an adequate choice as a reagent from which to formulate 2PP resins and define any advantages they offered compared to benchmark linear commercial monomers.

The formulations shown in **Table 5.2** were used to manufacture 50 µm cubes (see section **3.3.1.6.1**) that were subject to analysed by Raman spectroscopy to determine the level of reacted vinyl groups (RVG) achieved after printing (see section **3.3.1.11.2**). The Raman spectra used for RVG % calculation can be seen in **Figure 5.2**:

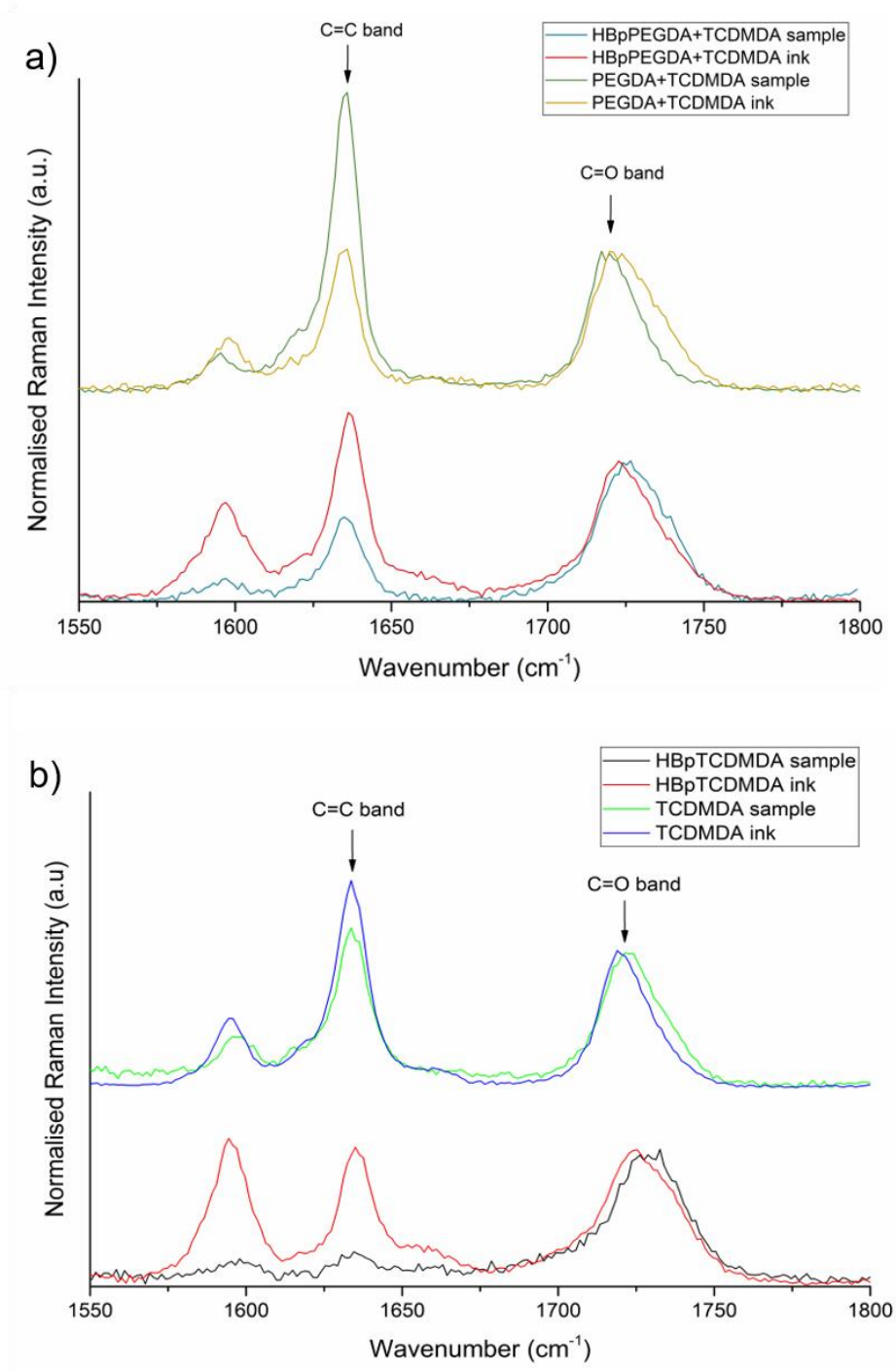



**Figure 5.2. Raman spectra of 2PP manufactured samples and the comparative un-polymerised formulations they were fabricated with. a) Blue (printed sample) and red (formulation) spectra were obtained from the HBpPEGDA 50 wt% + TCDMDA 50 wt% mixture. Green (printed sample) and yellow (formulation) spectra were obtained from the PEGDA 50 wt% + TCDMDA 50 wt% mixture. b) Blue (formulation) and green (printed structure) were obtained from TCDMDA monomer mixtures. Red (formulation) and black (printed sample) were obtained from the HBpTCDMDA mixture.**

All the spectra shown in **Figure 5.2** demonstrated a decrease in the C=C band after polymerisation while the C=O band did not change as that group does not participate in the polymerisation reaction. By measuring the area under these peaks and inputting this data into **Equation 3.3**, the RVG % was obtained for all the **Table 5.2** formulations. These results can be seen in **Figure 5.3**:

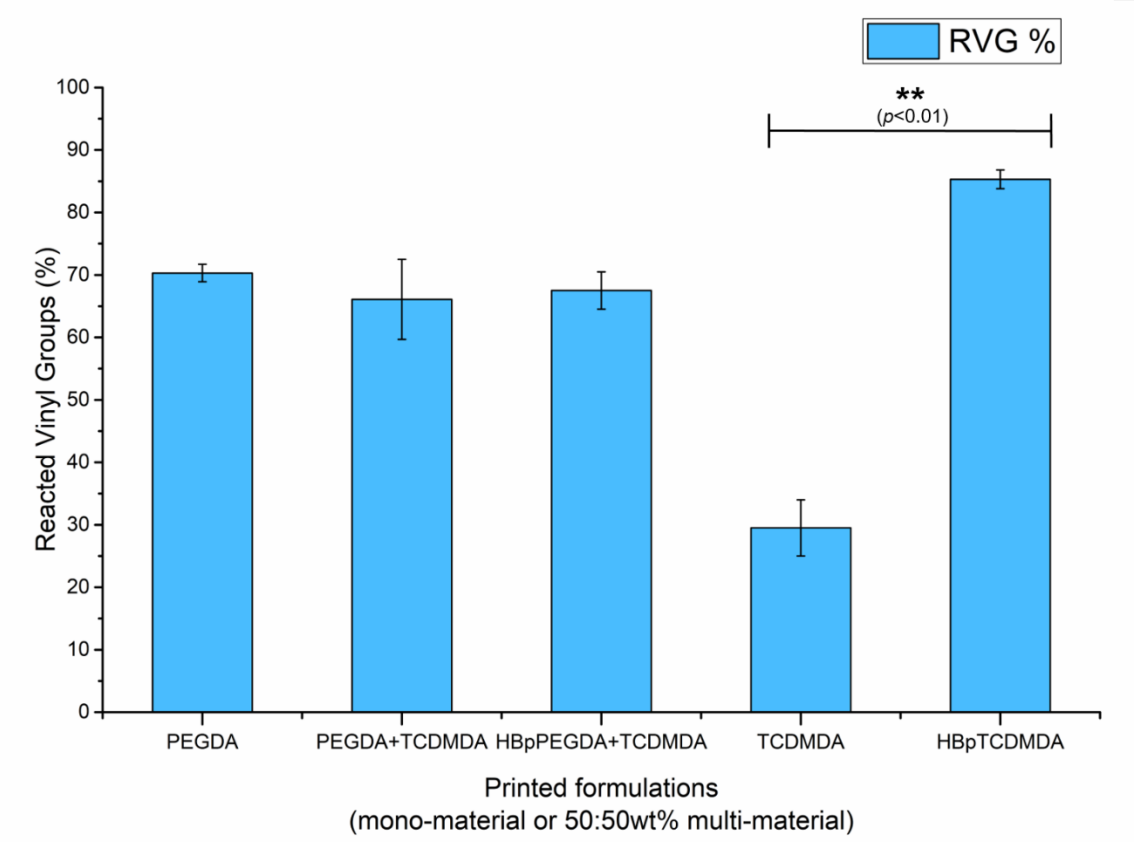



**Figure 5.3. RVG data for 50 µm cubes manufactures from the 2PP formulations prepared containing either one material or two materials formulations with 50:50 wt% concentrations of each material. 2 wt% photoinitiator (Irgacure 369) was utilised in every case, and the corresponding. Data points show the Mean ± Standard Deviation (SD). Statistical significance was determined with ONE-WAY Anova followed by Tukey test.**

Structures could not be manufactured with HBpPEGDA only resins due to the high reactivity of the material that would lead to gelation before finishing printing (see more details in section **5.2.3**), therefore no RVG results could be obtained for that material. When the Raman results from structures manufactured with TCDMDA alone and

structures produced with HBpTCDMDA alone were compared, a statistically significant sharp increase of above 50% of RVG (**Figure 5.3**) was observed. It was hypothesised that this was related to the rigidity of TCDMDA monomer [121], this inflexibility does not allow sufficient mobility of the growing chains to allow a high amount of vinyl groups to encounter one another and react and so increase the cross-linking network density above a certain value (i.e. 30 % RVG). However, when the hyperbranched poly(TCDMDA) was used, the material has already formed a pre-polymerised network that is still solvent-soluble and the pendant acrylates groups at the end of the branches are both available and closer to each other than in the linear monomer structure. This appeared to both: (a) allow for more of those groups to react to extend cross-linking and (b) the 2PP seemed to remove most of the remaining vinyl groups in the pre-formed HB structure [123]. Furthermore, this conclusion was supported by the fact that a 50 %:50 % mixed HBpPEGDA + TCDMDA ink when processed demonstrated a RVG of 70 % approximately halfway between the values exhibited by the single reagent resins of TCDMDA and HBpTCDMDA.

Meanwhile, in the case of PEGDA only system, the higher flexibility and greater length of the spacer group between the vinyl groups when compared to TCDMDA was concluded to allow for those groups to achieve great cross-linking as the network density increased when compared to TCDMDA only resin. Meanwhile, adding TCDMDA to PEGDA and HBpPEGDA to form mixed resins, produced RVG of approximately 70 %, which presented no significant differences to the results from the printed samples prepared with 100 % PEGDA inks. This indicated that adding TCDMDA mixtures instead of commercial PEGDA did not significantly influence the number of acrylate groups that reacted and suggested that the flexibility of the PEGDA dominated the cross-linking process in this ink.

### 5.2.3 Polymerisation threshold

Formulations from **Table 5.2** were tested in the 2PP system using different laser powers and printing speeds to determine their polymerisation threshold following the methodology described in section **3.3.1.7**. These experiments were conducted to observe the effect of a hyperbranched material on the operating 2PP printing window. To achieve this, the polymerisation threshold of HBpTCDMDA and commercial TCDMDA monomer only inks were compared alongside the threshold of 70 wt% TCDMDA and 30 wt% HBpPEGDA resin to further observe the effectiveness of the HBpPEGDA addition to TCDMDA threshold. The results are presented in **Figure 5.4** and showed that the hyperbranched formulation significantly broadens the range of parameters that can be used to manufacture structures with a 2PP printer.

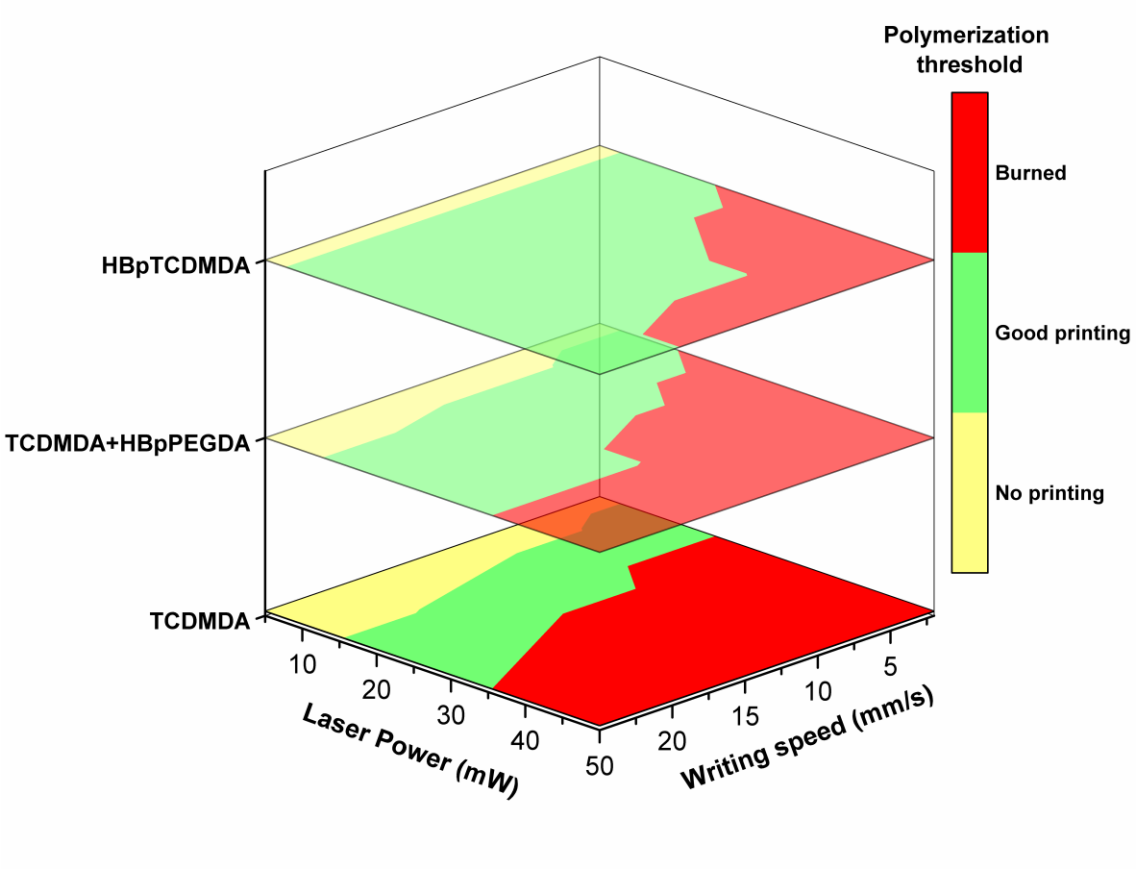



**Figure 5.4. Map of the Polymerisation thresholds for the following formulations (top to bottom): 100 wt% HBpTCDMDA, TCDMDA 70 wt% + HBpPEGDA 30 wt%, and TCDMDA 100 wt%.**

The presence of the HBpTCDMDA was demonstrated to positively influence both the polymerisation threshold (delivering a reduction) and burning threshold (raising the onset) compared to the commercial TCDMDA mixture, and so expanding the processing window of the 2PP technique. This was attributed to their HB molecular structure, as the branching acts as a "pre-polymerised" network, with a high available functional group density, that would require less energy to fully cross-link compared to the molecules of a low $M_w$ linear monomer. Therefore, the branching of the material allows faster cross-linking compared to non-branched resins.

The earlier onset of the polymerisation threshold is important because using lower laser power allows prints to be achieved with smaller voxel size, which leads to better resolution while manufacturing. Therefore, the addition of HBpTCDMDA to inks should enable printing at higher resolution compared to linear TCDMDA monomer alone. Meanwhile, enabling the manufacture of structures with higher laser powers, will lead to the production of samples with stronger cross-linking, which could lead to better mechanical properties [120]. Manufacturing at high laser powers and high writing speeds could also allow faster manufacturing times. However, too great levels of cross-linking may lead to the onset of brittleness.

HBpPEGDA was also formulated for 2PP assessment but the high reactivity of the material did not allow to determine its parameter's settings, as it would gelate before finishing printing the structures, trapping the samples inside the gelled network. Different photoinitiator concentrations (0.5 wt%, 1 wt%, 1.5 wt%, and 2 wt%) were added to HBpPEGDA and tested in the 2PP system. When 0.5 wt% was added, no printing was observed. When 1 wt% and 1.5 wt% were added printing was possible but at a smaller range of parameters than when 2 wt% was added. However, the material would still gelate with all PI concentrations and trap the structures inside while manufacturing. To slow its reactivity and gelation, the material was mixed with TCDMDA monomer at different

concentrations while maintaining the PI concentration at 2 wt% in all formulations, which allowed successful 2PP processing at a broad range of parameters. Again, this increase in reactivity was hypothesised to be related to the flexibility and greater inter-double bond length within the HBpPEGDA molecular structure making the double bonds more available than in the HBpTCDMDA structure. As shown in **Figure 5.4**, adding 30 wt% of HBpPEGDA to TCDMDA monomer also enabled the processing window to be significantly expanded by both reducing polymerisation onset and increasing burning thresholds as compared to printing an only TCDMDA resin. However, it does not expand the thresholds as much as the HBpTCDMDA only ink. This was attributed to the PEGDA ink having two different materials in the mixture. With each having their own reactivity ratios that potentially make it harder for them to react than when only one type of branched material is present which only has to react with itself. This type of influence has already been observed in the cure levels study detailed in the data within **Figure 5.3.**

To further understand the processing of HBpPEGDA, the polymerisation thresholds of commercial PEGDA, PEGDA 50 wt% + TCDMDA 50 wt%, and HBpPEGDA 50 wt% + TCDMDA 50 wt% were obtained and compared in **Figure 5.5**.

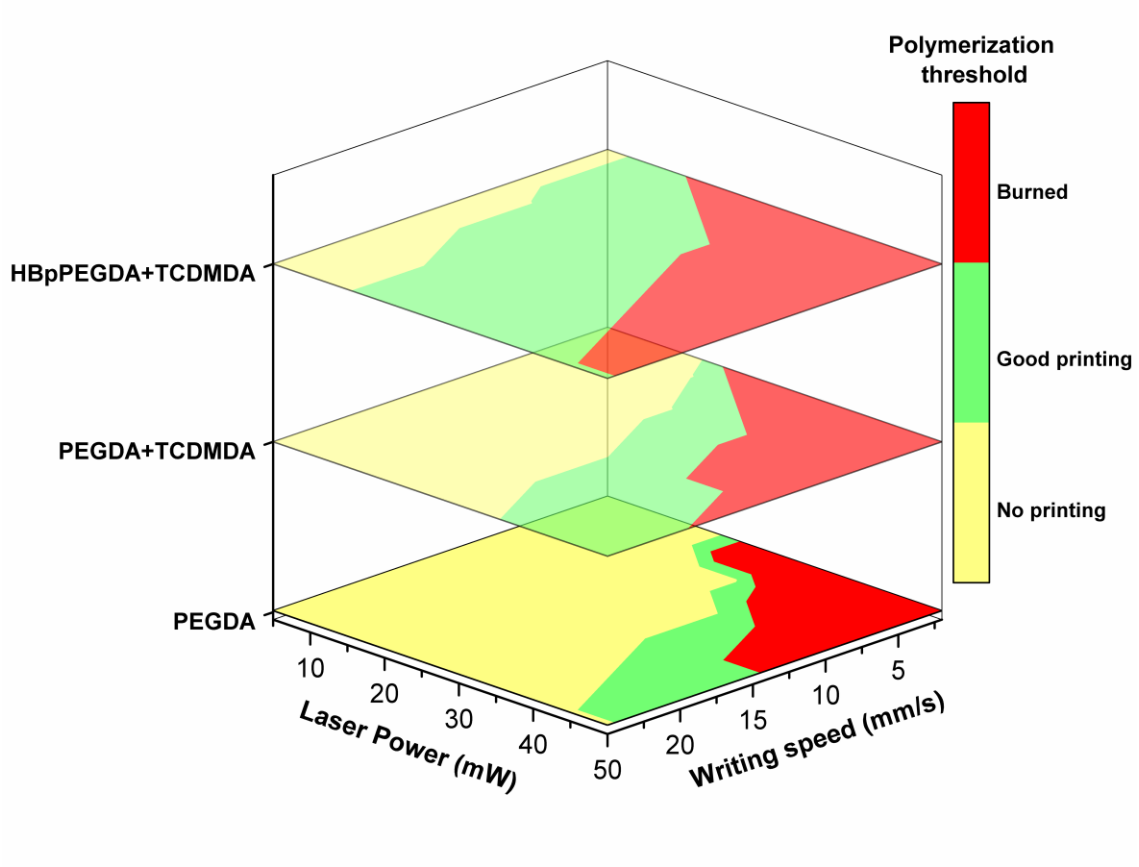



**Figure 5.5. Map of the polymerisation thresholds of the following formulations (top to bottom): HBpPEGDA 50 wt% + TCDMDA 50 wt%, PEGDA 50 wt% + TCDMDA 50 wt%, and PEGDA 100 wt%.**

The results showed that adding HBpPEGDA to the formulation had a more significant impact on the printing parameters than when mixing commercial PEGDA with TCDMDA. The hyperbranched material dramatically reduced the polymerisation threshold when compared to the other two formulations. However, HBpPEGDA also increased the burning threshold onset more dramatically than when commercial PEGDA was mixed with TCDMDA or printed alone. This was rationalised as relating to the high flexibility and thus reactivity observed with HBpPEGDA. Thus, it would need less energy density to quickly manufacture an extended network structure successfully, rapidly reducing the amount of "free" TCDMDA monomer ink. Resins formulated with only

PEGDA or PEGDA : TCDMDA mixture would have less reactivity than the hyperbranched material, which leads to more energy density required for onset burning.

To further study the effect on printing quality and resolution of replacing PEGDA with HBpPEGDA in ink formulations, the following mixed material inks were used to manufacture buckyball structures using similar parameters: HBpPEGDA 50 wt% + TCDMDA 50 wt% and PEGDA 50 wt% + TCDMDA 50 wt%. The resulting structures produced were subjected to SEM analysis (see section **3.3.1.10** for methodology) and the results of these experiments are shown in **Figure 5.6.**

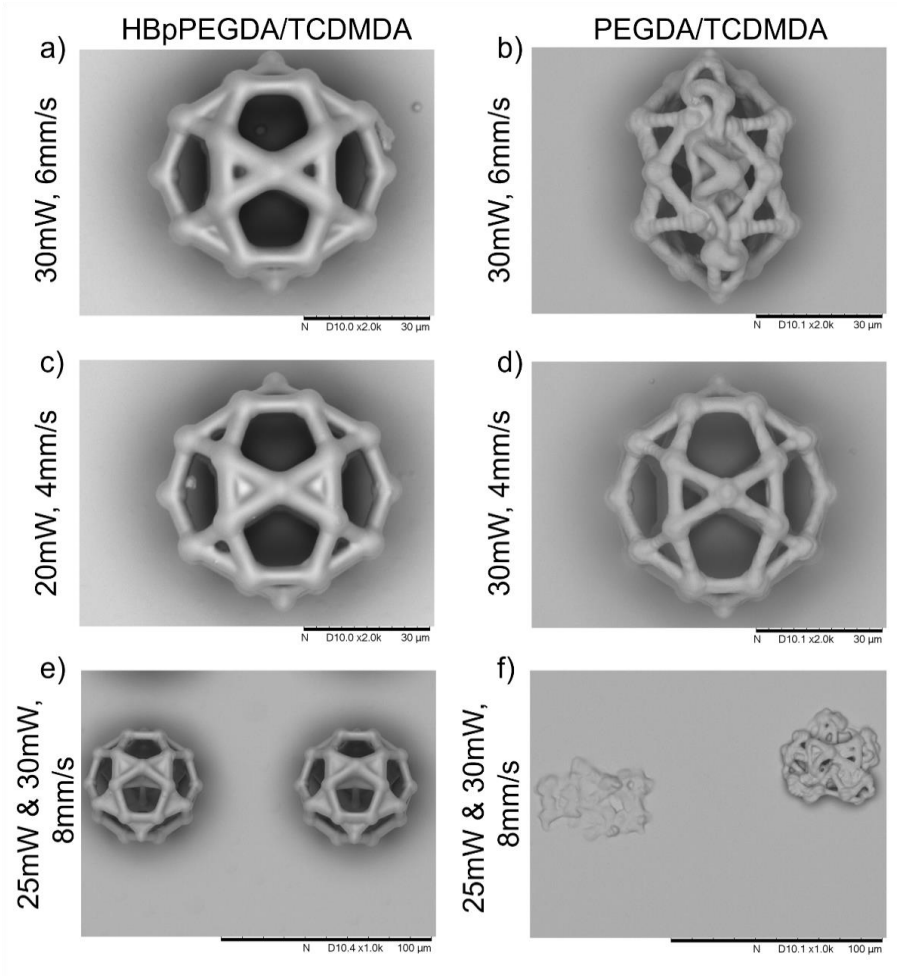



**Figure 5.6. SEM images of 2PP manufactured buckyball structure produced from the following mixed material inks a) HBpPEGDA 50 wt% + TCDMDA 50 wt% at 30 mW (laser power) and 6 mm/s (writing speed) b) PEGDA 50 wt% + TCDMDA 50 wt% at 30 mW and 6 mm/s c) HBpPEGDA 50 wt% + TCDMDA 50 wt% at 20 mW and 4 mm/s d) PEGDA 50 wt% + TCDMDA 50 wt% at 30 mW and 4 mm/s e) HBpPEGDA 50 wt% + TCDMDA 50 wt% at 25 mW and 30 mW at 8 mm/s. f) PEGDA 50 wt% + TCDMDA 50 wt% at 25 mW and 30 mW at 8 mm/s.**

The images in **Figure 5.6** indicate that using HBpPEGDA instead of commercial PEGDA in a formulation with TCDMDA allowed the successful manufacturing of articles that exhibited a smooth surface and better structural integrity (**Figure 5.6a-b**). Structures printed with commercial PEGDA with the same set of parameters used for HBpPEGDA were found to collapse, indicating the cross-linking with PEGDA was not sufficiently high enough to provide adequate mechanical properties for the structure to be stable, thus were less 2PP compatible compared to the HBpPEGDA. This could also be appreciated when using 25 mW laser power and 8 mm/s writing speed was adopted for manufacturing both with the hyperbranched and monomer formulations (**Figure 5.6e-f**). Using this set of parameters allowed structures to be successfully fabricated with the hyperbranched formulation, while printing with commercial PEGDA was impossible to achieve. Even when further tailoring the parameters to be closer to those that have been previously used with commercial PEGDA (**Figure 5.6c-d**), such that the resultant articles had enough structural integrity to allow good polymerisation and so avoid collapse. There was still a significant difference in the surface structure/quality of the articles, with samples fabricated with commercial PEGDA lacking smoothness throughout the buckyball surface. Therefore, these prints showed that the use of HBpPEGDA compared to its commercial di-functional, monomer version allows for faster printing with better structural integrity and surface finish of the samples. However, structures manufactured with HBpPEGDA have to be post-processed with longer solvent washing times, as the formulation was more viscous than that of commercial PEGDA, which was responsible for some unwashed resin visible on the samples (**Figure 5.6-a, c, e).**

The previous results indicated that hyperbranched polymers can be 2PP processed either on their own or in multi-material formulation with a commercial monomer, although the level of HB polymer reactivity was found to be related to the constituent monomer structure and had to be modified by mixing with other components to make a printable

resin. Both HBpTCDMDA and HBpPEGDA increased the polymerisation threshold allowing to manufacture structures with parameters that offer higher resolution. HBpTCDMDA also significantly expanded the burning threshold, allowing to print structures at higher laser powers, which could increase the mechanical properties of the samples produced. When preparing TCDMDA monomer multi-formulations with either PEGDA or HBpPEGDA added to the mixture, the formulation containing 50 wt% HBpPEGDA allowed manufacturing with better structural integrity and resolution than samples produced with the 50 wt% PEGDA formulation.

### 5.2.4 Microstructure characterization

**Acknowledgement**: The ToF-SIMS and Multivariate Analysis was performed by Dr Gustavo Ferraz Trindade (University of Nottingham).

To confirm the presence of both HBpPEGDA and TCDMDA within the final structures of the 2PP articles, time of flight secondary ion mass spectrometry (ToF-SIMS) analysis was performed upon a 50 µm manufactured cube printed using the HBpPEGDA 50 wt% + TCDMDA 50 wt% ink formulation adopting the methodology described in section **3.3.1.12**. The characteristic peak of each material was selected via MVA analysis. The data obtained indicated the presence of both HBpPEGDA and TCDMDA within the printed sample (**Figure 5.7**), with ions characteristic of each material being observed from both the top surface and to a depth of several µm deep into the structure (depth profiling).

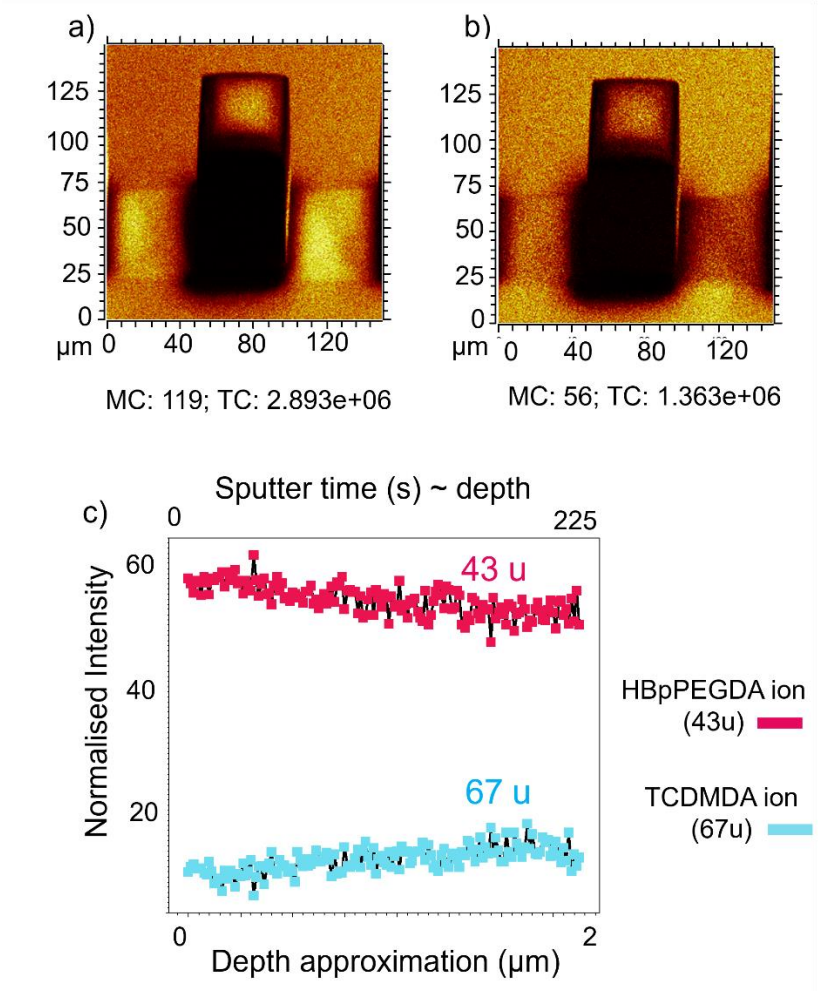



**Figure 5.7. ToF-SIMS spectra of 50 µm a HBpPEGDA+TCDMDA cube at a) the beginning of analysis characterising the top surface, b) the end of depth profile analysis, and c) detailing the normalised intensity of HBpPEGDA (43u) and TCDMDA (67u) ions obtained from depth profile analysis. MC = Maximal counts in one pixel. TC = Total counts in the image.**

Ions for HBpPEGDA ($[C_2H_3O^+]$, 43 u) and linear TCDMDA ($[C_5H_7^+]$, 67 u) were detected in the cube both at its surface and throughout the analysis of the first few µm of layers. Both materials showed good dispersity throughout the structure (**Figure 5.7 - c**), with the intensity of HBpPEGDA ions being stronger than those of TCDMDA due to a higher molar concentration of HBpPEGDA present in the ink formulation. The exact penetration distance of the GCBI ion beam expressed in µm could not be confirmed because of a low Argon pressure within the equipment during the measurement. For this reason, the sputtering time has been defined as a rough approximation of the depth instead

of µm. The depth could be roughly approximated by comparing **Figure 5.7– a, b**, as they showed the structure at the beginning and at the end of the analysis, respectively. This gave an approximate number of 2 µm to the depth profiling penetration into the structure.

These results indicated that multi-material printing with HB polymers was possible and that it could in fact produce structures with high RVG % and improved structural integrity. Quality printed articles could be manufactured with certain hyperbranched polymer-only ink formulations, and this has been linked to HB polymer reactivity. Meanwhile the appropriate mixed HB ; Monomer material inks were also shown to produce significantly improved printed structures and operating windows than HB or just commercial monomer only inks. It has been proposed that understanding the characteristics of these mixed inks could also allow different microstructure environments to be created throughout the printed structures depending on which materials are mixed. For example, by using materials with different $\chi$ parameters to control their disposition throughout the microstructure as previously done in chapter 4.

### 5.2.5 Biocompatibility of hyperbranched resin

**Acknowledgement**: The LIVE/DEAD assay, fluorescent microscope imaging and cell viability calculation was carried out by Dr Adja Touré.

In section **5.2.2**, it had been demonstrated that the HBpTCDMDA structures manufactured *via* 2PP had a significantly higher RVG % than the structures fabricated with solely TCDMDA monomer formulation. That high RVG % could make this material a good candidate for bio-applications, as this indicated the potential for the final material to contain either a reduced carbon : carbon double bond content and/or less unreacted monomeric material left in the structure. The former may result in further reaction with species in the bio-environment of choice, whilst the latter could potentially leach out of an article and cause cell toxicity. This toxicity had been related to the electrophilicity of

meth(acrylate) groups, which can promote covalent binding with nucleophilic molecules like proteins or DNA. This can cause inhibition of important protein functions leading to different types of cell toxicity [126]. To investigate this potential material property improvement, scaffolds prepared using HBpTCDMDA and TCDMDA only inks (i.e., cubes with dimensions 1 mm × 2 mm × 0.02 mm) were manufactured with the 2PP apparatus and the cell viability of the articles produced were assessed *via* a LIVE/DEAD assay using mouse fibroblast cells. A direct contact LIVE/DEAD assay was selected to evaluate cells viability on the scaffolds because of the limitation of the size of the scaffolds that could be manufactured with 2PP. The alive cells showed in green colour (calcein AM) and dead cells appeared in red (Ethidium homodimer-1) on fluorescence microscope images. The fibroblasts cultured on HBpTCDMDA and TCDMDA scaffolds can be seen in **Figure 5.8.**

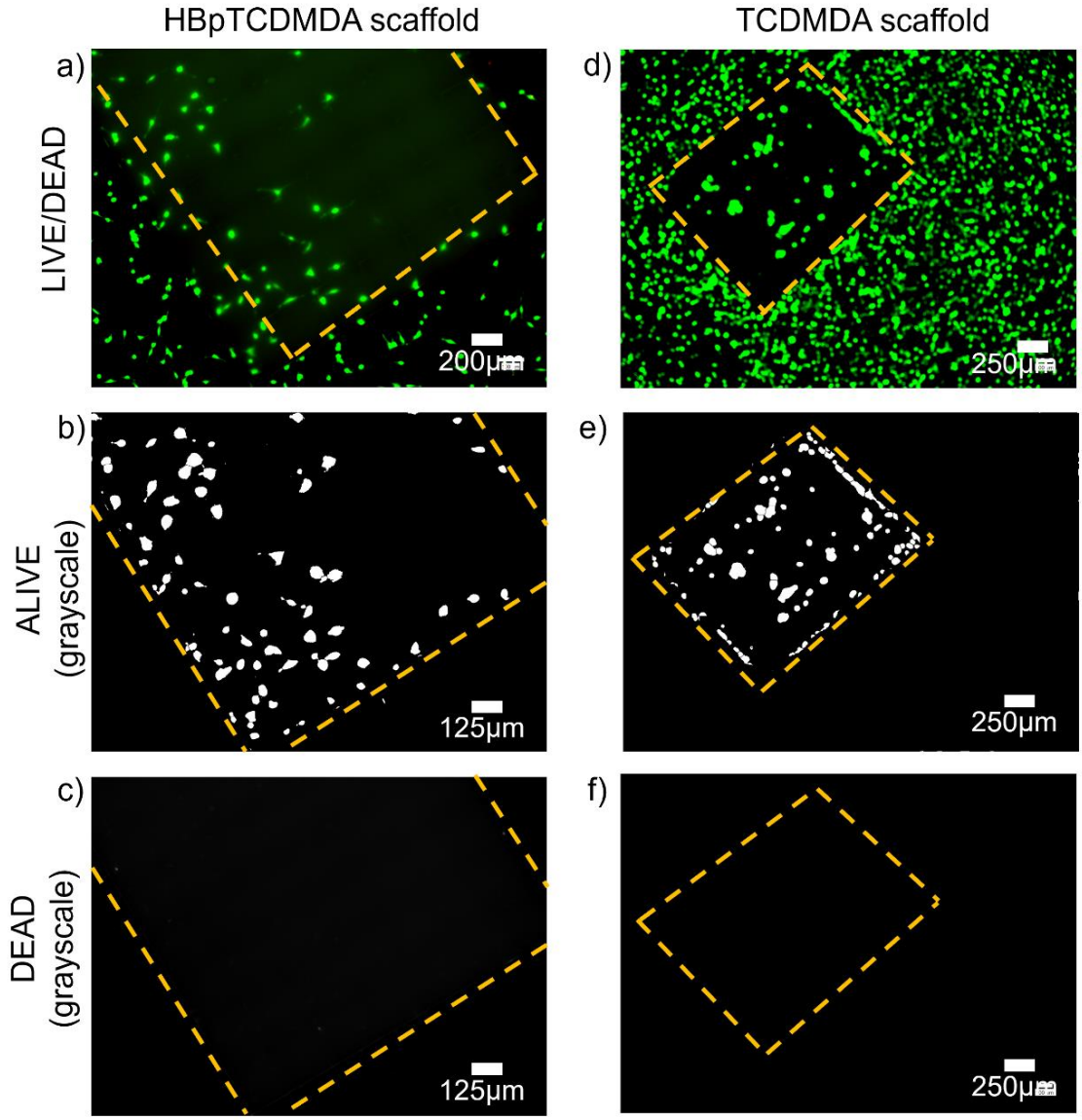



**Figure 5.8. Fluorescence microscope images from a LIVE/DEAD assay using mouse fibroblast cells: a) LIVE cells shown in green on HBpTCDMDA scaffold, b) Greyscale image of LIVE cells on HBpTCDMDA scaffold, c) Grayscale image of DEAD cells on HBpTCDMDA scaffold, d) LIVE cells shown in green on TCDMDA scaffold, e) Grayscale image of LIVE cells on TCDMDA scaffold, f) Grayscale image of DEAD cells shown on TCDMDA scaffold. The contour of the scaffolds was highlighted with the dashed orange line.**

The results in **Figure 5.8– d, e, f** showed the stronger attachment preference of fibroblasts for the treated coverslips instead of the TCDMDA printed structures. Meanwhile on the HBpTCDMDA structures (**Figure 5.8– a, b, c**) the images indicated that the cell distribution might be more even between samples and treated glass. It was hypothesised

that this could be related to a higher inclination towards the silane methacrylate groups of the treated glass than the acrylate groups of the monomer. A similar preference between the thiol and carboxylic acid pending groups of the HBpTCDMDA and the silane methacrylate groups was observed. Finding this represents a limitation on this assay. Because not many cells adhered to the scaffold. Therefore, further cell attachment experiments should be performed in the future to draw better conclusions. Future experiments in which the surface of the samples is modified to increase cell attachment could also be performed (e.g., with pro-attachment peptides), to broaden the biocompatibility results on this material.

The results from the viability assay showed that 92 % of the seeded cells were still alive after culturing them on the hyperbranched structure while 8 % of them were dead. In the case of the TCDMDA manufactured scaffolds, 98 % of the cells were alive and 2 % dead. This indicated high biocompatibility of the samples printed with both resins. As explained in section **3.3.1.16**, the cells were incubated on the structures for 24 h. Therefore, these results did not show the effect on viability for longer periods of time, where there could be a difference between structures manufactured with HBpTCDMDA ( i.e ~ 85 % RVG) and TCDMDA ( i.e ~ 30 % RVG) depending if the monomer printed structures would start leaching any unreacted resin after 24 h. Thus, for applications where the material has to be in contact with cells for long periods of time like sustained drug delivery implants, HBpTCDMDA structures might be more suitable due to their high viability combined with high RVG %. However, from these results it can only be concluded that the reduction in vinyl RVG does not significantly influence the cell viability over a 24-hour period. Further experiments involving longer cell incubation times would need to be performed in order to draw better conclusions.

## 5.3 Conclusions

The work presented in this chapter was still centered on the main goal of this project, which was developing new multi-material inks for 2PP manufacturing and their optimisation for the technique. Its specific focus was on investigating this issue from the perspective of utilising hyperbranched materials in such mixed ink formulations. Using as a starting point commercial monomers like TCDMDA or PEGDA, hyperbranched versions of these materials were synthesised and optimised for 2PP printing in different mono- or multi-material formulations. Samples manufactured with HBpTCDMDA instead of commercial TCDMDA showed an increase of over 50 % in the RVG value, while those printed with formulations that contained HBpPEGDA did not show a significant difference in RVG %. This could indicate that in the case of rigid monomers like TCDMDA, using their hyperbranched version could help increase the number of acrylate groups that react while printing. This could be beneficial regarding their mechanical properties or potential bio-applications.

The hyperbranched polymer-based formulations of this chapter also allowed the 2PP operability window to be expanded. Typically, the onset of polymerisation was observed at lower energy inputs, whilst the threshold was increased, compared to those containing commercial linear monomers. This was related to the greater reactivity of the HB polymers and that they allowed the monomer within the structure to be more rapidly and efficiently incorporated into the polymer matrixes network. Inclusion of the HB polymers was shown to allow the production of well-manufactured parts at lower laser powers, which could manufacture with smaller voxel sizes leading to higher resolution. In the case of HBpTCDMDA, it also allowed printing at higher laser powers than the monomer, which could potentially produce parts with stronger mechanical properties. These differences in polymerisation threshold of the hyperbranched polymers compared to the

linear monomers could be a consequence of their pre-polymerised structure, which makes them more reactive and needing less power to onset the polymerisation reaction. Their reactivity also influences if they can be printed just by themselves along with photoinitiator, like in the case of HBpTCDMDA, or if they need to be mixed with another material to slow down their reactivity and avoid gelation, like in the case of HBpPEGDA.

The research work presented in this chapter also showed that the hyperbranched materials could be printed in multi-material formulations using ToF-SIMS analysis on samples manufactured with HBpPEGDA and linear TCDMDA. This technique detected ions from both materials throughout the analysed sample layers. Multi-material printing could have potential benefits in the mechanical properties of the manufactured parts, by allowing mixing of rigid material like TCDMDA with a more flexible material. Or on the opposite hand, changing the mechanical properties of for example a brittle hyperbranched polymer, with a commercial monomer whichwould reduce this brittleness.

To determine the potential use of HBpTCDMDA for bioapplications, LIVE/DEAD cell viability assay was performed on scaffolds manufactured with this material. This experiment was also performed on scaffolds printed with commercial linear TCDMDA to observe if the difference in RVG % would have an impact on cell viability results. The results obtained indicated that scaffolds produced with both HBpTCDMDA and TCDMDA show high biocompatibility in short time assays (24 h). However, further tests should be contacted to determine if TCDMDA scaffolds with ~ 30 %RVG would not leach unreacted material in longer time frames. The viability assays also seemed to indicate a stronger preference of the fibroblast cells for silane methacrylate groups of the treated glass slides and for the thiol and carboxylic acid groups of the HBpTCDMDA scaffolds than for the acrylate groups of the TCDMDA scaffolds. However, further experiments should be performed to determine this.

# 6 Optimisation of photo-sensitive multi-material formulation for drug release application

## 6.1 Introduction

The samples manufactured with PTMCA + PEGDA formulations from chapter 4 presented several characteristics that could make them a suitable candidate for biomedical applications. They showed a high RVG % (see data in **Table 4.4**), which could potentially make them less prone to cytotoxicity as more material is cross-linked and there's less unreacted material that could potentially leach and interact with cells [126]. From the material's perspective, both PTMC and PEGDA have been extensively studied in biomedical research (see section **2.4.2.2** in chapter 2), which would fast track their use as they would be less prone to regulatory barriers compared to completely new materials [117]. These materials have also been studied for ocular applications (see section **2.7.3**). Taking all this into account and combining it with the unmet clinical need identified in section **2.9** regarding the need for biocompatible and biodegradable long-term sustained drug delivery devices for ocular therapy, the work of this chapter focused on developing such a device with a vat-photopolymerisation technique. Laser-based AM techniques would facilitate the fabrication of a small biomaterial-based device that could be inserted via injection to the posterior segment of the eye and perform a sustained release of corticosteroids throughout several weeks via degradation and induced porosity. Laser-based AM techniques would allow to produce a small construct with high

resolution, and they would also allow to manufacture implants with different geometries or porosity degrees.

PTMC is a biodegradable polymer that has no strongly acidic by-products and has long degradation times due to its resistance to non-enzymatic hydrolysis. Its degradation is accelerated in the presence of enzymes by hydrolysis into 1,3-propanediol and carbon dioxide [40]. PTMC has been previously tested for ocular therapy but was discarded in favour of PLA due to its slow degradation times owing to a possible lack of the enzymes needed for degradation in the vitreous [96]. To avoid this issue and allow degradation even if the required enzymes (i.e., lipase enzymes) are not present, NVP was selected as another component in the PTMCA + PEGDA formulation to induce porosity in the cross-linked devices that would allow for an adequate drug release in the selected time frame by accelerating hydrolysis. The addition of NVP was chosen based on the following reasons. Firstly, PVP has been studied and applied previously in ocular therapy (see section **2.7.3**). Secondly, NVP has been previously used to accelerate drug release from polymer networks in several research works. Haesslein *et al*. mixed NVP with poly(propylene fumarate) at different ratios to prepare cross-linked intravitreal drug delivery devices that allowed for *in vitro* sustained release of fluocinolone acetonide (FA) over almost 400 days [127]. Jansen *et al.* also used NVP – alongside with vinyl acetate – as a reactive diluent in PTMC fumarate-based cross-linked networks to increase the hydrolytic degradation and release of vitamin B12 from samples prepared with these mixtures [128]. All the different formulations tested contained 30 wt% NVP. The mixtures allowed for sustained release of vitamin B12 for 11 weeks and showed no cytotoxicity in an *in vitro* MTT assay with NIH 3T3 fibroblasts. The work by Haesslein *et al.* and Jansen *et al.* manufactured samples with moulds *via* UV cross-linking. More recently, work by Ruiz-Cantu *et. al* showed that adding 25 wt% NVP monomer to inkjet printing formulations based on PTMC methacrylate + PEGDA

allowed sustained release of pitavastatin from implants manufactured with these materials [117]. The implants released drug in aqueous media, without the presence of enzymes to accelerate their degradation. The results from the studies described above indicated that NVP cross-linked and formed PVP, a water-soluble polymer that degrades by hydrolysis. Therefore, it was assumed that in aqueous media PVP would wash away creating porosity throughout the structure that could accelerate its degradation by hydrolysis.

Besides the selection of materials and their formulation, another aspect that can be controlled and that can influence the drug release is the design of the medical device itself. The majority of intravitreal ocular implants researched and currently on the market are cylinder-shaped, as that makes them easy to manufacture and easy to insert via needles [129]. It was hypothesised that by still using a cylinder-shaped implant (to maintain the advantages previously mentioned) but modified to obtain a structure with higher degrees of surface area, different drug release profiles from the original full cylinder design could be obtained. Triply periodic minimal surfaces (TPMS) are a category of lattice structures known for having a minimal surface with a mean curvature of zero. This means that they are equally convex and concave at any point and without self-intersection [130]. One of their characteristics is their high surface area to volume ratio which has attracted the attention of the tissue engineering field [131]. Their high surface area, continuous surface, and porosity help to promote cell adhesion, migration, and proliferation as well as better transport of nutrients and growth factors. Between the different types of TPMS lattice geometries, the diamond matrix geometry shows one of the highest surface-area to volume ratio. Because of this, the diamond TPMS lattice was selected as a design to apply to cylinder-shaped implants [131]. These higher surface area designs would be based on a diamond matrix lattice structure applied to a cylinder shape with varying cell number, with the increasing cell number being proportionate to the

increase in surface area. It was hypothesised that these designs could be produced with vat-photopolymerisation techniques and allow a greater degree of control over the drug release profile that could not be achieved with standard manufacturing techniques (i.e., injection moulding). It has been previously shown by Kyobula *et al.* that applying a honeycomb design with increasing cell number to inkjet printed tablets allowed to modulate the drug release of fenofibrate from the structure [132]. They also showed that tablets with the highest surface area to volume ratio released the highest amount of drug. Therefore, it was hypothesised that increasing the surface area of vat-photopolymerised implants with diamond lattice design would also increase the amount of drug released from them, offering different release profiles with each design as in the inkjet printing case of Kyobula *et al*. It was hypothesised that increasing the surface area of the implants would also increase the amount of drug released from them, offering different release profiles with each design. Although TPMS lattices have been studied for several tissue engineering applications [130, 131] they haven't been extensively explored for drug delivery implants [133]. Using them for a sustained drug release application would further allow to study their properties in a new field.

Therefore, the goal of this chapter was to manufacture an intravitreal implant that would allow sustained drug release via vat- photopolymerisation. First, TPMS lattice-based designs were proposed for cylinder-shaped implants. To manufacture these implants, a printing optimisation process was started with a PTMCA + PEGDA 1:20 molar ratio formulation with 2PP and projection micro – stereolithography (PμSLA) to initially assess printability of the structures and determine the best manufacturing process for the application. 2PP was selected to determine the initial feasibility of lattice design printing at small scale, allowing to use smaller formulation amounts for optimisation than PμSLA while offering high resolution to produce diamond lattice implants. PμSLA was selected for scale-up implant manufacturing as it significantly increased the production line speed

and improved the manufacturability of scaled-up implants while still offering a good resolution to print lattice designs. The PTMCA + PEGDA formulation was also optimised to determine the concentration of NVP needed in the mixture for an adequate drug release profile. This was determined with an initial drug release study from UV-cast samples manufactured with PTMCA + PEGDA + NVP at different concentrations, using Rhodamine B as model drug. Once the needed wt% of the three materials in the formulation was determined, the mixture was further optimised for PμSLA by adding the concentration of photoabsorber (curcumin) that would allow manufacturing these structures with good resolution. Fluocinolone acetonide, a corticosteroid drug used for the targeted application in commercial implants, was also loaded into the formulation. After optimising the manufacturing process via PμSLA with the final mixture, 3D printed implants were obtained and their cell viability and cell cytotoxicity were assessed using human corneal epithelial cells. Cell metabolic activity as a proxy for cell viability tests were performed using PrestoBlue assay while membrane disruption activity was performed using a Lactate dehydrogenase (LDH) assay as proxy for cell toxicity. The drug release of FA from lattice implants was also assessed over a 35-day time period. The microstructure of the implants was analysed via ToF-SIMS to further understand the material and drug distribution inside the polymer matrix.

## 6.2 Results and Discussion

### 6.2.1 Designs of diamond lattice-based implants for sustained drug release for ocular therapy

**Acknowledgements:** Richard Sélo (Centre for Additive Manufacturing (CfAM), University of Nottingham (UoN)) helped to create the 3D designs and stl files needed for 2PP printing using FLattPack software (see *et al*. [134] for further software information). Eric Lehder (CfAM, UoN) helped to create the 3D designs and image files needed for

PμSLA by providing access to in-house developed software (see Lehder *et al* [135] for further software information).

Three diamond lattice designs were proposed for the ocular bioapplication by varying the cell number on each one (see **Figure 6.1**). The cell number indicates the number of cell units repeated in the three dimensions (x, y, z) [136]. By increasing the cell number, the surface area was increased as well. A normal cylinder design was also created as a control design. The volume fraction of the lattice is the volume of solid material as a fraction of the structure's total volume [134]. It is in the range of 0 to 1 (0 being only air and 1 being a completely solid structure).For the implants it was arbitrarily set to a fixed value of 0.4 to reduce the number of variables. The volume fraction was kept < 0.5 to obtain the benefits of a higher surface area that lower volume fraction numbers bring. The closer to 1 the volume fraction is, the closer its surface area would be to a normal cylinder. Initially, volume fractions of 0.2 and 0.3 were used for initial printing optimisation experiments (see section **6.2.2.1** and section **6.2.2.3**) to reduce manufacturing times. However, the optimisation process indicated that consequently to these volume fractions, the walls of medium surface area (MSA) and high surface area (HSA) structures were too thin when trying to scale-up in size. Thus, those implants could not be successfully printed as they would collapse. To avoid this issue, the volume fraction of the final design was increased to 0.4 to obtain thicker walls. This proved to be a successful solution as at this volume fraction, all implant designs could be printed with PμSLA without collapsing. The pore size is dependent on the cell number and was measured using Fiji ImageJ software (see methodology in section **3.3.1.25**).

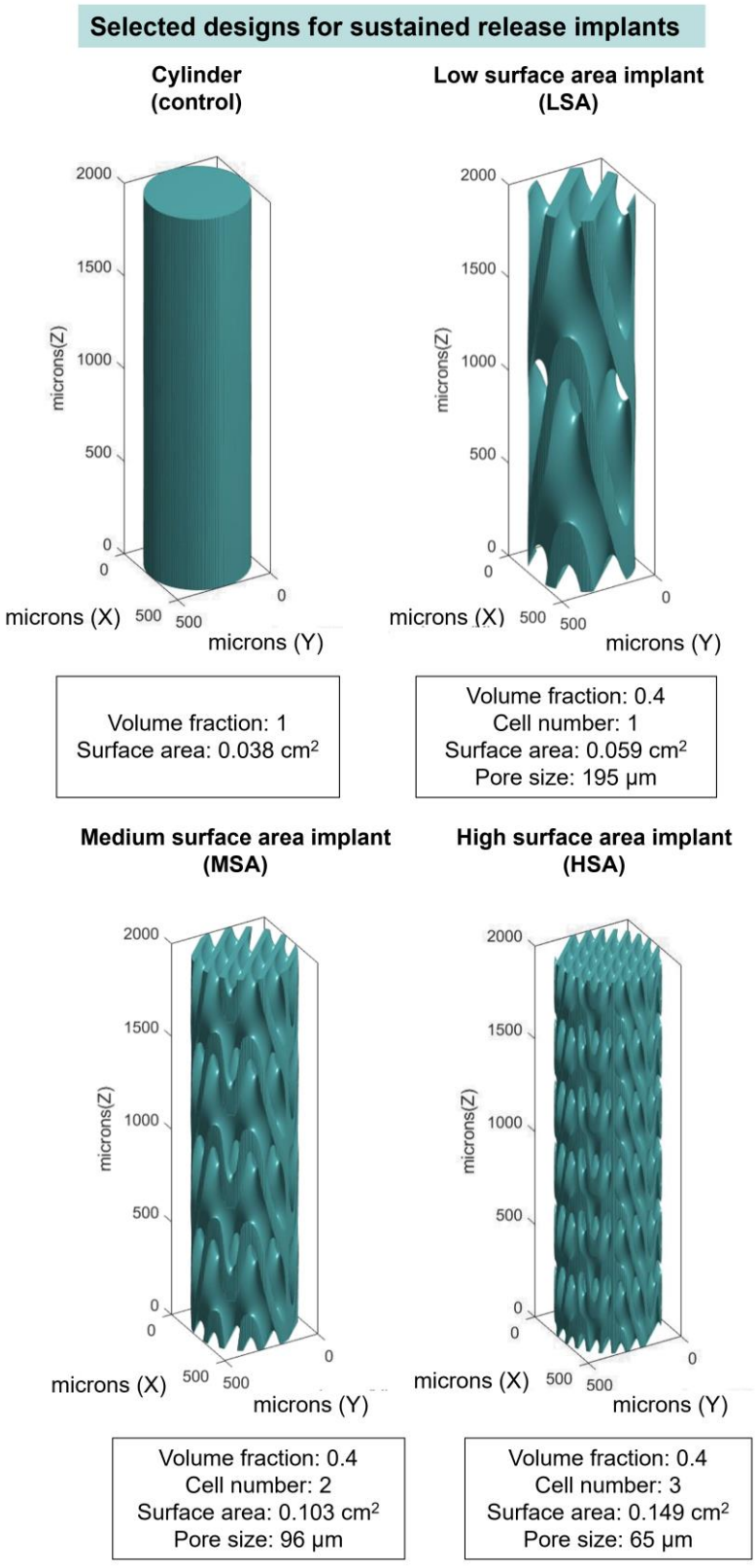



**Figure 6.1. Depiction of the implant's designs (2 mm × 0.5 mm) proposed for sustained drug delivery, showing from left to right a control design (cylinder) and 3 diamond matrix lattice designs that vary in cell number. The lattice implants were named based on their surface area: low surface area (LSA), medium surface area (MSA), and high surface area (HSA).**

The size of the implant was selected as 2 mm (height) × 0.5mm (diameter). This size was chosen considering the sizes of commercial intravitreal implants used for ocular therapy, which were reported to be in the range of 1.5 mm to 6 mm (see section **2.7.2** for examples and bibliography on implants available on the market). This size range allows intravitreal application through needles via injection as well as enough drug load to deliver the treatment (see section **2.7.2** for more information on drug load of commercial implants). The limitations of the available vat- photopolymerisation machines for manufacturing present in our lab were also considered. As well as the manufacturing time of the structures and the formulation quantity needed to manufacture them (see further details on these considerations in section **6.2.2**). After weighing all these aspects, the 2 mm × 0.5 mm size was selected as the targeted final dimension.

## 6.2.2 Initial implant printing optimisation of PTMCA + PEGDA 1:20 molar ratio mixture *via* 2PP and PμSLA systems

### 6.2.2.1 Implant manufacturing optimisation using 2PP

To determine if the designs outlined in section **6.2.1** could be successfully manufactured with vat-photopolymerisation techniques (2PP or PμSLA) and to determine which technique would be better suited for the task, several printing optimisation experiments were carried out. Initial experiments were performed with 2PP as this would allow tests using very small amounts of formulation (50 µl) compared to PμSLA (4 mL). The formulation selected for initial printing experiments was the PTMCA + PEGDA 1:20 molar ratio previously discussed in chapter 4. This formulation showed a high percent of reacted vinyl groups (RVG %), which might indicate less probability of cytotoxicity. It also allowed to print complex structures like buckyballs or spiky hemispheres (see **Figure 4.5** in section **4.2.3**), indicating that it might also allow to successfully manufacture other complex structures like the proposed lattice designs from **Figure 6.1**.

This formulation was used as a starting point in the printing optimisation process to know if the manufacturing was possible at all with this mixture and to know which process would be more suitable for printing. Once that goal was achieved, further formulation optimisation was performed to target adequate sustained drug release (see section **6.2.3** for NVP addition and concentration optimisation with PTMCA and PEGDA). This new optimised formulation was then used to manufacture the final implant designs (see section **6.2.5** for lattice manufacturing with PTMCA + PEGDA + NVP formulation loaded with Fluocinolone Acetonide (corticosteroid drug).

The initial designs tested in the 2PP system with PTMCA + PEGDA 1:20 molar ratio were diamond lattices and cylinder control implants with a volume fraction of 0.2 and a size of 0.1 mm × 0.03 mm (see methodology in section **3.3.1.6.1**). This small implant size and volume fraction were initially selected to shorten the printing times and accelerate the parameter optimisation for manufacturing. The parameters that allowed for successful manufacturing of these designs were 45 mW laser power and 40 mm/s writing speed and SEM images of the structures can be observed in **Figure 6.2**:

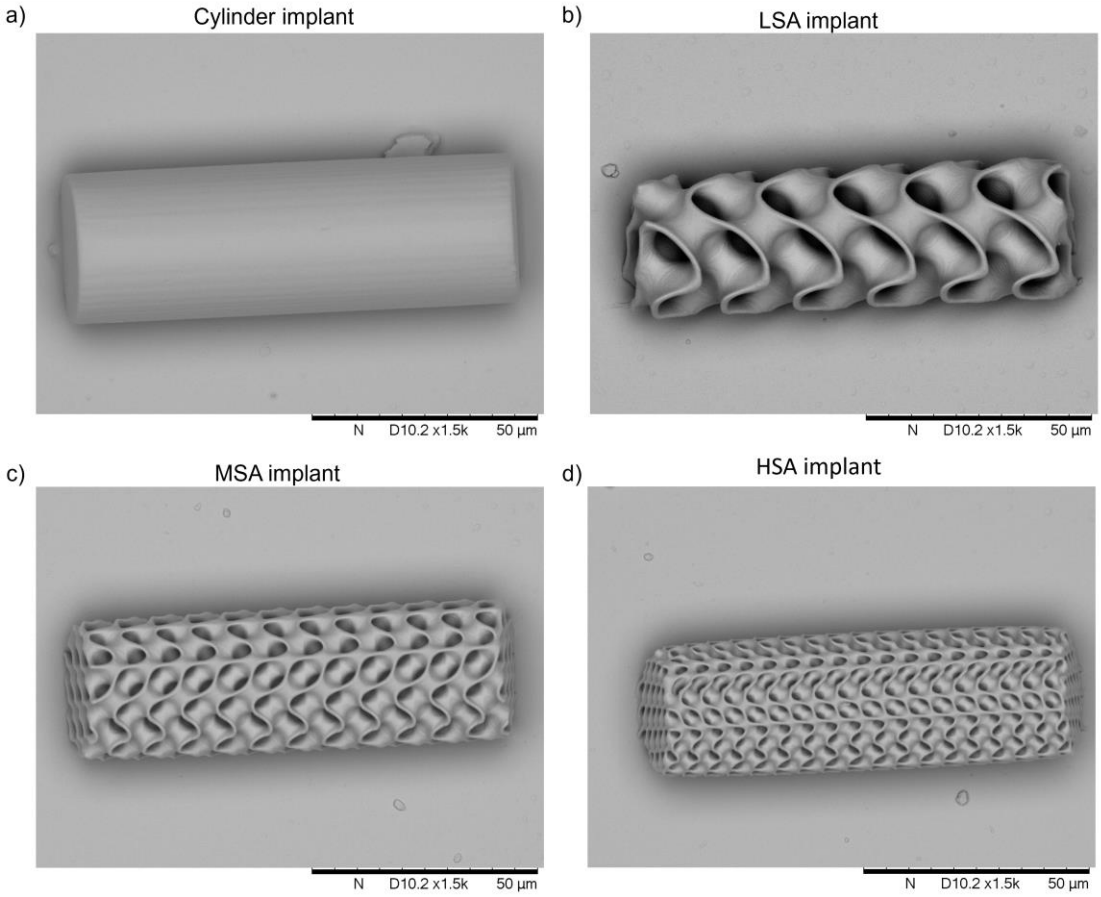



**Figure 6.2. Implant designs (0.1 mm length × 0.03 mm diameter and 0.2 volume fraction) printed with the 2PP system using PTMCA + PEGDA 1:20 molar ratio formulation. Parameters used for manufacturing: 45 mW laser power and 40 mm/s writing speed. Hatching and slicing distances were 0.2 µm and 0.4 µm, respectively.**

The structures from **Figure 6.2** showed that at small scale, the selected PTMCA + PEGDA mixture could manufacture well-defined implant structures. Thus, the optimisation process was scaled up and the following tests were also performed with the 2PP system with the same designs but with the following dimensions: 0.9 mm length × 0.3 mm diameter. When these bigger designs were tested into the 2PP system, they would produce structures that would collapse instead of the well-defined and sturdy structures seen at small scale in **Figure 6.2**. It was hypothesised that this could be related to the 0.2 volume fraction, as this parameter would result in thin walls that might not be strong

enough to support the whole structure at bigger scale. Therefore, the volume fraction was increased to 0.3 and the experiments were repeated.

Lattice implants (0.9 mm × 0.3 mm) could be manufactured with the 2PP system with 0.3 volume fraction without structures collapsing at 50 mW laser power and 33 mm/s writing speed (see **Figure 6.3**). However, two main issues were observed. First, the manufacturing time per implant was long (50 min for LSA, 60 min for MSA and 80 min for HSA), as the system manufactures one implant at a time voxel by voxel. Considering that many implants per design would need to be produced to perform further experiments with them (i.e., cell viability, drug release, etc), the production line with the 2PP system would be too slow. Second, there were size limits on the XY and Z stages of the 2PP system available at that time to our group that did not allow manufacturing structures above 0.3 mm (XY) × 0.4 mm (Z) without the need to use the stitching mode. Briefly, a part of structure is fabricated within the limits of the stage, then the stage is moved to the edge of that manufactured structure and the following part of the sample is manufactured again. This process is repeated several times until the desired dimensions are reached. In this case, for a 0.9 mm length in the XY, three parts of 0.3 mm had to be stitched together. Therefore, with the characteristics and settings of the 2PP system available at that time in our lab, it was not possible to print the implants uninterruptedly in one go. The stitching area is visible on SEM images from **Figure 6.3.**

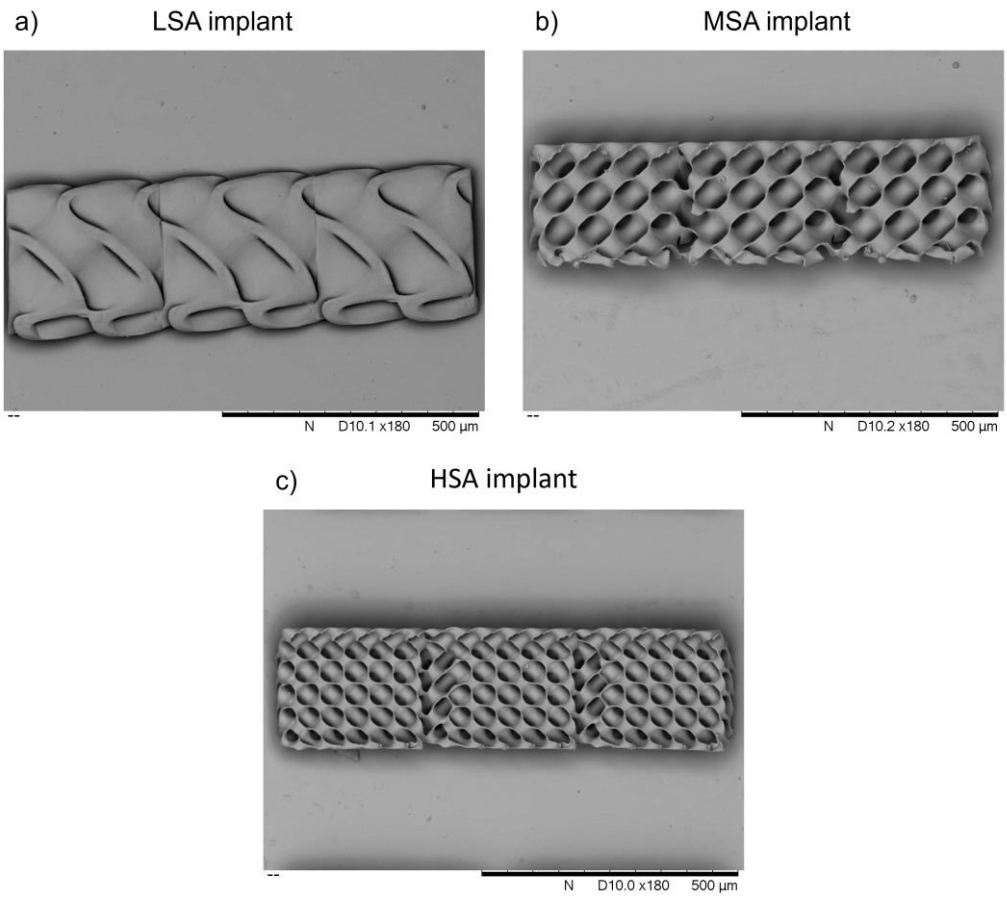



**Figure 6.3. Implant designs (0.9 mm length x 0.3 mm diameter and 0.3 volume fraction) printed with the 2PP system with PTMCA + PEGDA 1:20 molar ratio formulation using the stitching method: a) LSA implant b) MSA implant c) HSA implant. Parameters used for manufacturing all implants: 50 mW laser power and 33 mm/s writing speed. Hatching and slicing distances were both set to 0.4 µm.**

Although the stitching area was visible on all implants shown in **Figure 6.3**, the union between the LSA stitched parts was smooth and with no visible defects present (**Figure 6.3– a**). However, in the MSA and HSA implants (**Figure 6.3– b, c**, respectively), the unions between the stitched parts were not continuous like in the LSA implant. Also, in the stitching area of the MSA implant parts of the structure on the surface seemed broken. It was hypothesised this could have happened due to the wall thickness of the structure being too thin, which could have led to parts of it breaking during the post-processing washing step.

Therefore, to be able to manufacture implants without stitching and in shorter times than the ones the 2PP technique offers, PμSLA was considered as the next step in the optimisation process. This technique would provide a more practical production line for the application.

PμSLA is a vat-photopolymerisation technique that cross-links photo-reactive resins by projecting images layer by layer instead of voxel by voxel (see section **2.2.2** in literature review chapter). It is based on one-photon polymerisation instead of two-photon polymerisation and uses UV as light source instead of near-infrared light. Although the resolution obtained with PμSLA (finest feature: 0.6 μm) is not as high as the one obtained with 2PP (finest feature: 100 nm) [18], it is still acceptable for this application and allows much faster printing times. Also, the size limit of the printing area in our PμSLA system with the small vat was bigger (2 mm × 2 mm × 2 mm) than that of the 2PP machine (0.3 mm × 0.3 mm × 0.4 mm). It would allow to manufacture implants with a height of up to 2mm without needing stitching. It would also allow printing several implants at the same time. For implants with 2 mm × 0.5 mm dimensions, the PμSLA system would be able to manufacture 9 designs in one printing session. The standard vat of the PμSLA system (could manufacture structures of up to 50 mm × 50 mm × 10 mm) was discarded due to the high amounts of formulation needed for fabrication (400 mL), which would have made it unpractical for printing considering that preparing that amount of formulation for one printing session would have taken weeks.

Thus, the following step was to optimize the PTMCA + PEGDA 1:20 molar ratio formulation for PμSLA testing by determining the photoabsorber concentration needed to obtain the resolution needed to manufacture the lattice implants (see following section).

#### 6.2.2.2 Determination of photoabsorber concentration for PTMCA + PEGDA formulation for PμSLA manufacturing

**Acknowledgements:** The formulation optimisation of determining the curcumin wt% to be added to the formulation and the optical microscope analysis from **Figure 6.4** were carried out by Dr Yinfeng He (University of Nottingham).

To successfully manufacture at high resolutions with PμSLA systems, a photoabsorber must be added to the formulation to control the cure depth during printing. The photoabsorber selected was curcumin, a commonly available lipophilic food dye that has shown biocompatibility in previous works [137-139]. Zhu *et al.* studied the effect of curcumin on human aging retinal pigment epithelial (RPE) cells and observed that curcumin improved cell viability and decreased apoptosis and oxidate stress [138]. There have also been reports mentioning a cytotoxic effect of curcumin on human RPE cells but this cytotoxicity was only visible above certain concentrations of curcumin (>10 μM) [140]. Its lipophilicity would allow for good mixing with the PTMCA + PEGDA formulation. Its potential biocompatibility and its potential anti-inflammatory effect [141] could also make it potentially suitable for ocular bioapplication. Therefore, two concentrations of curcumin as photoabsorber for the implant formulation were considered for testing: 0.5 wt% and 0.75 wt%. PTMCA + PEGDA 1:20 molar ratio formulation was tested with both curcumin concentrations. The formulation with 0.75 wt% of curcumin allowed to manufacture well-defined rectangular and cylindrical lattice structures (see **Figure 6.4**).

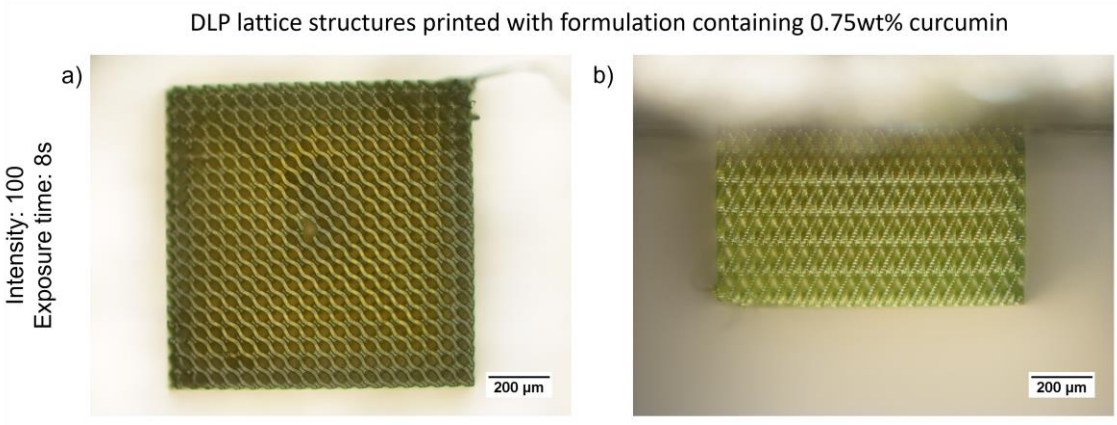



**Figure 6.4. Structures manufactured via DLP by Dr Yinfeng He using PTMCA + PEGDA 1:20 molar ratio formulation containing 2 wt% PI and 0.75 wt% curcumin**

The structures from optical microscope images **Figure 6.4- a, b** showed well-defined lines and pores throughout their lattice design. This indicated that this formulation could be suitable to manufacture the lattice implants with adequate resolution for their features. Therefore, this was the selected percent of curcumin for following experiments (for cell viability and cell cytotoxicity effects of this curcumin percent, see section **6.2.6**).

#### 6.2.2.3 Manufacturing lattice implants with DLP system using PTMCA + PEGDA formulation with 0.75 wt% curcumin photoabsorber

The PTMCA + PEGDA 1:20 molar ratio with 0.75 wt% curcumin was the mixture chosen to be tested in the PµSLA system. For this printing system, the design files were obtained using an in-house software developed by Eric Lehder (PhD student, CfAM, UoN), which was based on the work of Maskey *et. al* [134]. While Maskery's software (FlattPack) exports files in stl format suitable for the 2PP printer, Lehder's software allowed to export the lattice designs as portable graphic (png) file image stacks that are required for PµSLA systems (see designs prepared for PµSLA printing in **Figure 6.1**).

By using the selected formulation with the parameters optimized by Dr Yinfeng He (100 % intensity and 8 s exposure time), 0.9 mm × 0.3 mm lattice implants with 0.3 volume fraction were manufactured with the PµSLA machine. The first test was not

successful as several implants detached from the platform during printing. To avoid this issue, a rectangular support structure of 0.1 mm thickness (parameters for the support structure: 100 % intensity and 12s exposure time) was added to the design to keep the implants from detaching during manufacturing. The support structure avoided detachment and allowed for the successful manufacturing of 9 samples in 40 min. Once manufactured, implants were carefully removed from the platform with a razor blade and unreacted resin was washed away by submerging the implants in IPA for 4 h (see methodology in section **3.3.1.6.2**). After washing, the implants were dried, and further cross-linked in a UV oven for 15 min at 40 ºC and 405 nm wavelength (see full methodology in section **3.3.1.6.2**). The post-processed implants were analysed via SEM (see **Figure 6.5**)

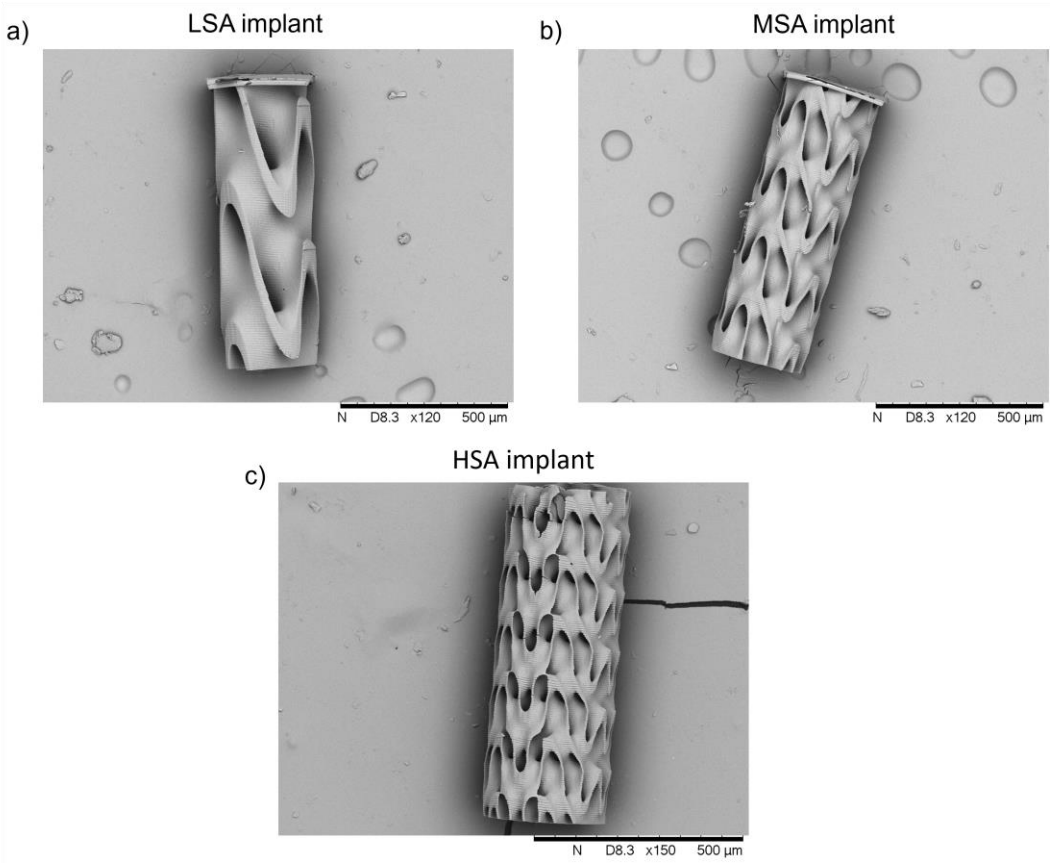



**Figure 6.5. Lattice implants (0.9 mm × 0.3 mm) manufactured *via* PµSLA using PTMCA + PEGDA 1:20 molar ratio mixture with 0.75 wt% curcumin as photoabsorber. Parameters used for manufacturing were 100 % intensity and 8 s exposure time. The layer thickness was set to 10 µm.**

The LSA, MSA and HSA implants manufactured with the PμSLA system showed well-defined features and pores, confirming that good resolution for diamond lattice structures can be obtained with the selected formulation and printing technique. It can be appreciated in images from **Figure 6.5– a, b** that part of the support structure at the bottom of the LSA and MSA implants was still present after detachment, while the HSA implant (**Figure 6.5– c)** was detached completely from the support structure. This was caused by the variability introduced by the manual detachment of the implants from their support structure using a razor blade.

The PμSLA system allowed to successfully manufacture 9 implants with good resolution in 55 min while the 2PP system would take between 1 h and 1 h 20 min (depending on the design) to manufacture one implant of the same size. This showed that the PμSLA system is more practical as a printing technique for this application and it was selected as the definitive manufacturing method for further optimisation to reach the targeted dimensions from section 6.2.1 (2 mm × 0.5 mm).

### 6.2.3 Selection of optimal NVP concentration in PTMCA + PEGDA formulation and sustained Rhodamine B drug release from PTMCA + PEGDA+NVP UV cast structures

To select the most suitable concentration of NVP for the PTMCA + PEGDA formulation that would help to achieve the desired sustained drug release from manufactured samples, the following steps were taken. Firstly, Rhodamine B was chosen as a model drug, as its characteristics would easily allow to visually observe if there was release during the experiment as well as easily quantify said release via fluorescence microscopy. Secondly, several PTMCA based formulations containing different weight percent of PEGDA/NVP were prepared (see section **3.3.1.20** for methodology) and 0.1 wt% of Rhodamine B was added to all of them (see **Table 6.1**). Previous work developed by Ruiz-Cantu *et al.* showed that 3D inkjet-printed implants with 50 wt% PTMC methacrylate formulated

with 25 wt% PEGDA and 25 wt% NVP allowed for sustained drug release of pitavastatin over a period of 60 days [117]. Therefore, to determine which concentrations of PEGDA/NVP would be suitable for an acrylated PTMC and Rhodamine B as model drug instead of pitavastatin, formulations reported in **Table 6.1** were developed. This was done by maintaining constant the PTMC wt% and varying the NVP/PEGDA from 15 wt% to 40 wt%.

**Table 6.1. Formulations prepared for UV-cast implants by maintaining a constant 50%wt of PTMCA while varying the wt% of PEGDA and NVP. All formulations had 2wt% (of total weight of all materials) of PI added and loaded with 0.1%wt (of total weight of all materials) of Rhodamine B.**

| Formulation No | PTMCA (wt%) | PEGDA (wt%) | NVP (wt%) |
|---|---|---|---|
| 1 | 50 | 35 | 15 |
| 2 | 50 | 30 | 20 |
| 3 | 50 | 25 | 25 |
| 4 | 50 | 15 | 35 |
| 5 | 50 | 10 | 40 |

Those formulations were then used to UV cast rectangle-shaped implants that were measured, weighted, and then submerged in 5 mL PBS media at 37 ºC and monitored for 39 days (see section **3.3.1.20** for more details on methodology). The size of the casted implants was 0.6 cm × 0.3 cm× 0.1 cm. At specific time points, the extracted media was analysed using a plate reader to determine its absorbance (see section **3.3.1.17**).

The results indicated that the co-polymerisation of NVP to the PTMCA and PEGDA mixture helped to accelerate the drug release and degradation of the samples in PBS without the need for enzymes to be present in the media. They also indicated that there is

an NVP concentration threshold above which significant results on drug release can be obtained. Samples that were manufactured with formulations containing 15 wt% and 20 wt% NVP did not show Rhodamine B release during the duration of the experiment. Although slight differences can be seen under optical microscope and SEM on the surface of samples prepared with 15 wt% and 20 wt% NVP. The 20 wt% NVP rectangles show some porosity and cracks visible on their surface compared to the smooth surface of the 15 wt% NVP specimens after 39 days in PBS media (**Figure 6.6**).

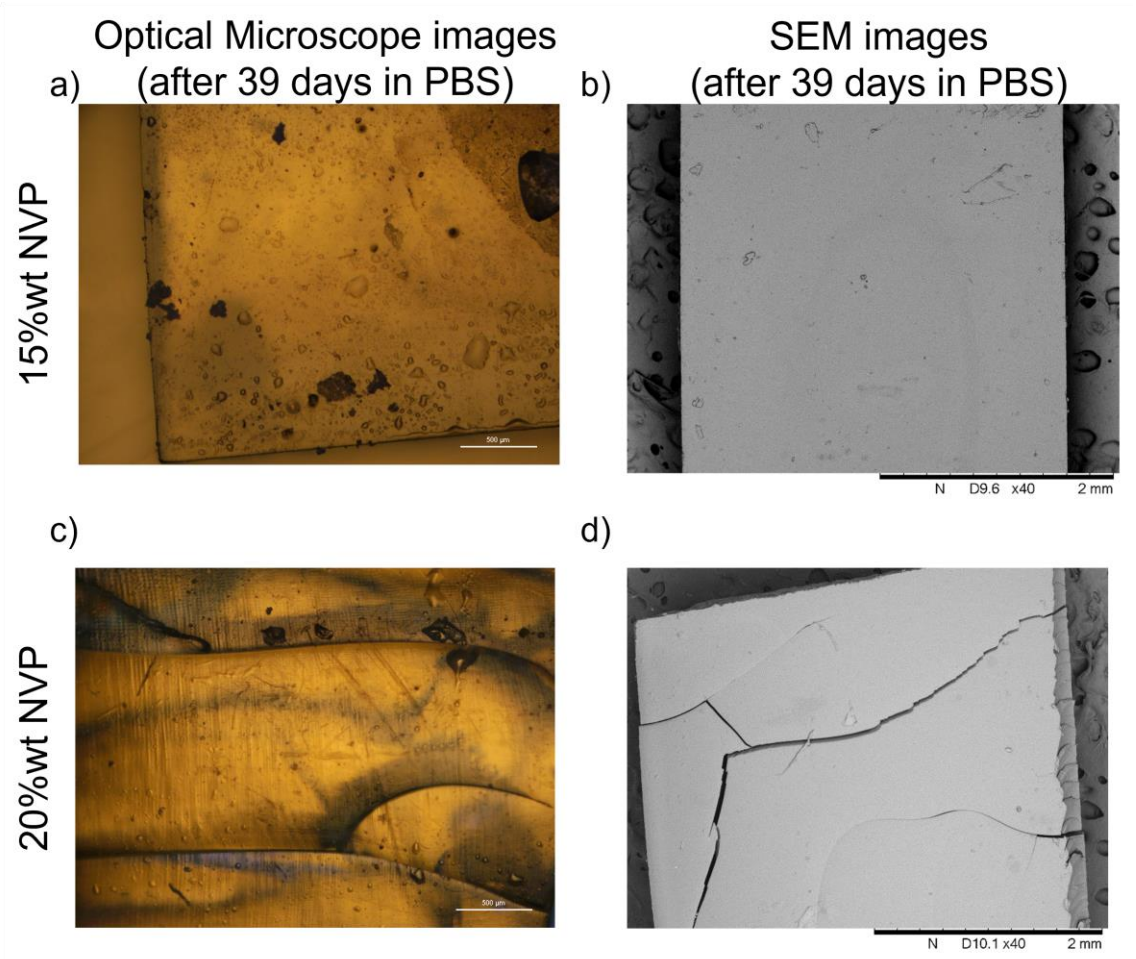



**Figure 6.6. a) Optical microscope image from the surface of a 15 wt% NVP UV-cast implant after 39 days in PBS. b) SEM image of the same sample shown in image a). c) Optical microscope image from the surface of a 20 wt% NVP UV-cast implant after 39 days in PBS. d) SEM image of the same sample shown in image c).**

However, this difference does not translate into their drug release results, as neither of these two formulations manufactured samples that released Rhodamine B.

On the other hand, samples cast with formulations containing 25 wt%, 35 wt%, and 40 wt% did show a significant release and these results can be seen in **Figure 6.7**.

The analysis of the submerged samples manufactured with 25 wt% NVP under SEM showed changes on their surfaces when comparing the top views of the structures from day 0 and day 39 (**Figure 6.7– a, b**). The mass loss of the samples (determined with **Equation 3.10** from section **3.3.1.23**) was more accentuated as the percent of NVP in the formulation increased. Structures prepared with formulations that contained 40 wt% NVP reached 35 % mass loss compared to the 13 % mass loss reached with samples of 25 wt% NVP (**Figure 6.7- c**). The SEM images and mass loss results supported the initial hypothesis about the NVP addition and indicated that the PVP was potentially successful in creating porosities inside the PTMCA and PEGDA matrix and dissolved in the PBS. The results indicated that for PVP to have this effect on manufactured samples, the concentration of NVP monomer in the mixtures should be 25 wt% or more. Under that concentration, the cross-linked PVP present in the matrix is not sufficient to induce significant porosity that would impact the drug release and degradation of the samples.

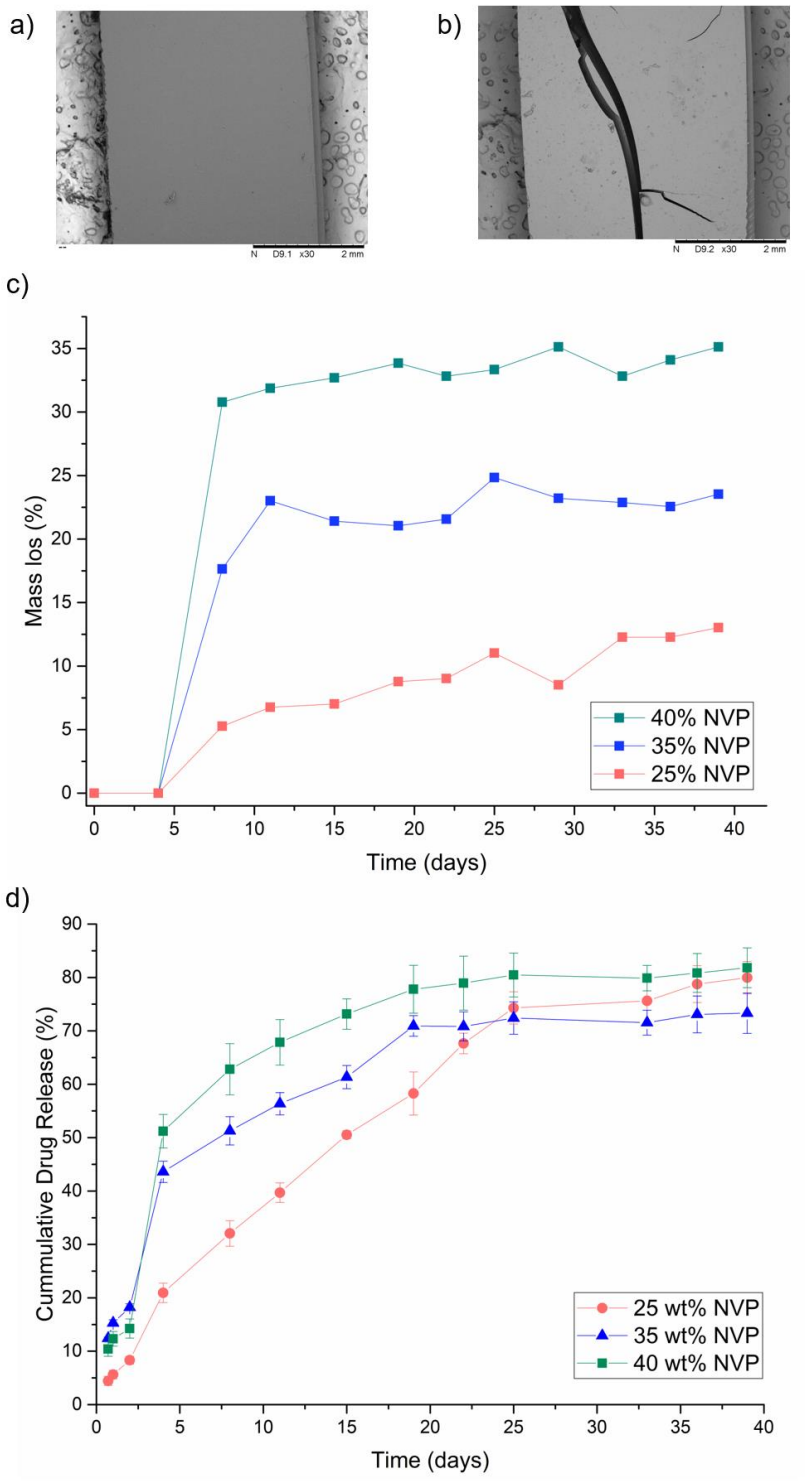



**Figure 6.7. a) Sample manufactured with formulation containing 25 wt% NVP on day 0 before being submerged in PBS. b) 25 wt% NVP sample on day 39. c) Mass loss of the UV-cast samples at different time points. d) Cumulative drug release of Rhodamine B from samples prepared with formulations containing 25 wt%, 35 wt%, and 40 wt% NVP. Data points from c) and d) show Mean values (n=3) ± SD.**

The release of Rhodamine B from structures prepared with the three different formulations showed a constant steady release from 25 wt% NVP samples throughout the time of the experiment (**Figure 6.7 - d**). Samples manufactured with 35 wt% NVP and 40 wt% NVP showed a burst release between day 4 and day 8 continued by a steady increase of drug release until day 25 when they started to reach a plateau. The burst release could be linked to the significant change in mass loss of 35 wt% and 40 wt% NVP samples between day 4 and day 8. Between those two time points, a significant part of PVP was dissolved in PBS which also could have caused a significant release of Rhodamine B in the media. On day 39, all samples had released between 74 % and 81 % of the drug (see section **3.3.1.22** for theoretical drug loading and cumulative drug release calculations), with those prepared with the highest concentration of NVP releasing the most.

These results indicated that the formulation prepared with PTMCA + PEGDA + NVP could enable drug release due in part to the porosity that the PVP induced in the samples and the solubility of any linear PVP present in the network in PBS and water. They also indicated that there is an NVP concentration threshold above which significant results on drug release can be obtained. This allowed for a sustained release of the model drug over 5 weeks at 37 °C. These samples might be able to release all the model drug loaded over several months. Therefore, they could be suitable for long-sustained drug release applications like implants.

### 6.2.4 Determination of maximum drug loading of FA to PTMCA + PEGDA + NVP formulation

To determine the maximum amount of corticosteroid drug that could be loaded into the PTMCA 50 wt% + PEGDA 25 wt% + NVP 25 wt% formulation, several vials with mixture were prepared, and different drug quantities were added to them to mix

(following the methodology from section **3.3.1.5.3**): 2.5 wt%, 5 wt%, 6.25 wt%, and 8 wt%. From these concentrations, only 8 wt% saturated the formulation (see **Figure 6.8**).

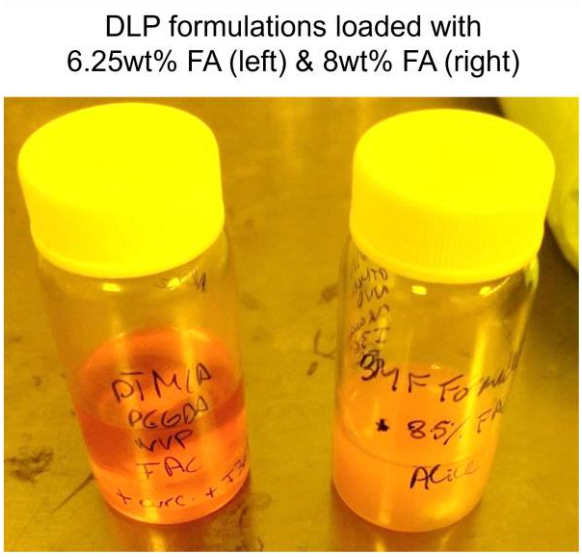



**Figure 6.8. Left vial: DLP formulation prepared with PTMCA/PEGDA/NVP and 0.75 wt% curcumin loaded with 6.25 wt% FA after 24h stirring at 60C. The clear formulation indicates adequate mixing and drug incorporation into the mixture. Right vial: DLP formulation prepared with PTMCA/PEGDA/NVP and 0.75 wt% curcumin loaded with 8 wt% FA after 24 h stirring at 60 ºC. The solution is visibly saturated.**

With this observation, new formulations were prepared with 6.5 wt% and 7 wt% of FA to determine the maximum concentration of drug that could be added to the mixture before saturating the formulation. In this case, both solutions were saturated. Therefore, the maximum drug loading achieved without saturating the solution was 6.25 wt% of FA.

### 6.2.5 Manufacturing optimisation of final implant prototypes loaded with FAc drug *via* PµSLA

The final formulation (Formulation 3, **Table 6.1)** with the addition of 0.75 wt% curcumin, 2 wt% PI, and 6.25 wt% FA (curcumin, PI, and FA wt% calculated from the total weight of materials) was then tested into the PµSLA system. The file prepared for

printing allowed for manufacturing 9 implants of 2 mm × 0.5 mm (3 LSA, 3 MSA, and 3 HSA) in one session (see section**3.3.1.6.2** for PμSLA manufacturing methodology). The printing parameters discussed in section **6.2.2.3** for PTMCA + PEGDA 1:20 molar ratio formulation (100 % intensity and 8 s exposure time) had to be modified as those did not polymerise the resin. It seemed that the NVP addition had reduced the reactivity of the mixture, as it reduced the number of difunctional groups in the formulation by substituting part of the PEGDA in the mixture. The UV light intensity had to be increased to counteract this effect. The initial parameter set that allowed to manufacture all 9 implants were 195 % intensity and 7.5 seconds of exposure time. However, all 3 designs showed poor resolution. It seemed that the exposure time was too high because the features of the implant were not well defined, and they seemed to merge (see **Figure 6.9**).

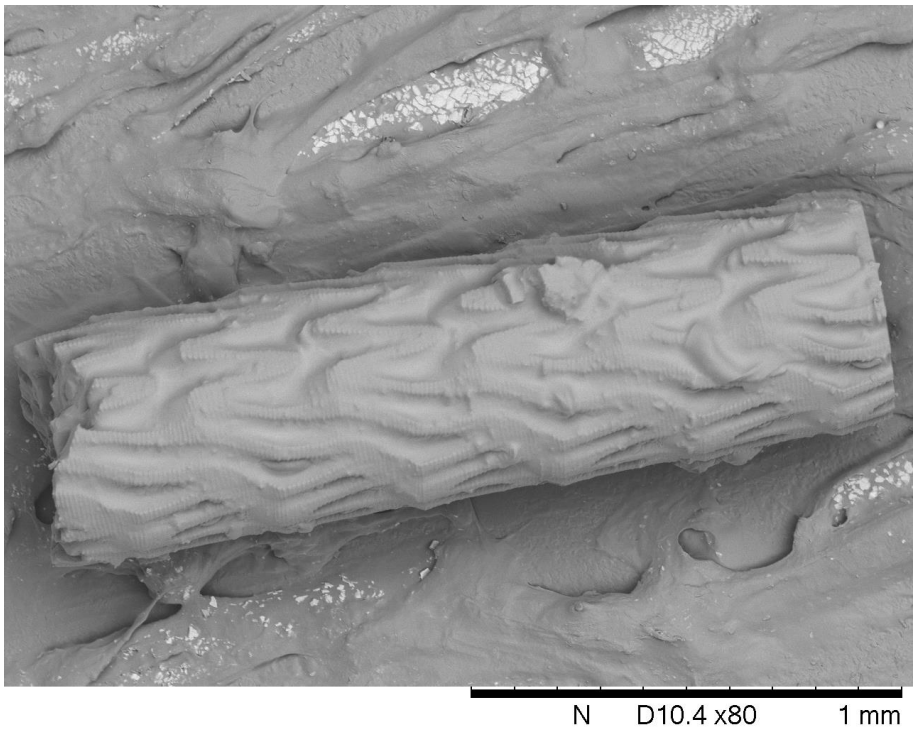



**Figure 6.9. HSA implant manufactured with PμSLA system at 195 % intensity and 7.5 seconds exposure time. SEM image shows sample after post-processing steps (24 h washing in IPA and 15 min UV oven at 40 ºC).**

To obtain better resolution while shortening the printing times, the intensity was kept the same (195 %) and the exposure time was lowered in steps of 0.5 seconds to as low as 4.5 seconds. The parameter set that allowed good manufacturability of the implants was 195 % intensity and 4.5 seconds of exposure. However, a couple of issues were observed while manufacturing. On one hand, in some printing sessions, some of the implants would detach from the platform as they had previously done while printing at smaller scale with PTMCA + PEGDA 1:20 molar ratio mixture (see section **6.2.2.3**). The reason for detachment was hypothesised to be related to the small amount of design that is initially in contact with the platform in the first layer, which would not allow a strong attachment to the platform of the initial layers. To avoid this problem, a support structure of 100 µm height (10 layers) was added again at the bottom of the implants to strengthen their attachment to the platform, as it was done in section **6.2.2.3**. The exposure time was varied throughout the 10 layers of the support structure (40 seconds for the first 4 layers and 20 seconds for the following 6). By doing this, the first four layers would be strongly attached to the platform and the following 6 layers would allow enough attachment of the implant to the support structure while also allowing the implants to be easily detached from the support structure once printing was finished. On the other hand, another problem was that the HSA design would collapse while printing. This could be due to the walls of the structure being too thin to support the structure when scaling up from 0.9 mm × 0.3 mm to 2 mm × 0.5 mm. This issue was previously noticed in section **6.2.2.1** when scaling up 2PP implants from 0.1 mm × 0.03 mm with 0.2 volume fraction to 0.9 mm × 0.3 mm. In section **6.2.2.1**, the problem was solved by increasing the volume fraction from 0.2 to 0.3. In the case of scaling up to 2 mm × 0.5 mm, the volume fraction of the implants was increased from 0.3 to 0.4. Therefore, the final printing file contained 9 implants of 1.9 mm × 0.5 mm with a volume fraction of 0.4 and a support structure of 0.1mm. This file printed at 195 % intensity and 4.5 seconds exposure time allowed to

manufacture all implants with good resolution, with none of the issues previously detected (see **Figure 6.10).**

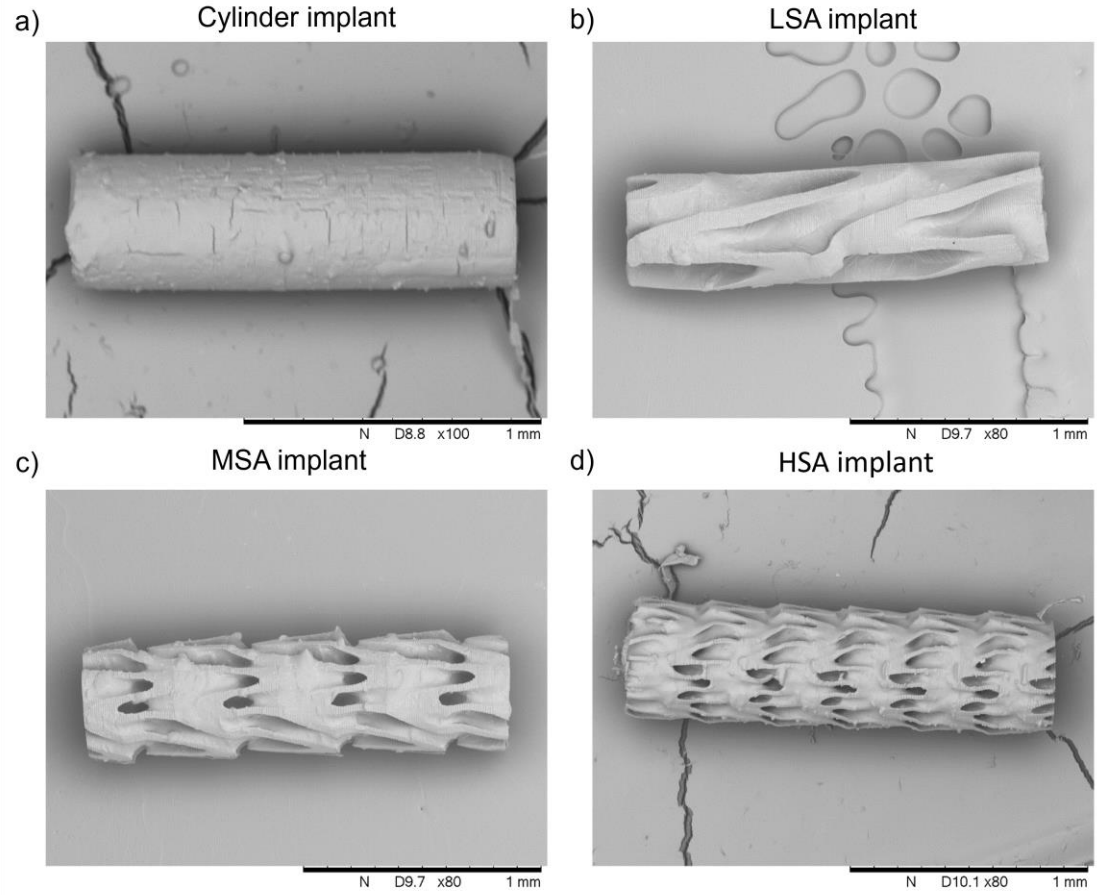



**Figure 6.10. PμSLA manufactured 1.85 ± 0.05 mm implants with PTMCA + PEGDA + NVP + FAc + curcumin + PI formulation: a) Cylinder implant b) LSA implant c) MSA implant d) HSA implant. SEM image shows samples after post-processing steps (24 h washing in IPA and 15min UV oven at 40°C).**

Once printed and analysed under SEM (see methodology in section **3.3.1.10**), their length was measured with ImageJ (see section **3.3.1.25**). The implants showed a length of 1.85 ± 0.05 mm. This was close to the 1.9 mm of the file. The 0.05 mm error was assumed to be related to manual measuring errors in ImageJ. The error could also be related to

small tears caused to the implants while removing them from the support structure, but no such tears were visible during SEM analysis.

### 6.2.6 Biocompatibility of drug loaded diamond lattice implants

**Acknowledgements**: Cell viability assays were carried out by Lydia Beeken (PhD student, Queens Medical Centre, University of Nottingham).

To assess the cytotoxicity of the implants manufactured and shown in **Figure 6.10**, *in vitro* biocompatibility tests were performed on them (see section **3.3.1.24**). Two assays were performed: a PrestoBlue metabolic activity assay (see methodology in section **3.3.1.24.4**) and a Lactate dehydrogenase (LDH) membrane disruption assay (see section **3.3.1.24.5**). PrestoBlue is an assay based on the reduction of the compound resazurin (non-fluorescent) to resorufin (fluorescent) during the cellular respiration process, which allows to determine the number of metabolically active cells [142]. On the other hand, LDH assays assess the cellular plasma membrane damage. When the membrane is damaged, LDH is released into the cell culture medium and participates in a chain of reactions that reduce a tetrazolium salt to red formazan (fluorescent) [143]. Both assays were performed on printed implants using human corneal epithelial cells (HCE2). Normally, for *in vitro* tests performed on intravitreal implants the most suitable and commonly used cell line would be human retinal pigment epithelial cells (ARPE-19) [144]. However, viability and cytotoxicity assays with RPE cell line could not be performed during the project's timeline due to unforeseen circumstances related to the COVID-19 pandemic. To obtain an indicative eye cytotoxicity for the implants in the project's timeline, HCE2 cells were selected as they were already available for experiments. Therefore, PrestoBlue and LDH assays were chosen to be performed with HEC2 cell line, as they have previously demonstrated their efficacy in viability and

cytotoxicity determination on this cell line [142, 145, 146]. The results of these experiments can be found in **Figure 6.11**:

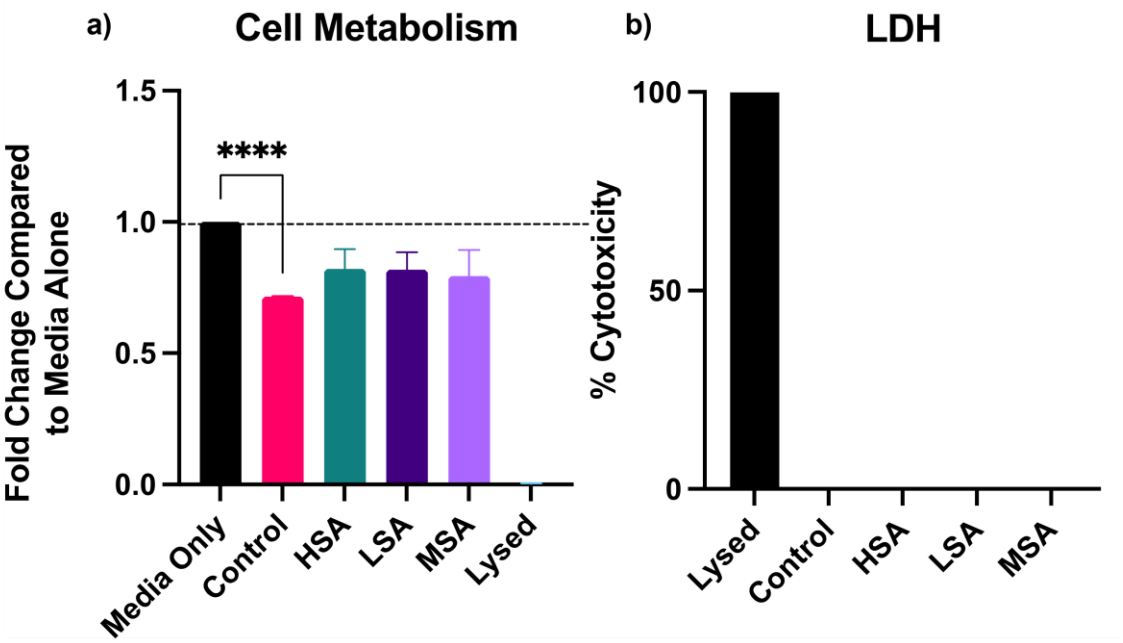



**Figure 6.11. Results from assays performed on all printed implants (cylinder (Control) plus lattice designs) with HCE2 cells: a) PrestoBlue assay results showing the fold change of the cells on the Y axis vs the positive control (media only), negative control (lysed) and the implant designs. b) LDH assay results showing the calculated percent of cytotoxicity for all implants plus the lysed cells. N=3 (3 x cell samples at different passages), n=3 (3 x implant technical repeats / sample). Data points show the Mean ± SD. Statistical significance was determined via ONE WAY Anova followed by Tukey test.**

The results from the PrestoBlue assay are shown in **Figure 6.11– a**. The positive control was set as the metabolic activity from cells cultured with media only while the negative control was set as the metabolic activity detected from lysed cells. The viability of lattice implants (LSA, MSA, HSA) showed no statistical significance with that of the positive control while the control implant (cylinder) did show a statistically significant difference in fold change compared to that of the positive control. All implant designs were manufactured and post-processed following the same methodology. Therefore, there was no clear reason for this statistical difference for cylinder control implants. It was

hypothesised that perhaps control implants would need longer washing and UV curing post-processing methods. However, this would need to be tested with further experiments as no clear conclusions could be extracted at this time with the available results.

The results regarding the LDH cytotoxicity assay are shown in **Figure 6.11– b**. As explained in section **3.3.1.24.5** (methodology), the maximum LDH was determined using lysed cells while the spontaneous LDH is determined by using cells cultured with only media. The results shown on the graph indicated that the implants did not release more spontaneous LDH than the cells cultured with media only. In this assay, no statistical difference was detected between the control cylinder design and the lysed cells while a statistical difference was detected in the PrestoBlue assay between the cylinder and the positive control. It was hypothesised that this could indicate that the cylinder design might have disturbed the metabolic activity of the cell, but it might not have caused damage to the membrane of the cells. Therefore, these results suggested that the implants were not membrane damaging to HCE2 cells.

Results obtained from both assays indicated a high biocompatibility of the implants, which would make them suitable candidates for bioapplications targeting ocular therapy. However, to assess that these implants could be potentially used for intravitreal applications, further *in vitro* viability and cytotoxicity assays should be performed using human RPE cell line.

### 6.2.7 Microstructure characterization of PμSLA structure manufactured with implant formulation

To better understand the microstructure and material disposition of PμSLA implants, a rectangle (1 mm × 1 mm×0.4 mm) was printed (see section **3.3.1.6.2**) and analysed *via* ToF – SIMS (see section **3.3.1.12.4**). A rectangle geometry was chosen for the experiment instead of the lattice-based cylinders geometry of the implants to facilitate the analysis of

the sample. Besides the printed sample, control samples of each material of the formulation were prepared by mixing the monomer/oligomers with 2 wt% photoinitiator (plus acetone solvent in the case of PTMCA to reduce viscosity and facilitate mixing). Then, a drop of each material with photoinitiator was cross-linked under UV light. These samples as well as FA powder were also analysed with ToF-SIMS (see section **3.3.1.12.4** for methodology) to obtain spectra of the individual components of the implant formulation. From the spectra, peaks of negative secondary ions representative of each formulation component were identified and selected for depth profile analysis of the 3D printed rectangle The results of these experiments can be seen in **Figure 6.12**.

Several secondary ions were detected from spectra of PTMCA, PEGDA, PVP, and FA (see **Figure 6.12– a**). For PTMCA, PEGDA, and PVP materials the characteristic ions were detected in the 0 to 150 m/z area. For FA, the $F^-$ ion was detected at 19 m/z while the rest of the characteristic ions of the drug were detected in the 350 to 450 m/z area. The combined intensities of the secondary ions of each material and drug were used to trace their disposition throughout the printed sample and recreate a 3D depth profile map. This 3D reconstruction map can be observed in **Figure 6.12– b**. The results displayed in the map indicated some phase separation in the sample. PTMCA and PEGDA materials were well dispersed throughout the whole structure while PVP seemed to concentrate more on one side of the structure than the other. The results also indicated a FA preference to migrate towards the region where the PVP polymer matrix was concentrated, as it followed the same phase separation pattern in the microstructure of the sample as that of the PVP material.

This possible FA preference for PVP was further reinforced with the drug release results from lattice implants (see section **6.2.8**), as the release of FA seemed to follow the hydrolysis pattern of the PVP matrix and its dissolution into PBS media.

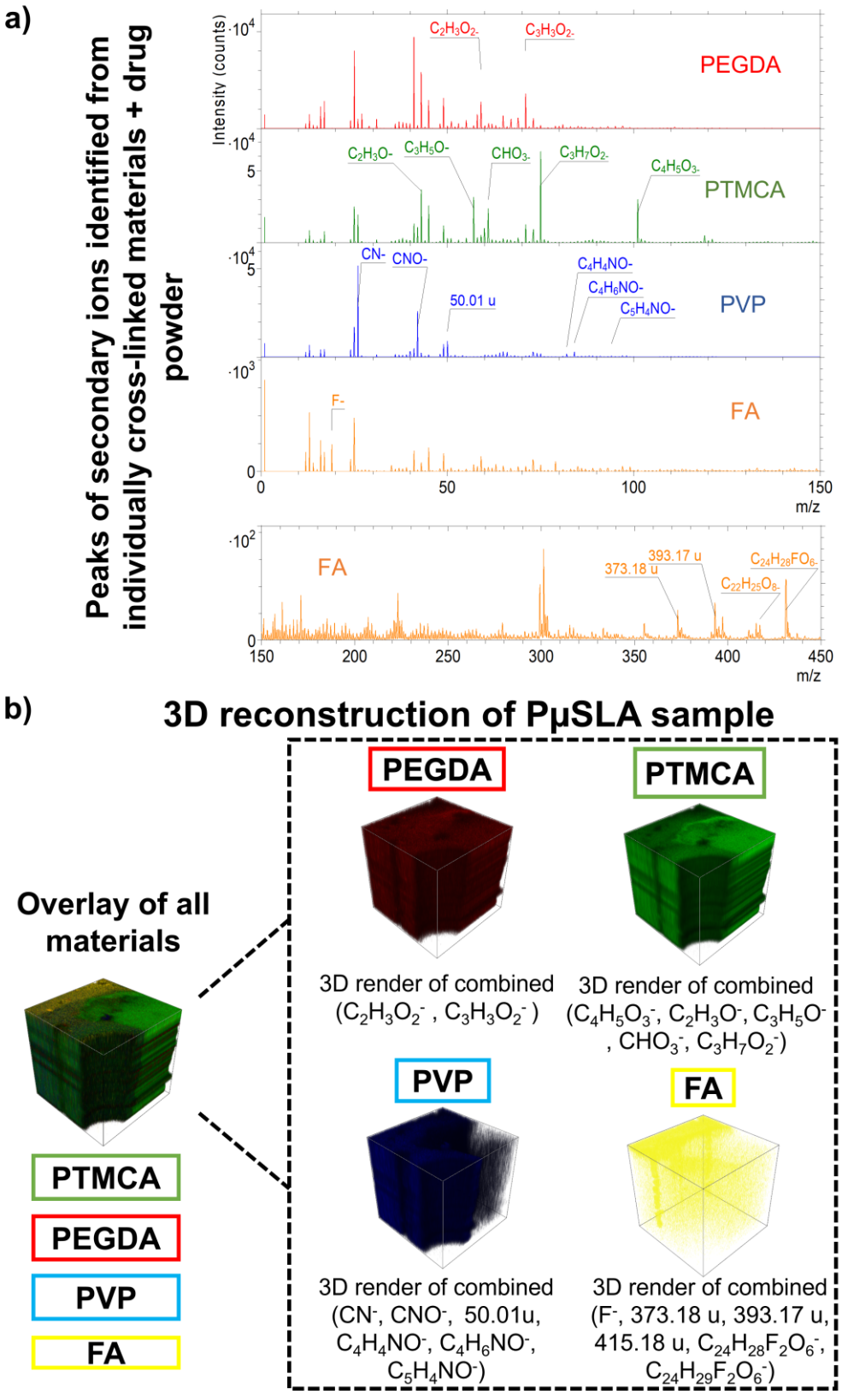



**Figure 6.12. a) ToF-SIMS spectras highlighting the peaks of secondary ions identified from each individual implant formulation component. b) ToF-SIMS 3D reconstruction of PµSLA manufactured rectangle with data obtained from depth profile analysis. All samples were analysed in triplicates.**

### 6.2.8 Drug release of Fluocinolone Acetonide from lattice implants manufactured *via* PμSLA

The lattice implants shown in **Figure 6.10** that demonstrated good biocompatibility in the previous section (see **Figure 6.11**) were submerged in 1.5 mL PBS media for 35 days at 37 ºC and the corticosteroid drug release was monitored at specific time points. The FA release was detected via HPLC at 238 nm (see methodology in section **3.3.1.21**). and at a retention time of 5.8 min. The cylinder control implant (**Figure 6.10– a**) could not be tested due to unforeseen circumstances. Therefore, drug release data for this implant design was not included in this section.

The drug release profiles obtained from LSA, MSA and HSA implants can be seen in **Figure 6.13**:

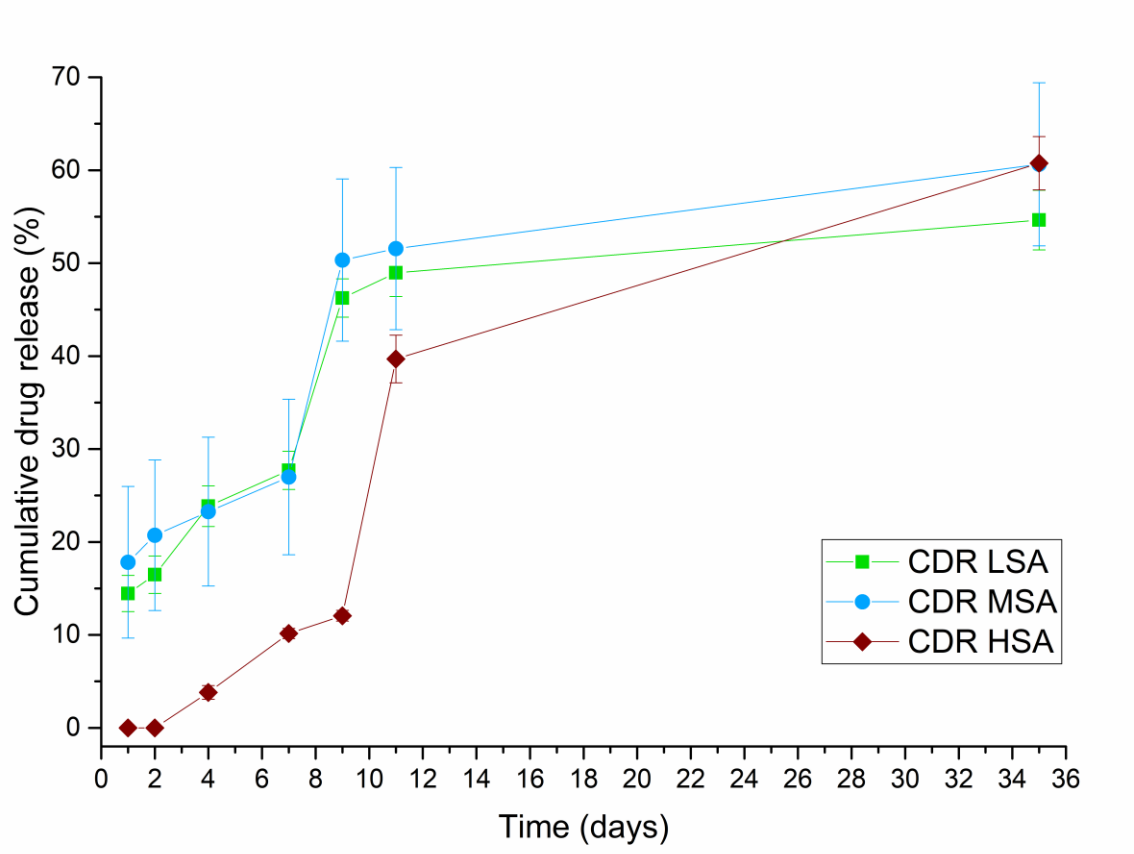



**Figure 6.13. Cumulative drug release values obtained from LSA, MSA, and HSA implants over 35 days. Data points show Mean values (*n* = 3) ± SD.**

The cumulative drug release results shown in **Figure 6.13** indicated that implants could release FA over a month. They also indicated that the different lattice designs might affect the drug release profile of the implants. Each implant was calculated to be loaded with 9.8 µg of drug (see section **3.3.1.22** for theoretical drug loading and cumulative drug release calculations). MSA and HSA implants released 60.6 % ± 8.7 % and 60.7 % ± 2.8 % of loaded drug over 35 days, respectively, while LSA implants released 54.6 % ± 3.2 %. This indicated that on day 35, there was no statistical difference ($p > 0.05$) between the percent of drug released by the three different implants. However, the results indicated a difference in the release profiles of HSA *vs.* MSA and LSA. The LSA and MSA implants followed a similar release profile, with an initial burst release of around 15 % in the first 24 h. This was followed by steady increases until a second burst release was observed between days 7 and 9. After the second burst release, the implants continued to slowly release drug until the last day of the experiment. For the HSA implant, the release was initially slower, with 3.8 % ± 0.7 % FA only being detected on the 4$^{th}$ day. It then continued to slowly release drug until a significant increase in release was observed between days 9 and 11, going from 12 % ± 0.5 % on day 9 to 39.7% ± 2.5 % on day 11. From this time point to the next, the implant continued releasing drug until reaching 60 % ± 2.8 % previously mentioned.

It was hypothesised that the burst release observed in all three implants could be related to the dissolution of PVP in PBS media. As shown in ToF-SIMS analysis, the FA might concentrate in the PVP region. Therefore, its dissolution could also lead to a higher amount of drug being released. It was also hypothesised that the different release profiles might have been influenced not only by the surface area of the implants but also by their pore size. The LSA design has a lower surface area than the MSA design. However, the LSA design also has a bigger pore size than the MSA design. This could have influenced both of their releases to be similar despite their different surface areas. In the beginning,

more water would pass through the LSA pores than the MSA ones, helping more PVP to dissolve from the LSA design and release a similar percent of drug as the MSA design. Although less water might have initially flown through the pores of the MSA design, the higher surface area of the design compared to the LSA one could have compensated for that. This mixed influence of surface area and pore size was also hypothesised to influence the release profile of the HSA design. In this case, smaller amounts of water to dissolve PVP would flow through the pores of this design compared to LSA or MSA pores. This could have been responsible for the release starting later and in smaller amounts than with the other two designs. It could have also been responsible for showing only one burst release episode (between days 9 and 11) instead of two episodes like in the LSA and MSA designs. However, the higher surface area of the HSA design compared to the other two might have allowed this implant to accelerate its release from day 9 onwards and reach a similar percent of FA in media as the LSA and MSA implants.

Another aspect to consider regarding drug release would be the disposition of the materials (PTMCA, PEGDA, PVP) throughout the printed samples and the drug affinity for these materials. It was shown by Ruiz-Cantu *et al*. [117] that inkjet printed implants with PTMC methacrylate/PEGDA/PVP formulation presented phase separation in their microstructure, with PVP pockets dispersed throughout the matrix. This further increased the drug release by providing a network through which the drug could elute faster. As shown in section **6.2.7**, the microstructure present in the lattice implants might also show phase separation of the PVP from the PTMCA and PEGDA materials, though less pronounced than in Ruiz-Cantu *et al*'s work. It was also indicated by the TOF-SIMS analysis that the FA might have a stronger preference for the PVP matrix than for PTMCA/PEGDA. Therefore, perhaps like in the case of Ruiz-Cantu *et al*., it was likely that the implant matrix microstructure also influenced the drug release with pockets of PVP dissolving in the media and accelerating the drug release by further increasing

porosity (besides the one created by the implant design) in the matrix. The preference of the drug for the PVP matrix could have also helped to release drug at a faster rate than if the FA was strongly accumulated in the PTMCA material, for example. Therefore, the results obtained from microstructure analysis and *in vitro* drug release indicated that the sample microstructure and the disposition of the drug inside the polymer matrix also influence the drug release rate alongside the implant design.

## 6.3 Conclusions

The work presented in this chapter showed that printing cylinder-shaped implants with diamond matrix lattice designs using a previously developed PTMCA + PEGDA formulation was possible with both 2PP and PμSLA systems. Depending on the implant size and the manufacturing process, the volume fraction of the lattices had to be adjusted to thicken the structure's walls and avoid collapse during printing. Support structures also had to be added when manufacturing with the PμSLA system to avoid structure detachment from the platform. Although both printing systems could manufacture lattice implants, the most suitable system for scale-up was PμSLA. It allowed to produce parts faster than 2PP and smooth structures with no visible stitching sections could be manufactured with it.

This research work also showed that mixtures of PTMCA 50 wt% + PEGDA 25 wt% + NVP 25 wt% were the most suitable for sustainable drug release over a 39 day time period when Rhodamine B was used as a model compound. This formulation allowed for a sustained CDR of 80 % of Rhodamine B from UV-cast samples. Lower NVP concentrations did not release drug while higher concentrations of NVP released a similar amount of Rhodamine B but with stronger burst release effects. Therefore, the formulation containing 25 wt% NVP was taken forward for PμSLA printing optimisation. A final optimised formulation loaded with 0.75 wt% curcumin and 6.25 wt%

Fluocinolone Acetonide was used to fabricate the final lattice implants, with 1.85 mm × 0.5 mm dimensions and 0.4 volume fraction. This showed that drug loaded lattice implants with good resolution could be successfully manufactured via PμSLA. Their biocompatibility was assessed via PrestoBlue and LDH assays with HCE2 cells. These *in vitro* assays showed that the implants did not cause metabolic activity damage or membrane damage to cells, indicating a high biocompatibility. The lattice implants also allowed to release FA in PBS media for the duration of the drug release experiment. At the last time point (day 35), the LSA implant had released 54.6 % ± 3.2 %. of the loaded drug while MSA and HSA implants had released ~60 % of FA. The results indicated that all three designs released a similar percent of FA but different release profiles could be obtained with the different lattice designs. The results suggested that these release profiles were influenced by the surface area, the pore size, and water diffusion through them. With bigger pore sizes (i.e., LSA and MSA implants) accelerating PVP dissolution from the matrix and facilitating more burst release than those implants with smaller pore sizes (i.e., HSA implant) that showed fewer burst release episodes. The influence of PVP dissolution on drug release was further strengthened by ToF-SIMS analysis of the microstructure of a sample, which indicated a phase separation of the PVP in the PTMCA + PEGDA matrix. It also indicated a FA preference of the PVP matrix, as the drug distribution in the microstructure followed the distribution of PVP.

# 7 Conclusions and Future Work

This chapter will be divided into two sections. The first part will provide a summary of the overall conclusions that can be drawn as a result of the research undertaken during this thesis project. The second part of the chapter proposes further research avenues to explore as part of the future work that can expand from this research and its conclusions.

## 7.1 Conclusions

### 7.1.1 Mono-acrylate oligomers for 2PP

Mono-acrylate materials have not been the focus of 2PP research. Multi-functional materials that are more reactive and are considered to produce stronger cross-linked networks than mono-functional materials have been the ones mainly used in the 2PP field. In chapter 4, a new poly(trimethylene carbonate) acrylate (PTMCA) oligomer was synthesised and optimised for 2PP processing in multi-material formulations with diacrylate monomers at different concentrations. Other commercial mono-acrylates with lower $M_w$ and shorter chain lengths were also used to prepare 2PP formulations with the previously mentioned diacrylate monomers at different concentrations. The PTMCA based formulations allowed successful manufacturing of 2PP structures at all concentrations while the commercial mono-acrylate based formulations only allowed successful manufacturing when the diacrylate monomer concentration was significantly high in them. The structures manufactured with PTMCA based multi-material formulations showed a statistically significant RVG % increase when compared to RVG % of structures manufactured with just the commercial diacrylates. Adding PTMCA to those materials can fabricate structures with a nearly 50 % RVG increase

depending on the concentration selected. Formulations that had the highest concentration of PTMCA in them were the ones that manufactured samples with the highest RVG %. These types of mixtures also expanded the polymerisation threshold, allowing to print samples successfully at lower and higher laser powers as well as faster speeds. PTMCA + TCDMDA formulations allowed for microstructure control in the manufactured specimens by selecting specific molar ratios of both materials in the mixture or by selecting specific optimisation parameters of the 2PP system. The presence and disposition of both materials in structures printed with multi-material PTMCA based formulations was analysed and confirmed via ToF-SIMS analysis.

Therefore, the work presented in chapter 4 has expanded the library of materials for 2PP and has opened the door for a new type of materials that can be further explored in this printing field. Materials like PTMCA can be obtained with a simple synthesis method previously developed by Ruiz-Cantu *et al.* [98], that does not require several functionalisation steps and does not use potentially toxic organocatalysts. The ability of PTMCA to be optimised in multi-material formulations with several diacrylate monomers that can successfully manufacture structures with high RVG % and controlled microstructures could allow to create a library of multi-material mixtures and associate them with different properties for those structures.

### 7.1.2 Hyperbranched materials for 2PP

To further expand the library of materials available for the 2PP field, PEGDA and TCDMDA hyperbranched materials were synthesised with carboxylic acid and thiols as functional groups at their terminal ends. Hyperbranched polymers were considered for 2PP as they could be considered “pre-polymerised” networks that could cross-link faster under the laser and would need less energy to do so. This was observed when determining their polymerisation threshold. Formulations containing hyperbranched polymer

significantly broadened this threshold compared to those containing commercial liner monomer. Hyperbranched materials allowed printing at lower laser powers, which can allow manufacturing at higher resolutions due to smaller voxel sizes being used, and at higher laser powers, which could increase the cross-linking density of the structure and influence their mechanical properties. This was tested when printing buckyballs with formulations containing HBpPEGDA + TCDMDA or PEGDA + TCDMDA at similar parameters. The structures produced with HBpPEGDA + TCDMDA formulation showed better resolution and better structural integrity compared to those manufactured with PEGDA + TCDMDA, indicating that the initial hypothesis was correct. Structures manufactured with HBpPEGDA + TCDMDA were also analysed under ToF-SIMS and secondary ions from both materials were detected on the surface and the first couple of μm of in-depth analysis, indicating that multi-material printing with hyperbranched polymers is possible.

Structures manufactured with HBpTCDMDA showed >50 % increase in RVG compared to those printed with linear TCDMDA. For structures printed with formulations containing HBpPEGDA or linear PEGDA, no statistical difference was observed in RVG. Therefore, this indicates that depending on which material is hyperbranched, the RVG can be significantly changed and improved. Scaffolds manufactured with HBpTCDMDA and TCDMDA were assessed for cell viability via LIVE/DEAD assay with mouse fibroblast for 24 h and both materials printed samples with >90 % viability. Thus, the difference in RVG % between HBpTCDMDA and TCDMDA scaffolds might not have an influence on cell viability at 24 h time periods. The cell attachment on the functional groups of the surface of the scaffolds indicated that cells could have a stronger preference for methacrylate and carboxylic acid groups than for acrylate functional groups.

### 7.1.3 Diamond lattice implants manufactured with photo-sensitive formulation for sustained release of FA

The work shown in this thesis related to implant manufacturing highlighted that a selected PTMCA/PEGDA mixture identified in Chapter 4 could be optimised to successfully manufacture diamond lattice cylinder-shaped implants with both 2PP and PμSLA systems. This demonstrated the adaptability of the mono- functional oligomer and of the PTMCA/PEGDA multi-material formulation to be used in several vat-photopolymerisation systems, not only in 2PP printing. It was also shown that for scale-up manufacturing, PμSLA was more suitable than 2PP as it still provided a good printing resolution while offering a faster production line.

The research presented in chapter 6 showed that optimising the PTMCA/PEGDA mixture with the addition of NVP allowed for sustained drug release of Rhodamine B and FA at specific concentrations. The concentration that provided the most suitable sustained release from rectangular UV-cast samples loaded with Rhodamine B was 50 wt% PTMCA + 25 wt% PEGDA + 25 wt% NVP. This formulation allowed to release ~80 % of Rhodamine B over 39 days. This formulation was also used to manufacture FA loaded lattice implants *via* PμSLA and in this case, around ~60 % of drug was released over 35 days. Therefore, the mixture allowed the release of two different drugs from samples produced with two different manufacturing processes.

The FA release from lattice implants showed that different release profiles could be obtained from the same formulation and manufacturing method by changing the design of the implant. Several characteristics such as surface area and pore size showed influence the release profile of FA. It was also shown that the microstructure of these samples showed a phase separation of the PVP in the matrix and a preference for the FA drug for the PVP. Last, the implants presented high viability on cell viability and cell toxicity

assays with HEC2 cell line. This indicated a high biocompatibility for structures manufactured with PTMCA/PEGDA/PVP mixture.

## 7.2 Future Work

### 7.2.1 Further characterization and optimisation for 2PP

The structures manufactured in chapter 4 with the different PTMCA-based multi-material formulations were studied in relation to their RVG %, polymerisation threshold influence and microstructure disposition. One aspect that was not analysed and should be tackled going forward is the mechanical properties of those samples. The mechanical properties of structures printed with TCDMDA, PEGDA, and BPAEDA could be obtained via Atomical Force Microscopy (AFM) or nanoindentation. These techniques could be used again to also obtain the mechanical properties of structures printed with the PTMCA-based multi-material formulations and then compare the influence of the oligomer on the mechanical properties of the printed structures. Therefore, in the future, formulations could be selected for use not only on their advantages over RVG % for example but also by manufacturing structures with the desired mechanical properties for upcoming investigations. Also, if any structures produced with these formulations want to be used in bioapplications, their cytotoxicity should be tested with cell viability experiments for *in vitro* testing. And for further development for bioapplications, their cytotoxicity should also be tested *in vivo*.

The successful manufacturing and the high RVG % that the PTMCA mono-acrylate oligomer has shown in the experiments presented in this work open the door to a new library of materials that could be further developed and explored for 2PP and other laser-based printing. Just as PTMCA/PEGDA mixtures could be optimised for 2PP and PμSLA

systems as shown in chapter 6, other multi-material formulations based on PTMCA could offer this possibility as well.

By needing fewer functionalisation steps in the case of monofunctional materials, oligomers with easier synthesis steps could be produced. These monofunctional oligomers could be formulated with different multi-functional materials to continue expanding the library of multi-material formulations that could be used in vat-photopolymerisation techniques.

In chapter 5, HBpPEGDA and HBpTCDMDA were the materials studied and optimised for 2PP. HBpPEGDA was explored in multi-material formulations with TCDMDA monomer, but new mixtures could be prepared and tested by formulating HBpPEGDA with other monomers or oligomers. As in section **4.2.1**, the Flory-Huggins parameter could be applied to the materials of these multi-material formulations to predict their mixability. The microstructure obtained in these manufactured samples and the presence of specific ions could be analysed with ToF-SIMS, and their RVG % could be determined via Raman Spectroscopy. The mechanical properties of the samples developed in chapter 5 plus others that could be developed in the future with new formulations, could be assessed via AFM or nanoindentation. These results would allow a better understanding of the chemistry behind the printing process and how this influences the characteristics of the printed parts. This knowledge would then allow selecting and tailoring the properties of the manufactured parts for different applications.

### 7.2.2 Exploring controlled phase-separated microstructure in multi-material printing

Chapter 4 showed that depending on the multi-material formulation prepared with mono-acrylate oligomer PTMCA, homogeneous or phase-separated structures could be produced. For PTMCA + TCDMDA mixtures, it was shown that the phase separation

could be controlled *via* the concentration of both materials and via the manufacturing parameters. The controlled phase-separation that can be obtained from samples produced with PTMCA + TCDMDA mixtures could be further investigated in several ways. The effect of the phase – separation on the mechanical properties of the printed samples could be analysed via AFM or nanoindentation. Knowing the different mechanical properties that can be achieved in the homogeneous and phase- separated structures, could lead to the development of a library that would link those mechanical properties to a specific combination of formulation concentration and printing parameters. This library could be accessed to select the adequate combination for the targeted application.

The structures mentioned above could also be explored in drug release applications. Drugs that have more affinity for one material than the other could be mixed into the formulation and their disposition in the microstructure of the printed sample could be manipulated. For example, if a drug that has more affinity for PTMCA is used and the concentration and parameters shown in **Figure 4.8** are used, most of the drug could be entrapped in the centre of the structure. This would give a certain drug release profile different from one in which the drug chosen has an affinity for the TCDMDA monomer and is mainly entrapped around the edges of the structure. Therefore, the phase-separation could be applied in pharmaceutical applications to provide a range of different controlled release profiles. This would have to be tested by studying the different release and degradation behaviours of the phase-separated structures in both *in vitro* and *in vivo* experiments. The cytotoxicity of these structures should also be studied to make sure they could be applied in bioapplications. All these experiments could lead to the creation of another library where the different types of phase-separation that can be obtained would be related to their release, degradation, and cytotoxicity profiles. Researchers would be then able to select the best combination of multi-material formulation and the most suitable processing parameters for their desired application.

### 7.2.3 Cell viability of 2PP manufactured scaffolds with hyperbranched polymers

The cell viability results from section **5.2.5** indicate that scaffolds manufactured with both HBpTCDMDA and TCDMDA monomer materials are both biocompatible in LIVE/DEAD assays performed within 24 h time frames. This experiment was performed with mouse fibroblast cells on 1 mm × 2 mm × 0.02 mm samples. Further cell viability experiments with longer durations, for example 2 weeks or one month, would be beneficial to determine if there would be any changes in cytotoxicity over time. It would also be beneficial to explore the biocompatibility of these scaffolds with different cell lines than the one used in this thesis that would be more suitable for the bioapplication selected. For example, if the goal is to produce scaffolds for bone regeneration, cell viability could be assessed using human osteoblasts cells. If printed parts bigger than those that can be produced with 2PP are be needed for future cell viability studies and applications, these formulations could be optimised for other vat-photopolymerisation systems.

Another aspect indicated by the results from section **5.2.5** is that cells might have different preferences over different functional groups. Further experiments in relation to this should be performed to better explore this alley. This could be done by manufacturing samples with the hyperbranched materials that would show pending functional groups at their surface. These groups could be further functionalised with different chemistries and cell attachment studies could be performed on them to study their preference for the different functional groups. These could be of importance in fields like regenerative medicine, where cell attachment to the scaffolds is desired for the application to be successful. Materials that originally do not exhibit good attachment properties, could be functionalised with the appropriate functional groups to modulate, and improve their attachment properties for the desired application.

### 7.2.4 Improving printing resolution with multi-material formulations

Part of the work developed in chapter 4 and 5 shows how PTMCA based formulations and hyperbranched polymer-based mixtures can significantly expand the polymerisation threshold during printing. This allows good manufacturability at lower laser powers, improving the structure's resolution that can be achieved with those materials, or at higher laser powers, which could improve the mechanical properties of the printed samples. Although part of the work from section **5.2.3** explores the resolution properties that hyperbranched materials can provide in comparison to their linear counterparts, further experiments should be performed in the future to study this research aspect more in-depth. In the case of HBpTCDMDA for example, lines at different printing parameters could be produced to determine the smallest line width that could be achieved with this material. This experiment could be repeated with TCDMDA monomer, and the results could be compared to understand the difference in resolutions that the hyperbranched version of the material could offer. If higher resolutions are needed for certain applications, like microfluidics or lab-on a chip, the formulations that offer this possibility could be selected to develop parts for these fields.

### 7.2.5 Biocompatibility of diamond lattice implants

The lattice implants manufactured *via* PμSLA showed high biocompatibility with HEC2 cells. To further determine if these implants are suitable for an intravitreal application, cell viability and cell cytotoxicity experiments should also be performed using human RPE cell line. Future work should also be carried out to determine the *in vivo* biocompatibility of the implant, which could be studied by implanting them in the vitreous of rabbits and performing a clinical evaluation of the rabbit's eyes after a determined amount of time to detect if any abnormalities and irritation were caused by the implants.

Another important aspect to determine regarding biocompatibility and the future possibility of obtaining approval from notified bodies, is to determine the undegradable portion of the implants. When crosslinked networks form via vat-photopolymerization, there are kinetic chains present in the new network. These kinetic chains, that are carbon-carbon chains that remain after network degradation, are not biodegradable. However, depending on the size of the chains, they can be removed from the body by renal clearance. For example, water soluble polymers with molecular weights > 50 kg/mol can be cleared by the kidneys while polymers with molecular weights > 200 kg/mol cannot be excreted by the kidneys and accumulate in the circulatory system [156]. The chain length of undegradable portions in biocompatible networks have been previously investigated by techniques such as GPC or high-resolution magnetic angle spinning nuclear magnetic resonance (HR-MAS NMR) [157, 158]. Future work should also be carried out to determine the undegradable portion of the biocompatible network developed in the manufacturing of the implants of this thesis. This would help to better understand the biocompatibility of the system and get closer to a potential approval by a notified body.

### 7.2.6 Drug release and microstructure

Lattice implants showed that it is possible to release FA from a degradable matrix over a month. The three different lattice implant designs (LSA, MSA, HSA) showed different release profiles of FA. To further understand the design influence on release, drug release studies with a normal cylinder design should also be performed in the future to be able to compare those results to the release of lattice implants. The four designs should also be tested for longer periods of time to observe the maximum of FA release that could be reached and over how long. Those experiments could be complemented with FA release studies from rectangular samples manufactured *via* PμSLA and rectangular samples

manufactured *via* UV casting. This could provide further insight into the influence of the manufacturing process itself on drug release. ToF – SIMS analysis could also be performed on FA loaded UV-cast rectangles to determine if the manufacturing process would influence the type of microstructure obtained in the sample matrix. The microstructure analysis could also be performed in UV-cast samples loaded with Rhodamine B, to observe the distribution of the materials and drug inside the sample matrix and to confirm if Rhodamine B shows a preference to migrate towards PVP like FA or towards another material of the formulation.

With the results obtained from the future experiments described above, a library could be created with that new knowledge that would allow researchers to tailor the release needed for a specific application. They would do so by selecting the best manufacturing process, structure design, structure microstructure, and drug distribution inside the matrix for the targeted application.

Future work should also be carried out to further increased the drug loading of the FA degradable implants. The commercially available implants that release FA, like Iluvien, are loaded with 0.19 mm of drug. The implants produced in this thesis have the advantages of commercial ones like Iluvien, releasing drug from a degradable matrix and offering different release profiles that could allow to personalise the implant to the needs of each patient. However, they are far from reaching the drug load of the commercial ones. This challenge could be tackled from a formulation point of view, by trying to modify the formulation to allow more drug loading. And it could also be tackled from a fabrication point of view, by increasing the size of the implants for example.

# 8 Bibliography

1. Zhang J, Jung Y-G. Additive Manufacturing: Materials, Processes, Quantifications and Applications. Saint Louis, UNITED STATES: Elsevier Science & Technology; 2018.

2. Gibson I. Additive manufacturing technologies / Ian Gibson, David Rosen, Brent Stucker, Mahyar Khorasani. Third edition. ed. Rosen DW, Stucker B, Khorasani M, editors: Cham, Switzerland : Springer; 2021.

3. Bertsch A, Renaud P. Chapter 1.2 - Microstereolithography. In: Baldacchini T, editor. Three-Dimensional Microfabrication Using Two-photon Polymerization. Oxford: William Andrew Publishing; 2016. p. 20-44.

4. Maruo S, Nakamura O, Kawata S. Three-dimensional microfabrication with two-photon-absorbed photopolymerization. Opt Lett. 1997;22(2):132-4.

5. Kawata S, Sun H-B, Tanaka T, Takada K. Finer features for functional microdevices. Nature. 2001;412(6848):697-8.

6. Zhou X, Hou Y, Lin J. A review on the processing accuracy of two-photon polymerization. AIP Advances. 2015;5(3):030701.

7. Fourkas JT. Chapter 1.3 - Fundamentals of Two-Photon Fabrication. In: Baldacchini T, editor. Three-Dimensional Microfabrication Using Two-photon Polymerization. Oxford: William Andrew Publishing; 2016. p. 45-61.

8. Malinauskas M, Farsari M, Piskarskas A, Juodkazis S. Ultrafast laser nanostructuring of photopolymers: A decade of advances. Physics Reports. 2013;533(1):1-31.

9. Selimis A, Mironov V, Farsari M. Direct laser writing: Principles and materials for scaffold 3D printing. Microelectronic Engineering. 2015;132:83-9.

10. LaFratta CN, Baldacchini T. Two-Photon Polymerization Metrology: Characterization Methods of Mechanisms and Microstructures. Micromachines. 2017;8(4):101.

11. de Miguel G, Vicidomini G, Harke B, Diaspro A. Chapter 8 - Linewidth and Writing Resolution. In: Baldacchini T, editor. Three-Dimensional Microfabrication Using Two-photon Polymerization. Oxford: William Andrew Publishing; 2016. p. 190-220.

12. Mian Rong L. Fabrication and applications of metallic and polymeric smart materials using two-photon lithography 2018.

13. Zipfel WR, Williams RM, Webb WW. Nonlinear magic: multiphoton microscopy in the biosciences. Nature Biotechnology. 2003;21(11):1369-77.

14. El-Tamer A, Hinze U, Chichkov BN. Two-Photon Polymerization in Optics, Microfluidics, and Biomedicine. In: Sugioka K, editor. Handbook of Laser Micro- and Nano-Engineering. Cham: Springer International Publishing; 2020. p. 1-44.

15. Mao M, He J, Li X, Zhang B, Lei Q, Liu Y, et al. The Emerging Frontiers and Applications of High-Resolution 3D Printing. Micromachines. 2017;8(4):113.

16. Han D, Lu Z, Chester SA, Lee H. Micro 3D Printing of a Temperature-Responsive Hydrogel Using Projection Micro-Stereolithography. Scientific Reports. 2018;8(1):1963.

17. Sun C, Fang N, Wu DM, Zhang X. Projection micro-stereolithography using digital micro-mirror dynamic mask. Sensors and Actuators A: Physical. 2005;121(1):113-20.

18. Ge Q, Li Z, Wang Z, Kowsari K, Zhang W, He X, et al. Projection micro stereolithography based 3D printing and its applications. International Journal of Extreme Manufacturing. 2020;2(2):022004.

19. Andrzejewska E. Chapter 2 - Free Radical Photopolymerization of Multifunctional Monomers. In: Baldacchini T, editor. Three-Dimensional Microfabrication Using Two-photon Polymerization. Oxford: William Andrew Publishing; 2016. p. 62-81.

20. Carraher Jr CE. Introduction to Polymer Chemistry. London, UNITED KINGDOM: Taylor & Francis Group; 2017.

21. Carlotti M, Mattoli V. Functional Materials for Two-Photon Polymerization in Microfabrication. Small. 2019;15(40):1902687.

22. Nguyen AK, Narayan RJ. Two-photon polymerization for biological applications. Materials Today. 2017;20(6):314-22.

23. Golvari P, Kuebler SM. Fabrication of Functional Microdevices in SU-8 by Multi-Photon Lithography. Micromachines. 2021;12(5):472.

24. Ligon SC, Liska R, Stampfl J, Gurr M, Mülhaupt R. Polymers for 3D Printing and Customized Additive Manufacturing. Chemical Reviews. 2017;117(15):10212-90.

25. Ovsianikov A, Chichkov B, Mente P, Monteiro-Riviere NA, Doraiswamy A, Narayan RJ. Two Photon Polymerization of Polymer–Ceramic Hybrid Materials for Transdermal Drug Delivery. International Journal of Applied Ceramic Technology. 2007;4(1):22-9.

26. Festas AJ, Ramos A, Davim JP. Medical devices biomaterials – A review. Proceedings of the Institution of Mechanical Engineers, Part L: Journal of Materials: Design and Applications. 2019;234(1):218-28.

27. Felipe-Mendes C, Ruiz-Rubio L, Vilas-Vilela JL. Biomaterials obtained by photopolymerization: from UV to two photon. Emergent Materials. 2020;3(4):453-68.

28. van Bochove B, Grijpma DW. Photo-crosslinked synthetic biodegradable polymer networks for biomedical applications. Journal of Biomaterials Science, Polymer Edition. 2019;30(2):77-106.

29. Wei S, Liu J, Zhao Y, Zhang T, Zheng M, Jin F, et al. Protein-Based 3D Microstructures with Controllable Morphology and pH-Responsive Properties. ACS Applied Materials & Interfaces. 2017;9(48):42247-57.

30. Kufelt O, El-Tamer A, Sehring C, Schlie-Wolter S, Chichkov BN. Hyaluronic Acid Based Materials for Scaffolding via Two-Photon Polymerization. Biomacromolecules. 2014;15(2):650-9.

31. Seidlits SK, Schmidt CE, Shear JB. High-Resolution Patterning of Hydrogels in Three Dimensions using Direct-Write Photofabrication for Cell Guidance. Advanced Functional Materials. 2009;19(22):3543-51.

32. Ovsianikov A, Deiwick A, Van Vlierberghe S, Pflaum M, Wilhelmi M, Dubruel P, et al. Laser Fabrication of 3D Gelatin Scaffolds for the Generation of Bioartificial Tissues. Materials (Basel). 2011;4(1):288-99.

33. Brigo L, Urciuolo A, Giulitti S, Della Giustina G, Tromayer M, Liska R, et al. 3D high-resolution two-photon crosslinked hydrogel structures for biological studies. Acta Biomater. 2017;55:373-84.

34. Van Hoorick JWE, Gruber P, Hölzl K, Markovic M, Tromayer M, Van Erps J, et al. Two-photon polymerization of gelatin hydrogels: carboxylic acid modification as the key to success. Lausanne; 2016.

35. Van Hoorick J, Gruber P, Markovic M, Tromayer M, Van Erps J, Thienpont H, et al. Cross-Linkable Gelatins with Superior Mechanical Properties Through Carboxylic Acid Modification: Increasing the Two-Photon Polymerization Potential. Biomacromolecules. 2017;18(10):3260-72.

36. Wang X, Wei Z, Baysah CZ, Zheng M, Xing J. Biomaterial-based microstructures fabricated by two-photon polymerization microfabrication technology. RSC Advances. 2019;9(59):34472-80.

37. Lasprilla AJR, Martinez GAR, Lunelli BH, Jardini AL, Filho RM. Poly-lactic acid synthesis for application in biomedical devices — A review. Biotechnology Advances. 2012;30(1):321-8.

38. Woodruff MA, Hutmacher DW. The return of a forgotten polymer—Polycaprolactone in the 21st century. Progress in Polymer Science. 2010;35(10):1217-56.

39. Lopes MS, Jardini AL, Filho RM. Poly (Lactic Acid) Production for Tissue Engineering Applications. Procedia Engineering. 2012;42:1402-13.

40. Fukushima K. Poly(trimethylene carbonate)-based polymers engineered for biodegradable functional biomaterials. Biomaterials Science. 2016;4(1):9-24.

41. Claeyssens F, Hasan EA, Gaidukeviciute A, Achilleos DS, Ranella A, Reinhardt C, et al. Three-Dimensional Biodegradable Structures Fabricated by Two-Photon Polymerization. Langmuir. 2009;25(5):3219-23.

42. Weiß T, Schade R, Laube T, Berg A, Hildebrand G, Wyrwa R, et al. Two-Photon Polymerization of Biocompatible Photopolymers for Microstructured 3D Biointerfaces. Advanced Engineering Materials. 2011;13(9):B264-B73.

43. Felfel RM, Poocza L, Gimeno-Fabra M, Milde T, Hildebrand G, Ahmed I, et al. In vitro degradation and mechanical properties of PLA-PCL copolymer unit cell scaffolds generated by two-photon polymerization. Biomedical Materials. 2016;11(1):015011.

44. Thompson JR, Worthington KS, Green BJ, Mullin NK, Jiao C, Kaalberg EE, et al. Two-photon polymerized poly(caprolactone) retinal cell delivery scaffolds and their systemic and retinal biocompatibility. Acta Biomaterialia. 2019.

45. Koroleva A, Gill AA, Ortega I, Haycock JW, Schlie S, Gittard SD, et al. Two-photon polymerization-generated and micromolding-replicated 3D scaffolds for peripheral neural tissue engineering applications. Biofabrication. 2012;4(2):025005.

46. Timashev P, Kuznetsova D, Koroleva A, Prodanets N, Deiwick A, Piskun Y, et al. Novel biodegradable star-shaped polylactide scaffolds for bone regeneration fabricated by two-photon polymerization. Nanomedicine. 2016;11(9):1041-53.

47. Gou X, Zheng M, Zhao Y, Dong X, Jin F, Xing J, et al. Mechanical property of PEG hydrogel and the 3D red blood cell microstructures fabricated by two-photon polymerization. Applied Surface Science. 2017;416:273-80.

48. Gittard SD, Ovsianikov A, Akar H, Chichkov B, Monteiro-Riviere NA, Stafslien S, et al. Two Photon Polymerization-Micromolding of Polyethylene Glycol-Gentamicin Sulfate Microneedles. Adv Eng Mater. 2010;12(4):B77-b82.

49. Do A-V, Worthington KS, Tucker BA, Salem AK. Controlled drug delivery from 3D printed two-photon polymerized poly(ethylene glycol) dimethacrylate devices. International Journal of Pharmaceutics. 2018;552(1):217-24.

50. Accardo A, Blatché M-C, Courson R, Loubinoux I, Vieu C, Malaquin L. Two-photon lithography and microscopy of 3D hydrogel scaffolds for neuronal cell growth. Biomedical Physics & Engineering Express. 2018;4(2):027009.

51. van Bochove B, Hannink G, Buma P, Grijpma DW. Preparation of Designed Poly(trimethylene carbonate) Meniscus Implants by Stereolithography: Challenges in Stereolithography. Macromolecular Bioscience. 2016;16(12):1853-63.

52. Schüller-Ravoo S, Zant E, Feijen J, Grijpma DW. Preparation of a Designed Poly(trimethylene carbonate) Microvascular Network by Stereolithography. Advanced Healthcare Materials. 2014;3(12):2004-11.

53. Geven MA, Varjas V, Kamer L, Wang X, Peng J, Eglin D, et al. Fabrication of patient specific composite orbital floor implants by stereolithography. Polymers for Advanced Technologies. 2015;26(12):1433-8.

54. Guillaume O, Geven MA, Varjas V, Varga P, Gehweiler D, Stadelmann VA, et al. Orbital floor repair using patient specific osteoinductive implant made by stereolithography. Biomaterials. 2020;233:119721.

55. Weisgrab G, Guillaume O, Guo Z, Heimel P, Slezak P, Poot A, et al. 3D Printing of large-scale and highly porous biodegradable tissue engineering scaffolds from poly(trimethylene-carbonate) using two-photon-polymerization. Biofabrication. 2020;12(4):045036.

56. Andrzejewska E. Chapter 2.1 - Free-radical photopolymerization of multifunctional monomers. In: Baldacchini T, editor. Three-Dimensional Microfabrication Using Two-Photon Polymerization (Second Edition): William Andrew Publishing; 2020. p. 77-99.

57. Kurdikar DL, Peppas NA. A kinetic study of diacrylate photopolymerizations. Polymer. 1994;35(5):1004-11.

58. Cook WD. Photopolymerization kinetics of oligo(ethylene oxide) and oligo(methylene) oxide dimethacrylates. Journal of Polymer Science Part A: Polymer Chemistry. 1993;31(4):1053-67.

59. Cook WD. Thermal aspects of the kinetics of dimethacrylate photopolymerization. Polymer. 1992;33(10):2152-61.

60. Jiang L, Xiong W, Zhou Y, Liu Y, Huang X, Li D, et al. Performance comparison of acrylic and thiol-acrylic resins in two-photon polymerization. Opt Express. 2016;24(12):13687-701.

61. Yan D, Gao C, Frey H. Chapter 1 - Promising Dentritic Materials: An Introduction to Hyperbranched Polymers. In: Yan D, Gao C, Frey H, editors. Hyperbranched Polymers : Synthesis, Properties, and Applications. Hoboken, UNITED STATES: John Wiley & Sons, Incorporated; 2011. p. 1-26.

62. Jeon I-Y, Noh H-J, Baek J-B. Hyperbranched Macromolecules: From Synthesis to Applications. Molecules. 2018;23(3):657.

63. Yan D, Gao C, Frey H, Yan D, Gao C, Frey H. Hyperbranched Polymers : Synthesis, Properties, and Applications. Hoboken, UNITED STATES: John Wiley & Sons, Incorporated; 2011.

64. Zhu X, Zhou Y, Yan D. Chapter 12 - Influence of Branching Architecture on Polymer Properties In: Yan D, Gao C, Frey H, editors. Hyperbranched Polymers : Synthesis, Properties, and Applications. Hoboken, UNITED STATES: John Wiley & Sons, Incorporated; 2011. p. 317-32.

65. Zheng Y, Li S, Weng Z, Gao C. Hyperbranched polymers: advances from synthesis to applications. Chemical Society Reviews. 2015;44(12):4091-130.

66. Massoumi B, Sarvari R, Agbolaghi S. Biodegradable and conductive hyperbranched terpolymers based on aliphatic polyester, poly(D,L-lactide), and polyaniline used as scaffold in tissue engineering. International Journal of Polymeric Materials and Polymeric Biomaterials. 2018;67(13):808-21.

67. Kavand A, Anton N, Vandamme T, Serra CA, Chan-Seng D. Synthesis and functionalization of hyperbranched polymers for targeted drug delivery. Journal of Controlled Release. 2020;321:285-311.

68. Zhuang Y, Su Y, Peng Y, Wang D, Deng H, Xi X, et al. Facile Fabrication of Redox-Responsive Thiol-Containing Drug Delivery System via RAFT Polymerization. Biomacromolecules. 2014;15(4):1408-18.

69. Zhao P, Mecozzi F, Wessel S, Fieten B, Driesse M, Woudstra W, et al. Preparation and Evaluation of Antimicrobial Hyperbranched Emulsifiers for Waterborne Coatings. Langmuir. 2019;35(17):5779-86.

70. Prabu S, Sultan Nasar A, Sivakumar C. Salicylic Acid Based Hyperbranched Polyester: Synthesis, Characterization, Optical Properties and Antimicrobial Activity. Macromolecular Research. 2018;26(9):831-7.

71. Smet M. Chapter 15 - Biological and Medical Applications of Hyperbranched Polymers. In: Yan D, Gao C, Frey H, editors. Hyperbranched Polymers : Synthesis, Properties, and Applications. Hoboken, UNITED STATES: John Wiley & Sons, Incorporated; 2011. p. 387-415.

72. Gottschalk C, Frey H. Hyperbranched Polylactide Copolymers. Macromolecules. 2006;39(5):1719-23.

73. Smet M, Gottschalk C, Skaria S, Frey H. Aliphatic Hyperbranched Copolyesters by Combination of ROP and AB2-Polycondensation. Macromolecular Chemistry and Physics. 2005;206(24):2421-8.

74. Chang C-J, Lin Y-H, Tsai H-Y. Synthesis and properties of UV-curable hyperbranched polymers for ink-jet printing of color micropatterns on glass. Thin Solid Films. 2011;519(15):5243-8.

75. Wheeler JSR, Longpré A, Sells D, McManus D, Lancaster S, Reynolds SW, et al. Effect of polymer branching on degradation during inkjet printing. Polymer Degradation and Stability. 2016;128:1-7.

76. Jafarifard S, Bastani S, Soleimani-Gorgani A, Sari MG. The chemo-rheological behavior of an acrylic based UV-curable inkjet ink: Effect of surface chemistry for hyperbranched polymers. Progress in Organic Coatings. 2016;90:399-406.

77. Xiang H, Wang X, Lin G, Xi L, Yang Y, Lei D, et al. Preparation, Characterization and Application of UV-Curable Flexible Hyperbranched Polyurethane Acrylate. Polymers. 2017;9(11):552.

78. Han J, Liu T, Zhang S, Hao C, Xin J, Guo B, et al. Hyperbranched Polymer Assisted Curing and Repairing of an Epoxy Coating. Industrial & Engineering Chemistry Research. 2019;58(16):6466-75.

79. Yavuz B, Kompella UB. Ocular Drug Delivery. In: Whitcup SM, Azar DT, editors. Pharmacologic Therapy of Ocular Disease Handbook of Experimental Pharmacology. 242: Springer, Cham; 2016. p. 57-93.

80. Yasin MN, Svirskis D, Seyfoddin A, Rupenthal ID. Implants for drug delivery to the posterior segment of the eye: A focus on stimuli-responsive and tunable release systems. Journal of Controlled Release. 2014;196:208-21.

81. Nayak K, Misra M. A review on recent drug delivery systems for posterior segment of eye. Biomedicine & Pharmacotherapy. 2018;107:1564-82.

82. Imperiale JC, Acosta GB, Sosnik A. Polymer-based carriers for ophthalmic drug delivery. Journal of Controlled Release. 2018;285:106-41.

83. Ratnapriya R, Chew EY. Age-related macular degeneration—clinical review and genetics update. Clinical Genetics. 2013;84(2):160-6.

84. Fleckenstein M, Keenan TDL, Guymer RH, Chakravarthy U, Schmitz-Valckenberg S, Klaver CC, et al. Age-related macular degeneration. Nature Reviews Disease Primers. 2021;7(1):31.

85. Wang W, Lo ACY. Diabetic Retinopathy: Pathophysiology and Treatments. Int J Mol Sci. 2018;19(6):1816.

86. Gaballa SA, Kompella UB, Elgarhy O, Alqahtani AM, Pierscionek B, Alany RG, et al. Corticosteroids in ophthalmology: drug delivery innovations, pharmacology, clinical applications, and future perspectives. Drug Delivery and Translational Research. 2021;11(3):866-93.

87. Haghjou N, Soheilian M, Abdekhodaie MJ. Sustained release intraocular drug delivery devices for treatment of uveitis. J Ophthalmic Vis Res. 2011;6(4):317-29.

88. Poornachandra B, Kumar VBM, Jayadev C, Dorelli SH, Yadav NK, Shetty R. Immortal Ozurdex: A 10-month follow-up of an intralenticular implant. Indian Journal of Ophthalmology. 2017;65(3):255-7.

89. Cao Y, Samy KE, Bernards DA, Desai TA. Recent advances in intraocular sustained-release drug delivery devices. Drug Discovery Today. 2019;24(8):1694-700.

90. Lee SS, Hughes P, Ross AD, Robinson MR. Advances in Biodegradable Ocular Drug Delivery Systems. In: Kompella UB, Edelhauser HF, editors. Drug Product Development for the Back of the Eye. Boston, MA: Springer US; 2011. p. 185-230.

91. Gupta SV. Chapter 7 - Physicochemical Requirements for Polymers and Polymer-Based Nanomaterial for Ophthalmic Drug Delivery. In: Pathak YV, Sutariya V, Hirani AA, editors. Nano-Biomaterials For Ophthalmic Drug Delivery: Springer International Publishing; 2016. p. 131-46.

92. Yin H, Gong C, Shi S, Liu X, Wei Y, Qian Z. Toxicity evaluation of biodegradable and thermosensitive PEG-PCL-PEG hydrogel as a potential in situ sustained ophthalmic drug delivery system. J Biomed Mater Res B Appl Biomater. 2010;92(1):129-37.

93. Junnuthula V, Sadeghi Boroujeni A, Cao S, Tavakoli S, Ridolfo R, Toropainen E, et al. Intravitreal Polymeric Nanocarriers with Long Ocular Retention and Targeted Delivery to the Retina and Optic Nerve Head Region. Pharmaceutics. 2021;13(4):445.

94. Niu G, Yang Y, Zhang H, Yang J, Song L, Kashima M, et al. Synthesis and characterization of acrylamide/N-vinylpyrrolidone copolymer with pendent thiol groups for ophthalmic applications. Acta Biomaterialia. 2009;5(4):1056-63.

95. Thakur RRS, Tekko IA, Al-Shammari F, Ali AA, McCarthy H, Donnelly RF. Rapidly dissolving polymeric microneedles for minimally invasive intraocular drug delivery. Drug Delivery and Translational Research. 2016;6(6):800-15.

96. Jansen J, Koopmans SA, Los LI, van der Worp RJ, Podt JG, Hooymans JMM, et al. Intraocular degradation behavior of crosslinked and linear poly(trimethylene carbonate) and poly(d,l-lactic acid). Biomaterials. 2011;32(22):4994-5002.

97. Spadaccini CM. Chapter 13.4 - Future perspectives on materials for two-photon polymerization. In: Baldacchini T, editor. Three-Dimensional Microfabrication Using Two-Photon Polymerization (Second Edition): William Andrew Publishing; 2020. p. 671-81.

98. Ruiz-Cantu LA, Pearce AK, Burroughs L, Bennett TM, Vasey CE, Wildman R, et al. Synthesis of Methacrylate-Terminated Block Copolymers with Reduced Transesterification by Controlled Ring-Opening Polymerization. Macromolecular Chemistry and Physics. 2019;220(2):1800459.

99. Ember KJI, Hoeve MA, McAughtrie SL, Bergholt MS, Dwyer BJ, Stevens MM, et al. Raman spectroscopy and regenerative medicine: a review. npj Regenerative Medicine. 2017;2(1):12.

100. Bumbrah GS, Sharma RM. Raman spectroscopy – Basic principle, instrumentation and selected applications for the characterization of drugs of abuse. Egyptian Journal of Forensic Sciences. 2016;6(3):209-15.

101. Cole DA, Attavar S, Zhang L. Chapter 8 - Surface Analysis Methods for Contaminant Identification. In: Kohli R, Mittal KL, editors. Developments in Surface Contamination and Cleaning (Second Edition). Oxford: William Andrew Publishing; 2016. p. 333-94.

102. Fearn S. An Introduction to Time-of-Flight Secondary Ion Mass Spectrometry (ToF-SIMS) and its Application to Materials Science: Morgan & Claypool Publishers; 2015. Available from: http://dx.doi.org/10.1088/978-1-6817-4088-1.

103. Thiel V, Sjövall P. Using Time-of-Flight Secondary Ion Mass Spectrometry to Study Biomarkers. Annual Review of Earth and Planetary Sciences. 2011;39(1):125-56.

104. Trindade GF, Abel M-L, Watts JF. simsMVA: A tool for multivariate analysis of ToF-SIMS datasets. Chemometrics and Intelligent Laboratory Systems. 2018;182:180-7.

105. Keenan MR, Smentkowski VS. The statistics of ToF-SIMS data revisited and introduction of the empirical Poisson correction. Surface and Interface Analysis. 2016;48(4):218-25.

106. Kozuch D, Zhang W, Milner S. Predicting the Flory-Huggins Parameter for Polymers with Stiffness Mismatch from Molecular Dynamics Simulations. Polymers. 2016;8:241.

107. Imre B, Renner K, Pukanszky B. Interactions, structure and properties in poly(lactic acid)/thermoplastic polymer blends. Express Polym Lett. 2014;8:2-14.

108. Xiong W, Liu Y, Jiang LJ, Zhou YS, Li DW, Jiang L, et al. Laser-Directed Assembly of Aligned Carbon Nanotubes in Three Dimensions for Multifunctional Device Fabrication. Advanced Materials. 2016;28(10):2002-9.

109. Xiong Z, Zheng C, Jin F, Wei R, Zhao Y, Gao X, et al. Magnetic-field-driven ultra-small 3D hydrogel microstructures: Preparation of gel photoresist and two-photon polymerization microfabrication. Sensors and Actuators B: Chemical. 2018;274:541-50.

110. Wang Q, Jackson JA, Ge Q, Hopkins JB, Spadaccini CM, Fang NX. Lightweight Mechanical Metamaterials with Tunable Negative Thermal Expansion. Physical Review Letters. 2016;117(17):175901.

111. Schwartz JJ, Boydston AJ. Multimaterial actinic spatial control 3D and 4D printing. Nature Communications. 2019;10(1):791.

112. Ge Q, Sakhaei AH, Lee H, Dunn CK, Fang NX, Dunn ML. Multimaterial 4D Printing with Tailorable Shape Memory Polymers. Scientific Reports. 2016;6(1):31110.

113. Ulery BD, Nair LS, Laurencin CT. Biomedical applications of biodegradable polymers. Journal of Polymer Science Part B: Polymer Physics. 2011;49(12):832-64.

114. Simon DM, Charkhkar H, St. John C, Rajendran S, Kang T, Reit R, et al. Design and demonstration of an intracortical probe technology with tunable modulus. Journal of Biomedical Materials Research Part A. 2017;105(1):159-68.

115. Black BJ, Ecker M, Stiller A, Rihani R, Danda VR, Reed I, et al. In vitro compatibility testing of thiol-ene/acrylate-based shape memory polymers for use in implantable neural interfaces. Journal of Biomedical Materials Research Part A. 2018;106(11):2891-8.

116. He Y, Luckett J, Begines B, Dubern J-F, Hook AL, Prina E, et al. Ink-jet 3D printing as a strategy for developing bespoke non-eluting biofilm resistant medical devices. Biomaterials. 2021:121350.

117. Ruiz-Cantu L, F Trindade G, Taresco V, Zhou Z, He Y, Burroughs L, et al. Bespoke 3D-Printed Polydrug Implants Created via Microstructural Control of Oligomers. ACS Applied Materials & Interfaces. 2021;13(33):38969-78.

118. Avdeef A. Absorption and Drug Development : Solubility, Permeability, and Charge State. Hoboken, UNITED STATES: John Wiley & Sons, Incorporated; 2012.

119. Latham M. Hydrophilic Polymeric Adhesives: A Case Study [M.E.]. Ann Arbor: University of Kansas; 2020.

120. Foerster A, Annarasa V, Terry A, Wildman R, Hague R, Irvine D, et al. UV-curable silicone materials with tuneable mechanical properties for 3D printing. Materials & Design. 2021;205:109681.

121. Gilbert M. Chapter 4 - Relation of Structure to Thermal and Mechanical Properties. In: Gilbert M, editor. Brydson's Plastics Materials (Eighth Edition): Butterworth-Heinemann; 2017. p. 59-73.

122. Thijs L, Verhaeghe F, Craeghs T, Humbeeck JV, Kruth J-P. A study of the microstructural evolution during selective laser melting of Ti–6Al–4V. Acta Materialia. 2010;58(9):3303-12.

123. Mondschein RJ, Kanitkar A, Williams CB, Verbridge SS, Long TE. Polymer structure-property requirements for stereolithographic 3D printing of soft tissue engineering scaffolds. Biomaterials. 2017;140:170-88.

124. Hao Y, Gao J, Xu Z, Zhang N, Luo J, Liu X. Preparation of silver nanoparticles with hyperbranched polymers as a stabilizer for inkjet printing of flexible circuits. New Journal of Chemistry. 2019;43(6):2797-803.

125. Ning L, Chen J, Sun J, Liu Y, Yi D, Cao J. Preparation and Properties of 3D Printing Light-Curable Resin Modified with Hyperbranched Polysiloxane. ACS Omega. 2021;6(37):23683-90.

126. Chan K, O'Brien PJ. Structure–activity relationships for hepatocyte toxicity and electrophilic reactivity of α,β-unsaturated esters, acrylates and methacrylates. Journal of Applied Toxicology. 2008;28(8):1004-15.

127. Haesslein A, Ueda H, Hacker MC, Jo S, Ammon DM, Borazjani RN, et al. Long-term release of fluocinolone acetonide using biodegradable fumarate-based polymers. Journal of Controlled Release. 2006;114(2):251-60.

128. Jansen J, Boerakker MJ, Heuts J, Feijen J, Grijpma DW. Rapid photo-crosslinking of fumaric acid monoethyl ester-functionalized poly(trimethylene carbonate) oligomers for drug delivery applications. Journal of Controlled Release. 2010;147(1):54-61.

129. Lp J. A Summary of Recent Advances in Ocular Inserts and Implants. Journal of Bioequivalence & Bioavailability. 2016;09(01).

130. Blanquer SBG, Grijpma DW. Triply Periodic Minimal Surfaces (TPMS) for the Generation of Porous Architectures Using Stereolithography. In: Rainer A, Moroni L, editors. Computer-Aided Tissue Engineering: Methods and Protocols. New York, NY: Springer US; 2021. p. 19-30.

131. Vijayavenkataraman S, Zhang L, Zhang S, Hsi Fuh JY, Lu WF. Triply Periodic Minimal Surfaces Sheet Scaffolds for Tissue Engineering Applications: An Optimization Approach toward Biomimetic Scaffold Design. ACS Applied Bio Materials. 2018;1(2):259-69.

132. Kyobula M, Adedeji A, Alexander MR, Saleh E, Wildman R, Ashcroft I, et al. 3D inkjet printing of tablets exploiting bespoke complex geometries for controlled and tuneable drug release. Journal of Controlled Release. 2017;261:207-15.

133. Yu H, Qiu X, Nunes SP, Peinemann K-V. Biomimetic block copolymer particles with gated nanopores and ultrahigh protein sorption capacity. Nature Communications. 2014;5(1):4110.

134. Maskery I, Parry LA, Padrão D, Hague RJM, Ashcroft IA. FLatt Pack: A research-focussed lattice design program. Additive Manufacturing. 2022;49:102510.

135. Lehder EF, Ashcroft IA, Wildman RD, Ruiz-Cantu LA, Maskery I. A multiscale optimisation method for bone growth scaffolds based on triply periodic minimal surfaces. Biomechanics and Modeling in Mechanobiology. 2021;20(6):2085-96.

136. Amin Yavari S, Ahmadi SM, Wauthle R, Pouran B, Schrooten J, Weinans H, et al. Relationship between unit cell type and porosity and the fatigue behavior of selective laser melted meta-biomaterials. Journal of the Mechanical Behavior of Biomedical Materials. 2015;43:91-100.

137. Pescosolido N, Giannotti R, Plateroti AM, Pascarella A, Nebbioso M. Curcumin: Therapeutical Potential in Ophthalmology. Planta Med. 2014;80(04):249-54.

138. Zhu W, Wu Y, Meng YF, Wang JY, Xu M, Tao JJ, et al. Effect of curcumin on aging retinal pigment epithelial cells. Drug Des Devel Ther. 2015;9:5337-44.

139. Grigoryan B, Paulsen SJ, Corbett DC, Sazer DW, Fortin CL, Zaita AJ, et al. Multivascular networks and functional intravascular topologies within biocompatible hydrogels. Science. 2019;364(6439):458-64.

140. Hollborn M, Chen R, Wiedemann P, Reichenbach A, Bringmann A, Kohen L. Cytotoxic Effects of Curcumin in Human Retinal Pigment Epithelial Cells. PLOS ONE. 2013;8(3):e59603.

141. López-Malo D, Villarón-Casares CA, Alarcón-Jiménez J, Miranda M, Díaz-Llopis M, Romero FJ, et al. Curcumin as a Therapeutic Option in Retinal Diseases. Antioxidants. 2020;9(1):48.

142. Xu M, McCanna DJ, Sivak JG. Use of the viability reagent PrestoBlue in comparison with alamarBlue and MTT to assess the viability of human corneal epithelial cells. Journal of Pharmacological and Toxicological Methods. 2015;71:1-7.

143. Kumar P, Nagarajan A, Uchil PD. Analysis of Cell Viability by the Lactate Dehydrogenase Assay. Cold Spring Harb Protoc. 2018;2018(6).

144. De Paiva MRB, Lage NA, Guerra MCA, Mol MPG, Ribeiro MCS, Fulgêncio GDO, et al. Toxicity and in vivo release profile of sirolimus from implants into the vitreous of rabbits' eyes. Documenta Ophthalmologica. 2019;138(1):3-19.

145. Lee JS, Lee SU, Che C-Y, Lee J-E. Comparison of cytotoxicity and wound healing effect of carboxymethylcellulose and hyaluronic acid on human corneal epithelial cells. Int J Ophthalmol. 2015;8(2):215-21.

146. Merz PR, Röckel N, Ballikaya S, Auffarth GU, Schmack I. Effects of ranibizumab (Lucentis®) and bevacizumab (Avastin®) on human corneal endothelial cells. BMC Ophthalmology. 2018;18(1):316.